



ELECTROCHEMICAL INVESTIGATION  
OF THE SOLID METAL/ELECTROLYTE SOLUTION INTERFACE

A thesis presented for the degree of

Doctor of Philosophy

at

The University of Adelaide

by

NIGEL WAYNE CURRIE, B.Sc.

Department of Physical and Inorganic Chemistry

November, 1984

*Awarded 20.8.85*

## CONTENTS

- CHAPTER 1      A Review of the Solid Metal Electrode/Electrolyte Solution Interface.
- CHAPTER 2      Chronopotentiometric Determination of Tracer Diffusion Coefficients of Thallium (I) in H<sub>2</sub>O+NMF Electrolyte Solutions Using Solid Metal Electrodes
- CHAPTER 3      Cyclic Voltammetric Study of the Solid Electrode/Electrolyte Solution Interface
- CHAPTER 4      Methods of Measurement of the Double Layer Capacitance of the Solid Electrode/Electrolyte Solution Interface
- CHAPTER 5      Double Layer Capacitance of the Solid Electrode/Electrolyte Solution Interface in H<sub>2</sub>O at 25°C
- CHAPTER 6      Determination of Electrolyte Activity in H<sub>2</sub>O+NMF Solvent Mixtures from emf Measurements at 25°C
- CHAPTER 7      Double Layer Capacitance of the Solid Electrode/Electrolyte Solution Interface in NMF at 25°C
- APPENDIX 1     Circuit of Galvanostat Used in Chronopotentiometry
- APPENDIX 2     Discussion Concerning the Scanning Electron Microscope (S.E.M.) Micrographs Presented in Figure 4 of Chapter 3

**SUMMARY**

The electrochemical investigation of the metal electrode/electrolyte solution interface has been largely centred around the use of the liquid mercury electrode. The proliferation of investigations using solid metal electrodes was retarded until the last decade by problems associated with the preparation of clean, smooth, well-defined electrode surfaces. These problems have been discussed in the text.

Investigations of hydrogen atom adsorption using cyclic voltammetry, thallium diffusion using chronopotentiometry, and double layer capacitance measurements using Single Current Pulse and A.C. Impedance methods have been made using solid metal electrodes.

The tracer diffusion coefficient of thallium(I) has been measured in high concentrations of background electrolyte in solvent mixtures ranging from pure water to pure NMF. The tracer diffusion coefficient of thallium(I) in 0.300M  $\text{KNO}_3$  was found to decrease from  $1.88 \times 10^{-5} \text{ cm}^2/\text{s}$  to  $0.506 \times 10^{-5} \text{ cm}^2/\text{s}$  as the NMF solvent mole fraction was increased from 0 to 1.000.

The techniques and results of the Single Current Method and the A.C. Impedance Method in measuring the capacitance of the solid electrode/electrolyte solution interface are reported. The techniques were found to give different results. The validity of the equivalent analogue circuits used to extract interfacial capacitance and resistance values is discussed.

The results of the measurement of the double layer capacitance of the solid electrode/aqueous electrolyte solution interface are presented for polycrystalline platinum and silver electrodes. The frequency

dispersion, hysteresis, and time dependence of measurements are discussed. The capacitance measurements were extended from aqueous systems to the solid electrode/NMF electrolyte solution interface. Measurements were made for the  $\text{NaNO}_3$  + NMF system using platinum and silver electrodes. The problems involved in using capacitance measurements to determine NMF adsorbance coverage on solid metal electrodes ~~is~~ *are* discussed.

As a preliminary step prior to the attempt to use capacitance measurements as a means of obtaining NMF adsorbance coverage data, a nitrate ion selective electrode was developed, and its response to  $\text{NaNO}_3$  in water and NMF recorded. The novel nitrate ion selective electrode presented here is of a solid state type, and differs from the conventional liquid ion exchanger based nitrate ion selective electrode in that it possesses no liquid ion exchanger or membrane diaphragm. The nitrate ion selective electrode coupled with a sodium ion glass electrode was used to determine the concentration of  $\text{NaNO}_3$  required to maintain constant electrolyte activity for solvents of various NMF +  $\text{H}_2\text{O}$  compositions. The concentration of  $\text{NaNO}_3$  required to maintain the same electrolyte activity as 0.100M  $\text{NaNO}_3$  in pure water was found to decrease with increasing mole fraction of NMF, to a value of  $5 \times 10^{-4}$  M  $\text{NaNO}_3$  in pure NMF.



I hereby declare that this thesis contains no material which has been accepted for the award of any other degree or diploma in any University, and that, to the best of my knowledge and belief, the thesis contains no material previously published or written by another person, except where due reference is made in the text of the thesis. I also declare that I am willing to make the thesis available for photocopying and loan if it is accepted for the award of the degree.

Nigel Currie

## ACKNOWLEDGEMENTS

I express my gratitude to Dr. B. J. Steel for his overall supervision and helpful discussion during the course of this research.

I acknowledge the invaluable technical support provided by Messrs. Arthur Bowers, Gavin Duthie and Keith Shepherdson and their colleagues in the three workshops in this department.

Dr. Dennis Mulcahy and Mr. Peter Dorsett provided assistance that proved invaluable in the ion-selective electrode work presented in Chapter 6.

Dr. B. J. Griffin of the Electron Optical Centre operated the Jeol Electron Microprobe Analyser to record the data presented in Figure 15 of Chapter 2.

I express my gratitude to Etta Clark for the efficient typing of all text and tables presented in this thesis.

I gratefully acknowledge the concern, encouragement and support given to me by my parents.

The tenure of a Commonwealth Post Graduate Research Award for four years is gratefully acknowledged.

Above all, I thank the Lord God through Jesus Christ, who guided me and taught me how to become efficient (Isaiah 48:17).

## CHAPTER 1

### A REVIEW OF THE SOLID METAL ELECTRODE/ ELECTROLYTE SOLUTION INTERFACE

A REVIEW OF THE SOLID METAL ELECTRODE/ ELECTROLYTE SOLUTION INTERFACE	1.1
REFERENCES	1.7



## 1.1

### A REVIEW OF THE SOLID METAL ELECTRODE/ELECTROLYTE SOLUTION INTERFACE

The phenomena connected with the double layer formed at the interface between a metal electrode and an electrolyte solution have been extensively reviewed.<sup>1-5</sup> The most commonly accepted structure of the interface formed between a metal electrode and an electrolyte solution is that originally suggested by Gouy<sup>6</sup> and Chapman,<sup>7</sup> and later modified by Stern.<sup>8</sup> The interface is considered to consist of an outer or diffuse layer, and an inner or compact layer. The two layers are separated by the outer Helmholtz plane, which conventionally defines the plane of closest approach of the centres of solvated ions held in averaged positions by the balance between diffusive forces and the electric field in the region. The inner or compact layer is thought to be a reasonably close-packed monolayer, containing solvent molecules and, in the case of specific ion adsorption, containing ions directly adsorbed on to the metal surface.

The separation of the double layer into the inner and diffuse regions came largely from the work of Stern,<sup>8</sup> but was widely accepted following the work of Grahame<sup>1,9</sup> using mercury electrodes. Grahame suggested that, assuming Stern's model, the total capacitance,  $C$ , of the metal electrode/electrolyte solution interface could be thought of as being due to the series combination of the separate contributions of the inner layer capacitance,  $C_i$ , and the diffuse layer capacitance,  $C_d$ , so that

$$1/C = 1/C_i + 1/C_d$$

## 1.2

Devanathan<sup>10</sup> further showed that the contribution to the capacitance made by the diffuse layer could be calculated from

$$C_d = 19.46(q^2 + 137.8c)^{\frac{1}{2}}$$

where  $q$  is the charge on the electrode surface, and  $c$  is the molar concentration of a 1:1 electrolyte in water. The equation predicting the diffuse layer capacitance reveals that  $C_d$  will only contribute to the measured capacitance,  $C$ , for low values of the electrode charge and the electrolyte concentration. The potential of the capacitance minimum found in dilute electrolyte solutions was thus equated with the influence of the diffuse layer capacitance at the potential of zero electrode charge. This was confirmed using mercury electrodes from the coincidence of the capacitance minimum with the electrocapillary maximum. The use of the capacitance minimum as a means of determining the potential of zero charge is very common in studies using solid electrodes. This is clearly revealed in a recent review by Hamelin et al.<sup>11</sup>

The inner layer capacitance,  $C_i$ , was thought of as being independent of the electrode charge and electrolyte concentration for a given system. Parsons and Zobel<sup>12</sup> suggested that a plot of  $1/C$  against  $1/C_d$  at constant charge should, in the absence of specific ion adsorption, yield a straight line of unit slope to reveal that  $C_i$  was constant. Deviation of the Parsons-Zöbel slopes from unity was interpreted as being due to specific ion adsorption or surface roughness of solid electrodes.<sup>11-16</sup>

### 1.3

Recently, Kornyshev and Vorotyntsev<sup>17</sup> gave formal approval of Grahame's parametrization of experimental data. In their reconsideration of the compact layer treatment, they were also able to forward reasons for the experimentally found dependence of the compact layer capacitance on the nature of the electrode and solvent.

The apparent success of the separation of the double layer into inner and diffuse layer contributions led many to publish results showing dependence of the inner layer capacitance,  $C_i$ , upon electrode charge, temperature and electrode type.<sup>13,14,18-24</sup> Experimentally it was found that the inner layer capacitance-charge curve displayed a maximum. This maximum, which showed up as a hump in total capacitance plotted against either charge or potential, has been interpreted as due to specific ion adsorption.<sup>25-29</sup> It is widely accepted now that this feature is rather related to solvent re-orientation occurring at the electrode surface.<sup>23,30</sup> A number of molecular theories based on statistical approaches have been proposed by many workers<sup>24,31</sup> to describe the solvent properties of the metal electrode/electrolyte solution interface.

Although the treatment of the double layer in terms of an inner layer and a diffuse layer has proved successful, such a treatment has not been without criticism.

Recently, Henderson et al<sup>31</sup> commented that such a treatment, although useful, was unsatisfactory because of its inconsistent treatment of the solvent. Cooper and Harrison<sup>33-39</sup> have been long-term critics of such a treatment, strongly expressing their opposition to

the treatment of the inner layer as a separate physical entity. These authors have recently proposed a new theory, taking into account ion-ion repulsions in a direction parallel to the electrode surface, which they believe is a more realistic theoretical model.<sup>38,39</sup> Schmickler<sup>40</sup> has criticised the treatment of the metal as a perfectly conducting medium. In his treatment of this problem, Schmickler combined a simple quantum-mechanical model of a metal surface with a dipole model for the solvent with some success.

The Gouy-Chapman-Stern (GCS) model has been used extensively to interpret data obtained for the mercury electrode/electrolyte solution interface. The apparent success of the model for the mercury electrode resulted in it also becoming the model used to describe the interfacial region for other metal electrodes. Most metal electrodes, however, are solid, and present a non-homogeneous surface to the electrolyte solution. The appropriateness of the GCS model in the case where the metal electrode surface is heterogeneous has, with few exceptions, been ignored.<sup>14,41</sup>

In the last decade many researchers have attempted to use solid electrodes having well-defined homogeneous surfaces by using electrodes formed from single crystals. Hamelin et al<sup>11</sup> have recently reviewed double layer capacitance investigations using sp metal single crystals. They found that the crystallographic structure of the metal surface strongly influenced the capacitance-potential curves obtained, and suggested that any crystallographic anisotropy would make quantitative data analysis difficult. It was recognized, however, that problems still remained in obtaining solid surfaces with a well-defined crystallographic orientation. Among the problems discussed were edge effects,

surface defects, and lack of precision of crystallographic orientation. In another article looking at problems encountered in trying to obtain well-defined solid surfaces,<sup>42</sup> the preparation of the surface was shown to be important in reducing crystallographic anisotropy.

The interpretation of the behaviour of heterogeneous surfaces has been looked at as the composite behaviour of individual single-crystal faces. Valette and Hamelin<sup>14</sup> constructed a capacitance-potential curve for polycrystalline silver from their experimental data obtained with low-indexed silver single-crystal electrodes. The shape and potential of the capacitance minimum was reported to be in good agreement with experimental results. Damaskin and co-workers<sup>43</sup> proposed two models to describe the polycrystalline metal electrode/electrolyte solution interface. Larkin et al<sup>44</sup> suggested that the behaviour of polycrystalline silver in dilute aqueous NaF was not inconsistent with one of the models proposed by Damaskin et al. Larkin<sup>45</sup> further reported the results of the interfacial behaviour predicted from computer simulated models of the polycrystalline silver electrode surface using the Damaskin models.

An important finding from Larkin's treatment was that one of Damaskin's models predicts the development of a capacitance minimum in the capacitance-potential curves at a potential that was not necessarily coincident with the condition of zero charge at the polycrystalline electrode/electrolyte solution interface.



## 1.6

Obviously, further high quality capacitance measurements using both single-crystal and polycrystalline electrodes are required to provide a basis for further testing and modification of the current theories concerning the solid metal electrode/electrolyte solution interface.

## REFERENCES

- 1 GRAHAME, D. C., *Chem. Revs.*, 41(1947) 441.
- 2 PARSONS, R., *Adv. Electrochem. Electrochem. Eng.*, 1(1961) 1.
- 3 BARLOW, C. A., Jr. and MACDONALD, J. R., *Adv. Electrochem. Electrochem. Eng.*, 6(1967) 1.
- 4 FRUMKIN, A. N., *J. Electrochem. Soc.*, 107(1960) 461.
- 5 PARSONS, R., *J. Electroanal. Chem.*, 118(1981) 3.
- 6 GOUY, G., *J. Phys. Radium.*, 9(1910) 457; *C. R. Acad. Sci. Ser. B*, 149(1910) 654.
- 7 CHAPMAN, D. L., *Phil. Mag.*, 25(1913) 475.
- 8 STERN, O., *Z. Electrochem.*, 30(1924) 508.
- 9 GRAHAME, D. C., *J. Am. Chem. Soc.*, 79(1957) 393.
- 10 DEVANATHAN, M. A. V., *Trans. Faraday Soc.*, 50(1954) 373.
- 11 HAMELIN, A., VITANOV, T., SEVASTYANOV, E. and POPOV, A., *J. Electroanal. Chem.*, 145(1983) 225.
- 12 PARSONS, R. and ZOBEL, F. G. R., *J. Electroanal. Chem.*, 9(1965) 333.
- 13 VALETTE, G. and HAMELIN, A., *C. R. Acad. Sci. (Paris)*, 272C(1971) 602.
- 14 VALETTE, G. and HAMELIN, A., *J. Electroanal. Chem.*, 45(1973) 301.
- 15 VITANOV, T. and POPOV, A., *Trans. S.A.E.S.T.*, 10(1975) 5.
- 16 VITANOV, T., POPOV, A. and SEVASTYANOV, E. S., *J. Electroanal. Chem.*, 142(1982) 289.
- 17 KORNYSHEV, A. A. and VOROTYNTSEV, M. A., *Can. J. Chem.*, 59(1981) 2031.
- 18 HILLS, G. and SILVA, F., *Can. J. Chem.*, 59(1981) 1835.
- 19 FAWCETT, W. R., LEVINE, S., de NOBRIGA, R. M. and McDONALD, A. C., *J. Electroanal. Chem.*, 111(1980) 163.
- 20 VALETTE, G., *J. Electroanal. Chem.*, 138(1982) 37.
- 21 VALETTE, G., *J. Electroanal. Chem.*, 122(1981) 285.
- 22 HAMELIN, A., *J. Electroanal. Chem.*, 138(1982) 395.

- 23 FAWCETT, W. R. and LOUTFY, R. O., *J. Electroanal. Chem.*, 39(1972) 185.
- 24 BORKOWSKA, Z., DENOBRIGA, R. M. and FAWCETT, W. R., *J. Electroanal. Chem.*, 124(1981) 263.
- 25 DEVANATHAN, M. A. V., *Trans. Faraday Soc.*, 50(1954) 373.
- 26 PAYNE, R., *J. Phys. Chem.*, 70(1966) 204.
- 27 MINC, S. and JASTRZEBSKA, J., *Electrochim. Acta*, 9(1964) 533.
- 28 WROBLOWA, H. and MULLER, K., *J. Phys. Chem.*, 73(1969) 3528.
- 29 BOCKRIS, J. O'M., DEVANATHAN, M. A. V. and MULLER, K., *Proc. Roy. Soc.*, A274(1963) 55.
- 30 PAYNE, R., *J. Phys. Chem.*, 73(1969) 3598.
- 31 See references 1-14 of reference 19.
- 32 HENDERSON, D., BLUM, L. and LOZADA-CASSOU, M., *J. Electroanal. Chem.*, 150(1983) 291.
- 33 COOPER, I. L. and HARRISON, J. A., *J. Electroanal. Chem.*, 86(1978) 425.
- 34 COOPER, I. L. and HARRISON, J. A., *J. Electroanal. Chem.*, 66(1975) 85.
- 35 COOPER, I. L. and HARRISON, J. A., *Electrochim. Acta*, 22(1977) 519.
- 36 COOPER, I. L. and HARRISON, J. A., *Electrochim. Acta*, 22(1977) 1365.
- 37 COOPER, I. L., HARRISON, J. A. and HOLLOWAY, J., *Electrochim. Acta*, 26(1981) 1273.
- 38 COOPER, I. L. and HARRISON, J. A., *Electrochim. Acta*, 29(1984) 1147.
- 39 COOPER, I. L. and HARRISON, J. A., *Electrochim. Acta*, 29(1984) 1165.
- 40 SCHMICKLER, W., *J. Electroanal. Chem.*, 150(1983) 19.
- 41 HAMPSON, N. A. and LARKIN, D., *Electrochim. Acta*, 15(1970) 581.
- 42 HAMELIN, A., *Soviet Electrochem.*, 18(1981) 1259.
- 43 BAGOTSKAYA, I. A., DAMASKIN, B. B. and LEVI, M. D., *J. Electroanal. Chem.*, 115(1980) 189.

- 44 LARKIN, D., GUYER, K. L. and WEAVER, M. J., *J. Electroanal. Chem.*, 138(1982) 401.
- 45 LARKIN, D., *J. Electroanal. Chem.*, 157(1983) 123.

## CHAPTER 2

### CHRONOPOTENTIOMETRIC DETERMINATION OF TRACER DIFFUSION COEFFICIENTS OF THALLIUM (I) IN $H_2O$ + NMF ELECTROLYTE SOLUTIONS USING SOLID METAL ELECTRODES

INTRODUCTION	2.1
EXPERIMENTAL	2.6
ELECTRONIC EQUIPMENT	2.6
ELECTROLYSIS CELLS	2.7
VIBRATION PROOFING	2.9
ELECTRODES	2.10
CLEANING PROCEDURE	2.13
CHEMICALS	2.14
SOLUTION PREPARATION	2.15
TECHNIQUE FOR OBTAINING A CHRONPOTENTIOGRAM	2.16
RESULTS AND DISCUSSION	2.18
PRELIMINARY RESULTS	2.18
CORRELATION BETWEEN THE TRACER DIFFUSION COEFFICIENT AND THE SOLUTION VISCOSITY	2.22
DETERMINATION OF THE SLOPE, Q	2.23
ALTERNATIVE METHOD TO CORRECT THE SAND EQUATION	2.25
NOTE ON THE SHAPE OF CHRONPOTENTIOGRAMS	2.26
System I. $TlNO_3 + NaClO_4 + H_2O$	2.28
System II. $TlNO_3 + KNO_3 + H_2O$	2.28
System III. $TlNO_3 + LiNO_3 + H_2O$	2.29
System IV. $TlNO_3 + NaNO_3 + H_2O$	2.30
System V. $TlNO_3 + KNO_3 + H_2O + NMF$	2.30
CONCLUSION	2.32
REFERENCES	2.36

## INTRODUCTION

Chronopotentiometry is the study of the variation of the potential of an electrode with time, during the passage of a constant electrolysis current. The technique has been extensively reviewed elsewhere.<sup>1-9</sup>

The earliest recorded use of the method was by Weber in 1879<sup>10</sup> and Sand in 1901.<sup>11</sup> The work of Gierst and Juliard<sup>12</sup> is acknowledged by many as being responsible for exposing the practical potentialities of chronopotentiometry. Delahay and Mamantov<sup>2</sup> optimistically envisaged chronopotentiometry as an analytical method that could replace conventional polarography. The predicted exaltation of chronopotentiometry as a versatile analytical technique never eventuated, however, because of inherent disadvantages.

One major setback to a wider application of the technique has been the failure to simply determine an unambiguous transition time for a given chronopotentiogram. Various graphical methods have been used to determine the transition time, but the methods themselves have little, or no, justification. Bos and Van Dalen<sup>13</sup> have compared the graphical methods used to determine the transition time by Delahay and Mamantov,<sup>2</sup> Reinmuth,<sup>14</sup> De Vries,<sup>15,16</sup> and Laity and McIntyre.<sup>17</sup> Such methods, whether justified or not, all suffer from cumbersomeness.

Fisher<sup>18</sup> and Currie<sup>19</sup> avoided the unnecessary graphical analysis by selecting the end-point of a chronopotentiogram to be the point of maximum change in potential in the region of electroactive ion depletion. The time taken for the potential of the electrode to change from its initial potential to the end-point potential was accurately

## 2.2

measured using a digital timer and comparator. This uncorrected time was regarded by Fisher and Currie as the transition time. The use of this method required the pre-determination of the end-point potential from a previous chronopotentiogram.

In this work, the author improved upon the reliability of the techniques of Fisher<sup>18</sup> and Currie<sup>19</sup> by determining the end-point potential and transition time simultaneously from each chronopotentiogram. The simultaneous determination was achieved using a transient recorder coupled to an on-line computer.

Classical cathodic chronopotentiometry requires that the principal means of mass transport in the region of the cathode is via diffusion. This means the elimination of mass transfer due to convection and migration.

Migration is the movement of charged species in the presence of an electric field, and can be effectively eliminated by swamping the solution with some chemically inert and electroinactive ionic species termed the supporting electrolyte. The inert ions of the supporting electrolyte, being in a large excess, act as the major charge carriers in the solution during electrolysis.<sup>20</sup> To minimize migration effects, the author maintained a value of 100 for the ratio of the concentrations of the supporting electrolyte and the electroactive species.

Convection is commonly caused by mechanical vibrations affecting the cell and movement of the solution due to density or temperature gradients. These effects were minimized in this study by: special

## 2.3

mounting of the cell to reduce vibration effects; orientation of electrodes such that diffusion occurred upwards, as suggested by Bard;<sup>21</sup> and maintaining the cell at a constant temperature using a water jacket through which water was pumped from a large volume, constant temperature, water bath. The results presented here were carried out at a constant temperature of  $25.00 \pm .05^\circ\text{C}$ .

Under conditions where mass transfer due to convection and migration has been eliminated, semi-infinite linear diffusion is approximated in the case of diffusion of a species to a planar electrode immersed in a large amount of solution. Under conditions of semi-infinite linear diffusion, diffusion of an electroactive species will be in accordance with Fick's law of diffusion<sup>22</sup>

$$\frac{\partial C}{\partial t} = D_0 \frac{\partial^2 C}{\partial X^2} \quad [1]$$

where  $D_0$  is the tracer diffusion coefficient of the reactant species, and  $C$  is the concentration of the reducible species as a function of time,  $t$ , and distance from the cathode,  $X$ .

Integration of equation [1] with the appropriate boundary conditions was shown by Paunovic<sup>1</sup> to yield the equation attributed to Sand

$$i\tau^{\frac{1}{2}} = nFC_0D_0^{\frac{1}{2}}\pi^{\frac{1}{2}}A/2 \quad [2]$$

where  $n$  is the number of electrons involved in the reduction, and  $A$  is the cathode surface area.

Sand<sup>11</sup> originally derived equation [2] showing how the transition time,  $\tau$ , was related to the electrolysis current,  $i$ , the bulk concentration,  $C_0$ , and the diffusion coefficient,  $D_0$ , of the electroactive



species. The Sand equation predicts that the product  $i\tau^{\frac{1}{2}}$  should be constant for a given bulk concentration of electroactive species, and be independent of both the electrolysis current and the transition time.

A number of researchers utilizing the Sand equation have used chronopotentiometry to determine a value of  $i\tau^{\frac{1}{2}}$  for particular systems. Due to poor experimental techniques, uncertainties of 1%, 2%, or even greater have been associated with the determined value of  $i\tau^{\frac{1}{2}}$ .<sup>24,25</sup> In the work presented here, it has been shown by the author that values of  $i\tau^{\frac{1}{2}}$  can be determined with an uncertainty of less than 0.1% for an individual solution.

A systematic deviation of  $i\tau^{\frac{1}{2}}$  from constancy was recognized by Bard<sup>21</sup> who attempted to correct for the inconstancy of the chronopotentiometric constant  $i\tau^{\frac{1}{2}}/C$ . Bard attempted to account for the inconstancy of the chronopotentiometric constant by taking into account the effect of double layer charging, electrode oxidation, and adsorption.<sup>21,23</sup> Bard modified the Sand equation by introducing a correction factor, B, so that the modified Sand equation became

$$i\tau^{\frac{1}{2}} = nFC_0D_0^{\frac{1}{2}}\pi^{\frac{1}{2}}A/2 + B\tau^{-\frac{1}{2}} \quad [3]$$

Bard claimed that his treatment was only approximate because it assumed that the charging of the double layer occurred constantly during the electrolysis, whereas this would not be the case in reality.<sup>21</sup>

In practice, however, the author found that equation [3] modelled what happened very accurately. For the reduction of thallium (I) in

## 2.5

an electrolyte solution at a platinum working electrode, the tracer diffusion coefficient,  $D_0$ , was calculated from the intercept of a plot of  $i\tau^{\frac{1}{2}}$  against  $\tau^{-\frac{1}{2}}$ . The slope of such a plot corresponds to an amount of charge,  $Q$ . So as not to confuse this slope with the B correction and interpretation of Bard, the modified Sand equation was used by the author with  $Q$  replacing the B of equation [3].

Tracer diffusion coefficients were determined for thallium (I) by the author at 25°C for aqueous solutions containing  $\text{NaClO}_4$ ,  $\text{KNO}_3$ ,  $\text{LiNO}_3$ , and  $\text{NaNO}_3$  as the supporting electrolyte, and for mixed  $\text{H}_2\text{O} + \text{NMF}$  solvents using  $\text{KNO}_3$  as the supporting electrolyte. The tracer diffusion coefficient for thallium (I) was found to decrease with increasing solvent NMF mole fraction, from  $1.88 \times 10^{-5} \text{ cm}^2/\text{s}$  in pure water to a minimum of  $0.506 \times 10^{-5} \text{ cm}^2/\text{s}$  in pure NMF.

The author used values of  $i\tau^{\frac{1}{2}}$  extrapolated to  $\tau^{-\frac{1}{2}} = 0$  to test the Sand equation. The predicted linear behaviour of  $i\tau^{\frac{1}{2}}/C$  with the geometric surface area was observed, implying that the effective electrode surface area was the same as its geometric surface area. This result was shown to be in agreement with the diffusion layer thickness being much greater than the profile of the electrode surface unevenness.

## EXPERIMENTAL

## ELECTRONIC EQUIPMENT

The electronic equipment used in these chronopotentiometric studies is schematically illustrated in Figure 1. The use of each component element is summarised below.

## 1. Galvanostat

A constant electrolysis current was provided by a galvanostat (see Appendix 1). The current was manually set in the range 1-5,000  $\mu\text{A}$ . The galvanostat has an in-built automatic current stop and reversing sequence that can be activated either manually or when a preset potential was reached during electrolysis.

## 2. Voltmeter and Known Resistance

The electrolysis current was determined using the Ohm's Law relationship by using a voltmeter to measure the potential drop across an accurately known resistance. A resistor of  $1,000.0\Omega \pm 0.05\%$  was used.

## 3. Variable Dummy Resistance

The electrolysis current was passed through a dummy cell resistance when electrolysis of the solution was not required. The dummy cell resistance was adjusted to a value comparable to the solution resistance between the counter and working electrodes so as to ensure the avoidance of a rapid current change upon switching the current from the dummy cell to the electrolysis cell. The switching of the current from the dummy cell to the electrolysis cell was effected by a single button press.

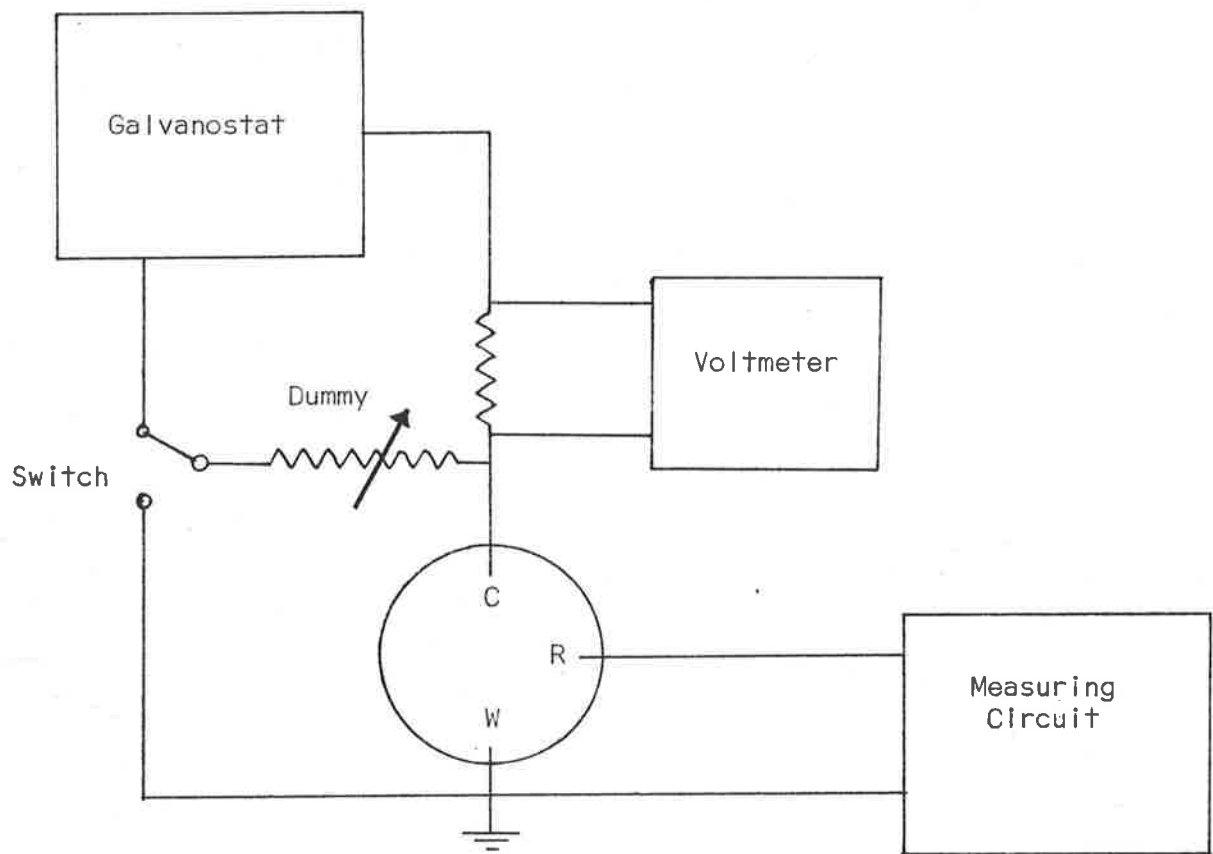


Figure 1. Instrumentation used for chronopotentiometry using 3 electrode system: working (W); counter (C); reference (R).

#### 4. Digital Voltmeter

The potential difference between the reference and working electrodes was monitored using a high input impedance Solartron A210 digital voltmeter.

#### 5. Cathode Ray Oscilloscope (C.R.O.)

The chronopotentiograms were observed using a Tektronix 434 storage cathode ray oscilloscope.

#### 6. Timer and Comparator

A digital timer coupled to a comparator was used to accurately measure the duration of electrolysis. The comparator initiated the timer when the current was first switched to the electrolysis cell, and then stopped the timer at the point of current reversal.

#### 7. Transient Recorder and Computer

The potential-time response of the electrolysis cell to the applied constant current was stored in a Data Lab DL905 Transient Recorder interfaced to a Hewlett Packard H.P.85 computer. The stored data was manipulated via the H.P.85 computer using an adapted Hewlett Packard spline function programme.

### ELECTROLYSIS CELLS

The electrolysis cell, depicted in Figure 2, has two main sections.

The lower part, made of Pyrex glass, consists of a simple outer jacket that is joined by silicone rubber to the flat broad rim of an

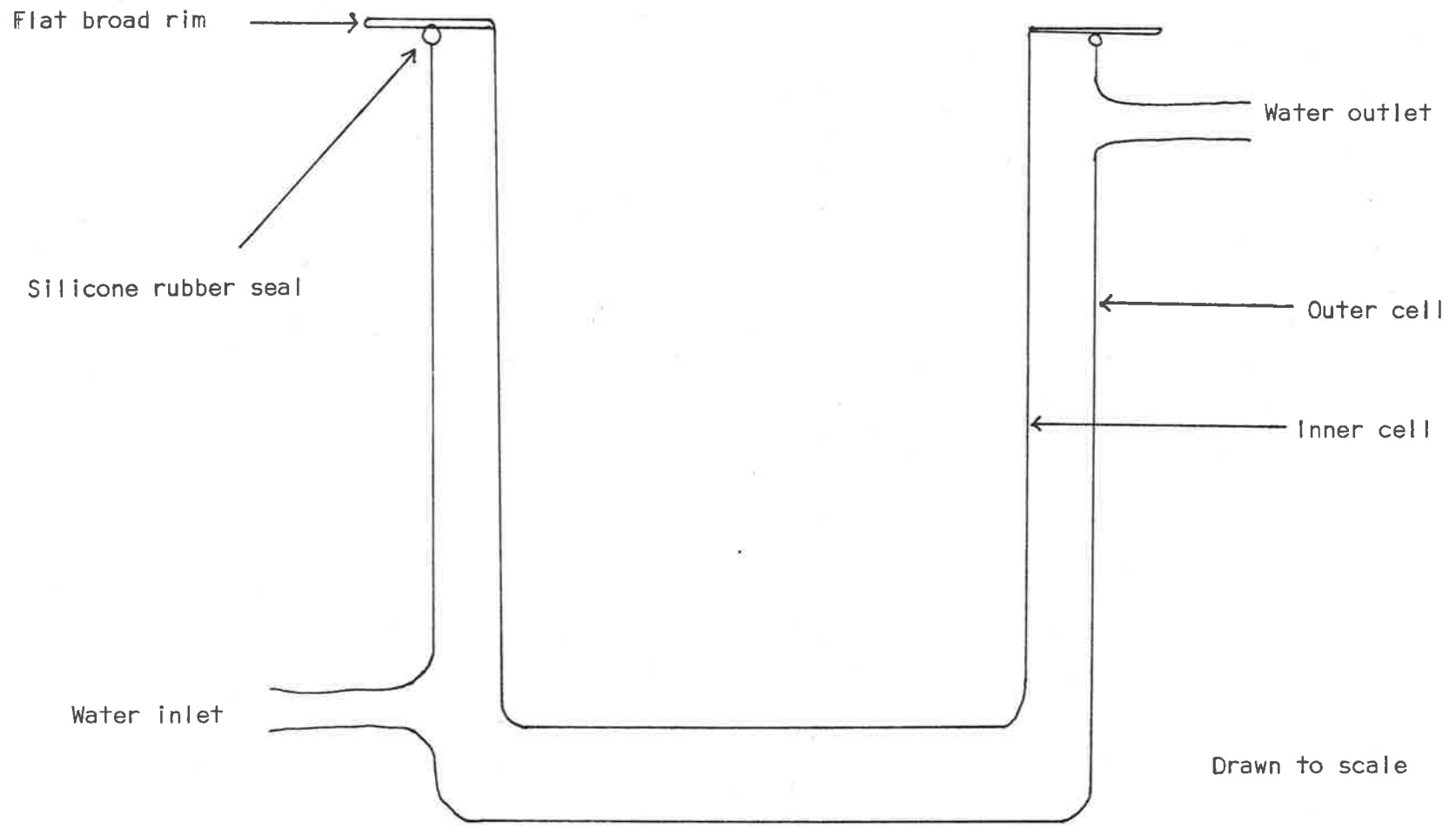


Figure 2. Cut-away view of electrolysis cell (lower part only).

## 2.8

inner cell. The outer jacket with inlet and outlet portals served as the water jacket that maintained the cell at a constant temperature as set by a water bath. The water bath was maintained at  $25.00 \pm .05^\circ\text{C}$ . Both inner and outer jackets had flat optic glass discs set into their bases so that the electrodes within the cell could be clearly visible using a mirror/light system positioned below the cell, as depicted in Figure 3.

The upper section was a top that served as the lid to the lower section. The top had a broad rim that was fitted on to the rim of the lower section, and was held in place using either clamps or three springs that were screwed into the side of the top and fixed on to the clamp holding the electrolysis cell. The middle portion of the top contained a number of tapered sockets machined to take standard Quickfit male cones. The sockets were of the appropriate number and size to accommodate the working, reference and counter electrodes, gas bubbler, gas outlet, and a J-shaped tube for flushing.

Another electrolysis cell that was also used is depicted in Figure 4. This cell allowed the optional use of a side arm inserted luggin capillary. It also consisted of an upper and lower section.

The upper section was a machined Teflon top that fitted on to the lower section, and was held in place using three springs. The middle portion of the top contained a suitable number and type of sockets machined to accept standard Quickfit cones. These sockets held the working, counter and auxillary electrodes, gas bubbler, gas outlet, and a J-shaped tube for flushing.

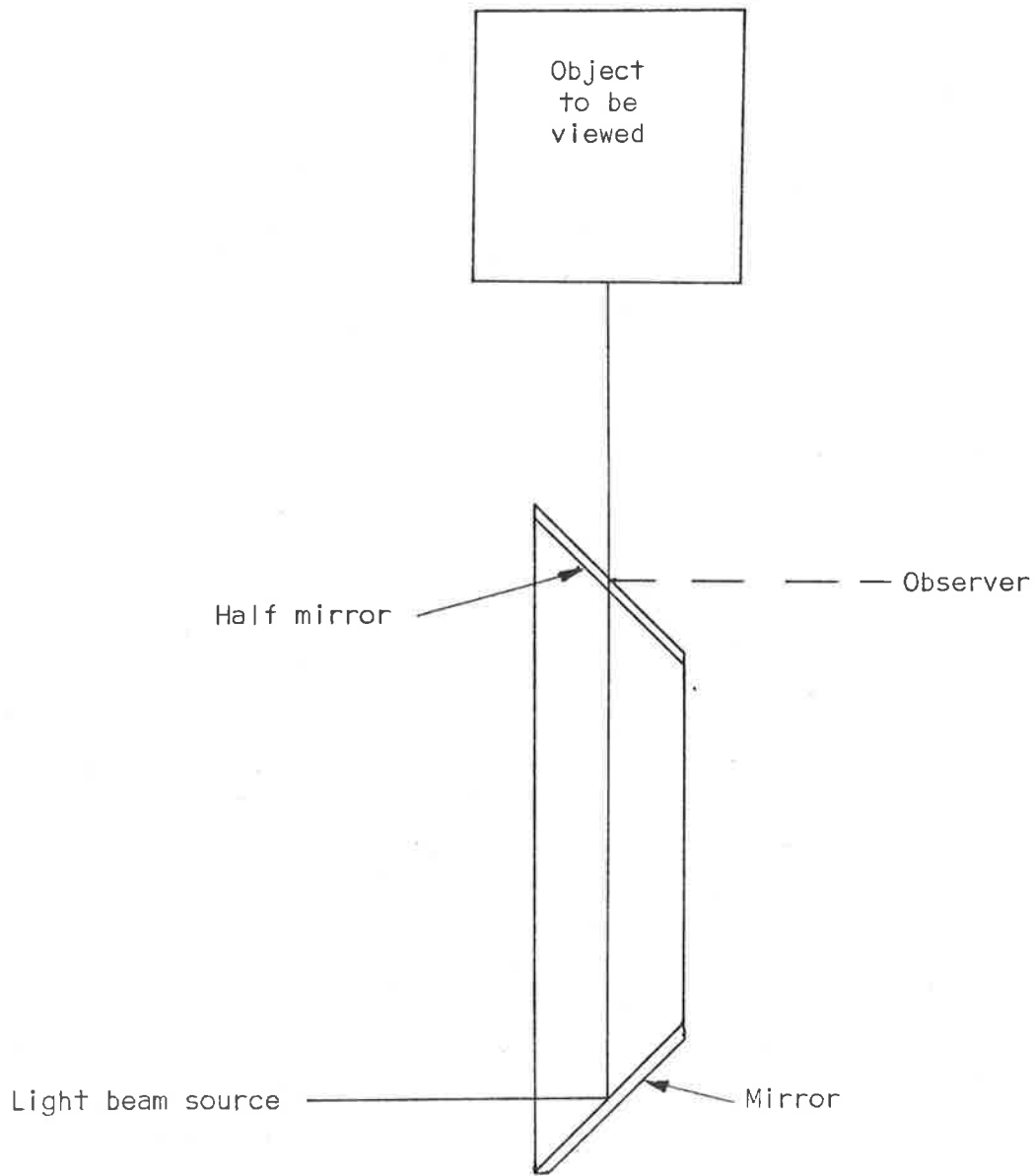


Figure 3. Mirror/light source arrangement for observation of underside of an object.



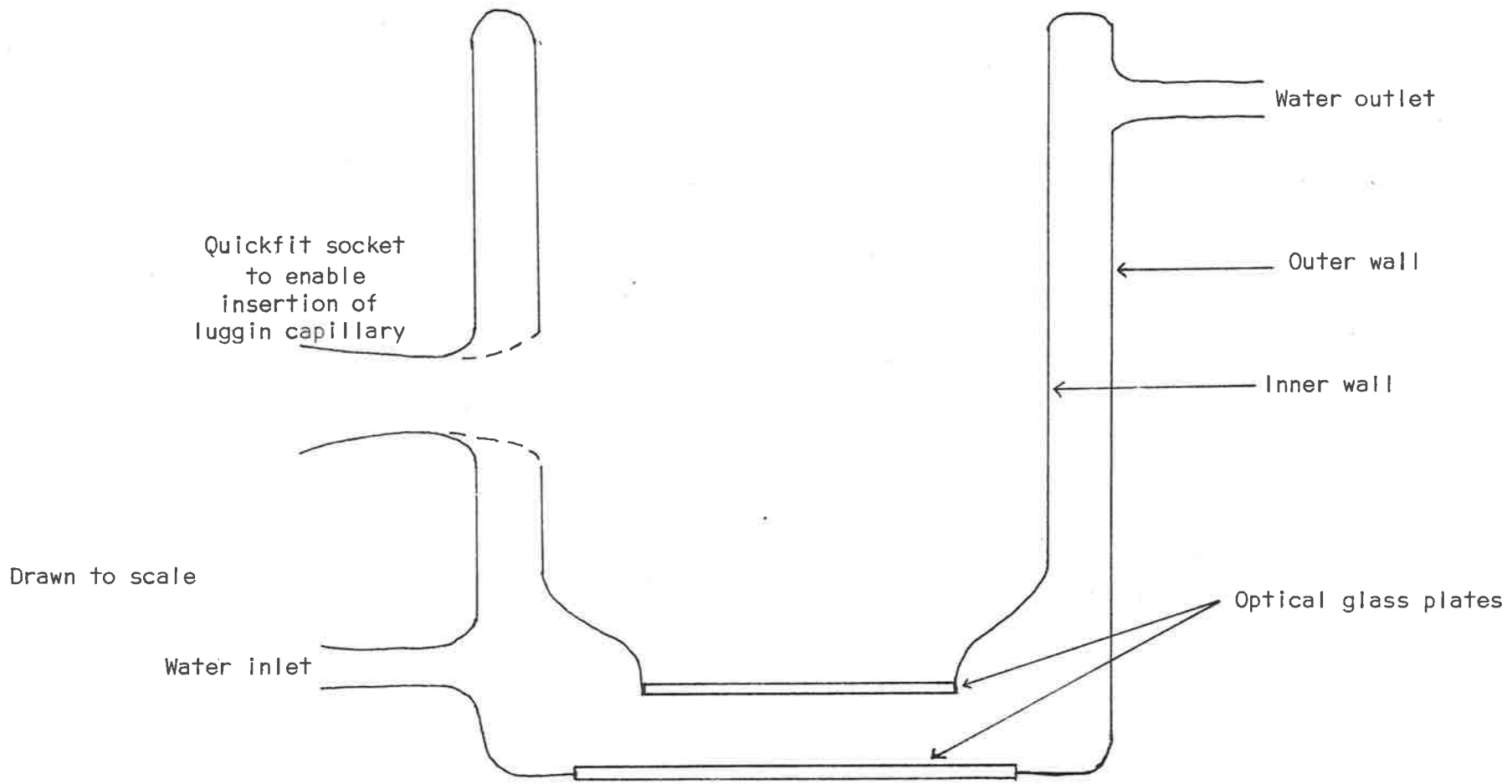


Figure 4. Cut-away view of electrolysis cell (lower part only).

The lower section was an all Pyrex glass, double-walled cell. The space between the inner and outer walls served as the water jacket, while the region within the inner wall served to hold the electrolyte solution. Provision was made for the use of a side projecting luggin capillary through the side Quickfit cone.

The fine tipped luggin capillary is depicted in Figure 5. The upper side arm enabled the luggin capillary to be flushed with gas. When the luggin capillary was stoppered, the gas pressure forced the solution out of the capillary into the bulk of the solution, and allowed the gas to be bubbled through the solution. When the electrolyte solution was de-oxygenated, the de-oxygenating gas was then passed continuously over the solution surface via the gas bubbler depicted in Figure 6. The electrolyte solution would then seep into the luggin capillary, and enable electrical contact to be made through the solution with the reference electrode held in the vertical section of the luggin capillary.

#### VIBRATION PROOFING

It was necessary to insulate the electrolysis cell from vibration sources likely to cause undesirable mass transfer effects. This was achieved by supporting the electrolysis cell on a brass ring, and also by clamping the cell firmly around its girth. Both the ring and girth clamp were clamped on to a solid rod fixed into a metal cage that enclosed the cell, and was firmly bolted on to a 5 cm thick slate slab. The whole assembly rested on rubber bushes on a sturdy metal table. The metal cage also doubled as a Faraday cage, cutting down on signal noise due to electronic pick-up.

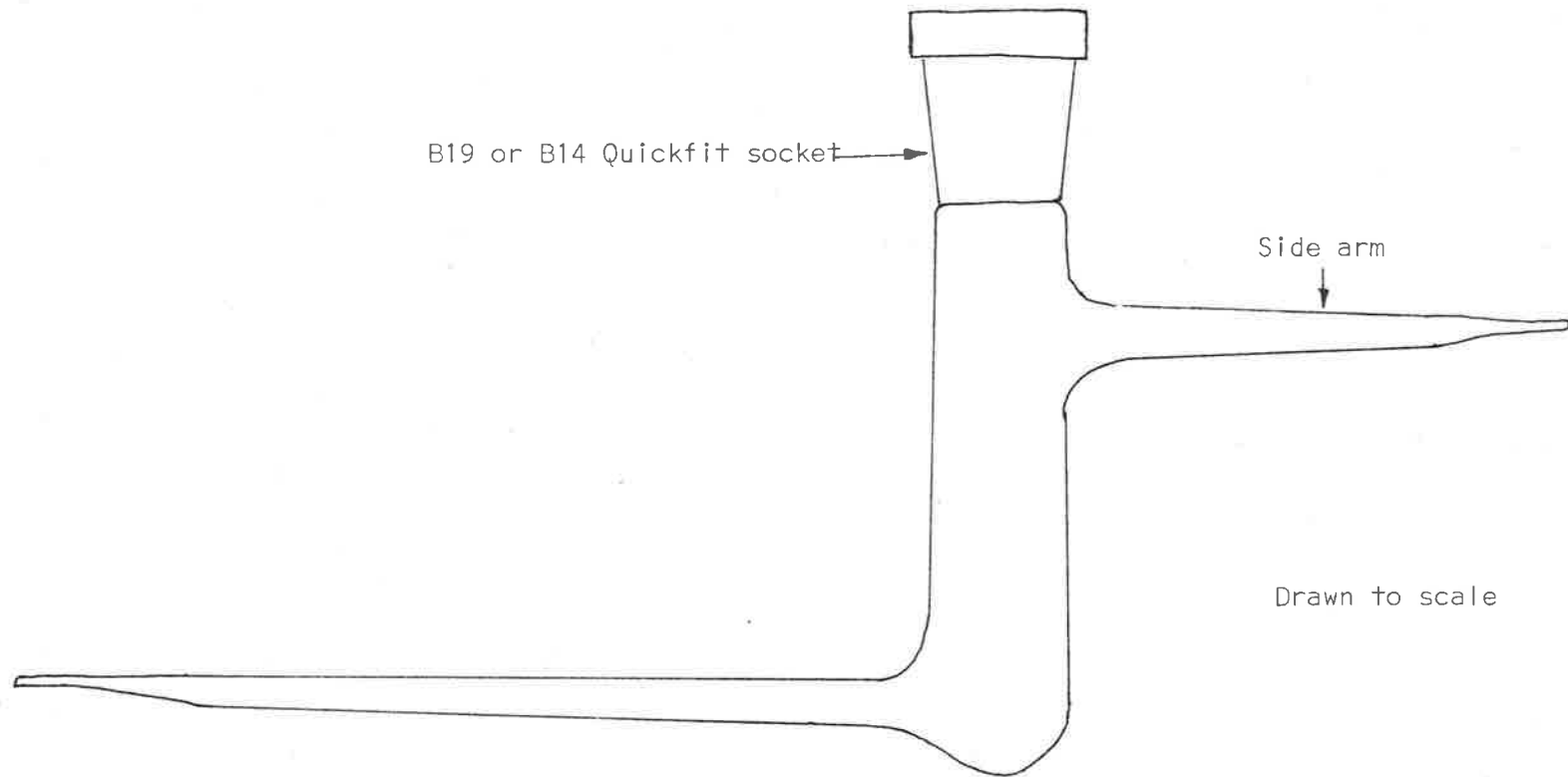


Figure 5. Luggin capillary.

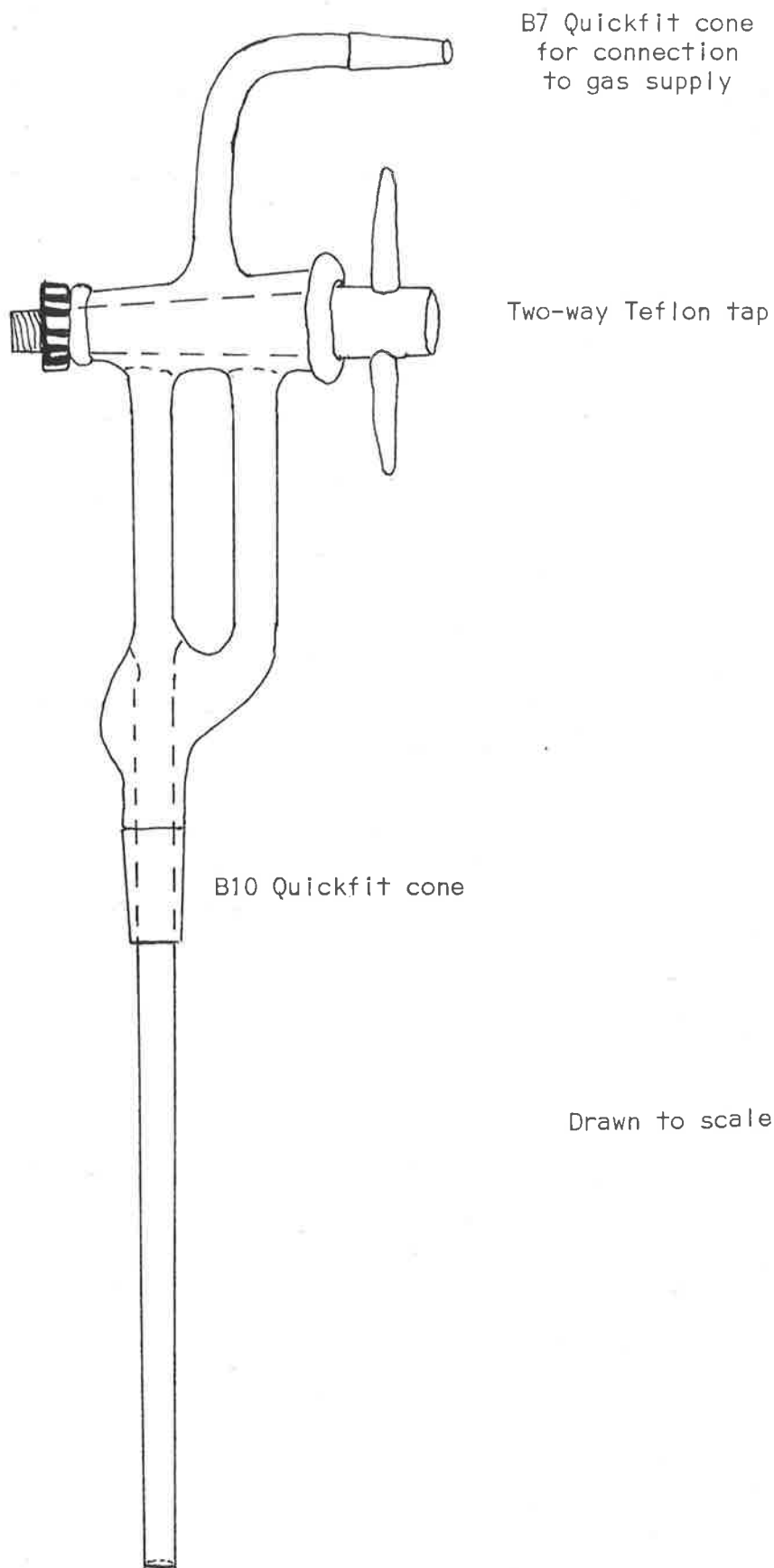


Figure 6. Gas bubbler.

## 2.10

The pump used to circulate water from the water bath through the cell water jacket was found to be a source of vibration that could cause a lengthening of the electrolysis time by more than 10%. This effect was avoided by the development of a technique that allowed for the non-circulation of water through the water jacket when the electrolysis current was applied to the electrolysis cell. Such a technique is described later.

### ELECTRODES

A standard three electrode system was used for chronopotentiometric measurements. The electrodes were fitted into their appropriate positions in the electrolysis cell such that the reference electrode was between the working and counter electrodes.

The counter electrode consisted of a large horizontal platinum disc joined to a connecting platinum wire sealed into a soda glass sheath. The platinum disc could be placed directly below the working electrode, or otherwise by rotating it from the top. The position of the disc, whether directly below the working electrode or otherwise, made no difference to the chronopotentiogram.

The <sup>pseudo</sup>reference electrode was a platinum wire sealed into a J-shaped glass sheath of such dimensions as to bring its tip near to the working electrode. The closeness of the reference electrode was not critical but, for consistency, once positioned, was left in that position for all measurements in the same solution.

## 2.11

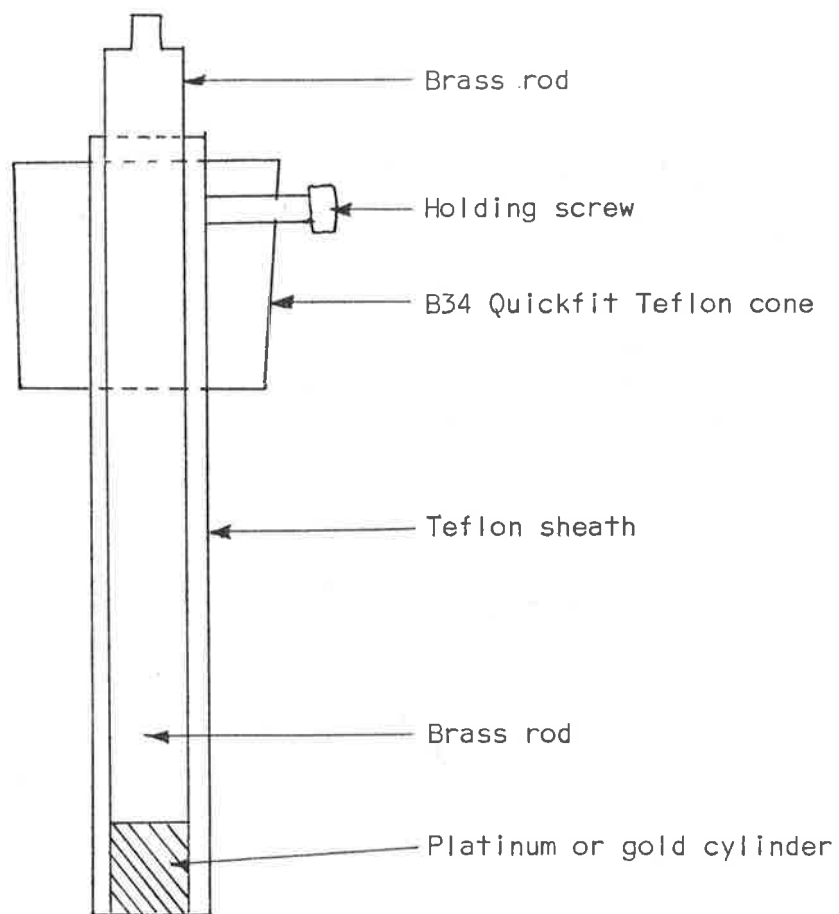
A simple unshielded planar working electrode is depicted in Figure 7. A high purity platinum cylinder or gold foil was soldered on to a brass contact rod, and masked with a teflon sheath so as to present a horizontal planar platinum or gold surface to the solution, respectively.

Another unshielded working electrode, depicted in Figure 8, was simply a vertically orientated platinum disc attached to a platinum wire which was enclosed in a soda glass sheath.

The development of a suitable shielded working electrode required much trial and effort. Preference was given to the development of an electrode that would allow ease of polishing of the metal surface, and lend itself to a simple procedure allowing flushing of the solution within the electrode shielding. A major problem that plagued early attempts was the attainment of a leak-proof seal between the metal electrode surface and the plastic material of the electrode shielding.

The working electrode that was finally developed, depicted in Figure 9, was an adapted version of the Cottrell Cell used by Ikeuchi et al.<sup>27</sup> The working electrode surface was plate material tin soldered on to brass stubs of such dimensions as to facilitate easy use in electron microscopy studies. The stubs also made mechanical polishing of the metal plate a simpler procedure.

Leak-proof sealing of the electrode stub/electrode casing contact was achieved by compressing the electrode stub on to a machined cell piece supported in a Kel-F holder. A suitable, reproducible pressure



Drawn to scale

Figure 7. Cut-away view of Teflon-encased working electrode.

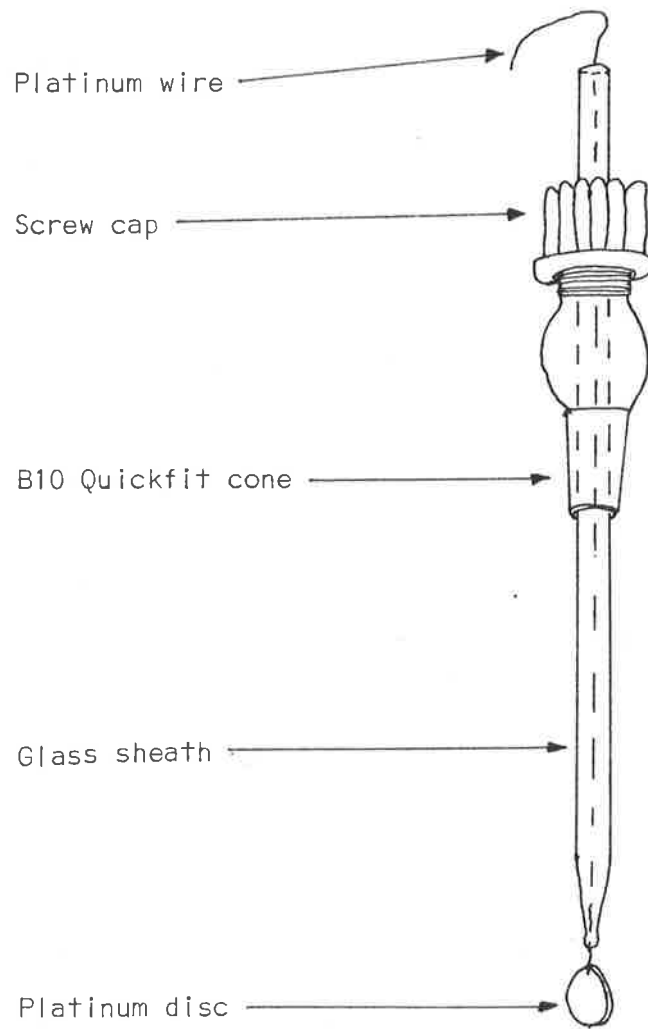
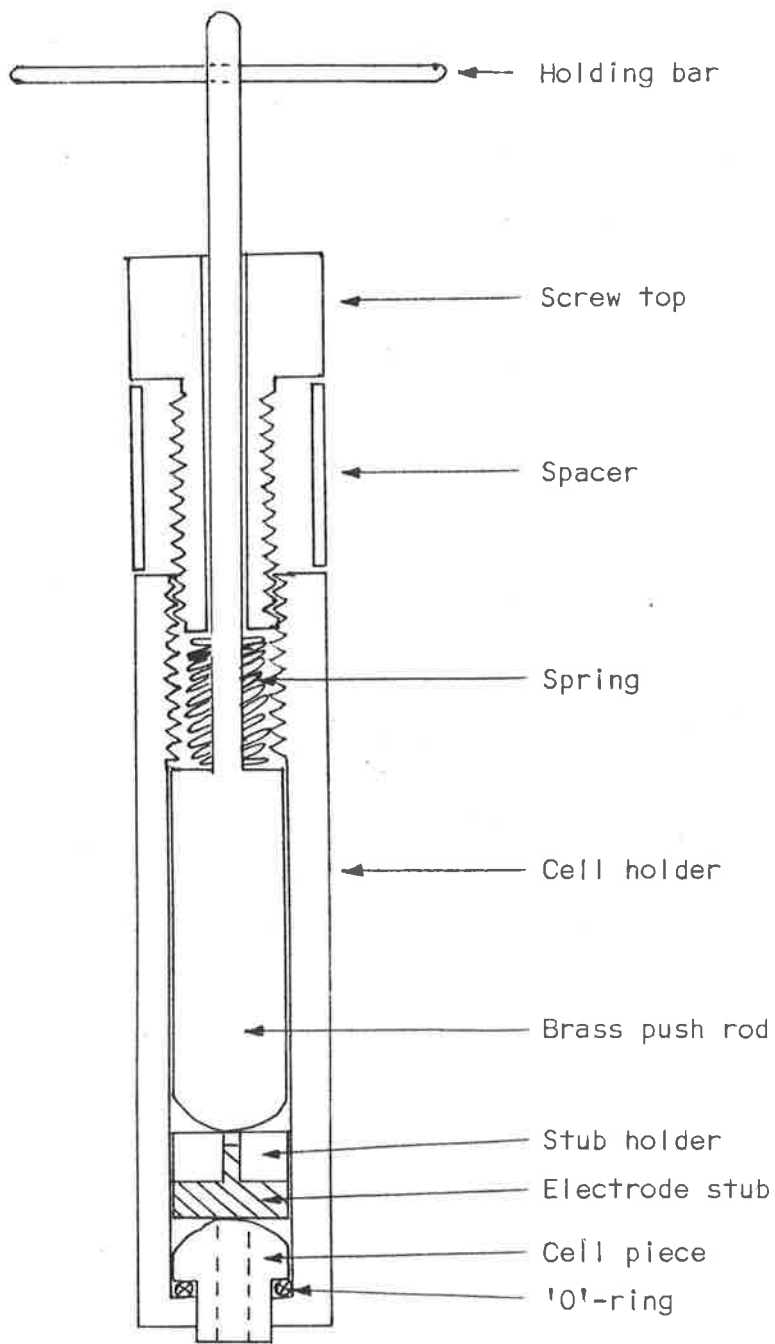


Figure 8. Platinum disc electrode





Drawn to scale

Figure 9. Cut-away view of Cottrell Cell electrode.

was achieved using a spacer that limited the maximum compressional pressure. A mushroom shaped cell piece with a knife-edge contact was found to give a much better seal than a flat broad contacting cell piece. Corning Machinable Glass was found to be too hard as cell piece material, Teflon was known to be too soft,<sup>27</sup> but Kel-F and perspex proved to be most suitable, enabling a good seal with soft metals such as gold and platinum. Kel-F was favoured as the cell piece material because of its superior resistance to attack by acid and organic solvents.

The diffusion cavity of the cell piece was simply flushed using a J-shaped Pyrex glass tube with a suitable nozzle that allowed access into the cavity up to the electrode surface. The diffusion cavity was a good trap for gas bubbles which, unless removed using the J-shaped tube, caused anomolous chronopotentiograms.

A light source and mirrors were set up, as depicted in Figure 3, so that the observer could detect the presence of even minute gas bubbles within, or near to, the diffusion cavity. The technique was very sensitive to the presence of gas bubbles because of the high reflectance of the mirror-finished polished electrode stubs. The light beam was cut off, and used only as deemed necessary, since the beam intensity could effect undesirable localised hot spots, and the chronopotentiogram itself revealed any gas bubble problems to the experienced observer.

All working electrode surfaces, excepting the vertically oriented disc electrode, were polished to a mirror finish using conventional

## 2.13

mechanical lap polishing techniques, using diamond or alumina paste. The electrode surfaces were then cleaned and etched for 30 seconds in aqua regia, prior to further cleaning preparation.

The apparent surface area of the shielded working electrode was taken to be that exposed by the cell piece, and hence determinable from the inner diameter of the cell piece. The inner diameter of the cell piece was measured at the contacting edge using Mitutoyo Small Hole Gages and a Mitutoyo Micrometer, readable to 0.01 mm.

### CLEANING PROCEDURE

All glassware and Teflon or Kel-F components were rinsed in de-ionised water, and then soaked in acid cleaning solution. The material was then rinsed, and soaked in pure water. The lower section of the electrolysis cell depicted in Figure 2 was finally inverted over clean filter paper, and allowed to drain dry. All other glassware was oven dried. The Teflon and Kel-F components were allowed to air dry on clean Whatman No.5 filter paper.

Initially pure dichromic acid was used as the cleaning solution. After this had been used for many months it was subsequently replaced with pure sulphuric acid, and then pure nitric acid. Dichromic acid was replaced as the cleaning medium because of the possibility of dichromate contamination of the material soaked in it, though this was never tested and proved by the author.

The counter and reference electrodes, previously described, were

soaked in acid cleaning solution, rinsed, and then allowed to soak in pure water until required.

The final stage of preparing the working electrode was to soak it for 2 minutes in acid cleaning solution, thoroughly rinse it in pure water, and then allow it to stand in pure water until required. From the acid cleaning stage to its positioning in the electrolysis cell, the working electrode metal surface was kept covered by solution so that no direct contact was made by it with the atmosphere.

#### CHEMICALS

Thalious Nitrate ( $\text{TlNO}_3$ ):

Ultrapure Analytical reagent was used without further purification.

Lithium Nitrate ( $\text{LiNO}_3$ ):

B.D.H. Laboratory reagent was used. Water was removed by vacuum oven drying.

Potassium Nitrate ( $\text{KNO}_3$ ):

B.D.H. Analytical reagent was used.

Sodium Nitrate ( $\text{NaNO}_3$ ):

B.D.H. Analytical reagent was used.

Sodium Perchlorate ( $\text{NaClO}_4$ ):

B.D.H. Analytical reagent was used.

**Water (H<sub>2</sub>O):**

Initially doubly-distilled charcoal filtered deionised water was used. The final distillation was from alkaline permanganate solution.

The charcoal filtering stage was then replaced by an in-line 0.22  $\mu\text{m}$  Millistak-GS filter.

The final series of experiments used Milli-Q water of  $>18\text{ M}\Omega/\text{cm}^2$  resistance with a final stage 0.22  $\mu\text{m}$  Millipore filter.

**N-methylformamide (NMF):**

NMF was prepared in a manner similar to that described previously.<sup>28,29</sup>

Fluka Purum n-methylformamide was dried over 4 Å molecular sieves and purified by a two-fold distillation under reduced pressure.

**SOLUTION PREPARATION**

All solutions were quantitatively prepared from the solid salts. The salts were dissolved in the solvent of interest, and made up volumetrically to the desired concentrations.

The solution to be investigated was initially flushed in the electrolysis cell with a de-oxygenating gas for about one hour. Either high purity hydrogen or argon was used, and was passed en route through a vanadyl oxygen scrubbing system.<sup>30</sup> The gas was passed into the electrolysis cell via the gas bubbler, depicted in Figure 6, which had a two-way tap enabling the gas to be continuously passed either through the solution or over its surface, as desired.

The J-shaped tube, depicted in Figure 10, was used to ensure proper mixing of the solution. It was also used to remove troublesome gas bubbles that were likely to affect the chronopotentiogram.

#### TECHNIQUE FOR OBTAINING A CHRONOPOTENTIОGRAM

Chronopotentiograms were found to be affected by the natural potential of the working electrode, and by the vibrations from water circulated through the electrolysis cell water jacket. Techniques in obtaining chronopotentiograms were devised to yield consistently similar initial electrode potentials, and to reduce the vibration effect of the circulating water.

For the unshielded working electrodes, a simple technique was devised. The water was allowed to circulate through the water jacket for two minutes, and then stopped from circulating for a further two minutes, and then for the duration of the electrolysis, which was begun after the four minute period. The cycle was then repeated.

For the shielded electrode, depicted in Figure 9, a more elaborate technique had to be devised that made provision for solution flushing and gas bubble removal from the diffusion cavity. The initial technique was that used for the unshielded electrode with an added period of one minute between the two two minute periods. During the one minute period the diffusion cavity was flushed, and any gas bubbles were removed using the J-shaped tube, while the water was circulated through the water jacket. This initial technique was then modified by adding another two minute period directly after the one minute flushing period,

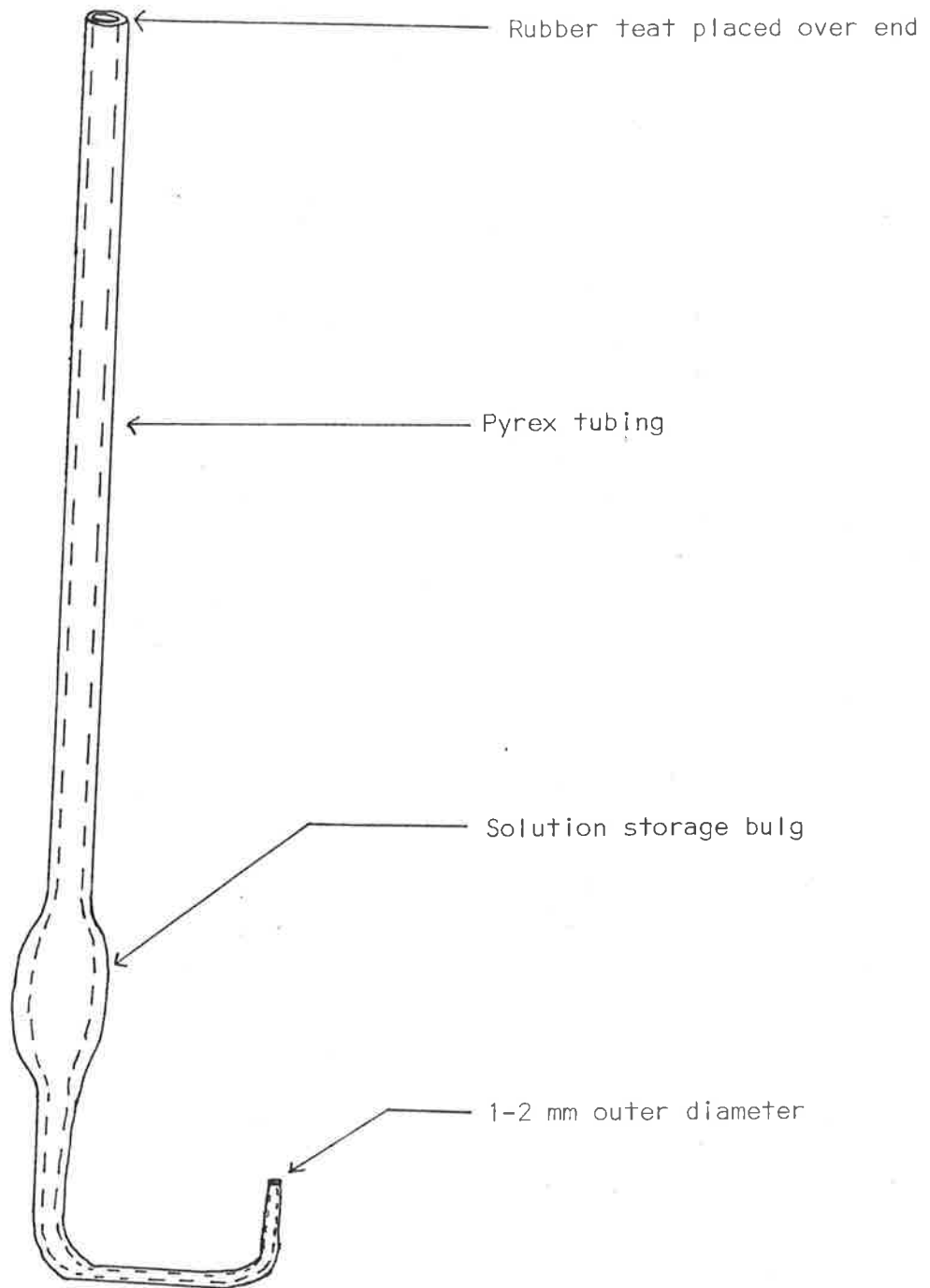


Figure 10. J-shaped tube.

during which the water was still circulated through the electrolysis cell water jacket. This latter addition was found necessary to reduce solution vibration after the vigorous flushing period. The final technique modification was to bubble the de-oxygenating gas through the solution for the initial two minute period on each occasion that the current was altered. This had the effect of ensuring that the electrolysis solution was still gas saturated at the completion of the experiments, which required a number of hours.

When the electrolysis current was passed through the electrolysis cell, the working electrode potential became increasingly cathodic, until the current direction was reversed. The electrode potential was then driven increasingly more anodic, until an end potential was reached, at which point the electrolysis current was switched from the electrolysis cell to the dummy cell. At this point, the electrode potential freely drifted, initially rapidly, and then more slowly. The electrode potential drifted until a maximum anodic potential was reached, and then drifted slowly in a cathodic direction. The technique discussed above for obtaining a single chronopotentiogram took a period of minutes. It was observed that, during the time prior to electrolysis, the electrode potential freely drifted to a maximum anodic potential, and then slowly drifted in a cathodic direction. The end potential, at which the electrolysis current was switched across the dummy cell, was selected so that the electrode potential was not driven more anodic than its free drift anodic potential maximum.



## RESULTS AND DISCUSSION

## PRELIMINARY RESULTS

Figure 11a shows the comparison of a typical experimentally obtained chronopotentiogram for an aqueous system with that calculated from the equation below expecting Nernstian behaviour<sup>1</sup>

$$E = E^{o'} + \frac{RT}{nF} \ln \left( \frac{2i}{nF(\pi D_0)^{\frac{1}{2}}} \right) + \frac{RT}{nF} \ln \left( \tau^{\frac{1}{2}} - t^{\frac{1}{2}} \right)$$

The potential of the experimental curve was normalised at  $\tau/4$  for convenience. It is evident that, for aqueous systems, good agreement is only found in the low potential change portion of the chronopotentiogram. Deviation from theory is evident at the initial and final portions of the chronopotentiograms where the potential undergoes rapid change.

In the pure NMF system, the deviation between practice and theory is much greater, as Figure 11b reveals.

From the above equation, it is evident that the basic shape of the chronopotentiogram should be determined only by the term  $\frac{RT}{nF} \ln \left( \tau^{\frac{1}{2}} - t^{\frac{1}{2}} \right)$ , since all the other terms on the lefthand side will be constant for a given chronopotentiogram. If all chronopotentiograms are normalised to a single value of  $\tau$ , and the potential scale fixed at a single value, at, say,  $\tau/4$ , then, for a given system, all chronopotentiograms should be identical, being independent of both the electrolysis current and the length of time of the electrolysis. In practice, this behaviour does occur.

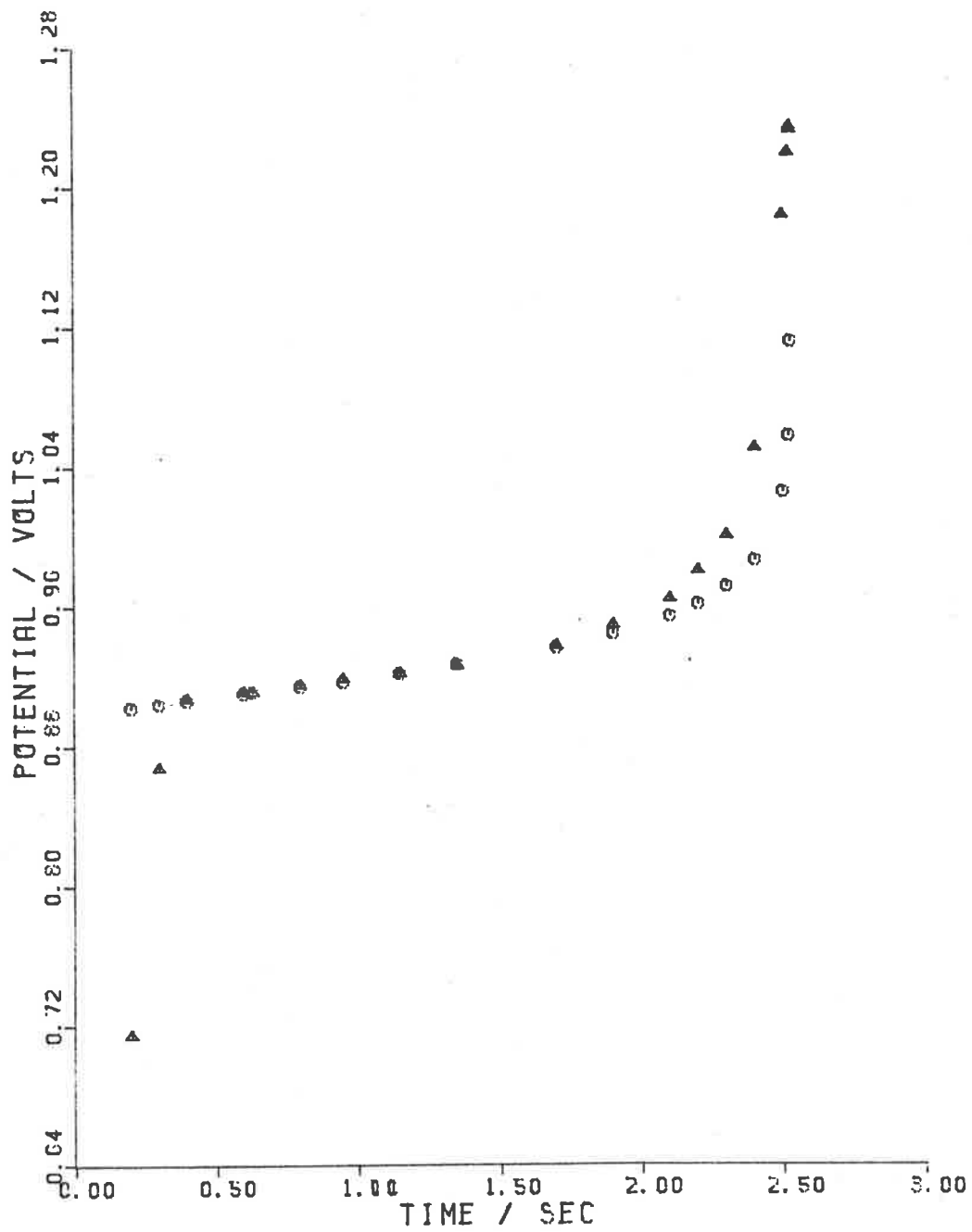


Figure 11a. Comparison of theoretical (O) and experimental (Δ) chronopotentiograms obtained for the  $TiNO_3 + KNO_3 + H_2O$  system.

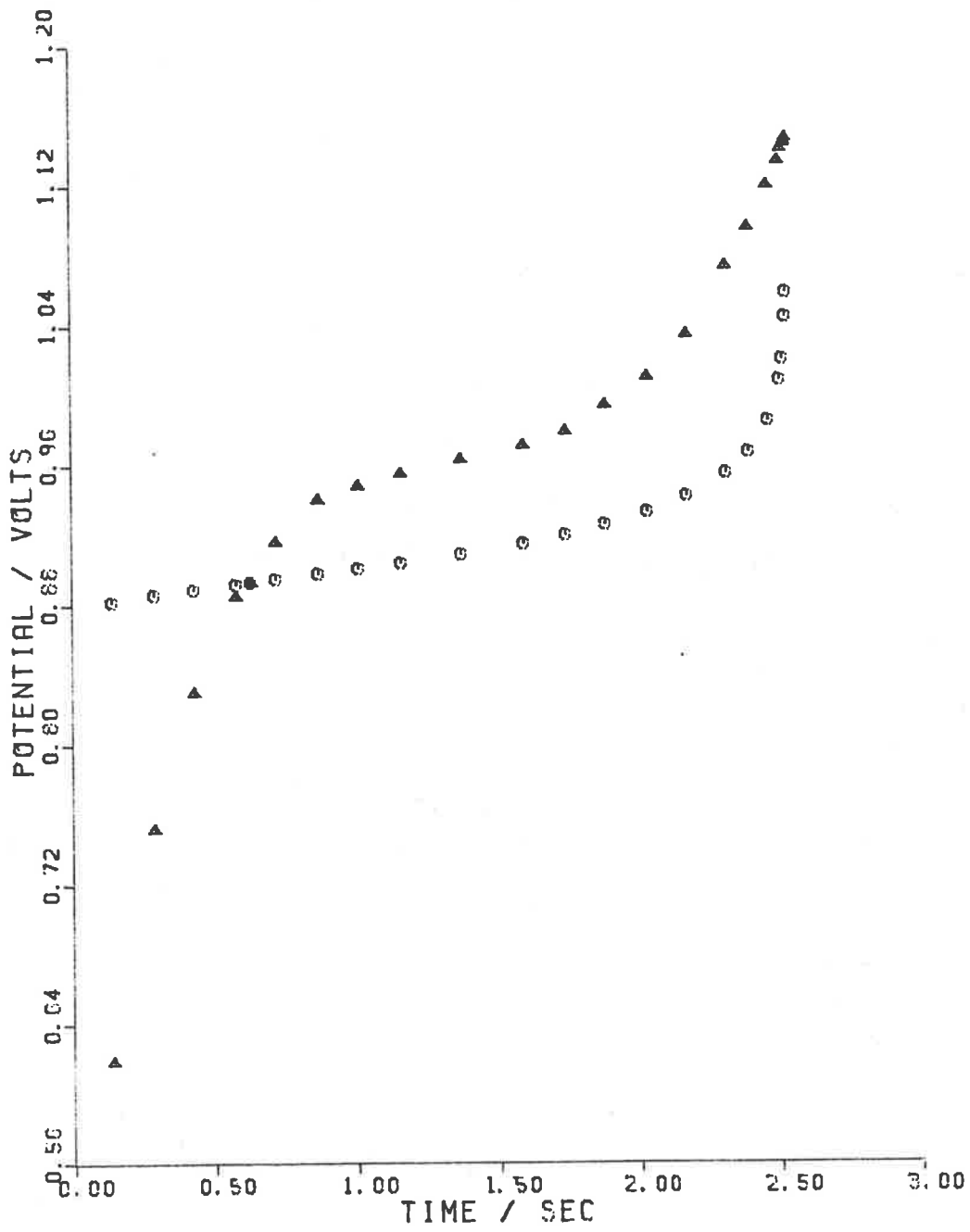


Figure 11b. Comparison of theoretical (O) and experimental (Δ) chronopotentiograms obtained for the  $TiNO_3 + KNO_3 + NMF$  system.

Figure 12 shows that the shape of experimentally obtained chronopotentiograms is not an artefact of the particular type of reference electrode used. In the example, the quasi-reference platinum wire probe was compared with a saturated calomel electrode (S.C.E.) in a luggin capillary, and the chronopotentiograms were superimposable. The use of the quasi-reference platinum wire or the S.C.E. in a luggin capillary was equally valid, but the former was preferred, on the basis of experimental convenience. The use of quasi-reference electrodes is discussed elsewhere.<sup>26</sup>

For the case of platinum working electrodes, the metal is known to adsorb hydrogen and oxygen, depending upon the electrode potential. Such reactions occurring on the electrode surface may be a cause of at least some of the observed deviation of the chronopotentiograms from theoretical behaviour. If the electrode potential is sufficiently anodic for oxide to form on the platinum surface, then the chronopotentiogram will show anomalous behaviour due to reduction of the oxide prior to the reduction of thallium (I). The technique for obtaining a chronopotentiogram was developed, as described previously, so that the natural electrode potential was not sufficiently anodic to allow oxide formation to occur.

From the modified Sand equation

$$i\tau^{\frac{1}{2}} = nFC_0D_0^{\frac{1}{2}}\pi^{\frac{1}{2}}A/2 + Q\tau^{-\frac{1}{2}}$$

it can be seen that a plot of  $i\tau^{\frac{1}{2}}$  against  $\tau^{-\frac{1}{2}}$  for a series of currents  $i$ , should yield a straight line with an intercept from which the tracer diffusion coefficient,  $D_0$ , can be calculated.

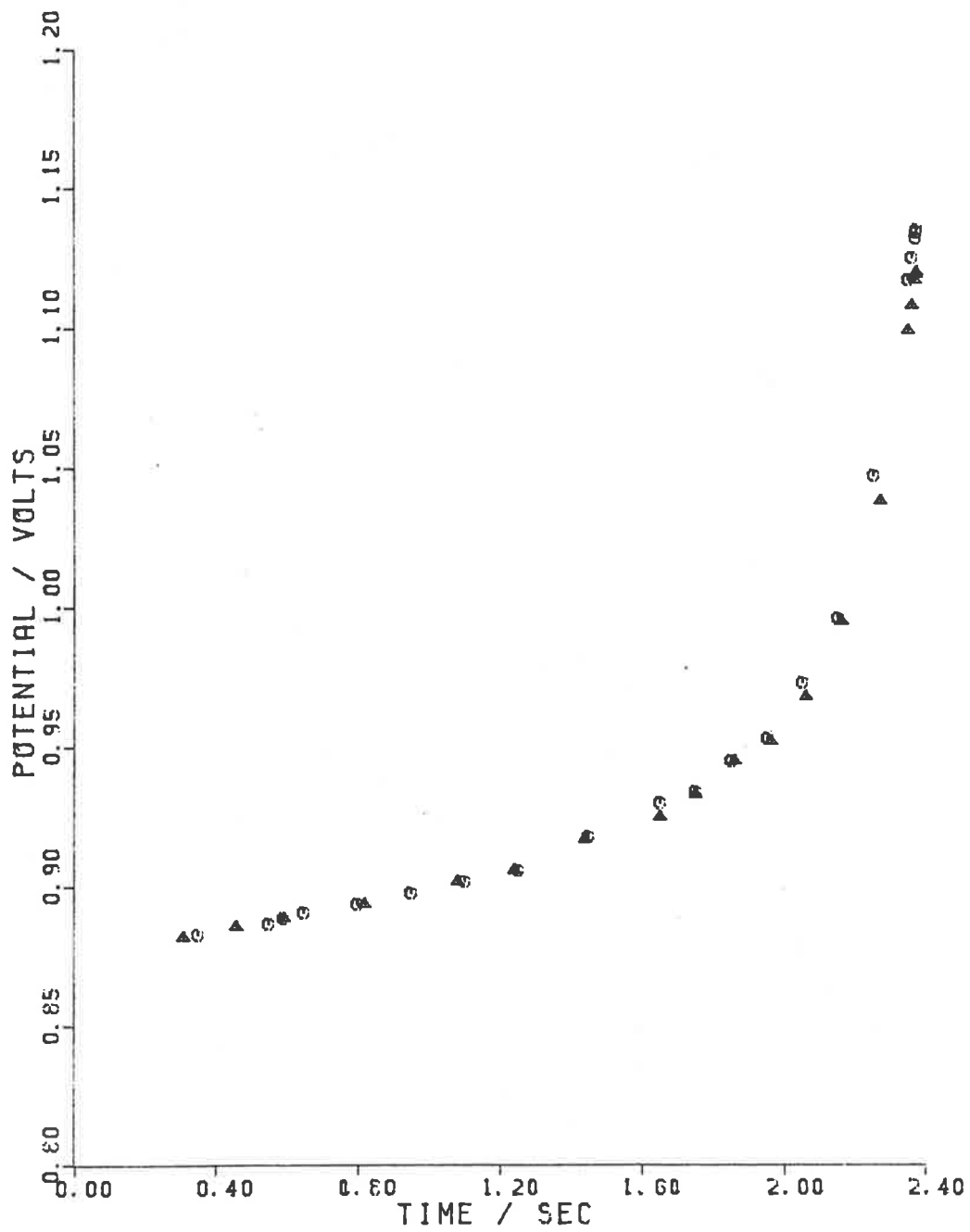


Figure 12. Comparison of chronopotentiograms obtained using different reference electrodes: saturated calomel reference in luggin capillary (O); platinum wire probe ( $\Delta$ ).

Linear behaviour of  $i\tau^{\frac{1}{2}}$  versus  $\tau^{-\frac{1}{2}}$  was found for all electrodes for small values of  $\tau$  or, correspondingly, large values of  $\tau^{-\frac{1}{2}}$ . However, as  $\tau^{-\frac{1}{2}} \rightarrow 0$ , deviation from linearity becomes evident. This deviation is due to convection causing the experimentally determined value of the transition time,  $\tau$ , and hence  $i\tau^{\frac{1}{2}}$ , to be greater than expected. The effect of convection can be removed using a shielded electrode where linearity of  $i\tau^{\frac{1}{2}}$  versus  $\tau^{-\frac{1}{2}}$  could be obtained for transition times greater than 90 seconds.

It was evident to the author that linear behaviour of  $i\tau^{\frac{1}{2}}$  versus  $\tau^{-\frac{1}{2}}$  was achievable to a high degree of accuracy for large values of  $\tau$ , so long as the working electrode was shielded. As such, the shielded working electrode depicted in Figure 9 was used for all subsequent experiments.

One of the difficulties encountered with the shielded electrode was in achieving a leak-proof seal between the metal surface of the electrode and the cell piece. With experience, efficiency was achieved in obtaining a good seal, and several criteria could be used to test it.

The criteria used to test the effectiveness of the seal were: the ratio of the times of the reduction and oxidation currents; the linearity of  $i\tau^{\frac{1}{2}}$  versus  $\tau^{-\frac{1}{2}}$ ; and the visual check for leakage upon dismantling the working electrode. A clear example of the results produced by a poor sealing shielded electrode is evident in Figure 13. The plotting of  $i\tau^{\frac{1}{2}}$  against  $\tau^{-\frac{1}{2}}$  yields a curve, and not a straight line. Visually, it was evident for the same system that leakage through the seal had occurred. For this system, the ratio of the

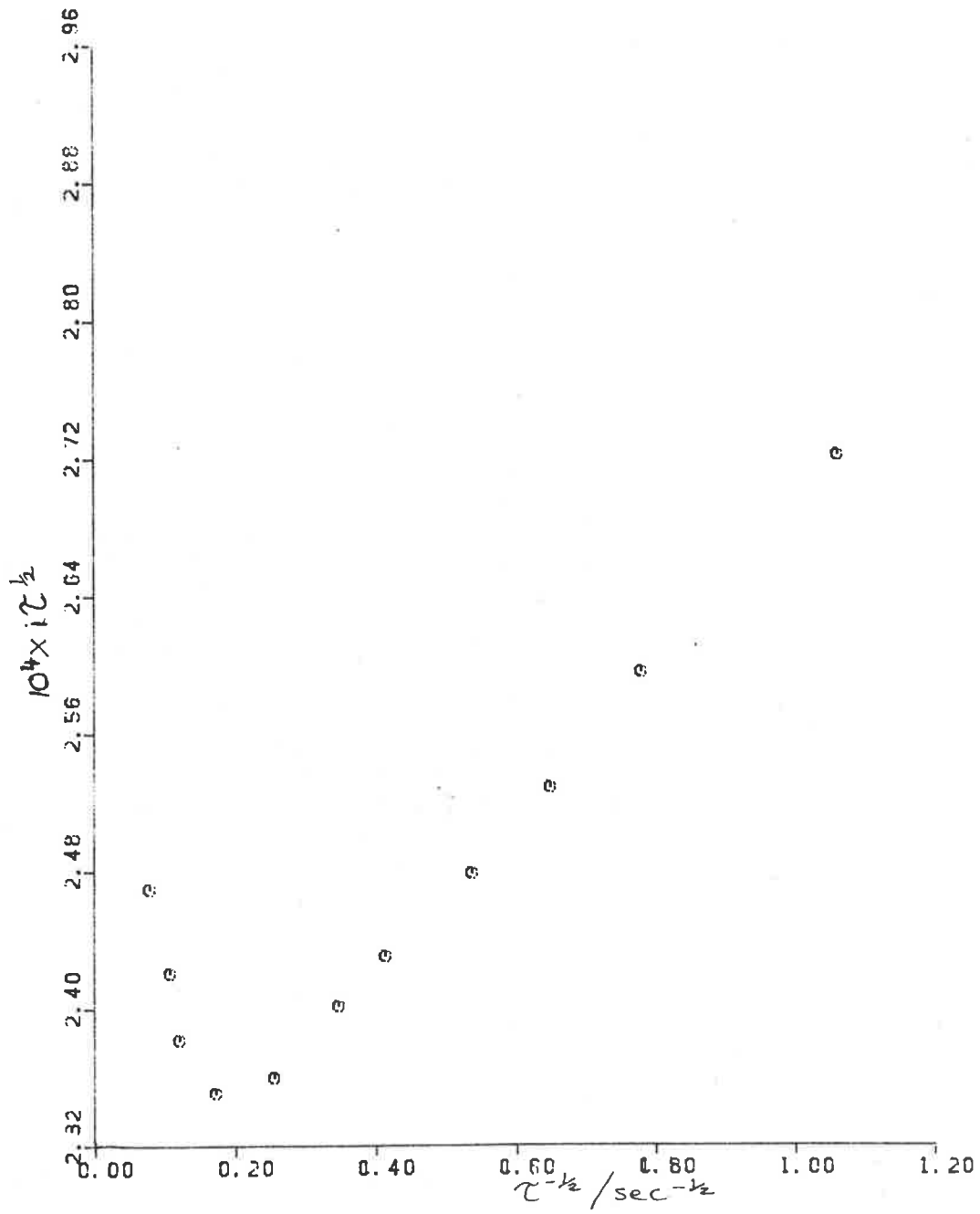


Figure 13.  $i\tau^{1/2}$  plotted against  $\tau^{-1/2}$  showing the effect of mass diffusion at low values of  $\tau^{-1/2}$ .

forward and reverse electrolysis times was also significantly different from the expected value of unity. The application of these above criteria was found to be an effective means of eliminating data affected by mass diffusion.

The effectiveness of a good seal between the cell piece and the electrode surface was demonstrated using electron microscopy. The photographs displayed in Figure 14 show scanning electron micrographs of silver electrodeposited on to platinum using the ETEC Autoscan. It is evident in Figure 14a that there is quite a sharp distinction between the central region exposed by the cylindrical diffusion cavity to the electrodeposited silver and the electrodeposit-free outer region that was masked by the cell piece. The sharpness of this contrast, and, hence, the effectiveness of the seal, is even more apparent in Figure 15.

Figure 15 shows the chart recorder record of X-ray intensity as a function of distance across the boundary of deposit-free, and silver electrodeposit covered regions on a platinum surface. The analysis was made with a Jeol Electron Microprobe Analyser using a P.E.T. crystal set to analyse for silver at 134.050 nm. The X-ray intensity was measured for a 5 second period before the electron beam spot was shifted to a position 1  $\mu\text{m}$  further along the transect. It is very evident from Figure 15 that there is a sharp contact between the low intensity region, corresponding to the electrodeposit-free platinum surface, and the high intensity region, corresponding to the region of silver electrodeposition. This is further emphasised by the fact that the high intensity peaks exceeding full-scale deflection actually have an average intensity many times greater than the full-scale maximum set on the chart recorder.



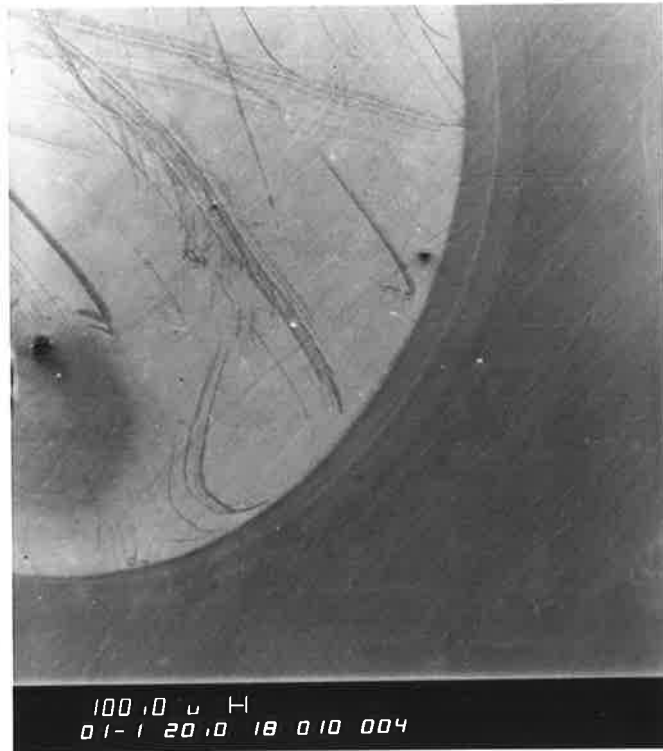


Figure 14a. Scanning electron micrograph of silver deposited on platinum stub using platinum Cottrell Cell electrode.

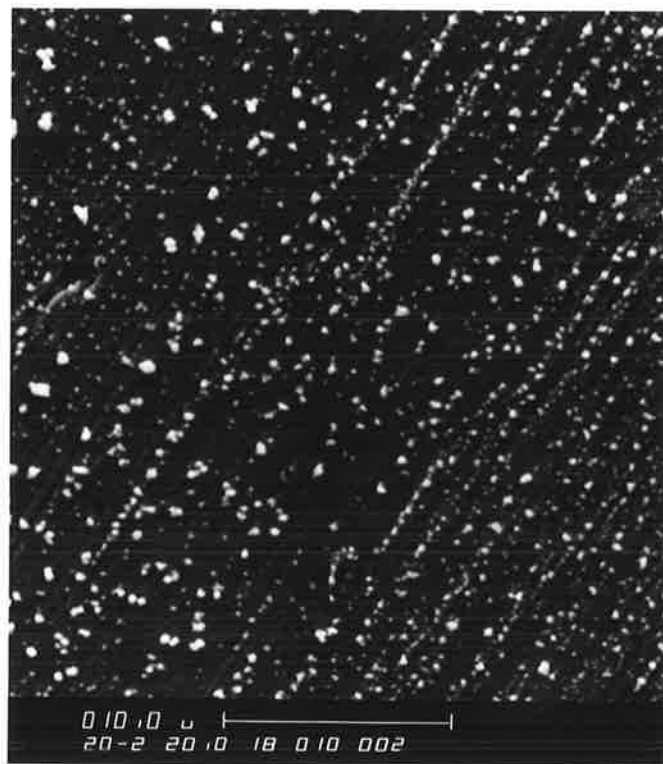


Figure 14b. Scanning electron micrograph showing the heterogeneous nature of the silver deposited on the platinum stub.

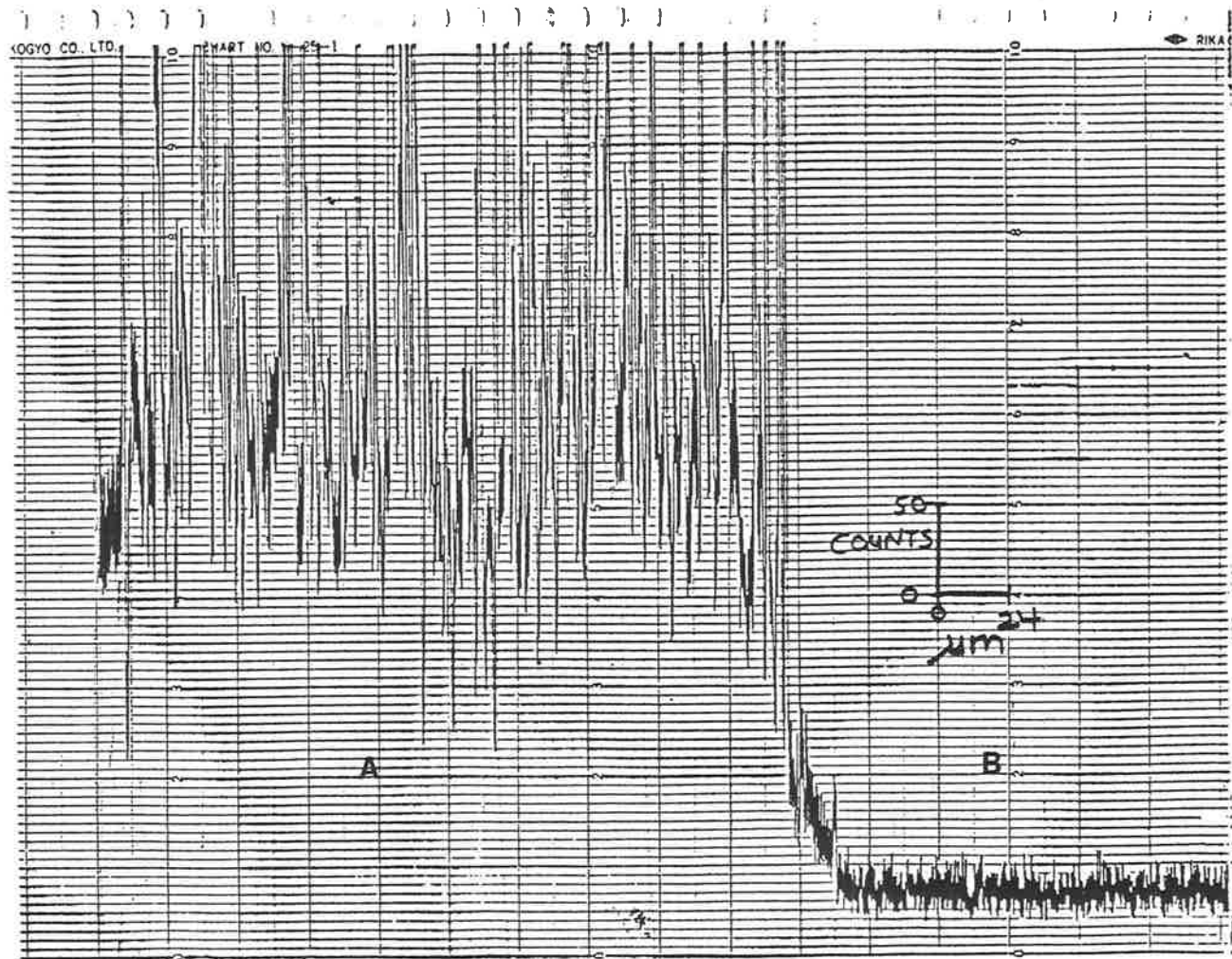


Figure 15. Recorder plot of silver X-ray intensity as a function of distance traversed across the junction of silver electrodeposit (A) and silver-free (B) regions on a platinum surface.

## 2.22

It can also be seen from Figures 14b and 15 that the silver electrodeposit is not homogeneous, but tends to be in the form of isolated grains of silver on the platinum surface, with little or no intergranular silver. Thallium electrodeposits on platinum were also found to be of a non-homogeneous nature.

All final measurements of the tracer diffusion coefficient of thallium (I) presented here were made using the platinum Cottrell Cell depicted in Figure 9.

It was noted earlier that the quality of water was improved during the series of measurements presented in this chapter. It was noted by the author that the improvement in the quality of the water used as the solvent made no difference to the determined value of the tracer diffusion coefficient. However, there may have been associated improvement in the reproducibility of experiments. Validation of this latter point, however, will require further experimentation.

### CORRELATION BETWEEN THE TRACER DIFFUSION COEFFICIENT AND THE SOLUTION VISCOSITY

Stokes' law describes the force experienced by a macroscopic sphere of radius  $r$  in a fluid medium. In combination with the treatment of Einstein, it has been applied to the diffusion of microscopic ions in a structured medium. The resultant Stokes-Einstein equation<sup>38</sup>

$$D = kT/(6\pi r\eta)$$

where  $k$  is the Boltzmann constant, predicts that the product of the tracer diffusion coefficient and the solution viscosity,  $\eta$ , should

be a constant for a given temperature,  $T$ , and particle of constant radius,  $r$ .

The author tested whether the prediction of the Stokes-Einstein equation could account for the variation in the tracer diffusion coefficient of thallium (I) measured in various aqueous electrolyte solutions.

The relative viscosity presented in Table 7 was determined by the author via interpolation of the viscosity data of other researchers.<sup>33-37</sup> The viscosity determined at electrolyte concentrations of 0.3315M in Reference 37, and 0.021061M and 0.29918M in Reference 35 were found to be erroneous, and were not used by the author.

Table 8 presents the results of the product of the tracer diffusion coefficient and the appropriate relative viscosity of the supporting electrolyte. The value of this product is quite similar for the electrolytes of  $\text{NaClO}_4$ ,  $\text{KNO}_3$  and  $\text{LiNO}_3$ , having an average value of  $(1.86 \pm 0.01) \times 10^{-5} \text{ cm}^2/\text{s}$ . The value of this product determined for  $\text{NaNO}_3$  as the supporting electrolyte, however, is about 8% greater than the other electrolytes.

#### DETERMINATION OF THE SLOPE, $Q$

The modified Sand equation

$$i\tau^{\frac{1}{2}} = nFC_0D_0^{\frac{1}{2}}\pi^{\frac{1}{2}}A/2 + Q\tau^{-\frac{1}{2}}$$

predicts that  $i\tau^{\frac{1}{2}}$  will be linear in  $\tau^{-\frac{1}{2}}$ . This was found to be the

**Table 7**

Relative viscosity,  $\eta_{rel}$ ,  
determined for a series of aqueous electrolyte solutions:

Electrolyte	$\eta_{rel}$	Reference
0.500M NaClO <sub>4</sub>	1.014	33
0.300M NaClO <sub>4</sub>	1.008	33
0.500M KNO <sub>3</sub>	0.983	34
0.300M KNO <sub>3</sub>	0.989	34
0.300M LiNO <sub>3</sub>	1.032	35
0.300M NaNO <sub>3</sub>	1.016	34,36,37

**Table 8**

Tracer diffusion coefficient of thallium (I),  $D_0$ ,  
and product  $D_0 \times \eta_{rel}$  determined for a series of aqueous electrolytes

Electrolyte	$D_0 \times 10^5 \text{ cm}^2/\text{s}$	$D_0 \times \eta_{rel} \times 10^5 \text{ cm}^2/\text{s}$
0.500M NaClO <sub>4</sub>	1.851 ± .014	1.88
0.300M NaClO <sub>4</sub>	1.837 ± .025	1.85
0.500M KNO <sub>3</sub>	1.878 ± .030	1.85
0.300M KNO <sub>3</sub>	1.877 ± .010	1.86
0.300M LiNO <sub>3</sub>	1.794 ± .034	1.85
0.300M NaNO <sub>3</sub>	1.981 ± .006	2.01

case. The slope of  $i\tau^{\frac{1}{2}}$  versus  $\tau^{-\frac{1}{2}}$  corresponds to an amount of charge,  $Q$ .

The value of  $Q$  varied considerably in the solutions investigated, from  $37 \mu\text{C}/\text{cm}^2$  up to  $341 \mu\text{C}/\text{cm}^2$ . The general unifying factor determining the value of  $Q$  was the gas used to deoxygenate and saturate the solution being studied. For example, in almost identical solutions of  $\text{TlNO}_3 + 0.500\text{M KNO}_3 + \text{H}_2\text{O}$ , the slope  $Q$  took values of 47 and  $62 \mu\text{C}/\text{cm}^2$ , and 259 and  $276 \mu\text{C}/\text{cm}^2$  for two solutions each deoxygenated with hydrogen and argon gas, respectively. As a general observation, it was found that using hydrogen gas gave values of  $Q < 100 \mu\text{C}/\text{cm}^2$ , while using argon gas gave values of  $Q > 100 \mu\text{C}/\text{cm}^2$ . From these results, it appears that the chemistry of the solid electrode/electrolyte solution interface dominates the value of the slope,  $Q$ . The charge could be due to reduction of surface adsorbed species that could include peroxides or radical species generated during electrolysis.

In Bard's<sup>21,23</sup> attempts to correct for the inconstancy of the chronopotentiometric constant, he postulated that an amount of charge,  $Q_c$ , could be used to charge the double layer. This charge was approximated as being the product of the average double layer capacitance and the maximum change in potential recorded during the electrolysis. From the results discussed here, it can be seen that the charging of the double layer could not be the dominant effect contributing to the observed slope  $Q$ . However, the results presented here are not inconsistent with double layer charging making some contribution to the charge  $Q$ .

## ALTERNATIVE METHOD TO CORRECT THE SAND EQUATION

The modification to the Sand equation carried out by Bard<sup>21,23</sup> was made assuming the applied current to be the sum of the currents involved in diffusion and other processes. Such an assumption is inherent in the procedure used by the author to determine the limiting value of  $i\tau^{\frac{1}{2}}$  and the value of  $Q$  from plots of  $i\tau^{\frac{1}{2}}$  against  $\tau^{-\frac{1}{2}}$ . This procedure also assumes that the correct transition time,  $\tau$ , has been measured.

If, however, one looks at the transition time measured,  $\tau_m$ , as being the sum of the true transition time,  $\tau$ , and an extra period of time,  $\tau_c$ , taken to charge the electrode an amount  $Q_c$ , then

$$\tau_m = \tau + \tau_c$$

$$\text{and } Q_c = i\tau_c$$

The latter equation can also be written as

$$Q_c = i\tau_c = i(\tau_{c1} + \tau_{c2} + \dots)$$

where  $\tau_{c1}$ ,  $\tau_{c2}$ , etc. are the time periods during which the electrode was charged an extra amount, and the electrode potential changed by an amount  $\Delta E_1$ ,  $\Delta E_2$ , etc. This approach has an advantage over the approach of Bard in that one does not have to assume that the charging of the double layer etc. will occur at a constant rate during the entire electrolysis. Rather, one can allow for a period of time during which no contribution was made to the value of  $Q_c$ .

Substitution for the true value of  $\tau$  into the Sand equation will give

$$i(\tau_m - Q_c/i)^{\frac{1}{2}} = nFC_0D_0^{\frac{1}{2}}\pi^{\frac{1}{2}}A/2$$

Using the above equation resulted in almost identical values being determined for the limiting value of  $i\tau^{\frac{1}{2}}$  and, hence, for the value of the tracer diffusion coefficient as those previously reported here. As such, these values have not been presented here. However, the value of  $Q_c$  tended to be of the order of 100% greater than the value of  $Q$  determined via the other method. The discussion made previously concerning  $Q$  still holds for  $Q_c$  in a qualitative manner.

The author found that there was not sufficient information to decide between the two modifications to the Sand equation presented here. It is worthy of restatement, however, that whichever approach was used resulted in the determination of almost identical tracer diffusion coefficients.

#### NOTE ON THE SHAPE OF CHRONOPOTENTIOTRAGRAMS

During the progress of this work, chronopotentiometric research was carried out in this laboratory without supporting electrolyte, resulting in a plausible reason as to why the shape of experimentally obtained chronopotentiograms deviate from the expected theoretical shape. The reasoning is based upon the observed increase in the resistance of the catholyte during the depletion of the reducible species. This increase in the resistance across the catholyte will cause the



electrode potential to be greater than that predicted by theory. This phenomenon is likely to be able to account for at least some of the deviation from theoretical behaviour observed in the vicinity of the transition time for chronopotentiograms obtained with supporting electrolyte. This topic is further discussed by Horwath.<sup>39</sup>

**System I.  $TlNO_3 + NaClO_4 + H_2O$** 

Five series of chronopotentiometric measurements were made for the  $TlNO_3 + NaClO_4 + H_2O$  system with transition times from 0.437 seconds up to 85.44 seconds being recorded. The results for  $i\tau^{\frac{1}{2}}$  versus  $\tau^{-\frac{1}{2}}$  are recorded for each measurement in Figures 16 and 17.

From a comparison of results recorded in Tables 1 and 2 it can be seen that the tracer diffusion coefficient for thallium (I) determined from these measurements was independent of the thallium (I) concentration, the  $NaClO_4$  supporting electrolyte concentration, and the platinum electrode surface area. Within the limits used in these experiments, it is expected that the tracer diffusion coefficient for thallium (I) will be unique.

The tracer diffusion coefficient of thallium (I) was determined to be  $1.845 \times 10^{-5} \text{ cm}^2/\text{s}$  with an uncertainty of 1%.

**System II.  $TlNO_3 + KNO_3 + H_2O$** 

The results for plots of  $i\tau^{\frac{1}{2}}$  versus  $\tau^{-\frac{1}{2}}$  are shown in Figure 18 for four series of measurements for aqueous solutions containing 5 mM  $TlNO_3$  and 0.500 M  $KNO_3$ . The measured transition times,  $\tau$ , ranged from 0.671 seconds up to 73.34 seconds.

From Table 3 it can be seen that the tracer diffusion coefficient for thallium (I) determined from the above-mentioned solutions is identical to that calculated from a solution containing 3 mM  $TlNO_3$  and 0.300 M  $KNO_3$ . These results show that the tracer diffusion coefficient deter-

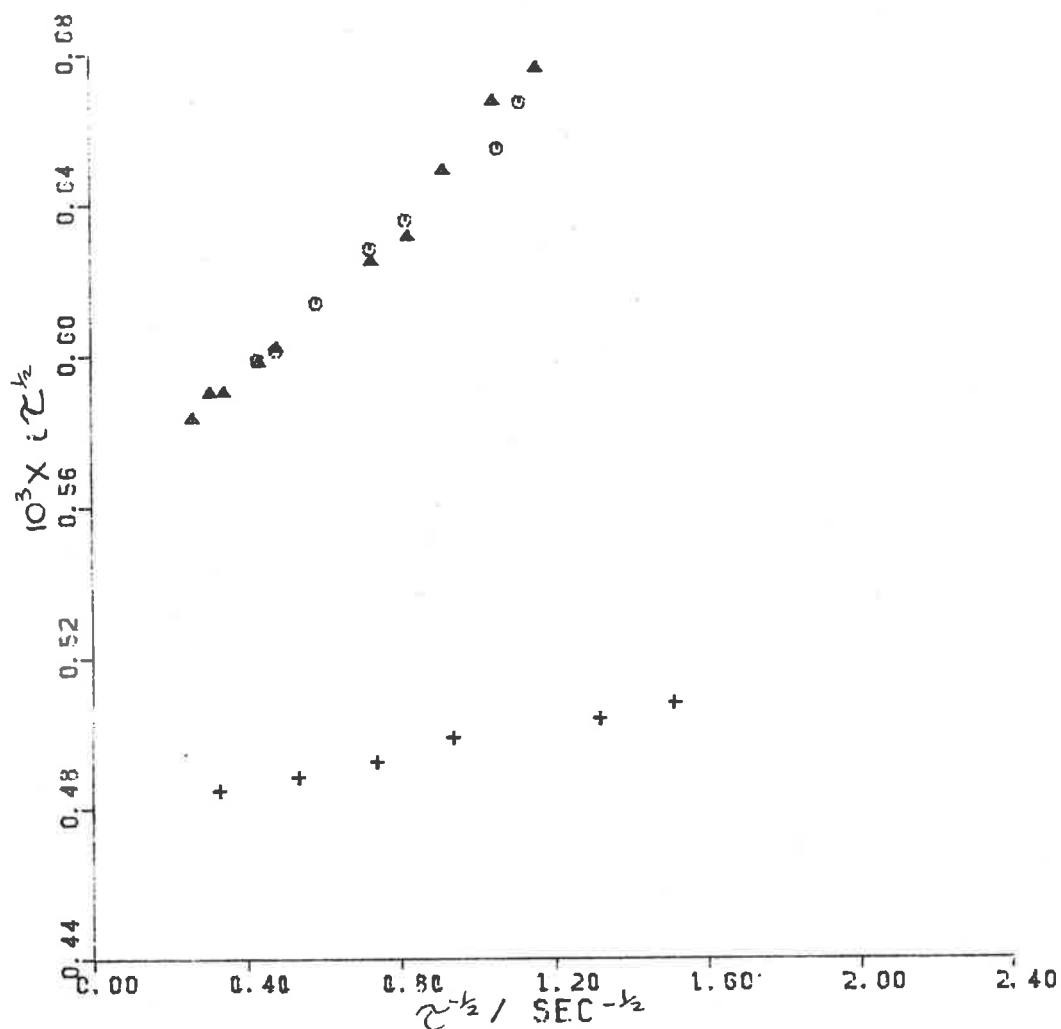


Figure 16.  $i r^{\frac{1}{2}}$  plotted against  $r^{-\frac{1}{2}}$  for 5mM  $TlNO_3$  + 0.5M  $NaClO_4$  +  $H_2O$ :  
Run 1 (O); Run 2 ( $\Delta$ ); Run 3 (+).

Table 1

Tracer diffusion coefficient,  $D_0$ , of thallium (I) in 0.5M  $NaClO_4$  +  $H_2O$

Run	Area/cm <sup>2</sup>	$C_{Tl+}/mM$	$C_{NaClO_4}/M$	Intercept $\times 10^3$	$D_0 \times 10^5$ cm <sup>2</sup> /s
1	.3004	5.021	0.500	.5548 $\pm$ .0031	1.849 $\pm$ .021
2	.3004	5.021	0.500	.5571 $\pm$ .0029	1.865 $\pm$ .019
3	.2570	5.079	0.499	.4785 $\pm$ .0010	1.838 $\pm$ .008

Average

1.851  $\pm$  .014

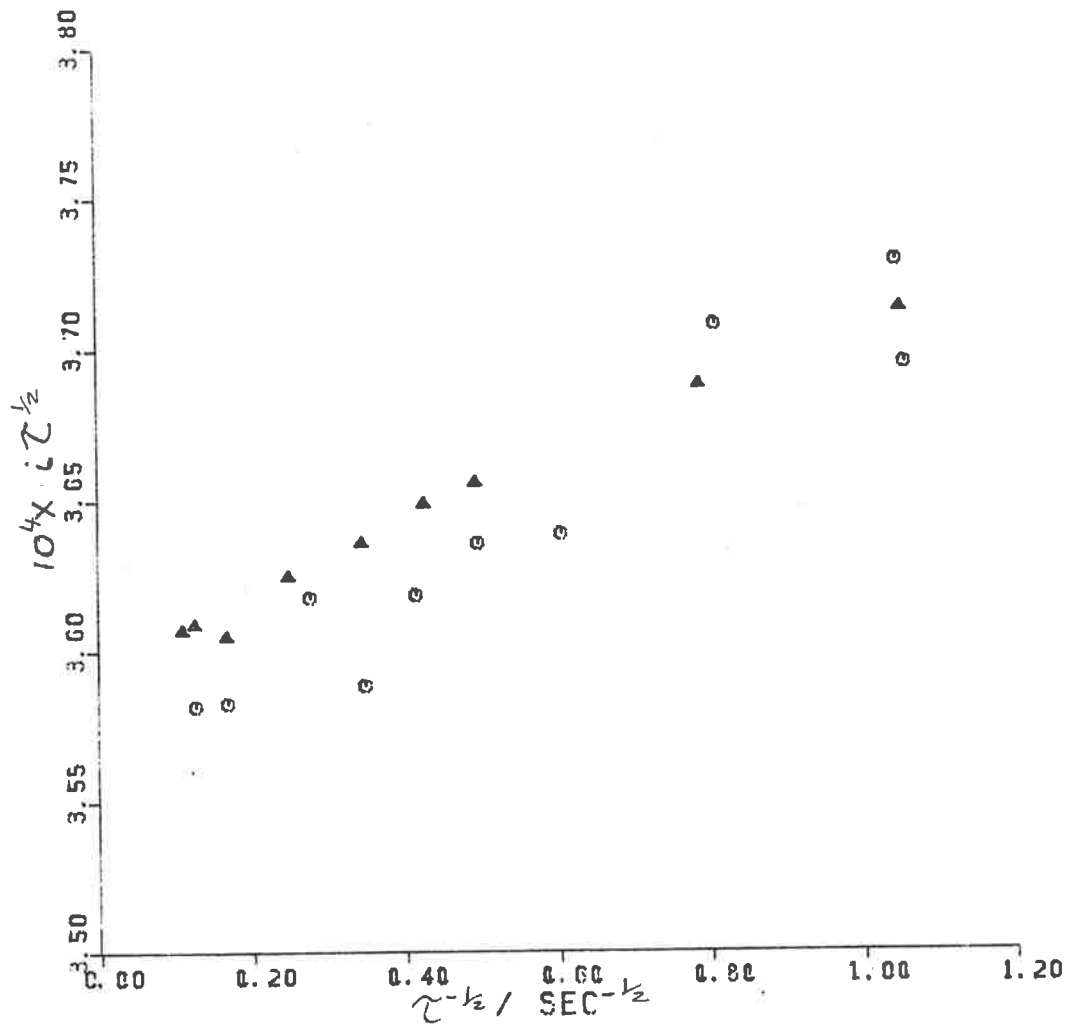


Figure 17.  $i\tau^{1/2}$  plotted against  $\tau^{-1/2}$  for 3mM  $\text{TlNO}_3$  + 0.3M  $\text{NaClO}_4$  +  $\text{H}_2\text{O}$ :  
Run 1 (O); Run 2 ( $\Delta$ ).

Table 2

Tracer diffusion coefficient,  $D_0$ , of thallium (I) in 0.3M  $\text{NaClO}_4$  +  $\text{H}_2\text{O}$

Run	Area/cm <sup>2</sup>	$C_{\text{Tl}^+}$ /mM	$C_{\text{NaClO}_4}$ /M	Intercept $\times 10^3$	$D_0 \times 10^5$ cm <sup>2</sup> /s
1	.3187	3.062	0.300	.3594 $\pm$ .0003	1.855 $\pm$ .003
2	.3187	3.062	0.300	.3559 $\pm$ .0011	1.819 $\pm$ .011

Average

1.837  $\pm$  .025

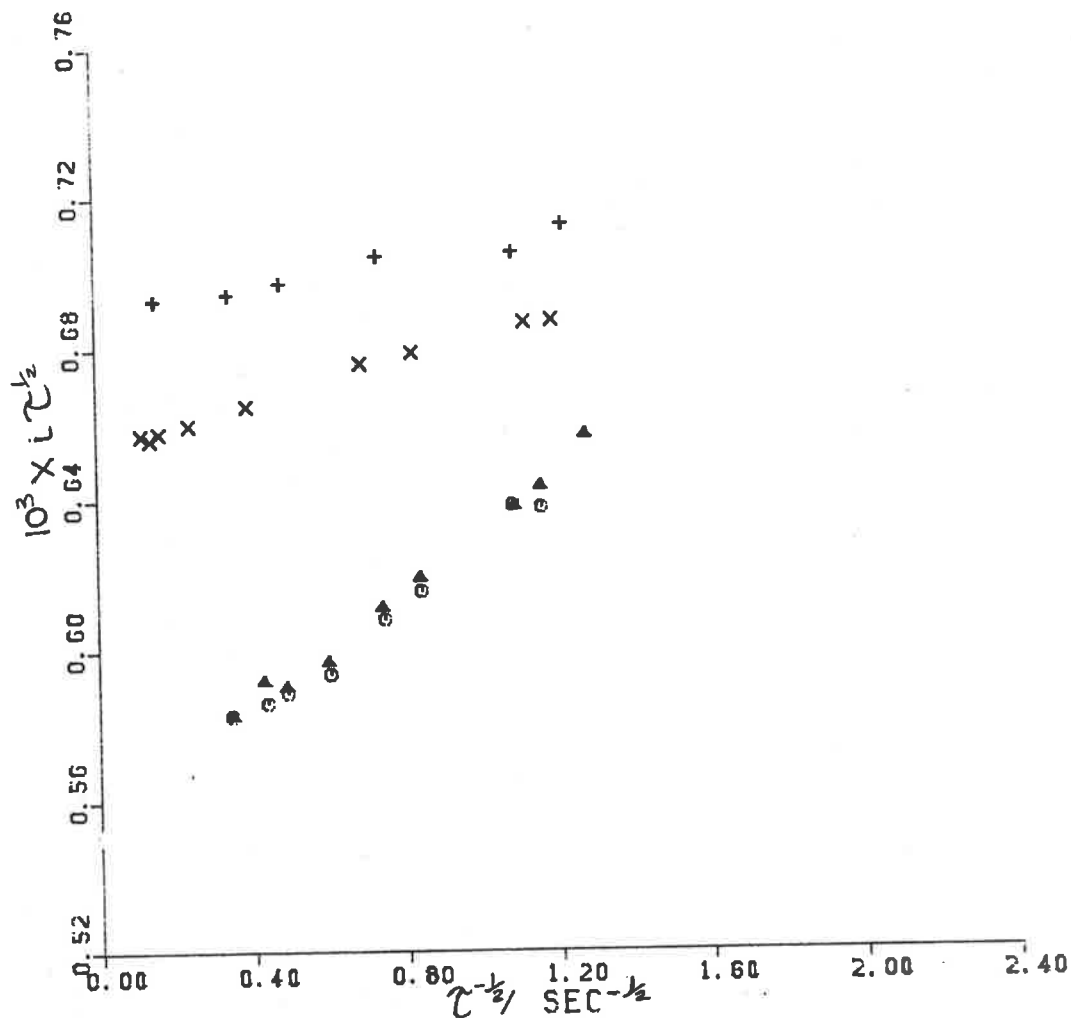


Figure 18.  $i\tau^{1/2}$  plotted against  $\tau^{-1/2}$  for 5mM  $\text{TlNO}_3$  + 0.5M  $\text{KNO}_3$  +  $\text{H}_2\text{O}$ :  
 Run 1 (O); Run 2 ( $\Delta$ ); Run 3 (+); Run 4 (X).

Table 3

Tracer diffusion coefficient,  $D_0$ , of thallium (I) in 0.5M  $\text{KNO}_3$  +  $\text{H}_2\text{O}$

Run	Area/cm <sup>2</sup>	$C_{\text{Tl}^+}$ /mM	$C_{\text{KNO}_3}$ /M	Intercept $\times 10^3$	$D_0 \times 10^5$ cm <sup>2</sup> /s
1	.3004	4.976	0.500	.5534 $\pm$ .0031	1.874 $\pm$ .021
2	.3004	4.976	0.500	.5544 $\pm$ .0024	1.880 $\pm$ .016
3	.3685	5.099	0.500	.6895 $\pm$ .0018	1.841 $\pm$ .010
4	.3339	5.227	0.500	.6531 $\pm$ .0007	1.915 $\pm$ .004
Average					1.878 $\pm$ .030

mined for thallium (I) is independent of the thallium (I) concentration, the  $\text{KNO}_3$  supporting electrolyte concentration, and the exposed platinum electrode surface area within the limits of this study.

The tracer diffusion coefficient of thallium (I) was found to be  $1.877 \times 10^{-5} \text{ cm}^2/\text{s}$  with an uncertainty of 1.4%.

The tracer diffusion coefficient of thallium (I) determined in aqueous solutions was similar using either  $\text{NaClO}_4$  or  $\text{KNO}_3$  as the supporting electrolyte. The tracer diffusion coefficient of thallium (I) determined from ten solutions containing either  $\text{NaClO}_4$  or  $\text{KNO}_3$  as the supporting electrolyte had an averaged value of  $1.86 \times 10^{-5} \text{ cm}^2/\text{s}$  with an uncertainty of 1.5%.

The Sand equation predicts that the limiting values of  $i\tau^{1/2}/C_{\text{Tl(I)}}$  will be a linear function of the electrode surface area, and pass through the origin. The results plotted in Figure 19 from the ten solutions containing either  $\text{NaClO}_4$  or  $\text{KNO}_3$  as the supporting electrolyte show that this is indeed the case. This suggests that the effective electrode surface area is the same as the geometrically measured electrode surface area.

### System III. $\text{TlNO}_3 + \text{LiNO}_3 + \text{H}_2\text{O}$

Figure 20 records the results of two separate measurements made in aqueous solutions of 3 mM  $\text{TlNO}_3 + 0.300 \text{ M LiNO}_3$ . Transition times were measured from 1.744 seconds up to 79.18 seconds.

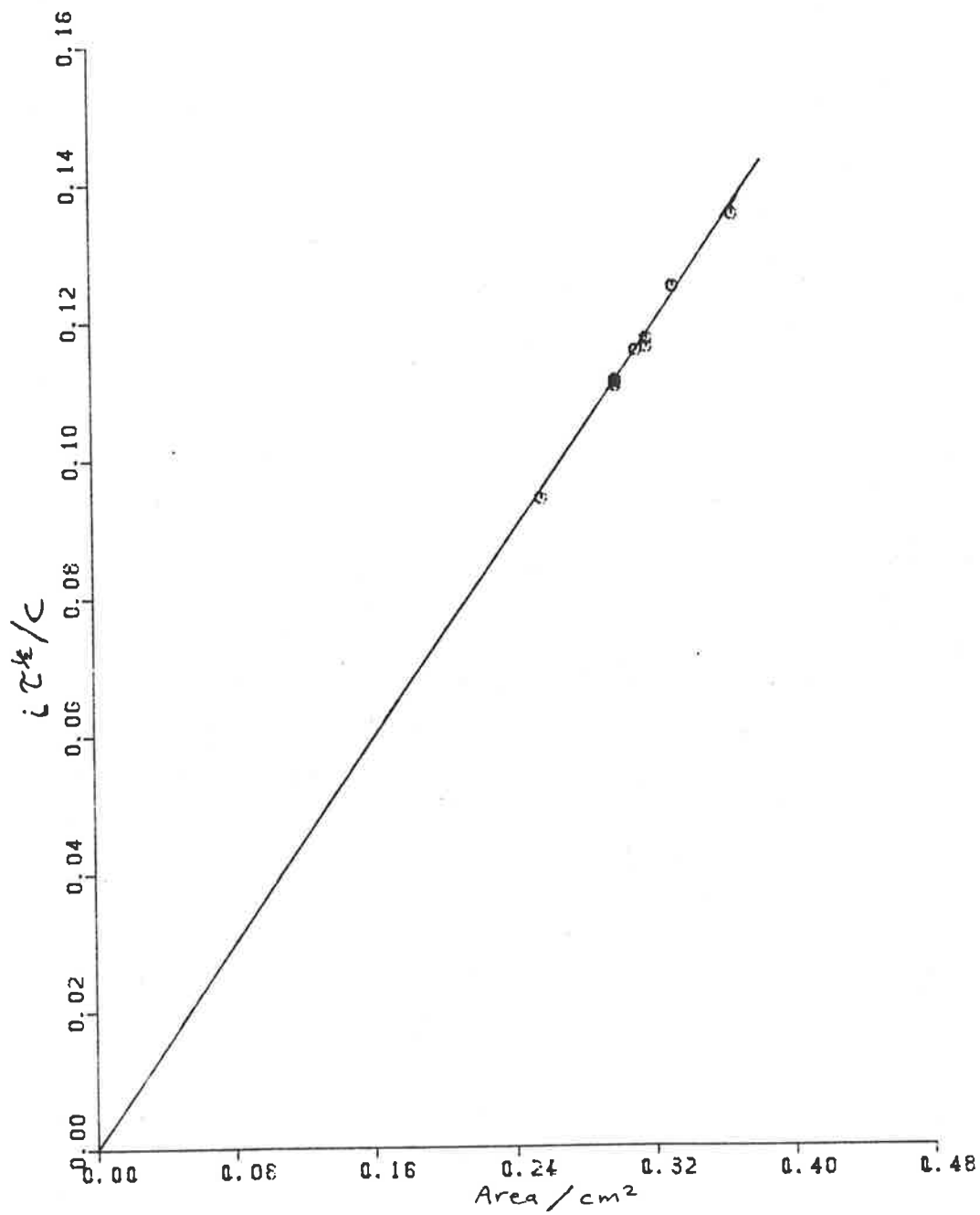


Figure 19.  $i_c^{1/2}/C$  plotted against apparent electrode surface area,  $A$ .

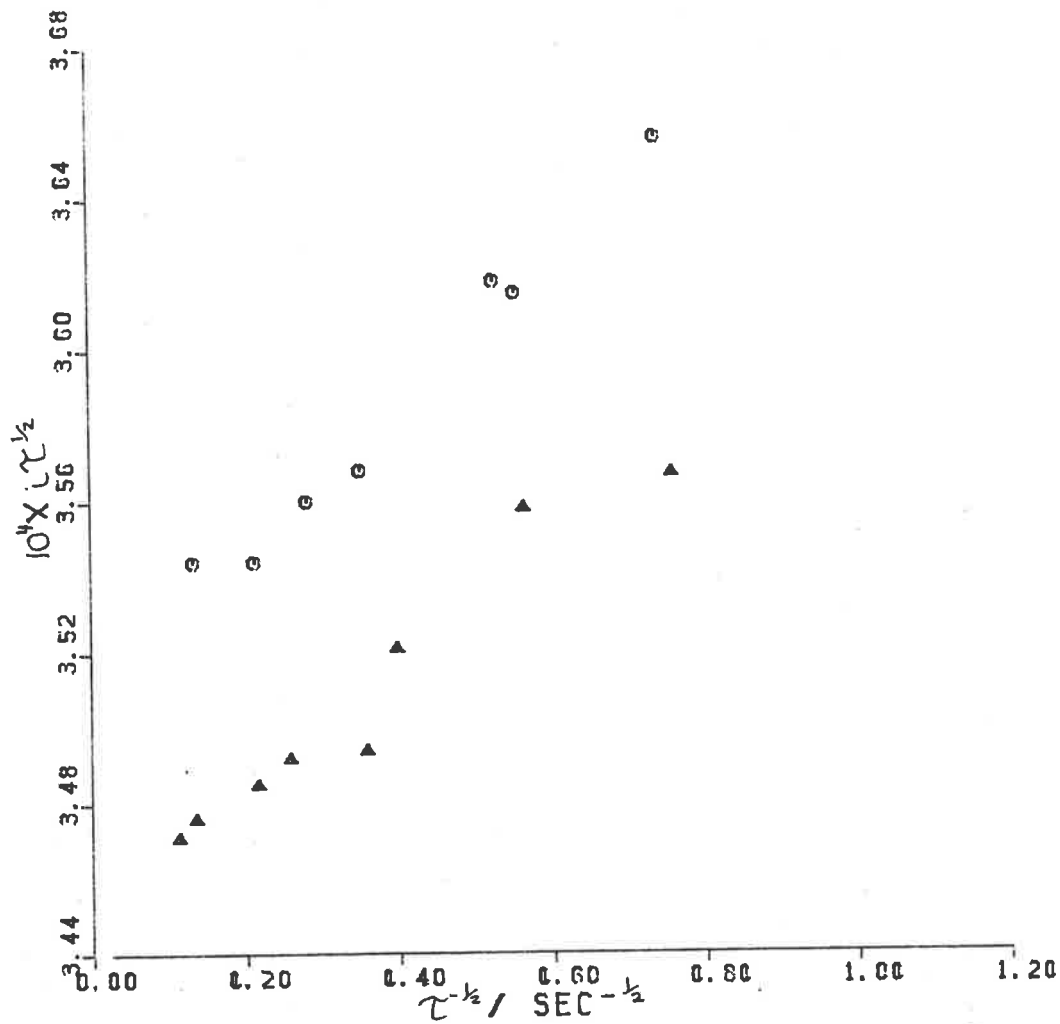


Figure 20.  $\tau^{1/2}$  plotted against  $\tau^{-1/2}$  for 3mM  $\text{TlNO}_3$  + 0.3M  $\text{LiNO}_3$  +  $\text{H}_2\text{O}$ :  
Run 1 (O); Run 2 ( $\Delta$ ).

Table 4

Tracer diffusion coefficient,  $D_0$ , of thallium (I) in 0.3M  $\text{LiNO}_3$  +  $\text{H}_2\text{O}$

Run	Area/cm <sup>2</sup>	$C_{\text{Tl}^+}$ /mM	$C_{\text{LiNO}_3}$ /M	Intercept $\times 10^3$	$D_0 \times 10^5$ cm <sup>2</sup> /s
1	.3187	3.010	0.300	.3498 $\pm$ .0005	1.818 $\pm$ .005
2	.3187	3.010	0.300	.3451 $\pm$ .0007	1.770 $\pm$ .007
Average					1.794 $\pm$ .034



The calculated tracer diffusion coefficient of thallium (I) was lower than that measured using  $\text{NaClO}_4$  or  $\text{KNO}_3$  as the supporting electrolyte. The measured tracer diffusion coefficient of thallium (I) was  $1.794 \times 10^{-5} \text{ cm}^2/\text{s}$  with an uncertainty of 1.9%.

#### System IV. $\text{TlNO}_3 + \text{NaNO}_3 + \text{H}_2\text{O}$

Figure 21 records the results of measurements made in two aqueous solutions of 3 mM  $\text{TlNO}_3 + 0.300 \text{ M NaNO}_3$ . Transition times from 0.860 seconds up to 84.83 seconds were measured.

The calculated tracer diffusion coefficient of thallium (I) was  $1.981 \times 10^{-5} \text{ cm}^2/\text{s}$ , which is very much higher than that measured using  $\text{NaClO}_4$ ,  $\text{KNO}_3$  or  $\text{LiNO}_3$  as the supporting electrolyte. The uncertainty in the tracer diffusion coefficient was only 0.3%.

#### System V. $\text{TlNO}_3 + \text{KNO}_3 + \text{H}_2\text{O} + \text{NMF}$

The results of plots of  $i\tau^{\frac{1}{2}}$  versus  $\tau^{-\frac{1}{2}}$  are presented in Figures 22 and 23 for solutions containing thallium (I) in 0.300 M  $\text{KNO}_3$  supporting electrolyte in solvents of 0.000, 0.253, 0.502 and 1.000 mole fractions of NMF. The tracer diffusion coefficient determined from these plots is presented in Table 6.

In Figure 24, the measured tracer diffusion coefficient of thallium (I) is presented as a function of NMF solvent mole fraction for a constant  $\text{KNO}_3$  supporting electrolyte concentration of 0.300 M. It is quite evident that the tracer diffusion coefficient decreases from a maximum in pure water to a minimum in pure NMF in an exponential manner.

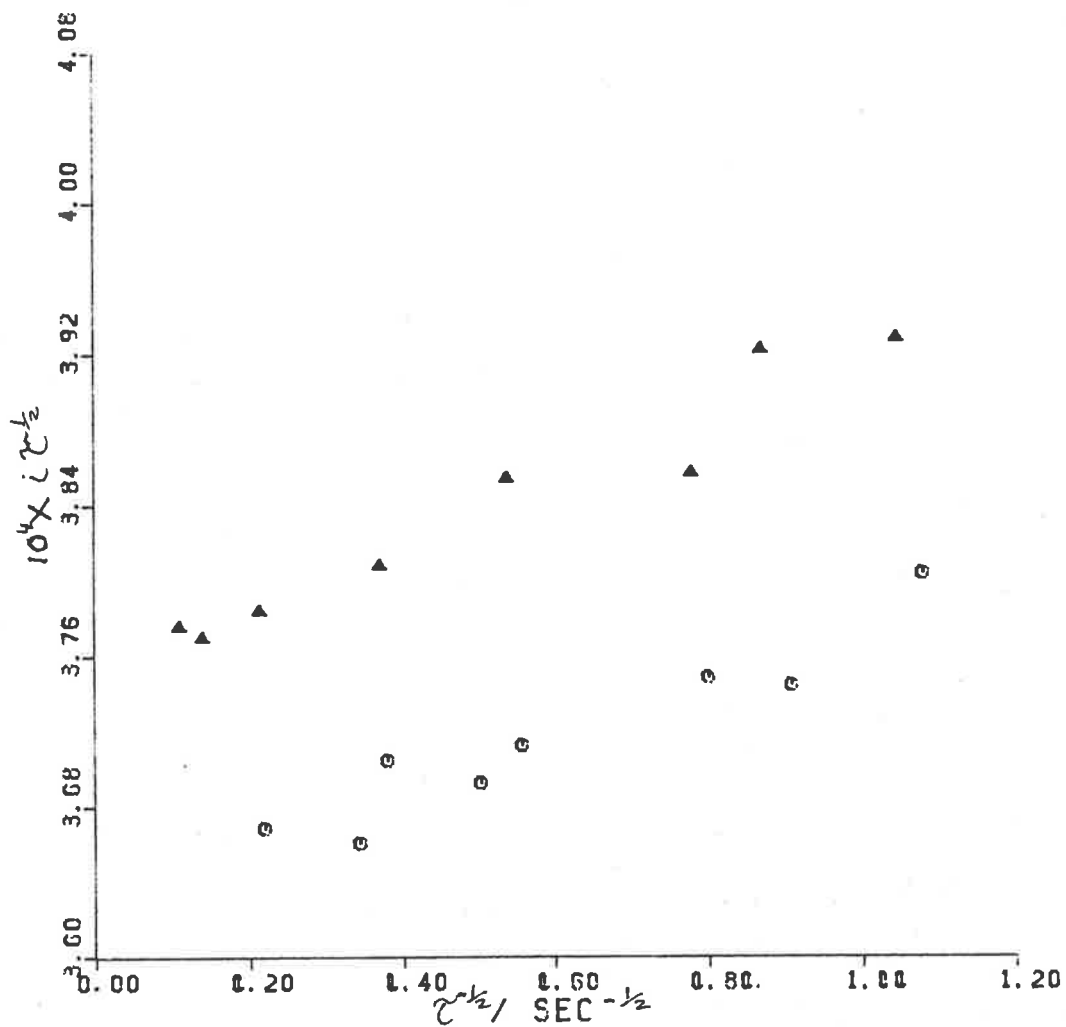


Figure 21.  $i\tau^{1/2}$  plotted against  $\tau^{-1/2}$  for 3mM  $\text{TlNO}_3$  + 0.3M  $\text{NaNO}_3$  +  $\text{H}_2\text{O}$ :  
Run 1 (O); Run 2 ( $\Delta$ ).

Table 5

Tracer diffusion coefficient,  $D_0$ , of thallium (I) in 0.3M  $\text{NaNO}_3$  +  $\text{H}_2\text{O}$

Run	Area/cm <sup>2</sup>	$C_{\text{Tl}^+}$ /mM	$C_{\text{NaNO}_3}$ /M	Intercept $\times 10^3$	$D_0 \times 10^5$ cm <sup>2</sup> /s
1	.3197	2.979	0.300	.3629 $\pm$ .0013	1.985 $\pm$ .014
2	.3197	3.085	0.300	.3750 $\pm$ .0010	1.976 $\pm$ .011
Average					1.981 $\pm$ .006

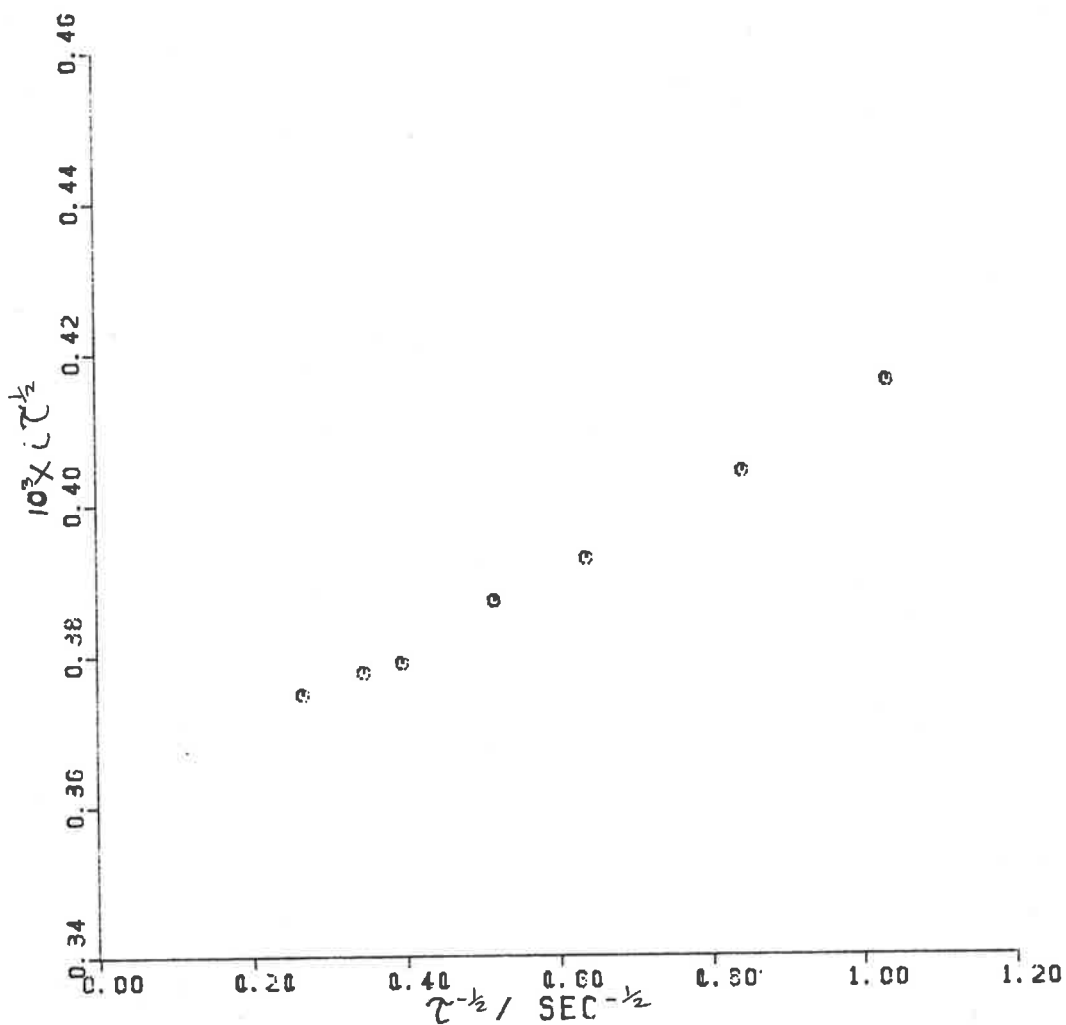


Figure 22.  $i\tau^{1/2}$  plotted against  $\tau^{-1/2}$  for 3mM  $TlNO_3$  + 0.300M  $KNO_3$  +  $H_2O$ : Run 1 (O).

Table 6

Dependence of tracer diffusion coefficient,  $D_0$ , for thallium (I) on NMF mole fraction,  $X_{NMF}$ , for the  $H_2O + NMF + 0.300M KNO_3$  system

Run	$X_{NMF}$	Intercept $\times 10^3$	$D_0 \times 10^5 \text{ cm}^2/\text{s}$
1	0.000	$.3589 \pm .0010$	$1.877 \pm .010$
2	0.253	$.1920 \pm .0008$	$0.935 \pm .008$
3	0.502	$.2097 \pm .0006$	$0.678 \pm .004$
4	1.000	$.1794 \pm .0006$	$0.506 \pm .0035$

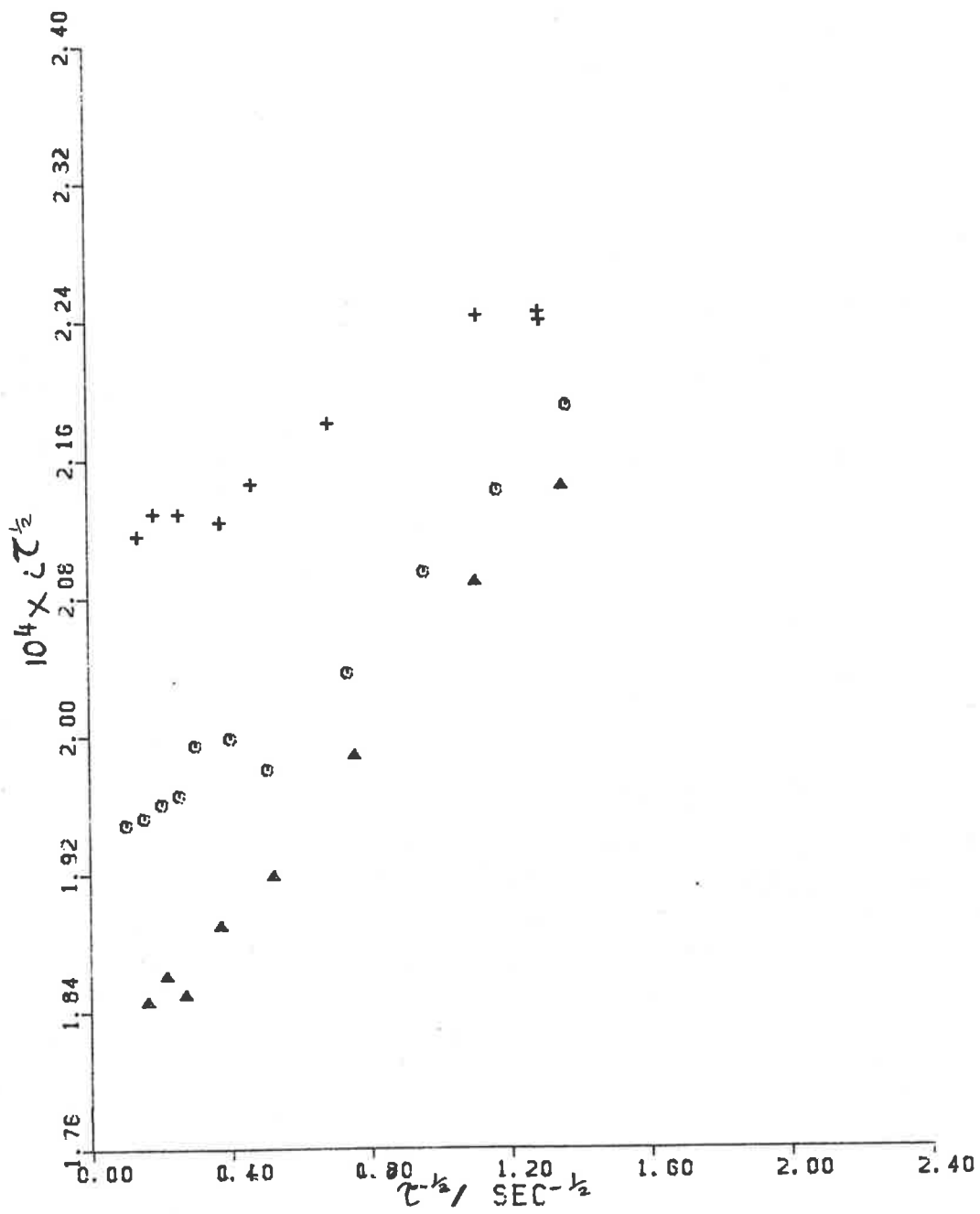


Figure 23.  $i\tau^{1/2}$  plotted against  $\tau^{-1/2}$  for the 3mM  $\text{TINO}_3$  + 0.300M  $\text{KNO}_3$  +  $\text{H}_2\text{O}$  + NMF system: Run 2,  $X_{\text{NMF}} = 0.253$  (O); Run 3,  $X_{\text{NMF}} = 0.502$  ( $\Delta$ ); Run 4,  $X_{\text{NMF}} = 1.000$  (+).

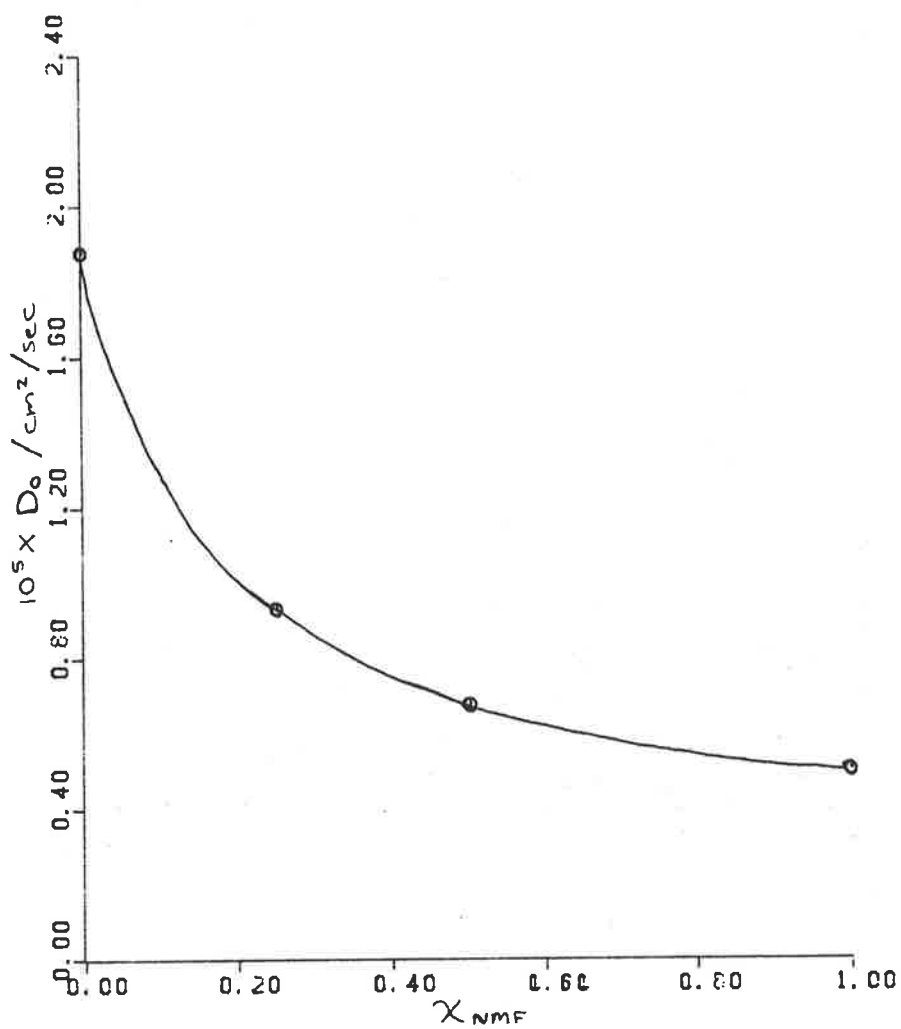


Figure 24. Dependence of the tracer diffusion coefficient,  $D_0$ , of thallium (I) on NMF mole fraction.

The  $\text{TlNO}_3 + \text{KNO}_3 + \text{H}_2\text{O} + \text{NMF}$  system has been investigated previously by Hale and Parsons.<sup>31</sup> They used polarography to measure the limiting diffusion current for thallium (I) in mixed  $\text{H}_2\text{O} + \text{NMF}$  solvents using 0.1 N  $\text{KNO}_3$  as the background electrolyte. It is known from polarographic theory that the square of the limiting diffusion current is proportional to the tracer diffusion coefficient.<sup>32</sup> It is not surprising, then, to find qualitative agreement between the square of the limiting diffusion current recorded by Hale and Parsons and the tracer diffusion coefficient of thallium (I) determined by the author as a function of  $\text{H}_2\text{O} + \text{NMF}$  solvent composition. It is worthy of note here that, in Figure 5 of the paper by Hale and Parsons,<sup>31</sup> the square of the limiting diffusion current for thallium (I) at 0.75 NMF mole fraction appears erroneously high. The author would suggest that their curve should be redrawn, ignoring that point, on the evidence presented here. It is also of interest to note that the change in the tracer diffusion coefficient of thallium (I) in  $\text{H}_2\text{O} + \text{NMF}$  solvents is not reflective of the change of the macroscopic viscosity of  $\text{H}_2\text{O} + \text{NMF}$  solvents. This is in agreement with the observations of Hale and Parsons.<sup>31</sup>

## CONCLUSION

The author has shown that a simple non-graphical method can be used to accurately determine the transition time,  $\tau$ , from an individual chronopotentiogram.

The product  $i\tau^{\frac{1}{2}}$  was found to show a distinct dependence upon  $\tau^{-\frac{1}{2}}$ , which is not predicted from the theory proposed by Sand.<sup>11</sup> The linear extrapolation to  $\tau^{-\frac{1}{2}} = 0$  of a plot of  $i\tau^{\frac{1}{2}}$  against  $\tau^{-\frac{1}{2}}$  was found to be a good method of obtaining accurate values of the tracer diffusion coefficient of thallium (I) in a variety of electrolyte solutions. The slope of such a plot corresponds to an amount of charge,  $Q$ . The author found that the magnitude of  $Q$  depended largely upon the chemistry of the electrode/electrolyte solution interface which could be influenced by the nature of the gas used to saturate the solution. The contribution of double layer charging to the value of  $Q$  as suggested by Bard,<sup>21,23</sup> while not inconsistent with the results, is not likely to be easily separated from other dominating influences which are still not fully understood and require further investigation.

The author also treated the chronopotentiometric data by the novel approach of considering the measured transition time to be the sum of the true transition time and an extra period of time due to other charging processes occurring at the electrode/electrolyte solution interface. The resultant form of the Sand equation due to this approach is

$$i(\tau_m - Q_c/i)^{\frac{1}{2}} = nFC_0D_0^{\frac{1}{2}}\pi^{\frac{1}{2}}A/2$$

where  $\tau_m$  is the transition time measured by the procedure presented by the author.

### 2.33

The tracer diffusion coefficients determined by both approaches were almost identical, whereas the amount of charge  $Q_c$  was found to be considerably greater than the value of  $Q$  determined from the slope of  $i\tau^{\frac{1}{2}}$  against  $\tau^{-\frac{1}{2}}$ .

The tracer diffusion coefficient of thallium (I) was determined to be  $1.845 \times 10^{-5}$ ,  $1.88 \times 10^{-5}$ ,  $1.79 \times 10^{-5}$ , and  $1.98 \times 10^{-5}$   $\text{cm}^2/\text{s}$  in concentrated aqueous solutions of  $\text{NaClO}_4$ ,  $\text{KNO}_3$ ,  $\text{LiNO}_3$ , and  $\text{NaNO}_3$ , respectively. The difference in the calculated tracer diffusion coefficients could be minimized by taking into account the relative viscosities of the aqueous electrolyte solutions. The adjusted tracer diffusion coefficient yielded an averaged value of  $(1.86 \pm 0.01) \times 10^{-5}$   $\text{cm}^2/\text{s}$ , independent of the electrolyte type and concentration for the electrolytes  $\text{NaClO}_4$ ,  $\text{KNO}_3$  and  $\text{LiNO}_3$ . The difference in the tracer diffusion coefficient determined in  $\text{NaNO}_3$  solution could not be accounted for in terms of a viscosity effect. No explanation for the unusual behaviour of the  $\text{TlNO}_3 + \text{H}_2\text{O} + \text{NaNO}_3$  system can be forwarded at this stage. The author suggests that further tracer diffusion coefficient measurements in solutions of different  $\text{NaNO}_3$  concentrations may bring further enlightenment on this matter.

The tracer diffusion coefficient was also measured for thallium (I) in a series of  $\text{H}_2\text{O} + \text{NMF} + \text{KNO}_3$  solutions at constant electrolyte concentration. The tracer diffusion coefficient was found to decrease from a maximum of  $1.88 \times 10^{-5}$   $\text{cm}^2/\text{s}$  in pure water to a minimum of  $0.506 \times 10^{-5}$   $\text{cm}^2/\text{s}$  in pure NMF. The change in the tracer diffusion coefficient with change in solvent composition did not correlate with the known change of the macroscopic viscosity of  $\text{H}_2\text{O} + \text{NMF}$  solutions.



The author tested the prediction of the Sand equation, that values of  $i\tau^{1/2}/C$  should be a linear function of the electrode surface area, and pass through the origin. This was indeed found to be the case using extrapolated  $i\tau^{1/2}$  values determined from measurements in solutions containing either  $\text{NaClO}_4$  or  $\text{KNO}_3$  as the supporting electrolyte. The inference from this agreement is that the effective electrode surface area is the same as its geometrically measured surface area, even though the platinum electrode surface was known to show surface scratches and defects. A photomicrograph showing a typical electrode surface is shown in Figure 4a of Chapter 3 of this thesis.

The insensitivity of chronopotentiometry to minor surface irregularities in solid electrode surfaces can best be understood when one considers the concept of diffusion layer thickness. The diffusion layer thickness,  $X_d$ , is related to the tracer diffusion coefficient,  $D_0$ , and the transition time,  $\tau$ , by the relation<sup>1</sup>

$$X_d = (D_0 \cdot \tau)^{-1/2}$$

If the profile of surface unevenness is small in comparison with the diffusion layer thickness, then the diffusion during electrolysis will be dominated by semi-infinite linear diffusion to a plane electrode. If, however, the profile of surface unevenness is significant in comparison with the diffusion layer thickness, then the surface unevenness will become important, and the effective diffusion area will increase.

For a typical tracer diffusion coefficient of  $1.86 \times 10^{-5} \text{ cm}^2/\text{s}$  and values of  $\tau$  ranging from 1 second up to 100 seconds, the diffusion layer thickness will be 43  $\mu\text{m}$  and 430  $\mu\text{m}$ , respectively. The platinum

### 2.35

surfaces used in these studies were polished and etched such that surface irregularities were of the order of  $1\ \mu\text{m}$  or less. It can be seen from the above example calculations that the surface irregularities in the electrodes used here are not going to be significant when compared with the diffusion layer thickness.

It is expected, however, that measurements such as double layer capacitance are likely to be more sensitive to surface irregularities in the electrodes used.

## REFERENCES

- 1 PAUNOVIC, M., *J. Electroanal. Chem.*, 14(1967) 447.
- 2 DELAHAY, P. and MAMANTOV, G., *Anal. Chem.*, 27(1955) 478.
- 3 DELAHAY, P. and BERZINS, T., *J. Am. Chem. Soc.*, 75(1953) 2486.
- 4 BERZINS, T. and DELAHAY, P., *J. Am. Chem. Soc.*, 75(1953) 4205.
- 5 DELAHAY, P. and MATTAX, C. C., *J. Am. Chem. Soc.*, 76(1954) 874.
- 6 DELAHAY, P., MATTAX, C. C. and BERZINS, T., *J. Am. Chem. Soc.*, 76(1954) 5319.
- 7 DELAHAY, P. and MATTAX, C. C., *J. Am. Chem. Soc.*, 76(1954) 5314.
- 8 LAITINEN, H. A. and GAUR, H. C., *Anal. Chim. Acta*, 18(1958) 1.
- 9 JAIN, R. K., GAUR, H. C. and WELCH, B. J., *J. Electroanal. Chem.*, 79(1977) 211.
- 10 WEBER, H. F., *Wied. Ann. Physik*, 7(1879) 536.
- 11 SAND, H. J. S., *Phil. Mag.*, 1(1901) 45.
- 12 GIERST, L. and JULIARD, A., *J. Phys. Chem.*, 57(1953) 701.
- 13 BOS, P. and VAN DALEN, E., *J. Electroanal. Chem.*, 45(1973) 165.
- 14 REINMUTH, W. H., *Anal. Chem.*, 33(1961) 485.
- 15 DE VRIES, W. T., *J. Electroanal. Chem.*, 17(1968) 31.
- 16 DE VRIES, W. T., *J. Electroanal. Chem.*, 18(1968) 469.
- 17 LAITY, R. W. and McINTYRE, J. D. E., *J. Am. Chem. Soc.*, 87(1965) 3806.
- 18 FISHER, M., Honours Thesis, University of Adelaide (1976).
- 19 CURRIE, N. W., Honours Thesis, University of Adelaide (1978).
- 20 WEISSBERGER, A. (Ed.), *Techniques of Chemistry*, Vol. 1 IIA (1971).
- 21 BARD, A. J., *Anal. Chem.*, 33(1961) 11.
- 22 FICK, A., *Pogg. Ann.*, 94(1855) 59.
- 23 BARD, A. J., *Anal. Chem.*, 35(1963) 340.
- 24 BRUCKENSTEIN, S. and ROUSE, T. O., *Anal. Chem.*, 36(1964) 2039.
- 25 REILLEY, C. N., EVERETT, G. W. and JOHNS, R. H., *Anal. Chem.*, 27(1955) 483.

- 26 SAWYER, D. T. and ROBERTS, J. L. Jr., *Experimental Electrochemistry for Chemists*. John Wiley and Sons, 1974. p.50.
- 27 IKEUCHI, H., SHIWA, Y., TSUJIMOTO, H., KAKIHANA, M., TAKEAWA, S. and SATO, G. P., *J. Electroanal. Chem.*, 111(1980) 287.
- 28 KOZMINSKA, D., BORKOWSKA, Z. and BEHR, B., *Can. J. Chem.*, 59(1981) 2043.
- 29 BORKOWSKA, Z., DENOBRIGA, R. M. and FAWCETT, W. R., *J. Electroanal. Chem.*, 124(1981) 263.
- 30 See Appendix 3 of reference 19.
- 31 HALE, J. M. and PARSONS, R., *Adv. Polarogr.*, 3(1960) 829.
- 32 KOLTHOFF, I. M. and LINGANE, J. J., *Polarography*, Vol. 1., Interscience, New York, 1952. p.192.
- 33 NIGHTINGALE, E. R., *J. Phys. Chem.*, 63(1959) 742.
- 34 ISONO, T., *J. Chem. Eng. Data*, 29(1984) 45.
- 35 CAMPBELL, A. N. and FRIESEN, R. J., *Can. J. Chem.*, 37(1959) 1288.
- 36 JANZ, G. J., OLIVER, B. G., LAKSHMINARAYANAN, G. R. and MAYER, G. E., *J. Phys. Chem.*, 74(1970) 1285.
- 37 KARTZMARK, E. M., *Can. J. Chem.*, 50(1972) 2845.
- 38 BOCKRIS, J. O'M. and REDDY, A. K. N., *Modern Electrochem.*, 1(1970) 380.
- 39 HORWATH, C. C., Honours Thesis, University of Adelaide (1982).

## CHAPTER 3

### CYCLIC VOLTAMMETRIC STUDY OF THE SOLID ELECTRODE/ ELECTROLYTE SOLUTION INTERFACE

INTRODUCTION	3.1
EXPERIMENTAL	3.4
ELECTRONIC EQUIPMENT	3.4
ELECTROCHEMICAL CELL	3.4
CHEMICALS	3.5
PRELIMINARY RESULTS	3.6
RESULTS AND DISCUSSION	3.8
CONCLUSION	3.15
REFERENCES	3.17

## INTRODUCTION

Cyclic voltammetry is the method of applying a triangular voltage ramp to an electrochemical system over a potential range, with reversal of the direction of the voltage ramp at the potential extremes. The resultant d.c. current plotted as a function of electrode potential is called a cyclic voltammogram.

The technique of cyclic voltammetry has found useful application in the study of reaction kinetics, and chemical species identification. Cyclic voltammetry has also proved a valuable method of characterizing the state of the electrode/electrolyte solution interface. The technique can yield information concerning the purity of the electrolyte, the cleanness and structure of the electrode surface, and can permit identification of regions of adsorption/desorption phenomena and oxidation/reduction reactions.

Will and Knorr<sup>1</sup> applied this method to investigate the platinum/ $\text{H}_2\text{SO}_4$  system. They found distinct current peaks in their cyclic voltammograms, which were due to hydrogen atom adsorption/desorption, at potentials anodic to the onset of molecular hydrogen gas evolution. Since the experiments of Will and Knorr, many papers have been published showing cyclic voltammograms for polycrystalline and single crystal platinum electrodes in acid solutions.<sup>2-20</sup> The cyclic voltammograms for such systems clearly demonstrate differences related to the surface structure of the platinum electrodes.

The interpretation of hydrogen atom adsorption on platinum has been complicated by the different methods employed by research groups in preparing the electrode surfaces. Some researchers in their criti-

### 3.2

cism of cyclic voltammograms published by others claim that their methods of electrode preparation have resulted in contamination of the electrode surface, or else resulted in poorly defined crystal surfaces.<sup>3,4,8,9</sup>

However, since hydrogen atom adsorption should be reflective of the electrode surface on an atomic level, the technique has been used as a means of determining the effective area of platinum electrodes. If one hydrogen atom is adsorbed per platinum surface atom, then the amount of charge required to form a monolayer of adsorbed hydrogen atoms can be determined from crystallographic parameters. The amount of charge adsorbed due to hydrogen atom adsorption can be calculated from the cyclic voltammograms and compared with the theoretical value calculated for a single monolayer. The ratio of these charges is termed the roughness factor, as it gives an estimate of the deviation of the electrode surface from perfect smoothness. The roughness factor is a useful concept, since electrochemical measurements at electrode surfaces often require knowledge of the effective surface area.

From the chronopotentiometric study of tracer diffusion coefficients discussed in the previous chapter, it was concluded by the author that the effective surface area of a polycrystalline platinum electrode was the same as its geometric surface area. This was found to be the case even when the electrode was known to exhibit minor surface irregularities. It was expected that the hydrogen adsorption technique would be more sensitive to electrode surface irregularities, and result in roughness factors being determined that were much greater than unity. The measurement of roughness factors of variously prepared polycrystalline platinum

### 3.3

electrodes, using the hydrogen atom adsorption method, have been made and commented upon by the author. The results of the author indicate that properly prepared electrodes can yield low roughness factors, and that a roughness factor of unity could be achievable with due care.

It must be noted, however, that the estimation of the surface roughness of solid metal electrodes via the above method is limited in its application to only a few metals that display distinct hydrogen atom adsorption/desorption peaks. Other methods have to be employed to determine roughness factors for other metals. The roughness of silver polycrystalline and single crystal electrodes, for example, has been estimated using the method of Parsons and Zobel<sup>24</sup> by a number of authors.<sup>25-28</sup> Also, the method of Brummer and Makrides<sup>29</sup> has been used to estimate roughness factors for gold electrodes.<sup>30</sup>



## EXPERIMENTAL

### ELECTRONIC EQUIPMENT

A d.c. triangular voltage ramp was generated using a PAR175 Universal Programmer, and potentiostatically applied to a standard three electrode electrochemical cell using a PAR373 Potentiostat-Galvanostat. The potential range extremes and the potential scan rate were preset manually on the Universal Programmer.

The cell output current was amplified, and then displayed as a cyclic voltammogram using either a Tektronix 603 Storage Oscilloscope or a Houston Instruments Omnigraphic 2000 X-Y Recorder. Alternatively, the amplified cell output current was stored in a Data Lab DL905 Transient Recorder, and accessed through a Hewlett Packard H.P.85 computer using an original computing programme that enabled integration and graphical display of a cyclic voltammogram. The integration programme was based upon the Newton-Coates formula,<sup>31</sup> taking seven data points each time.

The combination of the Data Lab DL905 Transient Recorder and the Hewlett Packard H.P.85 computer was used to develop a cycle averaging procedure whereby a number of single cycle voltammograms could be manipulated to give a single averaged cyclic voltammogram.

### ELECTROCHEMICAL CELL

A standard three electrode system was used. The electrodes and electrolysis cells used were the same as those previously described and depicted in Figures 2-9 of Chapter 2 of this thesis.

### 3.5

Three types of platinum working electrodes were studied. These were the platinum disc electrode, the Teflon-encased platinum electrode, and the shielded platinum Cottrell cell electrode.

All solutions were de-oxygenated prior to any measurements by bubbling pure argon or hydrogen gas through the solution for about one hour.

All measurements were made at  $25.00 \pm 0.05^\circ\text{C}$ .

#### CHEMICALS

Solutions of the desired acid concentration were made up by diluting stock solutions of either B.D.H. 98% Aristar Sulphuric Acid, or Merck 70% Pro Analyti Perchloric Acid. Dilution was made using pure water, as described previously in Chapter 2 of this thesis.

## PRELIMINARY RESULTS

The generated d.c. triangular voltage ramp also contained a small 50 hz a.c. noise component associated with the mains power supply. The effect of the a.c. signal component was evident when a cyclic voltammogram was displayed on an oscilloscope, but not when recorded on an X-Y recorder, due to its response limitations.

The noise ripple was found to cause a problem at low scan rates, and in the hydrogen atom adsorption region. Modification to the power supply of the PAR175 Universal Programmer reduced the a.c. ripple to less than 1 mV RMS, which in turn reduced the a.c. response in the cyclic voltammograms. Modification of the power supply could not entirely remove the a.c. component from the generated signal, and other means had to be employed to remove it.

Figure 1 shows the record of cyclic voltammograms before and after the power supply modification. Before the modification, the a.c. ripple component swamped the voltammograms at low to moderate scan rates, as shown in Figure 1a. After the modification, the a.c. ripple effect was diminished so that accurate cyclic voltammogram traces could be measured at moderate scan rates. The records of Figure 1, excepting Figure 1a, show the post-modification results.

A cycle averaging procedure and a capacitive filtering technique were used by the author to remove the residual a.c. component. Placing a capacitor of an appropriate value across the output of either the PAR175 or PAR373 devices was found to be an effective method of filtering out the a.c. component. The averaging of a number of cycles without any capacitive filtering produced an identical result to that of a single cycle

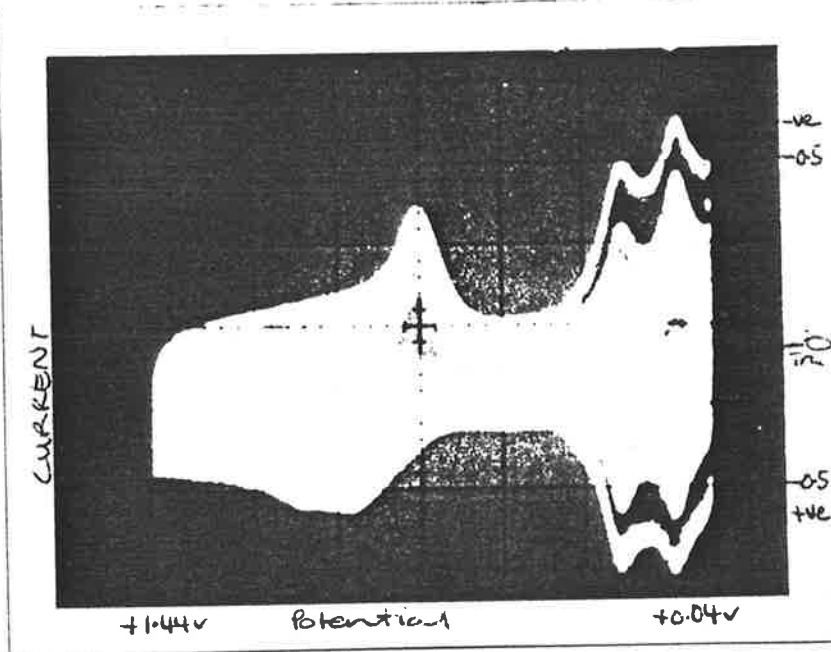


Figure 1a. Cyclic voltammogram of polycrystalline platinum in  $H_2SO_4$  recorded on a cathode ray oscilloscope (C.R.O.) showing swamping effect due to a.c. noise ripple. Scan rate = 50 mV/s

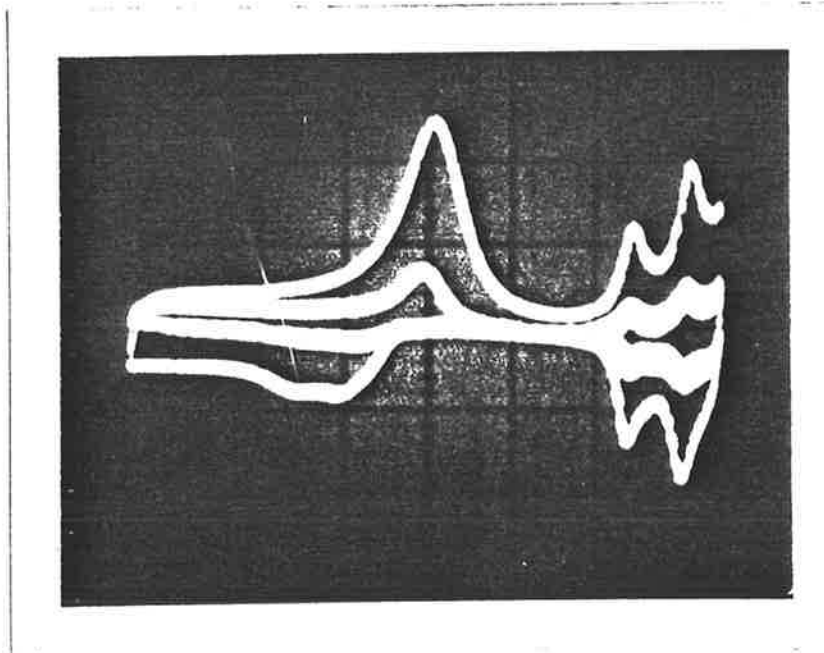


Figure 1b. Cyclic voltammograms of polycrystalline platinum in  $H_2SO_4$  recorded on a C.R.O. at scan rates of 50 mV/s (inner trace) and 500 mV/s (outer trace). Post power supply modification.

### 3.7

with capacitive filtering. These results are presented in Table 1, and discussed in the following section.

It is noteworthy that the response limitations of an X-Y recorder produce an effect similar to a filtering capacitor. Therefore, any cyclic voltammogram recorded on an X-Y recorder will not record any a.c. ripple effect unless the a.c. component is extremely large. For poorly earthed electronic equipment, the a.c. mains ripple can be sufficiently large to give rise to false peaks in hydrogen atom adsorption/desorption studies where an X-Y recorder was used to record the cyclic voltammograms. Obviously, well-earthed electronic equipment is essential in avoiding any complications.

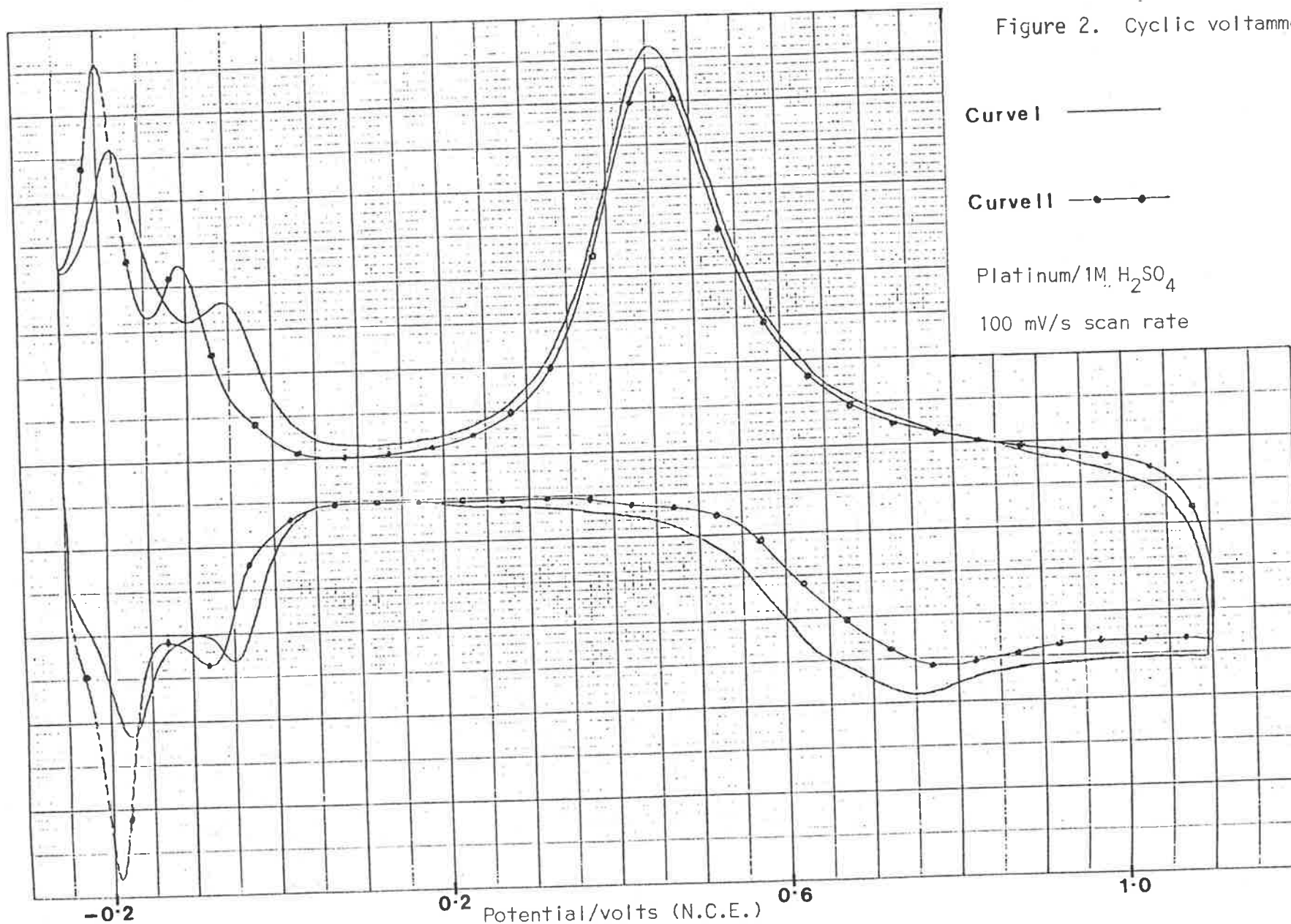
## RESULTS AND DISCUSSION

Figure 2 shows typical cyclic voltammograms for polycrystalline platinum electrodes in  $H_2SO_4$  obtained by cycling through the hydrogen adsorption and oxide formation regions. Scanning in a cathodic direction from the double layer region toward the region of hydrogen gas evolution reveals two distinct adsorption peaks due largely to hydrogen atom adsorption. The total cathodic charge measured in this region is the sum of the charges associated with the adsorption of hydrogen atoms, double layer charging, and faradaic reaction during the evolution of molecular hydrogen.

The use of cyclic voltammetry in  $H_2SO_4$  to determine platinum surface areas is a well-established technique. However, it is fraught with assumptions, and relies upon the ability to isolate the charge passed in adsorbing a monolayer of hydrogen atoms from charges due to other processes that occur simultaneously. The commonly accepted assumptions are that each surface metal atom can adsorb one hydrogen atom, and that double layer charging is constant over the potential range of interest. The controversy arises in the attempts of various researchers to separate the charge associated with hydrogen atom adsorption from that associated with faradaic reaction.<sup>19-23</sup> In a recent paper, Barna, Frank and Teherani<sup>21</sup> described a scan rate dependent cyclic voltammetric technique to separate the charge due to hydrogen atom adsorption from the scan rate dependent charge associated with faradaic reaction. The disadvantage of using such a technique is that the length of time required for measurements is a prohibitive 8-16 hours.

The total charge measured, corrected for the amount due to faradaic reaction and double layer charging, is divided by the charge per

Figure 2. Cyclic voltammetry



unit area expected from crystallographic considerations to give a measure of the effective surface area. For polycrystalline platinum the accepted theoretical value is  $210 \mu\text{C}/\text{cm}^2$ , even though this is recognized as a somewhat arbitrary choice.<sup>19</sup> The effective electrode area divided by its known geometric area is termed the roughness factor.

The technique used by the author involved scanning in a cathodic direction from a potential in the double layer region to the potential of the current minimum after the most cathodic adsorption peak. The total charge adsorbed in this region was determined by square counting or integration based upon the Newton-Coates formula, depending on whether an X-Y recorder or a data logging system was used, respectively. Correction for the double layer charging component was made in the usual way, by subtracting the current between the zero charge axis and the baseline defined by the current in the double layer region.<sup>16</sup>

Table 1 shows roughness factors determined by the author for a variety of polycrystalline platinum electrodes, with correction for double layer charging where that was considered significant.

Figure 2 compares cyclic voltammograms obtained in  $1 \text{ M H}_2\text{SO}_4$  under similar conditions using polycrystalline platinum electrodes. Curve I was obtained using a Teflon-encased platinum electrode, while curve II was obtained using a platinum disc electrode. Curve II was shifted 20 mV more cathodic to normalise the positions of the extreme cathodic minimum in both curves I and II. This resulted in superposition of the oxide reduction peak, but clearly revealed distinct differences in the hydrogen atom adsorption and desorption phenomena on the different electrode surfaces.



**Table 1**

Roughness factors determined in acid solutions  
for a number of polycrystalline platinum electrodes

Electrode	Acid Solution	Roughness Factor
Platinum disc <sup>a</sup>	0.92M H <sub>2</sub> SO <sub>4</sub>	1.09
Teflon-encased platinum <sup>b</sup>	0.92M H <sub>2</sub> SO <sub>4</sub>	6.1
	0.8m H <sub>2</sub> SO <sub>4</sub>	6.1
	1.29m HClO <sub>4</sub>	6.5
Teflon-encased platinum <sup>c</sup>	0.99m H <sub>2</sub> SO <sub>4</sub>	1.35
	0.99m H <sub>2</sub> SO <sub>4</sub>	1.39
	0.99m H <sub>2</sub> SO <sub>4</sub>	1.48
	0.99m H <sub>2</sub> SO <sub>4</sub>	1.47
Platinum Cottrell Cell <sup>d</sup>	1.04m H <sub>2</sub> SO <sub>4</sub>	1.77 (lowest cycle)
	1.04m H <sub>2</sub> SO <sub>4</sub>	1.90
	1.04m H <sub>2</sub> SO <sub>4</sub>	2.05 (highest cycle)

<sup>a</sup>Platinum disc prepared by flame cleaning procedure.

<sup>b</sup>Electrode not mechanically polished or etched, but cleaned in acid solution.

<sup>c</sup>Electrode mechanically polished, etched, and cleaned in acid solution.

<sup>d</sup>Electrode mechanically polished, etched, and cleaned in acid solution. Roughness factors given in order of increasing number of potential cycles.

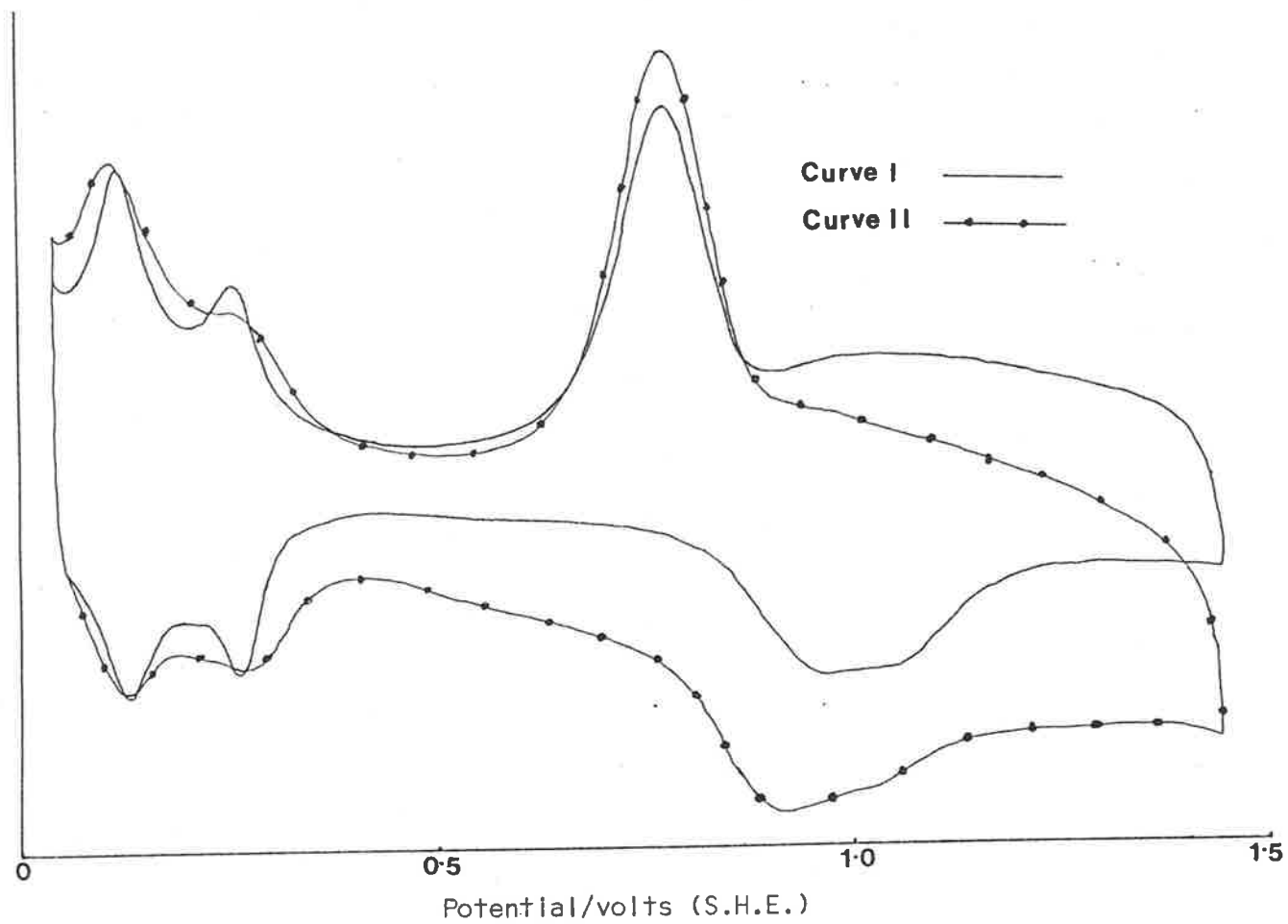


Figure 3. Cyclic voltammograms of polycrystalline platinum in acid solution:  $\text{H}_2\text{SO}_4$  (Curve I);  $\text{HClO}_4$  (Curve II).  
50 mV/s scan rate.

The different hydrogen atom adsorption/desorption structure in the cyclic voltammograms is reflective of differences in the surface structure of the platinum atoms. The relative proportion of the charge under the two hydrogen atom adsorption peaks in Figure 2 is different for the two different electrodes. The most cathodic adsorption peak is more dominant in the case of the platinum disc electrode than for the Teflon-encased platinum electrode. From platinum single crystal studies by Hubbard,<sup>32</sup> this may imply that there are relatively more crystals with (111) orientation in the surface of the polycrystalline platinum disc than in the surface of the other electrode.

A comparison of cyclic voltammograms is made in Figure 3 that shows differences related to anionic species present in the solution. The cyclic voltammograms were obtained for the same Teflon-encased platinum electrode in  $\text{H}_2\text{SO}_4$  and  $\text{HClO}_4$  under similar conditions. The anionic species certainly must influence the adsorption of hydrogen atoms on to platinum surfaces. The influence of anionic species on hydrogen atom adsorption has been studied and discussed previously.<sup>6,8,10-12</sup> The electrode roughness factor was calculated to be 6.1 and 6.5 in the  $\text{H}_2\text{SO}_4$  and  $\text{HClO}_4$  solutions, respectively. The average roughness factor is  $6.3 \pm 3\%$ .

At the centre of much controversy in hydrogen atom adsorption studies using cyclic voltammetry has been the use of potential cycling. It is widely recognized that cycling an electrode through the oxide formation and hydrogen adsorption regions can remove impurities adsorbed on to the electrode. Such cycling, however, can also result in a roughening of the surface<sup>33</sup> and surface restructuring.<sup>34</sup> The first potential cycle and any change in the cyclic voltammogram structure with successive cycles will reflect the true nature of the prepared

### 3.11

electrode surface. For a clean electrode surface, the shape of the first cyclic voltammogram should not alter with successive cycles, so long as surface restructuring was minimized.

A number of intricate systems were developed to minimize contamination of the electrode surfaces during their transfer from the place of cleaning into the electrochemical cell.<sup>3,4,14,15</sup> Using such methods made the practice of prolonged potential cycling to clean the electrode redundant. A simpler method, due to Clavilier and Chauvineau,<sup>35</sup> recognized the importance of protecting the electrode surface from contact with the atmosphere during the transfer stage. They achieved this by covering the electrode surface with a droplet of pure water.

The author tested the method of Clavilier and Chauvineau using cyclic voltammetry to investigate hydrogen atom adsorption on to polycrystalline platinum electrodes. It was found that, for an electrode that had been exposed to the atmosphere after the final cleaning, the first cyclic voltammogram showed very poorly defined hydrogen atom adsorption peaks. Upon successive potential cycles, the hydrogen atom adsorption peaks became more distinct. However, for an electrode that had been transferred to the cell with its surface covered by a droplet of pure water, the first potential cycle showed clearly defined hydrogen atom adsorption peaks, which did not alter significantly with successive potential cycles.

Obviously, adsorption of atmospheric contaminants will be a hindrance in electrode surface studies, so the author has adopted the procedure of transferring cleaned working electrodes into electrochemical cells with the electrode surface protected by a droplet of

pure water or the electrolyte solution of interest. It is also obvious that the first cyclic voltammogram will provide information concerning the cleanliness of the electrode surface.

Breiter<sup>36</sup> recognized that flame cleaning could be used to prepare platinum electrodes with low levels of surface contaminants. Clavilier et al<sup>16</sup> used low energy electron diffraction and auger electron spectroscopy to show that their flame treatment method produced Pt(100) surfaces that were clean, and properly defined with a 1x1 structure. In contrast, however, Grant and Haas<sup>37</sup> found that the Pt(100) surface could not be cleaned by high temperature cleaning alone, as low energy electron diffraction patterns showed a ring-like structure due to carbon contamination of the surface.

The only flame-cleaned working electrode used in these studies by the author was the platinum disc electrode. From Table 1 it can be seen that such an electrode was found to have a roughness factor of 1.09. This is lower than that for any other electrode represented in Table 1. From the scanning electron microscope photographs recorded in Figure 4, it is apparent that the platinum disc electrode shows many surface flaws, especially when it is compared with a mirror-finished, polished, platinum stub.<sup>40</sup> It is quite possible, then, that the platinum disc electrode was contaminated by carbon material during the flame cleaning process, effectively reducing the available platinum surface area by acting as a blocking agent. This would account for the apparently low surface roughness factor. If the disc electrode were contaminated by carbon material, the material would most probably be present as islands on the surface rather than as a sheet, because the author was able to obtain first sweep cycles which showed distinct hydrogen atom adsorption peaks which did not alter markedly with successive potential cycles.

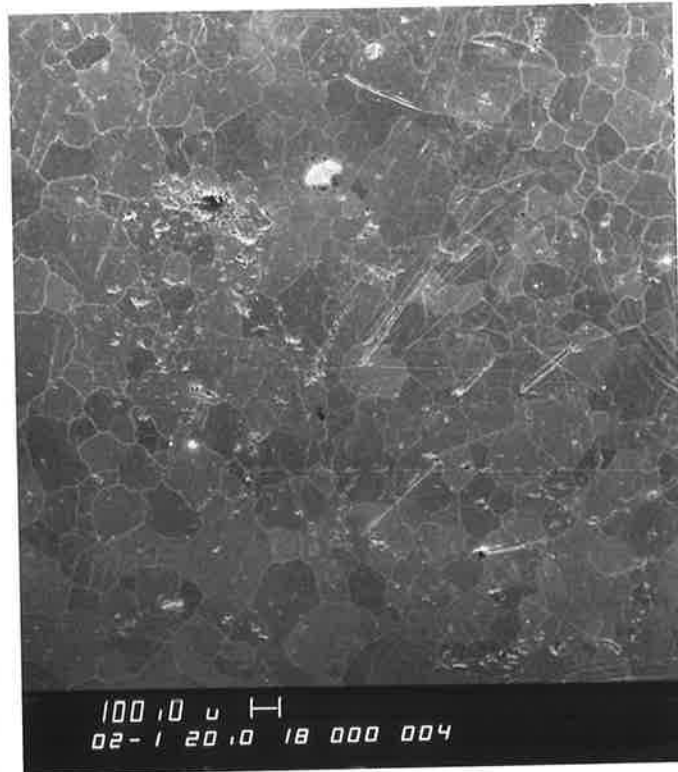


Figure 4a. S.E.M. micrograph of platinum disc surface showing polycrystalline nature.

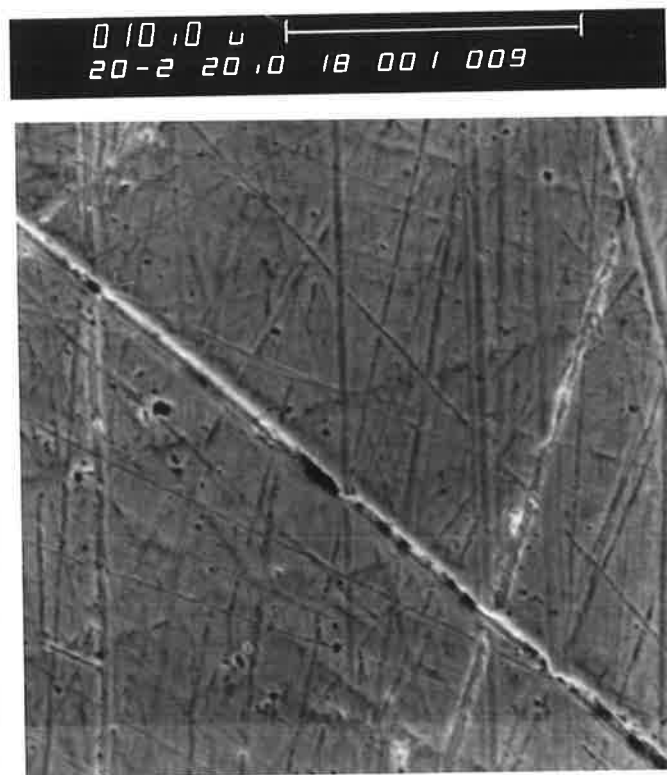


Figure 4b. S.E.M. micrograph of mechanically polished platinum surface showing scratches  $< 1 \mu\text{m}$  in width. See Appendix 2 for discussion.

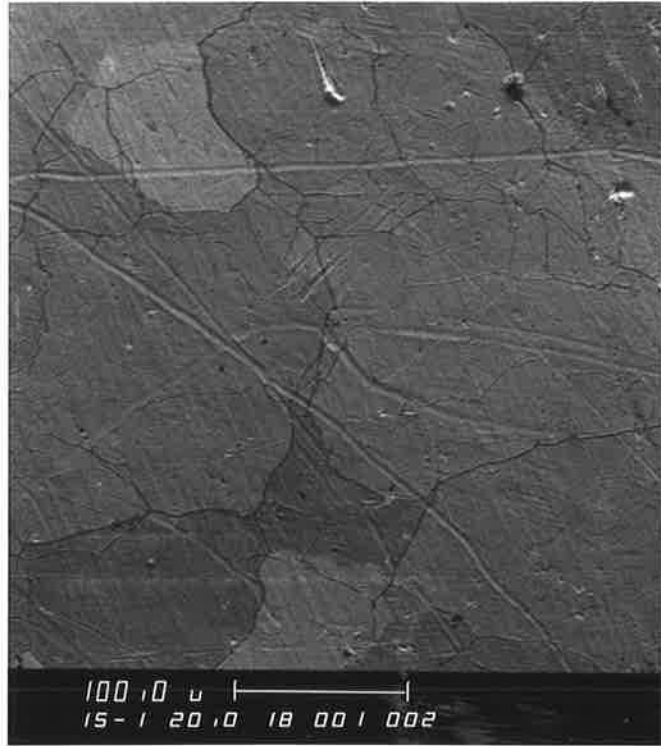


Figure 4c. S.E.M. micrograph of platinum disc surface using normal secondary electron image.

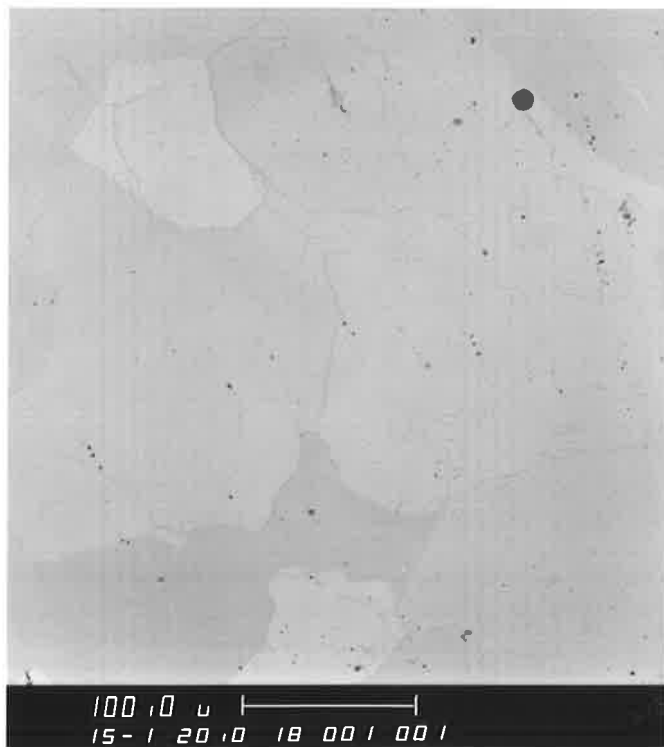


Figure 4d. S.E.M. micrograph of platinum disc showing same area as Figure 4c, but using back scattered electron image.

The other electrodes represented in Table 1 were prepared by mechanical polishing techniques. It is well known that a disturbed layer exists at the surface of mechanically polished metals. The packing and position of the surface metal atoms are not the same as they are at equilibrium or in the bulk metal.<sup>38</sup> This disturbed layer, however, can be removed by chemical etching or electrochemical cleaning methods.

Many researchers have used conventional mechanical polishing and acid etching techniques to produce smooth, regular electrode surfaces. The dangers of using chemical and electrochemical etching techniques have recently been pointed out by Caracciolo and Schmidt.<sup>39</sup> They found that etching modified the crystallographic nature of the electrode surface, and suggested that standard cleaning procedures for platinum surfaces would be highly effective in forming facets of another crystallographic orientation.

As a result, the author decided upon a short, 30 second hot aqua regia etch after mechanical polishing of platinum electrodes, to remove the disturbed surface layer but prevent excessive surface crystallographic modification.

Figures 5 and 6 show cyclic voltammograms from which roughness factors were determined. Figures 5 and 6 are reproductions of the printer output from the Hewlett Packard H.P.85 computer. To ensure that reproducible conditions were maintained, the potential of the Teflon-encased platinum working electrode was cycled over the range +1.307 V to -0.178 V (versus S.C.E.) in between measurements. A single cycle over the range +0.307 V to -0.178 V (versus S.C.E.)



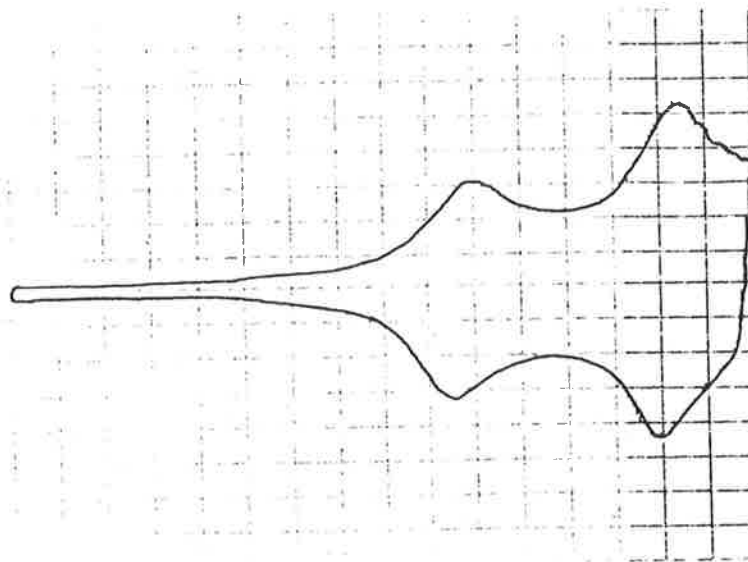


Figure 5, Curve I. Cyclic voltammogram of hydrogen atom adsorption on platinum using capacitive filtering. Reduction current upward.

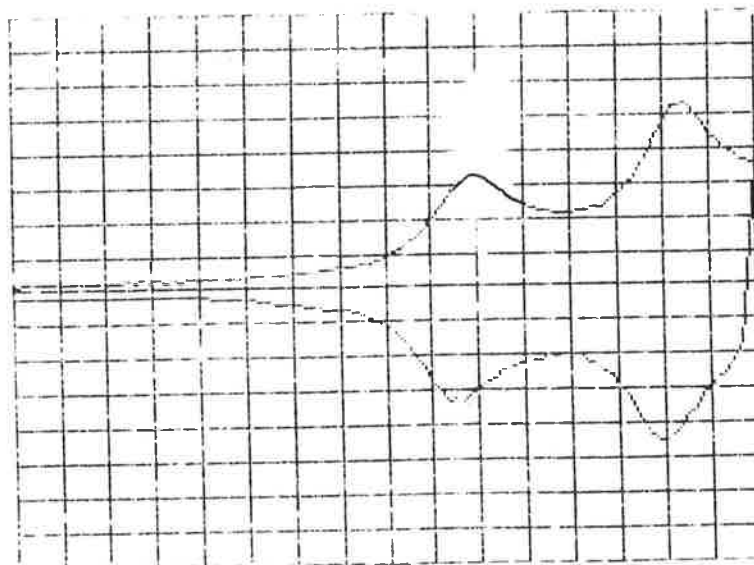


Figure 5, Curve II. Cyclic voltammogram of hydrogen atom adsorption on platinum using cycle averaging procedure.

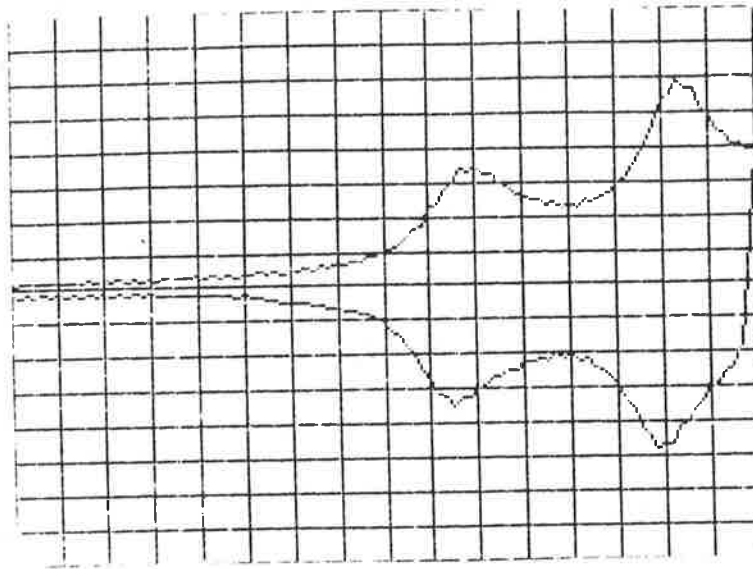


Figure 6, Curve I. Cyclic voltammogram of hydrogen atom adsorption on platinum using capacitive filtering. Reduction current upward.

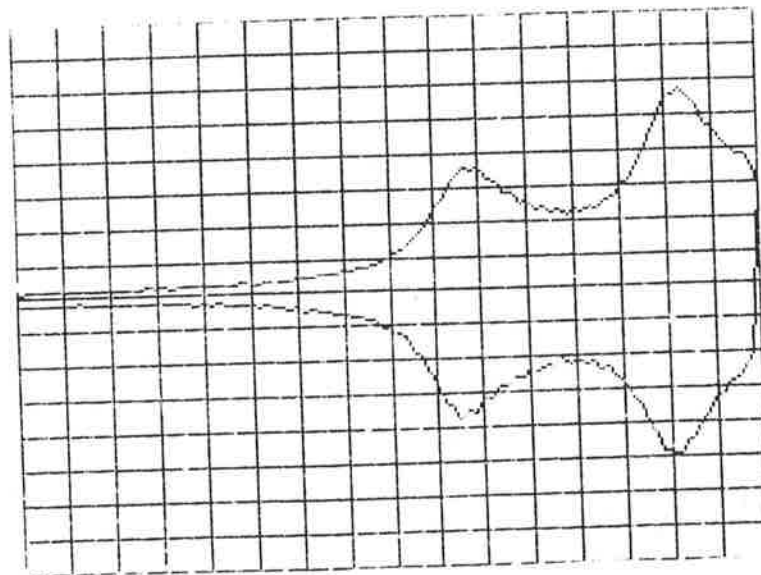


Figure 6, Curve II. Cyclic voltammogram of hydrogen atom adsorption on platinum using cycle averaging procedure.

was recorded between the extended range cycles. Curve I in each case was a single cycle using a capacitive filter. Curve II was obtained by averaging seven individual cycles without any capacitive filtering.

The roughness factor determined from Figure 5 was 1.35 and 1.39, and 1.48 and 1.47 from Figure 6, for curves I and II, respectively. From these results it can be seen that the capacitive filtering technique and the cycle averaging procedure both produced identical results, allowing for an expected experimental error of a few percent. The difference in the average roughness factors, of 1.37 from Figure 5 and 1.48 from Figure 6, shows that the electrode became rougher between the two sets of measurements. This was due to a prolonged period of cycling over the extended potential range in between the sets of measurements.

The roughness factors of 1.37 and 1.48 were determined for a Teflon-encased platinum electrode. The electrode had been mechanically polished to a mirror finish using diamond and alumina polishing pastes, and then etched with aqua regia. For a similar platinum electrode that had not been polished or etched, the roughness factor was determined to be 6.1 on two separate occasions. The great difference in the roughness factors determined for unpolished and polished electrodes shows the effectiveness of the polishing technique in producing smooth surfaces.

Table 1 also shows the roughness factor determined for a platinum Cottrell cell electrode as a function of increasing number of cycles through the oxide formation region. The roughening of the electrode surface is evident with increasing number of cycles.

## CONCLUSION

Cyclic voltammetry is a powerful electrochemical tool for investigating the solid metal electrode/electrolyte solution interface. The first cycle and successive cycles can yield information regarding the cleanliness and structure of electrode surfaces.

The author tested the electrode transfer method of Clavilier and Chavineau,<sup>35</sup> and found the method to be successful in maintaining a clean electrode surface. The method was adopted by the author as a standard procedure for electrochemical studies using solid metal working electrodes.

The investigation of hydrogen atom adsorption from acid solutions using platinum electrodes is well established. From such studies, the effective roughness of the surface can be determined. The author used this technique to measure roughness factors for a number of polycrystalline electrodes. The roughness factors measured varied from 1.09 up to 6.5, showing a marked dependence upon the cleaning and polishing techniques used.

The determination of roughness factors using cyclic voltammetry is not free from assumptions or controversy. A more thorough attempt to eliminate charge associated with faradaic reaction would most likely result in a lowering of the roughness factors presented in Table 1. The author, however, used a consistent technique to determine roughness factors, so that the values recorded are of value, at least, in a comparative sense.

In the preceding chapter of this thesis it was concluded that the technique of chronopotentiometry was insensitive to minor electrode surface defects. The use of cyclic voltammetry to study hydrogen atom adsorption on solid metal electrode surfaces has been shown to be more sensitive to surface defects than chronopotentiometry, as was expected. This was supported by the measurement of roughness factors greater than unity.

The lowness of the measured roughness factors of prepared platinum electrodes suggests that a roughness factor of unity is attainable with due care. This is the belief also of a number of researchers.<sup>3-6,16</sup>

## REFERENCES

- 1 WILL, F. and KNORR, C. A., *Z. Elektrochem.*, 64(1960) 258.
- 2 WILL, F. G., *J. Electrochem. Soc.*, 112(1965) 451.
- 3 HUBBARD, A. T., ISHIKAWA, R. M. and KATEKARU, J., *J. Electroanal. Chem.*, 86(1978) 271.
- 4 YAMAMOTO, K., KOLB, D. M., KOTZ, R. and LEHMPFUHL, G., *J. Electroanal. Chem.*, 96(1979) 233.
- 5 CLAVILIER, J., FAURE, R., GUINET, G. and DURAND, R., *J. Electroanal. Chem.*, 107(1980) 205.
- 6 CLAVILIER, J., *J. Electroanal. Chem.*, 107(1980) 211.
- 7 ADZIC, R. R., O'GRADY, W. E. and SRINIVASAN, S., *Surface Sci.*, 94(1980) L191.
- 8 ROSS, P. N., *Surface Sci.*, 102(1981) 463.
- 9 SCORTICHINI, C. L. and REILLEY, C. N., *J. Electroanal. Chem.*, 139(1982) 233.
- 10 SCORTICHINI, C. L. and REILLEY, C. N., *J. Electroanal. Chem.*, 139(1982) 247.
- 11 SCORTICHINI, C. L. WOODWARD, F. E. and REILLEY, C. N., *J. Electroanal. Chem.*, 139(1982) 265.
- 12 WOODWARD, F. E., SCORTICHINI, C. L. and REILLEY, C. N., *J. Electroanal. Chem.*, 151(1983) 109.
- 13 ROSS, P. N., *J. Electroanal. Chem.*, 76(1977) 139.
- 14 ROSS, P. N., *J. Electrochem. Soc.*, 126(1979) 67.
- 15 YEAGER, E., O'GRADY, W. E., WOO, M. Y. C. and HAGANS, P. L., *J. Electrochem. Soc.*, 125(1978) 348.
- 16 CLAVILIER, J., DURAND, R., GUINET, G. and FAURE, R., *J. Electroanal. Chem.*, 127(1981) 281.
- 17 HUANG, J. C., O'GRADY, W. E. and YEAGER, E., *J. Electrochem. Soc.*, 124(1977) 1732.
- 18 ANGERSTEIN-KOZLOWSKA, H. and CONWAY, B. E., *J. Electroanal. Chem.*, 95(1979) 1.
- 19 BIEGLER, T., RAND, D. A. J. and WOODS, R., *J. Electroanal. Chem.*, 29(1971) 269.
- 20 WOODS, R., *J. Electroanal. Chem.*, 49(1974) 217.

- 21 BARNA, G. G., FRANK, S. N. and TEHERANI, T. H., *J. Electrochem. Soc.*, 129(1982) 746.
- 22 GILMAN, S., *J. Phys. Chem.*, 67(1963) 78.
- 23 GILMAN, S., *J. Electroanal. Chem.*, 7(1964) 382.
- 24 PARSONS, R. and ZOBEL, F. G. R., *J. Electroanal. Chem.*, (1965) 333.
- 25 VALETTE, G. and HAMELIN, A., *J. Electroanal. Chem.*, 45(1973) 301.
- 26 VALETTE, G., *J. Electroanal. Chem.*, 122(1981) 285.
- 27 HAMELIN, A., VITANOV, T., SEVASTYANOV, E. and POPOV, A., *J. Electroanal. Chem.*, 145(1983) 225.
- 28 MILKOWSKA, M. and MINC, S., *Electrochim. Acta*, 29(1984) 257.
- 29 BRUMMER, S. B. and MAKRIDES, A. C., *J. Electrochem. Soc.*, 111(1964) 1122.
- 30 KATOH, K. and KOSEKI, M., *J. Electrochem. Soc.*, 131(1984) 303.
- 31 MARGENAU, H. and MURPHY, G. M., *The Mathematics of Physics and Chemistry*. D. Van Nostrand Company, Inc., 1943. p.456.
- 32 HUBBARD, A. T., *J. Vac. Sci. Technol.*, 17(1980) 49.
- 33 BIEGLER, T., *J. Electrochem. Soc.*, 116(1969) 1131.
- 34 WAGNER, F. T. and ROSS, P. N., *J. Electroanal. Chem.*, 150(1983) 141.
- 35 CLAVILIER, J. and CHAUVINEAU, J. P., *J. Electroanal. Chem.*, 100(1979) 461.
- 36 BREITER, M. W., *J. Electroanal. Chem.*, 8(1964) 230.
- 37 GRANT, J. T. and HAAS, T. W., *Surface Sci.*, 18(1969) 457.
- 38 HAMELIN, A., *Elektrokhimiya*, 18(1982) 1413.
- 39 CARACCILOLO, R. and SCHMIDT, L. D., *J. Electrochem. Soc.*, 130(1983) 603.
- 40 See also scanning electron micrograph examples in ARMSTRONG, R. D. and BURNHAM, R. A., *J. Electroanal. Chem.*, 72(1976) 257.

## CHAPTER 4

### METHODS OF MEASUREMENT OF THE DOUBLE LAYER CAPACITANCE OF THE SOLID ELECTRODE/ ELECTROLYTE SOLUTION INTERFACE

GENERAL INTRODUCTION	4.1
SINGLE CURRENT PULSE METHOD	4.2
INTRODUCTION	4.2
TECHNIQUE	4.3
<i>Two Point Linear Approximation Method</i>	4.3
<i>Polynomial Least Squares Curve Fit Method</i>	4.4
<i>Isaacs-Leach Log (<math>\Delta V/\Delta t</math>) Plot Method</i>	4.8
INSTRUMENTATION	4.9
SERIES RESISTANCE CONSIDERATIONS	4.10
RESULTS AND DISCUSSION	4.11
ALTERNATING CURRENT IMPEDANCE METHOD	4.14
INTRODUCTION	4.14
INSTRUMENTATION	4.19
SERIES RESISTANCE CONSIDERATIONS	4.20
RESULTS AND DISCUSSION	4.21
CONCLUSION	4.22
REFERENCES	4.23



## GENERAL INTRODUCTION

The theory of double layer capacitance is discussed in Chapter 1. The purpose of this chapter is to describe the techniques employed to measure the double layer capacitance. Various techniques, such as sine wave alternating current, and charging techniques using square wave currents or constant current pulses have been used to obtain data which is converted into capacitance and resistance elements of the double layer on the basis of simple RC analogue circuits.

The mercury/aqueous electrolyte solution interfacial capacitance has been measured by a multitude of researchers, and considerably reviewed. For this system, excellent independent agreement was found for the properties of the interface calculated from surface tension data and electrocapillary theory, and those from differential capacitance measurements.<sup>1</sup> Literature, however, is lacking whereby the different techniques of obtaining double layer capacitance for solid electrode/electrolyte solution interfaces are directly compared.

The essentially independent Single Current Pulse<sup>2</sup> and Alternating Current Impedance (A.C. Impedance)<sup>3</sup> methods have been used to measure the double layer capacitance associated with the solid electrode/electrolyte solution interface. The author seeks here to bring the two methods mentioned above into comparison from the point of view of data acquisition as applied to the solid electrode/electrolyte solution interface.

## SINGLE CURRENT PULSE METHOD

### INTRODUCTION

For a system of electrodes at equilibrium, maintained at a constant potential, the application of a single pulse of current will perturb the system, causing a resultant change in potential. If the electrodes are properly selected, such that the reference electrode is non-polarizable, then the resultant change in potential will occur across the working electrode.

If the electrode/electrolyte solution interface behaves as a simple RC circuit, as in Figure 1a, then the capacitance of the system can be calculated.

The most common way of determining capacitance using single current pulse measurements was dubbed the Two Point Linear Approximation Method. In this method it is assumed that the parallel resistance is infinite, and that the capacitance,  $C$ , is related to the applied current,  $I$ , and the rate of change of the electrode potential,  $dv/dt$ , according to the equation

$$C = I/(dv/dt) \quad [1]$$

When the effective parallel resistance is finite, the above method will yield erroneous capacitance values. The effect of a finite parallel resistance will be to reduce the potential change as a function of time. The resultant potential-time response of the electrode system will be curved, and not linear as expected from equation [1].



Figure 1a. Simple model of the electrode/electrolyte solution interface consisting of a capacitor and resistor in series.

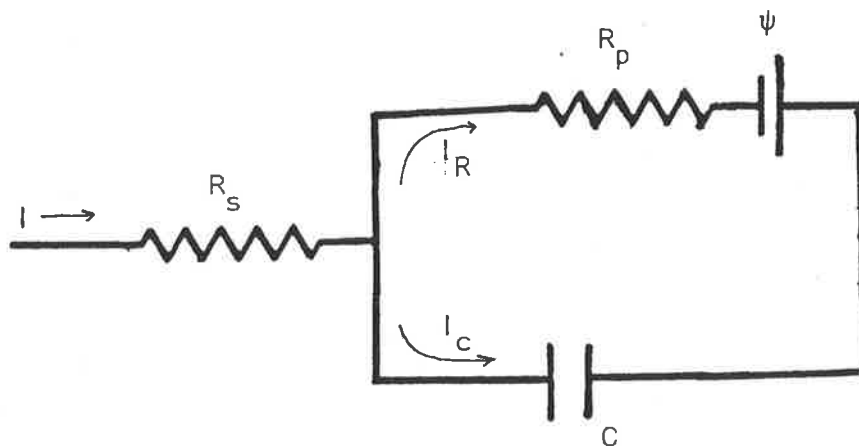


Figure 1b. Model of the electrode/electrolyte solution interface with finite parallel resistance.

### 4.3

The author adapted a polynomial least squares curve fitting routine successfully to curved potential-time responses in order to obtain true values of the parallel resistance and capacitance. This method has not been used previously by any other researcher.

An independent method of obtaining parallel resistance and capacitance values has also been used with favourable results. The method attributed to Isaacs and Leach<sup>4</sup> yields parallel resistance and capacitance values from a plot of  $\log(dv/dt)$  against time,  $t$ .

The results of the Single Current Pulse Method are presented and discussed for a number of analogue RC circuits.

#### TECHNIQUE

##### *Two Point Linear Approximation Method*

The earliest users of the Single Current Pulse Method used measurements taken from the potential-time response recorded on an oscilloscope in an attempt to determine double layer capacitance. Two suitable points were selected at the extremes of a highly linear portion of the potential-time response, and the slope between them taken to be the rate of change of the potential,  $dv/dt$ . From the knowledge of the applied current,  $I$ , the capacitance,  $C$ , was determined using the equation

$$C = I/(dv/dt) \quad [1]$$

#### 4.4

This method will yield unambiguous capacitances only when  $dv/dt$  is a constant. This will only be the case when the parallel resistance, associated with the electrode/electrolyte solution interface, is infinite.

##### *Polynomial Least Squares Curve Fit Method*

In the case where the electrode/electrolyte solution interface possesses a finite parallel resistance, it will no longer be possible to determine a true capacitance using equation [1], since  $dv/dt$  will no longer be a constant.

Let us now look at how  $C$ ,  $I$ ,  $V$  and  $t$  will be related to a finite parallel resistance as portrayed in Figure 1b.

At  $t=0^-$ , before the current pulse is fired, if the system is equilibrated, then  $I_C=0$ , and the capacitor will be charged to a potential  $\psi$ .

At  $t=0^+$ , at the triggering of the current pulse, all the current must flow instantaneously through the capacitor to establish a potential difference across the capacitor to enable current to flow through the circuit.

From Figure 1b it must be true that

$$V_C = \psi + V_{R_p} \quad [2]$$

$$\text{and } I = I_R + I_C = \text{constant} \quad [3]$$

4.5

Differentiating with respect to time we get

$$\begin{aligned}\frac{\delta V_C}{\delta t} &= \frac{\delta \psi}{\delta t} + \frac{\delta V_{R_P}}{\delta t} \\ &= \frac{\delta V_{R_P}}{\delta t} \quad (\text{since } \psi = \text{constant})\end{aligned}\quad [4]$$

$$\begin{aligned}\text{and } \frac{\delta I}{\delta t} &= 0 = \frac{\delta I_R}{\delta t} + \frac{\delta I_C}{\delta t} \\ \Rightarrow \frac{\delta I_R}{\delta t} &= -\frac{\delta I_C}{\delta t}\end{aligned}\quad [5]$$

It will be true, by definition, that

$$\begin{aligned}C &= I_C / \frac{\delta V_C}{\delta t} \\ \text{or } \frac{\delta V_C}{\delta t} &= I_C / C\end{aligned}\quad [6]$$

From [4]

$$\frac{\delta V_{R_P}}{\delta t} = I_C / C \quad [7]$$

Now, since

$$\begin{aligned}V_{R_P} &= R_P \times I_R \\ \Rightarrow \frac{\delta V_{R_P}}{\delta t} &= R_P \frac{\delta I_R}{\delta t}\end{aligned}$$

From [5]

$$\frac{\delta V_{R_P}}{\delta t} = -R_P \frac{\delta I_C}{\delta t} \quad [8]$$

Equating equations [7] and [8] we find

$$\begin{aligned} I_C / C &= -R_P \frac{\delta I_C}{\delta t} \\ \Rightarrow (1/I_C) \frac{\delta I_C}{\delta t} &= -\frac{1}{R_P C} \\ \text{i.e. } \frac{\delta \ln I_C}{\delta t} &= -\frac{1}{R_P C} \\ \Rightarrow \delta \ln I_C &= -\frac{1}{R_P C} \times \delta t \\ \Rightarrow \ln I_C &= -\frac{t}{R_P C} + \text{constant} \quad [9] \end{aligned}$$

At  $t = 0^-$ ,  $V_C = \psi$  and  $I_C = 0$ .

At  $t = 0^+$ ,  $I_C = I$  which upon substituting into [9]

$$\begin{aligned} \Rightarrow \text{constant} &= \ln I \\ \Rightarrow \ln I_C &= \frac{-t}{R_P C} + \ln I \\ \Rightarrow \ln \left( \frac{I_C}{I} \right) &= \frac{-t}{R_P C} \\ \Rightarrow I_C / I &= \exp \left( \frac{-t}{R_P C} \right) \quad [10] \end{aligned}$$

From [3]

$$I_C = I - I_R$$

Substituting into [10]

$$\Rightarrow \frac{I - I_R}{I} = \exp\left(\frac{-t}{R_P C}\right)$$

$$\Rightarrow 1 - \frac{I_R}{I} = \exp\left(\frac{-t}{R_P C}\right)$$

$$\Rightarrow \frac{I_R}{I} = 1 - \exp\left(\frac{-t}{R_P C}\right)$$

$$\Rightarrow I_R = I \left(1 - \exp\left(\frac{-t}{R_P C}\right)\right)$$

So 
$$V_R = IR_P \left(1 - \exp\left(\frac{-t}{R_P C}\right)\right)$$

If  $t \ll R_P C$  then

$$\begin{aligned} V_R &= IR_P \left(1 - \left(1 - \frac{t}{R_P C} + \frac{t^2}{2R_P^2 C^2} - \frac{t^3}{6R_P^3 C^3} + \dots\right)\right) \\ &= IR_P \left(\frac{t}{R_P C} - \frac{t^2}{2R_P^2 C^2} + \frac{t^3}{6R_P^3 C^3} - \dots\right) \\ &= \frac{1}{C}t - \frac{1}{2R_P C^2}t^2 + \frac{1}{6R_P^2 C^3}t^3 - \dots \end{aligned}$$

From [2]

$$V_C = \psi + V_R$$

$$\Rightarrow V_C = \psi + \frac{1}{C}t - \frac{1}{2R_P C^2}t^2 + \frac{1}{6R_P^2 C^3}t^3 - \dots \quad [11]$$



Equation [11] is of the form

$$V_c = A_0 + A_1t + A_2t^2 + A_3t^3 + \dots$$

which states that the potential drop across the double layer capacitance will be a polynomial function with respect to time,  $t$ .

The derivation of equation [11] shows the validity in using a polynomial least squares curve fitting routine to extract values of  $R_p$  and  $C$  from the recorded potential-time response of a system represented by Figure 1b.

From equation [11] it can be simply shown that equation [1] will result from the special case of  $R_p = \infty$ , as expected.

#### *Isaacs-Leach Log( $\Delta V/\Delta t$ ) Plot Method*

For an electrode/electrolyte solution interface that can be represented as a resistor and capacitor in parallel, then, for a constant current,  $I$ , the voltage drop across the circuit will be given by the equation

$$V = IR(1 - e^{-t/CR}) \quad [12]$$

Differentiation of [12] gives

$$\frac{dV}{dt} = \frac{I}{C} \times e^{-t/CR}$$

which can be expressed in the form

$$\log\left(\frac{dV}{dt}\right) = \log\left(\frac{I}{C}\right) - \frac{t}{RC} \times \frac{1}{2.303} \quad [13]$$

A plot of  $\log \left( \frac{dV}{dt} \right)$  against time,  $t$ , should give a slope of  $1/(2.303RC)$ , and an intercept at  $t=0$  of  $\log \left( \frac{I}{C} \right)$ .<sup>4</sup>

Dyer and Leach showed that the same method could be used to distinguish multiple RC networks, as long as each time constant for the RC networks differed by at least a factor of ten.<sup>5</sup>

#### INSTRUMENTATION

Figure 2 schematically depicts the instrumentation used for the single current pulse measurements. Each section is discussed below.

A single d.c. current pulse was applied between the counter electrode and the working electrode using a constant current source designed and built within the Chemistry Department Electronics Workshop<sup>6</sup> after the design of Riney, Schmid and Hackerman.<sup>2</sup> Further specifications of the device are obtainable from Reference 6. The current applied to the cell was nominally 1, 2 or 4 mA. Calibration of the current was made for each series of measurements from the measured potential drop across an accurately known resistor. The length of the current pulse could be varied from 0.1 ms to 10 ms.

The working electrode was polarized with respect to an auxiliary electrode using a battery powered variable potential source. The working electrode potential was monitored relative to the reference electrode using a high input impedance Keithley Instruments 602 Electrometer. For measurements made on pure resistor-capacitor

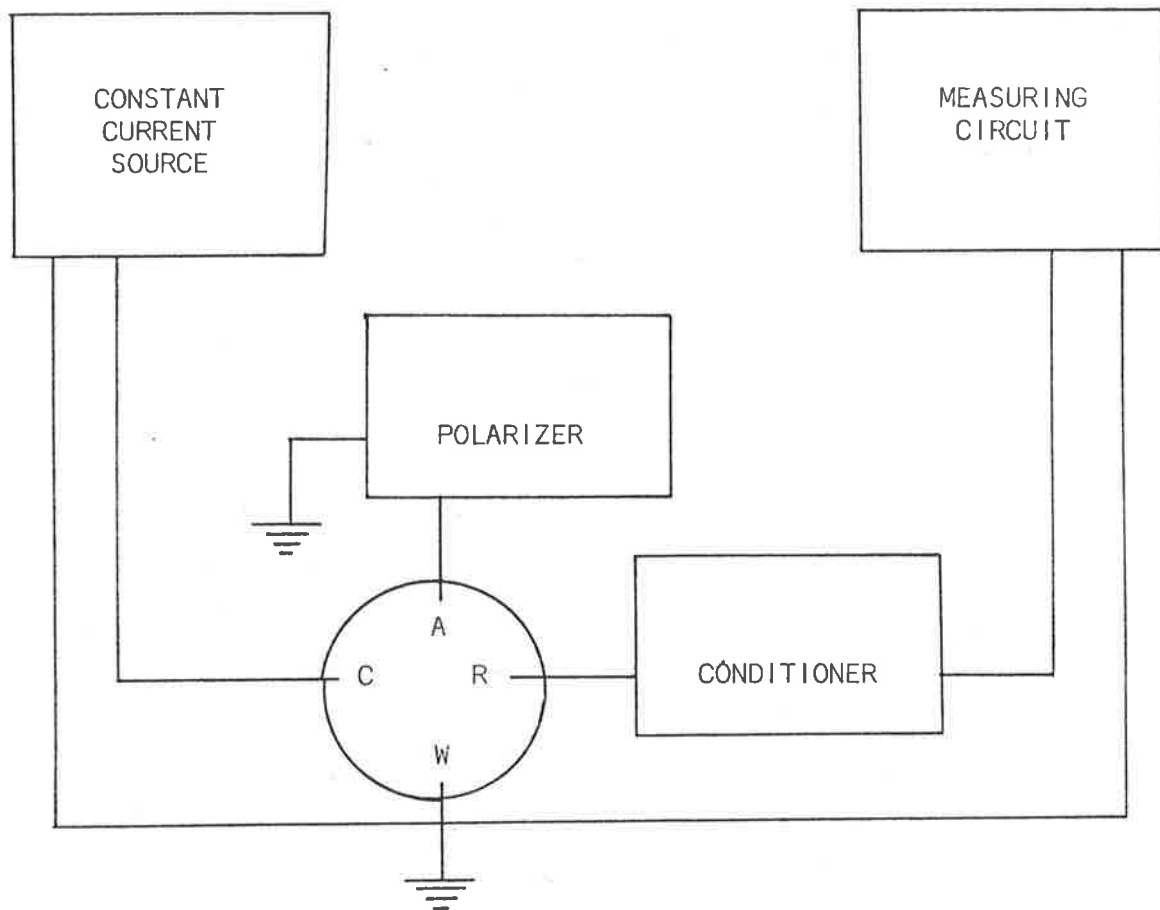


FIGURE 2. Instrumentation used for the Single Current Pulse Method using 4 electrode system: working (W); counter (C); reference (R); auxiliary (A).

#### 4.10

circuits, results were independent of the polarizing potential and, hence, the polarizer was not required in those experiments.

The potential-time response of the cell was recorded using a Data Lab DL905 Transient Recorder, and visually followed using a Tektronix 434 Storage Oscilloscope. Data stored in the Transient Recorder was accessed and manipulated via an interfaced Hewlett Packard HP85 Computer using an original computer programme. The computer programme devised enabled selectivity of data to yield capacitance and resistance values in accordance with the three techniques mentioned previously.

#### **SERIES RESISTANCE CONSIDERATIONS**

The series resistance between the working and reference electrodes will show up in the potential-time response of the cell as an initial potential jump prior to the charging of the double layer. Ideally, the magnitude of this initial jump will be given by the product of the applied current and the series resistance. This initial potential jump and the electrode potential was successfully compensated for using a d.c. polarizing source so that the potential-time response could be optimized to yield accurate values of the parallel resistance and capacitance.

It was found necessary to reduce the series resistance between the working and reference electrodes in order to reduce the value of the RC element associated with the series resistance and inherent capacitance of the connecting cable and leads. If this RC element were allowed to be sufficiently large, then it could interfere with the

#### 4.11

identification of the RC element associated with the double layer. The effect of the non double layer RC element is an initial bending of the potential-time curve.

The series solution resistance was minimized using either a luggin capillary or a close contact, low resistance electrode probe.

In the case where a luggin capillary was used, it was necessary to use a voltage follower between the high impedance reference electrode and the  $1\text{ M}\Omega$  input impedance of the Data Lab DL905 Transient Recorder before true capacitances could be determined.

#### RESULTS AND DISCUSSION

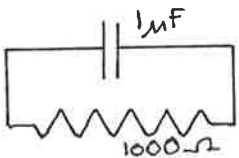
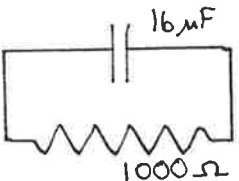
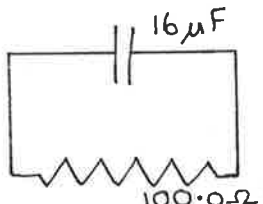
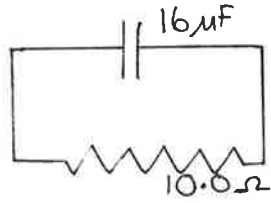
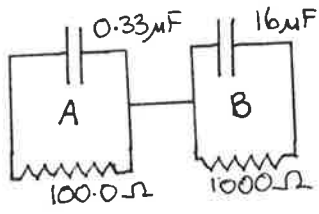
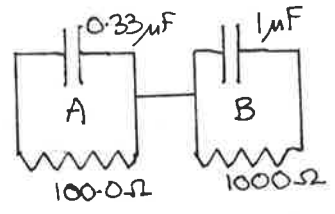
From the results presented in Table 1 it can be seen that the Single Current Pulse Method can be used to accurately determine the resistive and capacitive components in double layer analogue circuits.

The resistive and capacitive components have been measured accurately using the Isaacs-Leach  $\text{Log}(\Delta V/\Delta t)$  Plot Method, and the Polynomial Least Squares Curve Fit Method. Both methods yield very similar results. The determined parallel resistance and capacitance values correspond to those of the analogue circuits within the quoted experimental error in all but a few cases.

For the single RC component systems, circuits 1-4, only for circuit 2 is there poor agreement between the measured and expected value for the parallel resistance.

Table 1

Capacitance and resistance determined for double layer analogue circuits using the Polynomial Least Squares Curve Fit Method (Polynomial Method) and the Isaacs-Leach Log ( $\Delta V/\Delta t$ ) Plot Method (Log ( $\Delta V/\Delta t$ ) Plot Method)

Circuit Number	Analogue Circuit	Capacitance $\mu\text{F}$	Resistance $\Omega$	Method
1		$0.965 \pm .011$	$1076 \pm 110$	Polynomial
2		$16.77 \pm .12$	$679 \pm 320$	Log ( $\Delta V/\Delta t$ ) Plot
		$16.74 \pm .10$	$500 \pm 81$	Polynomial
3		$16.07 \pm .20$	$95.9 \pm 15.0$	Log ( $\Delta V/\Delta t$ ) Plot
		$16.21 \pm .10$	$108.9 \pm 5.8$	Polynomial
4		$16.98 \pm .59$	$9.47 \pm .76$	Log ( $\Delta V/\Delta t$ ) Plot
		$16.63 \pm .18$	$10.20 \pm .53$	Polynomial
5		A $0.384 \pm .010$	$94.9 \pm 3.6$	Log ( $\Delta V/\Delta t$ ) Plot
		B $16.58 \pm .85$	-	Log ( $\Delta V/\Delta t$ ) Plot
6		A $0.301 \pm .002$	$264.2 \pm 1.7$	Log ( $\Delta V/\Delta t$ ) Plot
		B $0.931 \pm .024$	$704 \pm 93$	Log ( $\Delta V/\Delta t$ ) Plot
		B $0.987 \pm .016$	$913 \pm 59$	Polynomial

#### 4.12

It must be remembered here that the magnitude of the parallel resistance determines the curvature evident in the potential-time response. The lower the value of the parallel resistance, the greater will be the curvature of the potential-time response over a fixed time domain. This effect is evident in Figure 3. The accuracy of measurement of the parallel resistance is related to how much curvature there is in a particular potential-time response. If the curvature is low, then accuracy of determining the parallel resistance will also be low. Therefore, the accuracy of determining the parallel resistance will be greater for smaller resistances when measurements are made over the same time domain. For systems with a high parallel resistance component, it is necessary, therefore, to extend the time scale of measurement so as to maintain a reasonable level of accuracy.

In Table 1, all measurements were made over a time domain of 200  $\mu\text{s}$  or 500  $\mu\text{s}$ . The agreement between the measured and expected parallel resistance is markedly improved by increasing the time domain to 5000  $\mu\text{s}$ . For a time domain of 5000  $\mu\text{s}$ , the resultant parallel resistance derived for circuit 2 was found to be  $876 \pm 153 \Omega$  using the Isaacs-Leach Method, and  $1028 \pm 53 \Omega$  using the Polynomial Least Squares Curve Fit Method. This is in good agreement with the expected value of 1000  $\Omega$ .

The value of the parallel capacitance is determined from the initial portion of the potential-time response which inherently is a region of low curvature. The accuracy of determination of capacitance using the Isaacs-Leach and Polynomial Least Squares Curve Fit

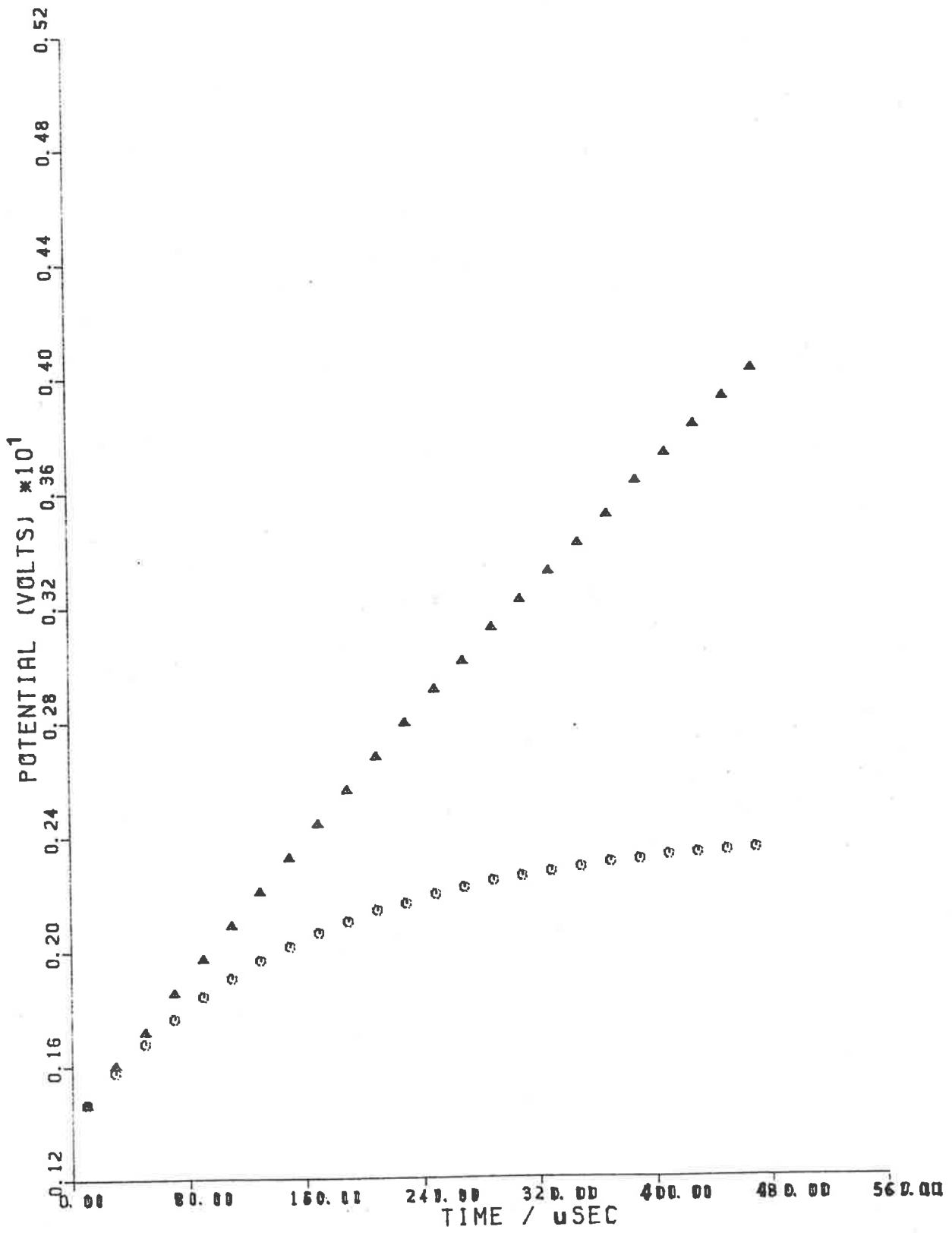


Figure 3. Effect of parallel resistance on the potential-time response of a capacitor ( $16\ \mu\text{F}$ ) in parallel with a resistor  $R_p$ :  $R_p = 10\ \Omega$  ( $\circ$ );  $R_p = 100\ \Omega$  ( $\Delta$ ).



#### 4.13

Methods is therefore reasonably independent of the curvature of the potential-time response and, hence, also of the value of the parallel resistance.

The Two Point Linear Approximation Method will obviously give accurate capacitance values only for extremely linear potential-time responses. As such, this method was not discussed here, but is discussed in Chapter 5, where it is applied to real systems.

For the dual RC component systems, circuits 5 and 6, the results show that the Isaacs-Leach Method can be used to distinguish between various RC components for  $R_B C_B \gg R_A C_A$ . Good agreement was achieved for circuit 5 where  $R_B C_B = 480 \times R_A C_A$ , but agreement was not as good for circuit 6 where  $R_B C_B = 30 \times R_A C_A$ . The Isaacs-Leach Method is a powerful means of separating real RC elements, and determining suitable time domains to determine accurate values for parallel resistances and capacitances. This is clearly seen in Figure 4.

It is evident from the results presented here that the investigator of an unknown system, with an unknown number of RC elements, needs to apply the method of Isaacs and Leach<sup>4</sup> to distinguish the number of such elements and the suitable choice of a time domain for measurements. When the number of RC elements and the desired time domains have been discerned using the Isaacs-Leach Method, then, and only then, could one expect to determine unambiguous capacitance and resistance values using a polynomial curve fitting procedure as that used in the Polynomial Least Squares Curve Fit Method.

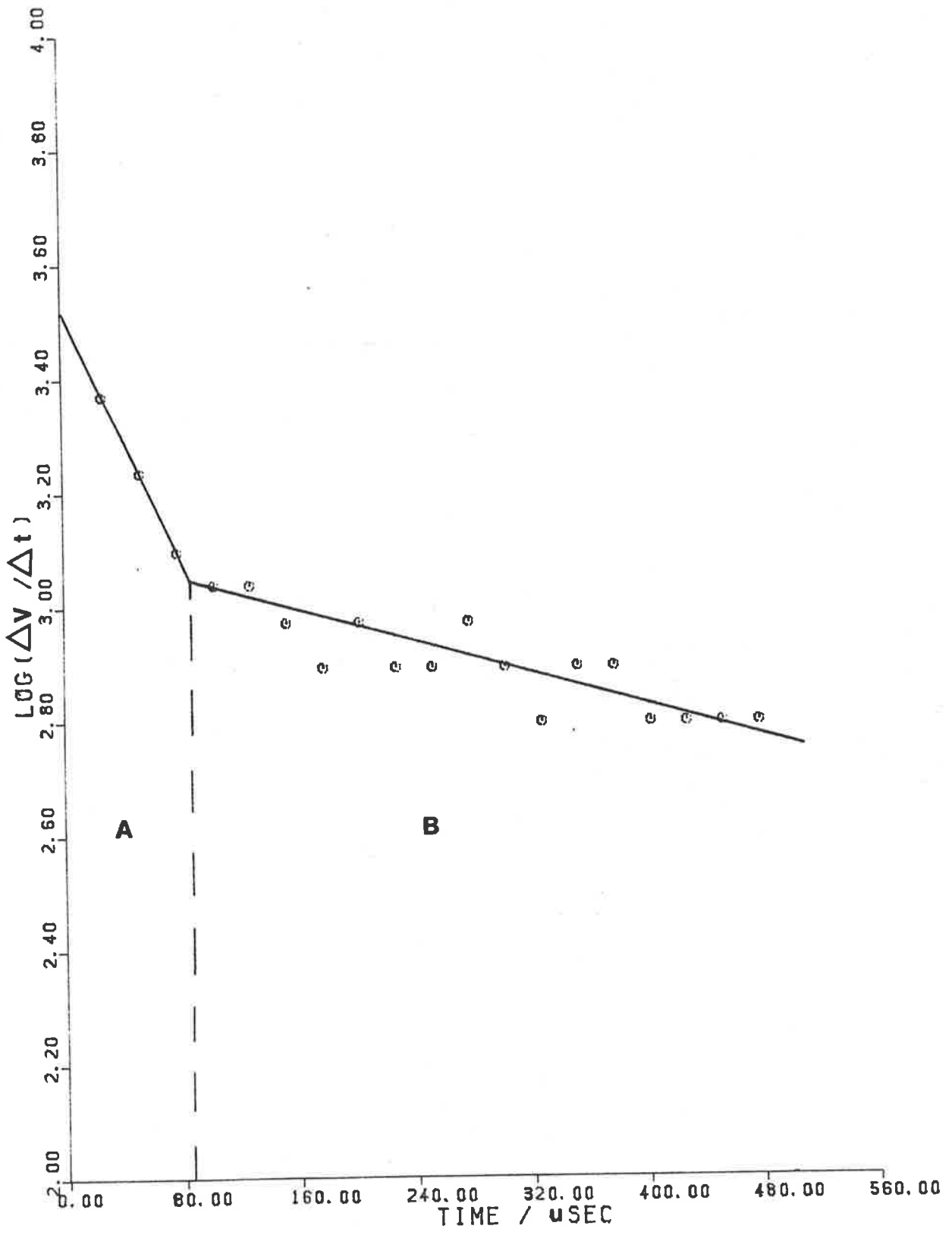


Figure 4. Separation of multiple RC elements using Isaacs-Leach Log ( $\Delta V/\Delta t$ ) Plot Method. Results presented for circuit 6 in Table 1, where  $R_B C_B = 30 \times R_A C_A$ .

## ALTERNATING CURRENT IMPEDANCE METHOD

## INTRODUCTION

Akin to the method widely used for polarography with superimposed alternating voltage on mercury electrodes, a small a.c. signal was superimposed on a triangular voltage sweep to measure the a.c. impedance of solid electrodes.

This measured impedance is generally interpreted assuming the electrode/electrolyte solution interface to be equivalent to a resistance and capacitance in series. This is equivalent to assuming an infinite resistance in parallel with the capacitance, which is the property of an ideally polarizable interface.

For a system that is equivalent to a resistance,  $R_s$ , and a capacitance,  $C_s$ , in series, the total impedance,  $Z$ , will be given by<sup>7</sup>

$$Z = R_s + \frac{1}{j\omega C_s} \quad [14]$$

Therefore

$$\begin{aligned} \frac{1}{Z} &= \frac{1}{R_s + \left(\frac{1}{j\omega C_s}\right)} \\ &= \frac{j\omega C_s}{1 + j\omega C_s R_s} \\ &= \frac{j\omega C_s + \omega^2 C_s^2 R_s}{1 + \omega^2 C_s^2 R_s^2} \end{aligned} \quad [15]$$

where  $\omega$  is the angular frequency of the applied a.c. signal.

4.15

Also

$$I = \frac{V}{Z} \quad [16]$$

$$= V \times \left( \frac{j\omega C_s + \omega^2 C_s^2 R_s^2}{1 + \omega^2 C_s^2 R_s^2} \right) \quad [17]$$

The real component of the current,  $I_0$ , will be given by

$$I_0 = \frac{V\omega^2 C_s^2 R_s^2}{1 + \omega^2 C_s^2 R_s^2} \quad [18]$$

and the imaginary component of the current,  $I_{90}$ , will be given by

$$I_{90} = \frac{\omega V C_s}{1 + \omega^2 C_s^2 R_s^2} \quad [19]$$

Therefore

$$\frac{I_0}{I_{90}} = \frac{V\omega^2 C_s^2 R_s^2}{V\omega C_s} = \omega C_s R_s \quad [20]$$

From equation [18]

$$\begin{aligned} I_0 &= \frac{V\omega^2 C_s^2 R_s^2}{1 + \omega^2 C_s^2 R_s^2} \\ &= \frac{V \left( \frac{\omega^2 C_s^2 R_s^2}{\omega^2 C_s^2 R_s^2} \right)}{\left( \frac{1 + \omega^2 C_s^2 R_s^2}{\omega^2 C_s^2 R_s^2} \right)} \end{aligned}$$

4.16

$$\begin{aligned}
 &= \frac{V}{R_s \left( \left( \frac{1}{\omega^2 C_s^2 R_s^2} \right) + 1 \right)} \\
 &= \frac{V}{R_s \left( \frac{1}{\left( \frac{I_0}{I_{90}} \right)^2} + 1 \right)} \\
 &= \frac{V}{R_s \left( 1 + \left( \frac{I_{90}}{I_0} \right)^2 \right)} \quad [21]
 \end{aligned}$$

Upon rearrangement of equation [21] we get

$$R_s = \frac{V}{I_0 \left( 1 + \left( \frac{I_{90}}{I_0} \right)^2 \right)} \quad [22]$$

From equation [19]

$$I_{90} = \frac{\omega V C_s}{1 + \omega^2 C_s^2 R_s^2}$$

Therefore

$$\begin{aligned}
 C_s &= \frac{I_{90}}{V\omega} (1 + \omega^2 C_s^2 R_s^2) \\
 &= \frac{I_{90}}{V\omega} \left( 1 + \left( \frac{I_0}{I_{90}} \right)^2 \right) \quad [23]
 \end{aligned}$$

For a system, however, that is equivalent to a resistance,  $R_p$ , and capacitance,  $C_p$ , in parallel, the total impedance,  $Z$ , will be given by<sup>7</sup>

$$Z = ((1/R_p) + j\omega C_p)^{-1} \quad [24]$$

Therefore

$$\frac{1}{Z} = \frac{1}{R_p} + j\omega C_p \quad [25]$$

Also

$$\begin{aligned} I &= \frac{V}{Z} \\ &= V \times \left( \frac{1}{R_p} + j\omega C_p \right) \end{aligned} \quad [26]$$

The real component of the current,  $I_0$ , will be given by

$$I_0 = \frac{V}{R_p} \quad [27]$$

which rearranges to give

$$R_p = \frac{V}{I_0} \quad [28]$$

The imaginary component of the current,  $I_{90}$ , will be given by

$$I_{90} = V\omega C_p \quad [29]$$

which rearranges to give

$$C_p = I_{90}/V\omega \quad [30]$$

It should be noted here that other analogue circuits are also possible. Such analogue circuits may involve combination of simple series and parallel circuits or contain a warburg impedance. The other simple system of interest to these studies is the combination of a resistance,  $R_p$ , and a capacitance,  $C_p$ , in parallel, along with a resistance in series,  $R_s$ .

The applicability of a given analogue circuit, however, can be tested by plotting the complex-plane impedance spectrum for the analogue circuit, and comparing it with the experimentally obtained complex-plane impedance spectrum. The requirements for such a spectrum are that the real and imaginary impedances are determined as a function of the frequency of the applied a.c. signal. The distinctiveness of the spectra for various analogue circuits is seen in Figure 6, and also in Figure 3 of reference 7.

**INSTRUMENTATION**

Figure 5 schematically depicts the instrumentation used to determine capacitances using the A.C. Impedance Method. Each component element is discussed below.

A small a.c. potential was taken from the internal oscillator of a PAR Model 122 Lock-In Amplifier, and added to a d.c. triangular voltage ramp taken from a PAR 174 Polarographic Analyzer. The frequency of the applied 10.15 mV RMS a.c. signal could be selected from 5 hz to 50,000 hz. The scan rate of the d.c. triangular voltage ramp could be altered from 0.1 mV/s to 500 mV/s.

The signal was applied potentiostatically to the cell via the PAR 174 Polarographic Analyzer, and the cell response monitored through a PAR Accessory 174/50 A.C. Polarographic Analyzer Interface.

The d.c. potential response of the cell was monitored using a Data Precision 3500 digital voltmeter.

The cell output current was monitored through the PAR Model 122 Lock-In Amplifier, which has phase angle selectivity. The output a.c. component of the current at selected phase angles or the d.c. component of the current were recorded as a function of potential using a Houston Instrument Omnigraphic 2000 X-Y Recorder.



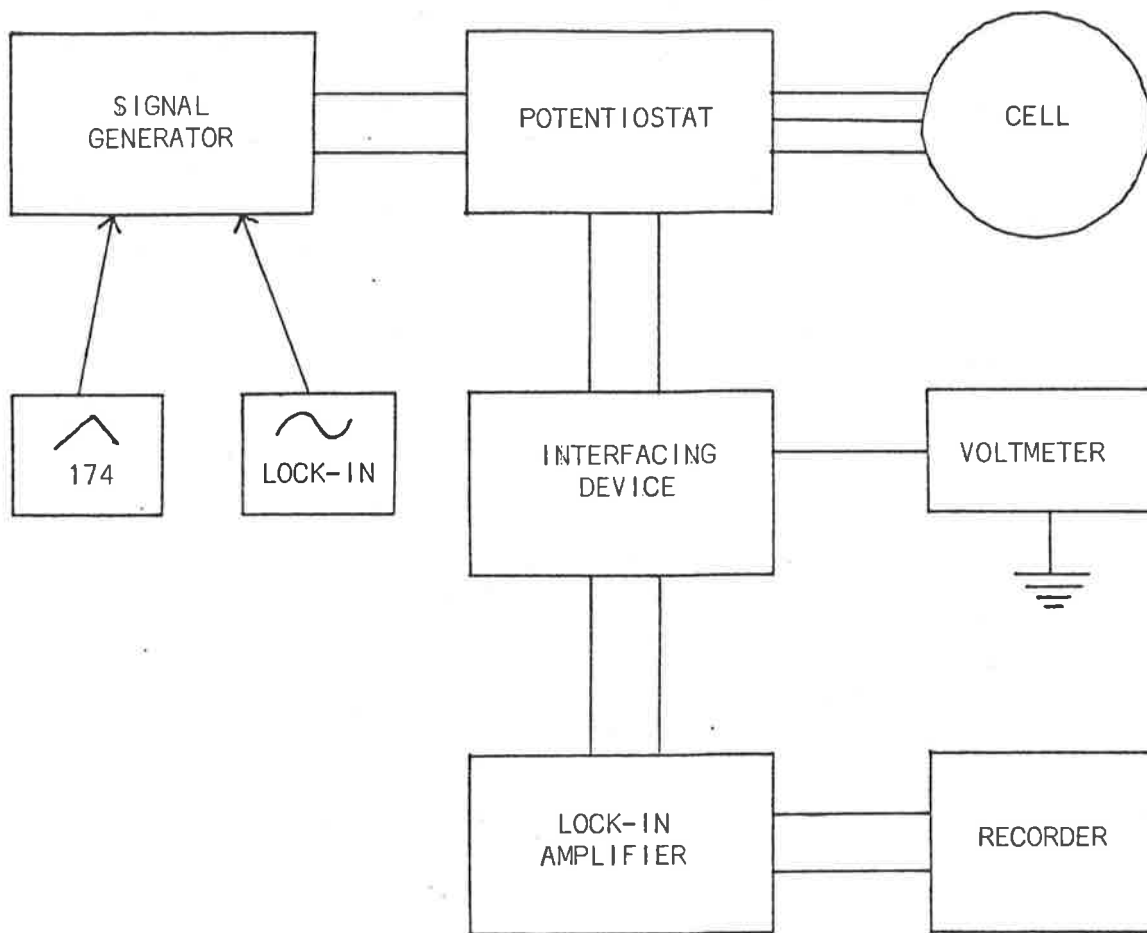


Figure 5. Instrumentation used for the A.C. Impedance Method.

**SERIES RESISTANCE CONSIDERATIONS**

It is most common to interpret the double layer as the equivalent of a resistance and capacitance in series using equations [22] and [23]. From equation [23] it is obvious that the magnitude of the correction factor,  $\left(\frac{i_0}{i_{90}}\right)^2$ , will affect the accuracy of determination of the measured capacitance. For this reason, it is desirable that the resistive component current be minimized.

The reduction of the resistive component current was effected in two ways.

Firstly, the series resistance between the working and reference electrodes was lowered. This could be achieved by using either high electrolyte concentrations or a luggin capillary to bring the reference electrode physically closer to the working electrode.

Secondly, iR positive feedback could be used to compensate for the iR drop through the solution, hence reducing the resistive component of the current. The use of such a method is commonly practised even though there appears to be some uncertainty concerning the correct procedure of applying iR compensation.<sup>8</sup>

The author used the PAR Accessory 174/50 A.C. Polarographic Analyzer Interface to apply iR compensation to the cell through the PAR 174 Polarographic Analyzer. The technique used, described elsewhere,<sup>9</sup> employed the gradual application of positive feedback until the current response began to oscillate. The feedback was then set at a point just before oscillation would occur, to give maximum iR compensation.

**RESULTS AND DISCUSSION**





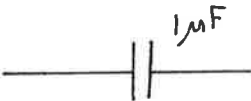
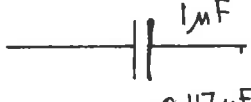
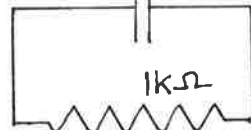
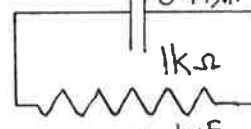
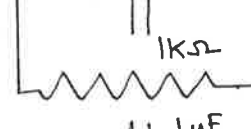
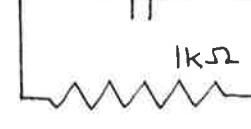
From the results presented in Table 2 it can be seen that the A.C. Impedance Method can be used to accurately determine the resistance and capacitance elements in simple double layer analogue circuits.

Figure 6 shows the distinctiveness of the complex-plane impedance spectra for the series, and parallel combination of a resistance and capacitance. It is evident that the analogue circuit for the electrode/electrolyte solution interface should be discernable from its complex-plane impedance spectrum.

It must be mentioned here that the method used to apply iR compensation presumes that 100% iR compensation is applied. This may not be the case, however, as the technique uses a somewhat arbitrary setting of the applied compensation. This fact is the basis of the uncertainty concerning the correct procedure of applying iR compensation. A device is now available that Kuo<sup>8</sup> claims is able to accurately apply 100% iR compensation. The exact amount of iR compensation applied need not concern us here, though, because the author found the measured capacitances to be independent of the extent of the applied iR compensation.

Table 2

Capacitance and resistance  
determined for simple double layer analogue circuits  
using the A.C. Impedance Method

Analogue Circuit	Frequency hz	Capacitance $\mu\text{F}$	Resistance $\Omega$
	20	-	1000
	40	-	968
	400	-	1000
	40	-	1953
	40	0.91	-
	400	0.90	-
	20	0.41	1000
	400	0.46	960
	40	0.95	968
	400	0.94	995

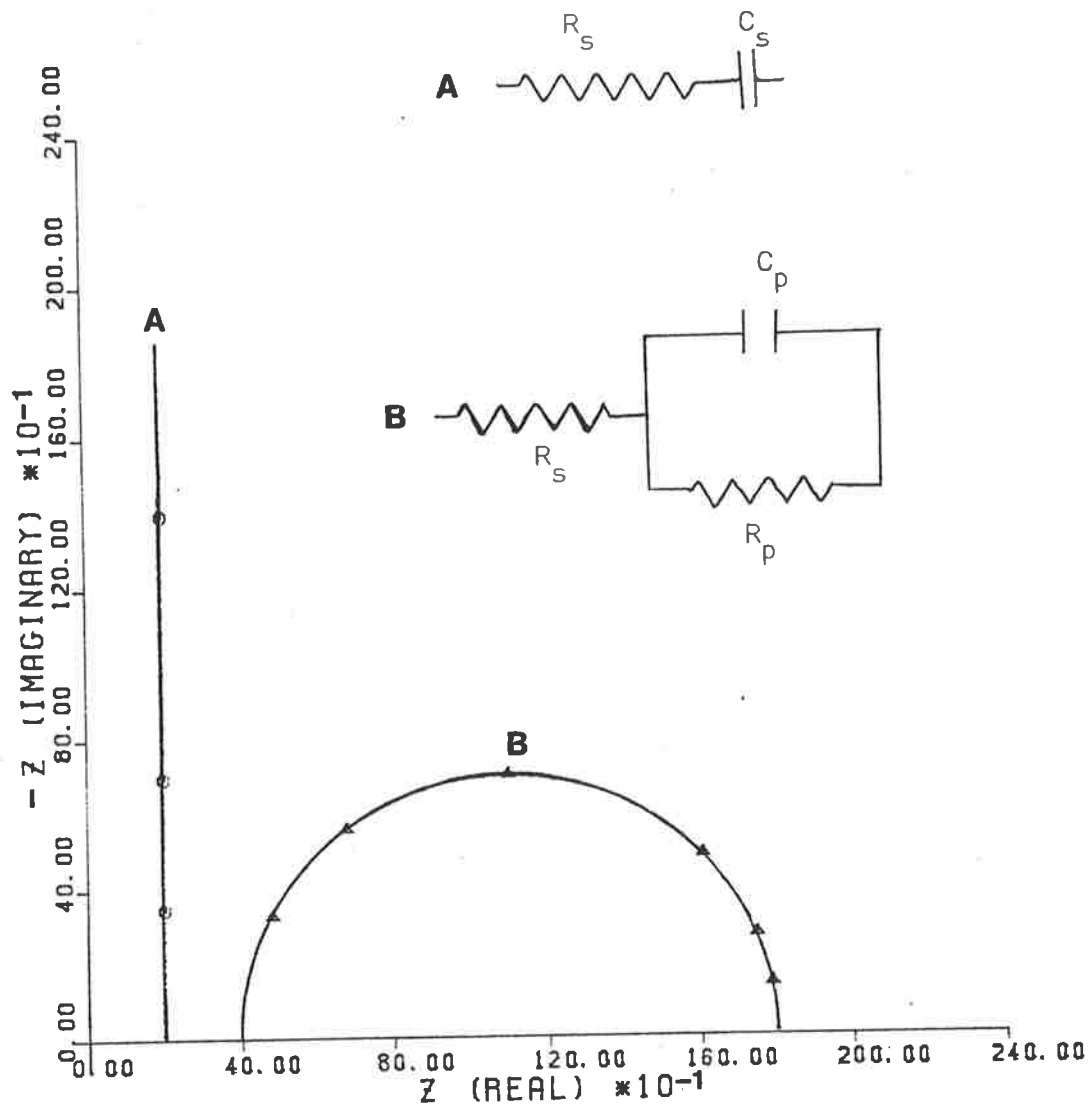


Figure 6. Complex plane impedance spectra with matching analogue circuits:

- A. capacitor and resistor in series ( $C_S = 1.14\mu\text{F}$ ;  $R_S = 200\Omega$ ).
- B. capacitor and resistor in parallel combined with series resistor ( $C_P = 1.14\mu\text{F}$ ;  $R_P = 1400\Omega$ ;  $R_S = 400\Omega$ ).

## CONCLUSION

From the results presented here, if the electrode/electrolyte solution interface for particular systems can be represented by a simple RC analogue circuit, then, use of the Single Current Pulse Method and the A.C. Impedance Method should enable determination of the appropriate analogue circuit, and yield accurate capacitance values. The two methods are quite independent in their application, but should be able to yield the same results for identical analogue circuits.

The Single Current Pulse Method will provide rapid evaluation of the appropriate analogue circuit from a single measurement using the Isaacs-Leach  $\text{Log}(\Delta V/\Delta t)$  Plot Method. Both the Isaacs-Leach  $\text{Log}(\Delta V/\Delta t)$  Plot Method and the Polynomial Least Squares Curve Fit Method should enable accurate determination of the capacitance and parallel resistance of the electrode/electrolyte solution interface.

The value of the capacitance determined using the A.C. Impedance Method, on the other hand, will be very sensitive to the equivalent analogue circuit selected. This stresses the importance of using complex-plane impedance plots to determine the appropriate equivalent analogue circuit before calculating the capacitance.

The results presented here suggest that there should be enough information obtainable from the Single Current Pulse Method and the A.C. Impedance Method to say something definite about the appropriateness of various equivalent analogue circuits for the electrode/electrolyte solution interface.

## REFERENCES

- 1 BOCKRIS, J. O'M. and REDDY, A. K. N. *Modern Electrochemistry*, 2 (1970) Chapter 7. Plenum Press, New York.
- 2 RINEY, J. S., SCHMID, G. M. and HACKERMAN, N. *Rev. Sci. Instr.*, 32 (1961) 588.
- 3 BREITER, M. W. *J. Electroanal. Chem.*, 7 (1964) 38.
- 4 ISSACS, H. S. and LEACH, J. S. L. *J. Electrochem Soc.*, 110 (1963) 680.
- 5 DYER, C. K. and LEACH, J. S. L. *Electrochim. Acta*, 19 (1974) 695.
- 6 *Electronics Workshop*. Physical and Inorganic Chemistry Department, University of Adelaide.
- 7 ARCHER, W. I. and ARMSTRONG, R. D. *Electrochemistry (Specialist Periodical Reports)*, 7 (1980) 157. H. R. Thirsk (Sen. Reporter).
- 8 KUO, Kuo-Nan. *Current Separations*, 5 (1982) 26. Bioanalytical Systems.
- 9 BARD, A. J. and FAULKNER, L. R. *Electrochemical Methods. Fundamentals and applications*, p. 571. John Wiley and Sons, 1980, New York.

## CHAPTER 5

### DOUBLE LAYER CAPACITANCE OF THE SOLID ELECTRODE/ ELECTROLYTE SOLUTION INTERFACE IN H<sub>2</sub>O AT 25°C

INTRODUCTION	5.1
EXPERIMENTAL	5.5
GENERAL	5.5
ELECTRODES	5.5
CLEANING AND PREPARATION PROCEDURES	5.6
CHEMICALS	5.8
SOLUTION DE-OXYGENATION	5.9
RESULTS AND DISCUSSION	5.10
PRELIMINARY RESULTS	5.10
System I. Pt + 1M HCl + H <sub>2</sub> O	5.11
<i>Pt + 1M HCl + H<sub>2</sub>O</i>	5.11
<i>Conclusion</i>	5.22
System II. Pt + 0.100M X + H <sub>2</sub> O	5.24
<i>Pt + 0.100M NaCl + H<sub>2</sub>O</i>	5.24
<i>Pt + 0.100M KNO<sub>3</sub> + H<sub>2</sub>O</i>	5.24
<i>Pt + 0.100M NaNO<sub>3</sub> + H<sub>2</sub>O</i>	5.26
<i>Conclusion</i>	5.31
System III. Pt + 0.001M NaNO <sub>3</sub> + H <sub>2</sub> O	5.32
<i>Pt + 0.001M NaNO<sub>3</sub> + H<sub>2</sub>O</i>	5.32
<i>Conclusion</i>	5.34
System IV. Ag + X + H <sub>2</sub> O	5.36
<i>Ag + 0.100M NaNO<sub>3</sub> + H<sub>2</sub>O</i>	5.36
<i>Ag + 0.010M NaNO<sub>3</sub> + H<sub>2</sub>O</i>	5.36
<i>Ag + 0.010M NaF + H<sub>2</sub>O</i>	5.40
<i>Conclusion</i>	5.45
CONCLUSION	5.49
REFERENCES	5.54





## INTRODUCTION

The Gouy-Chapman-Stern (GCS) model of the interface has been extensively used to interpret data obtained for the mercury/electrolyte solution interface. The apparent success of the model for the mercury electrode resulted in it also becoming the model used to describe the solid metal/electrolyte solution interface. The model has its limitations, however, and this is particularly the case when applied to the solid metal/electrolyte solution interface, as was discussed in Chapter 1 of this thesis. The simplicity of the GCS model, while making it useful in treating interfacial data, is too simple to provide reasons as to why different solid metals, and even different crystal faces of the same metal, show different behaviour.

It is a well-documented truth that crystallographic structure of the metal surface influences the double layer capacitance. This is clearly shown in a recent review by Hamelin et al.<sup>1</sup> It is true, however, that most work of a practical nature involves polycrystalline electrodes. It is necessary, therefore, to maintain an overall balance between investigations using single-crystal and polycrystalline electrodes, so that the advancement of double layer theory from accumulated data will ultimately manifest itself in the everyday world. The work presented here has been based solely on the use of polycrystalline material. It is expected, however, that further work in this laboratory will involve single-crystal electrodes.

The results from many solid metal/electrolyte solution interface studies have been presented in literature, in which different electrode surface preparations and measuring techniques have been employed. Al-

## 5.2

though this is beneficial, the different procedures can cause chaos and stagnation unless the good experimental techniques are clearly highlighted, and the poor experimental techniques are exposed.

For example, the investigation of hydrogen atom adsorption on single-crystal and polycrystalline platinum electrodes from acid solution is an area where much controversy has arisen due to different procedures used in preparing the electrode surfaces (see Chapter 3 of this thesis). Obviously, the data presented by some of the researchers has no positive value because of the poor experimental procedures used to gather the data. The same, undoubtedly, can be said for some of the double layer capacitance data accumulated over the years. It will have no positive value because it does not truly represent what it claims. The advancement of the theory of the double layer interface can only be impeded by the unwitting use of poor experimental data.

It is noteworthy that a number of different methods are currently employed to measure the capacitance of the solid electrode/electrolyte solution interface. In the preceding chapter of this thesis, the author discussed two essentially independent methods used to measure the double layer capacitance of the solid metal/electrolyte solution interface. It was noted that, if the solid metal/electrolyte solution interface corresponded to a simple analogue circuit, then the capacitance determined by the two methods should be the same. The results of those methods are presented in this chapter for aqueous electrolytes, and in Chapter 7 for electrolytes dissolved in n-methylformamide (NMF).

### 5.3

The two methods used by the author were the Single Current Pulse Method<sup>2</sup> and the A.C. Impedance Method.<sup>3</sup> Both methods provide sufficient information to test simple analogue circuits from which the double layer capacitance can be obtained.

Only the behaviour of one system investigated, the platinum + 0.001M NaNO<sub>3</sub> + H<sub>2</sub>O system, failed to conform to a simple analogue circuit. The results for the other systems studied appeared to behave in apparent conformity to simple analogue circuits. The results obtained by the Single Current Pulse Method and the A.C. Impedance Method, however, gave only moderate to poor agreement.

A further complication to interpreting double layer capacitance measurements is introduced by the roughness of solid electrodes. Borisova and Ershler<sup>4</sup> found that the frequency dependence of the double layer capacitance in A.C. Impedance measurements could be decreased by effectively smoothing the electrode surface by melting shortly before making the measurements.

A number of researchers<sup>5-8</sup> have clearly established that roughness of solid electrodes affects the double layer capacitance measurements. Ideally, the solid electrode/electrolyte solution interface is looked upon as being equivalent to a perfect capacitor in series with the solution resistance. Measurement of such an ideal system at a number of frequencies should produce a vertical line on a complex plane impedance plot. It was found, however, that surface roughness caused a deviation from the ideal behaviour, such that the impedance plane plot formed an angle to the horizontal between 90° and 45°. De Levie<sup>5</sup> claim-

#### 5.4

ed that polishing of polycrystalline platinum electrodes caused this angle to approach, but not attain, the ideal angle of  $90^\circ$  to the horizontal. When this angle is close to  $90^\circ$ , then the determined capacitance will be equal to the double layer capacitance.<sup>7</sup>

The author would like to point out here a further complication in these studies that can arise, making the effects of surface roughness and a parallel resistance component hard to distinguish. Figure 1 shows an example of the complex plane impedance spectrum obtained for the solid metal electrode/electrolyte solution interface. In Figure 1a, the data has been fitted by a straight line making an angle of  $74^\circ$  to the horizontal. In Figure 1b, the data has been fitted by an arc of a hemi-circle. The interpretation of Figure 1a might be that the interface behaves as a capacitor in series with the solution resistance, with distortions due to surface roughness. The interpretation of the same system as represented in Figure 1b would be that of a capacitor and resistor in parallel combined with the series resistance of the solution.

The author found that complex plane impedance plots were required at a number of potentials to give a better understanding as to the most likely double layer analogue circuit for the system studied. However, the author has presented in the text only a representative number of complex plane impedance plots - that thought sufficient to support the author's choice of a particular analogue circuit.

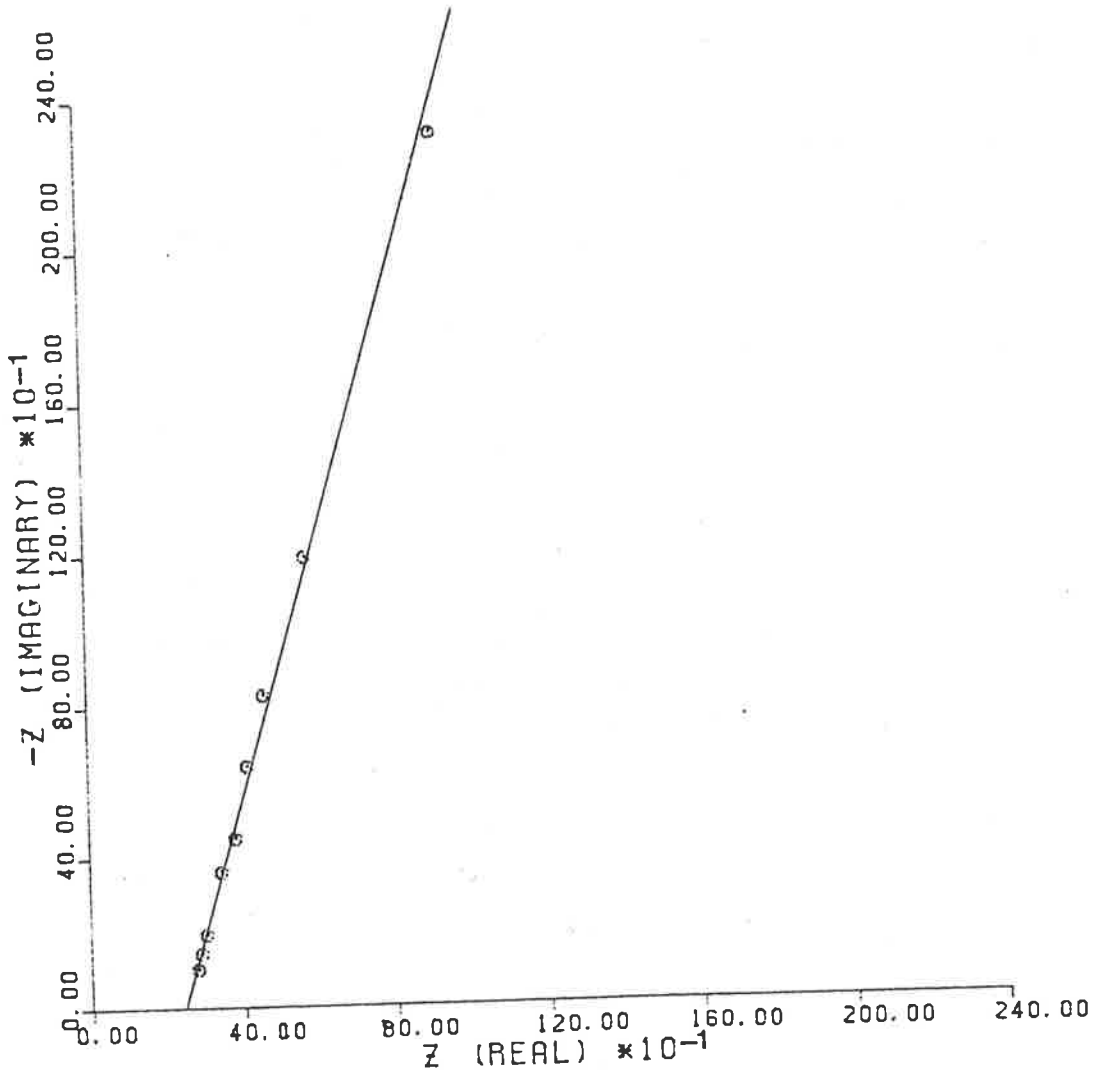


Figure 1a. Complex plane impedance spectrum with data fitted by a straight line making an angle of  $74^\circ$  with the real axis.

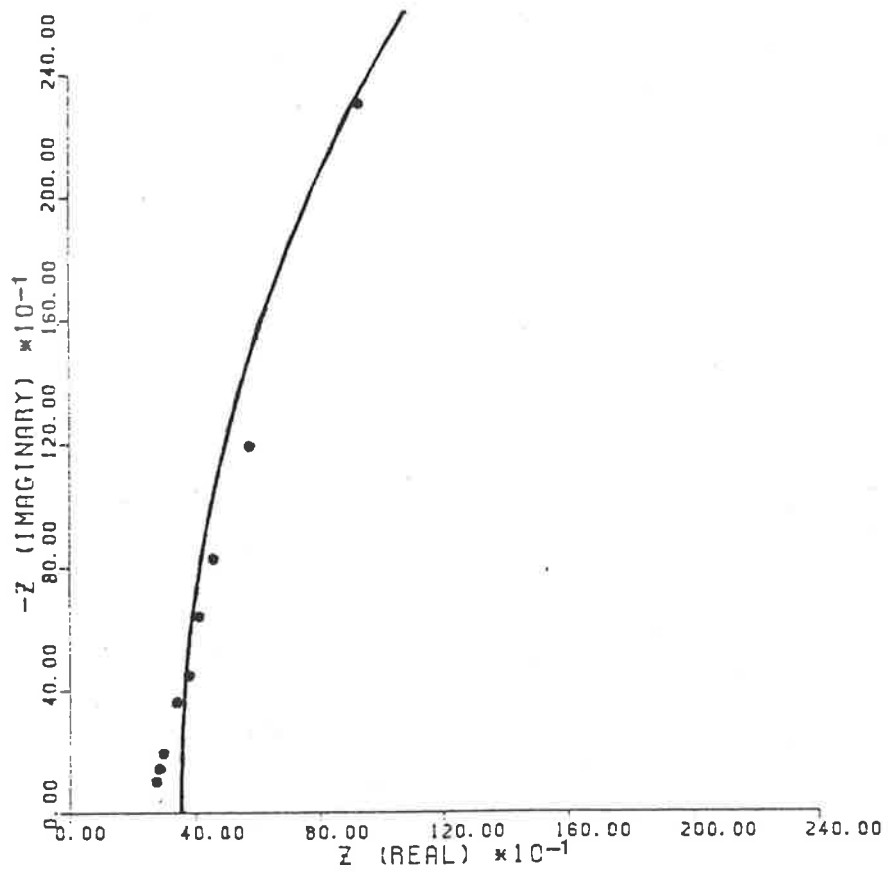


Figure 1b. Complex plane impedance spectrum with data fitted by an arc of a hemi-circle corresponding to a parallel resistance of 10 k $\Omega$ .

## EXPERIMENTAL

### GENERAL

The methods used to obtain information in these double layer capacitance studies, and the equipment used, have already been described in Chapter 4 of this thesis.

The electrolysis cells used in these experiments have been described in Chapter 2 of this thesis.

### ELECTRODES

A standard three electrode system was used for the A.C. Impedance Method, whereas an extra auxiliary electrode was deemed necessary for the Single Current Pulse Method measurements, as discussed in Chapter 4 of this thesis.

The polycrystalline platinum working electrodes used in these studies have been previously described in Chapter 2. They are the Teflon-encased polycrystalline platinum electrode, the polycrystalline platinum disc electrode, and the polycrystalline platinum Cottrell Cell electrode.

The polycrystalline silver working electrode used in these studies is depicted in Figure 2. A polycrystalline silver cylinder was encased in Kel-F material, and screw fitted into a perspex support which was kept out of contact with the solution. Electrical contact with the silver cylinder was made via a brass rod.

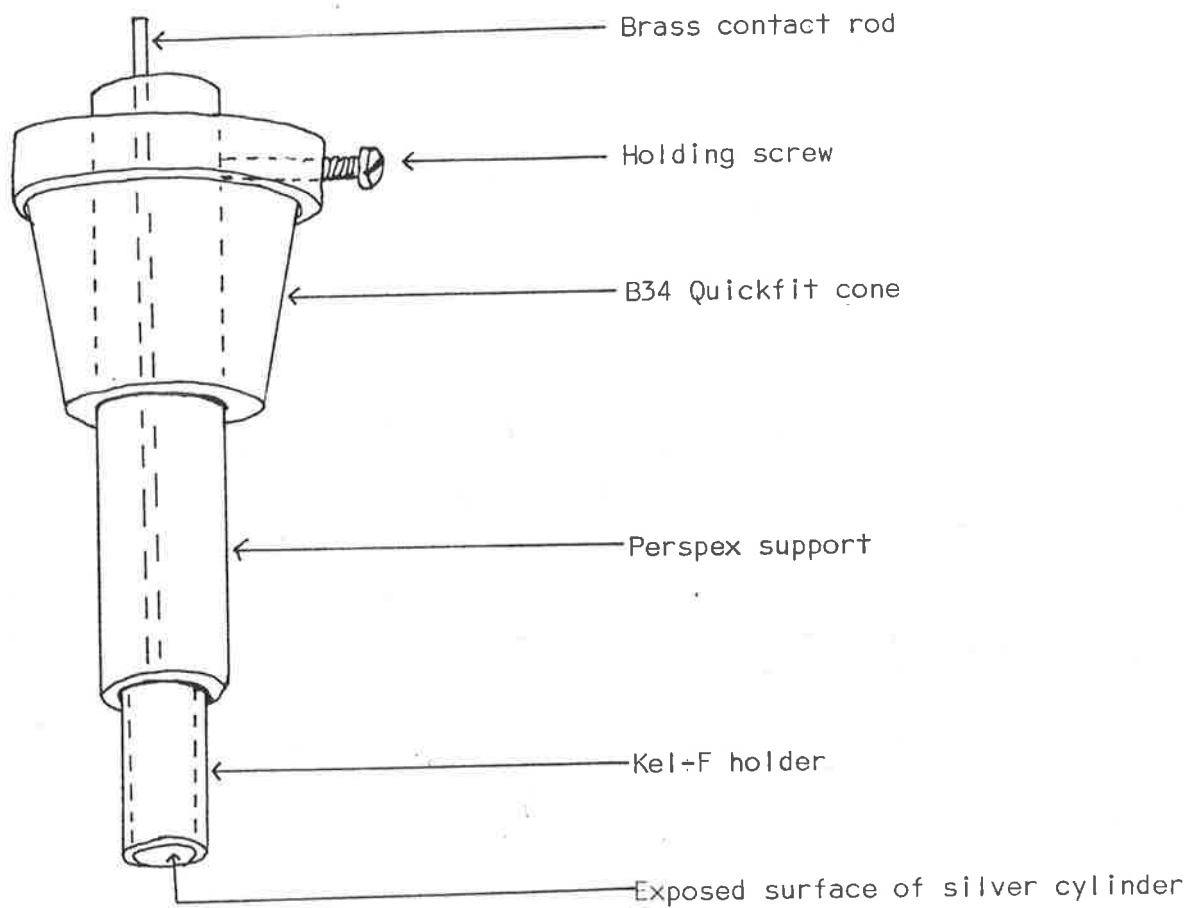


Figure 2. Polycrystalline silver electrode.



## 5.6

The counter electrode used was either the horizontally orientated large platinum disc electrode or a vitreous graphite rod obtained from Atomergic Chemetals Corporation, New York.

A platinum wire sealed in a J-shaped glass sheath was used as the auxiliary electrode in the Single Current Pulse measurements.

The reference electrode used for all studies in this chapter was a saturated calomel electrode separated from the electrolysis cell in a side-arm of a luggin capillary. All potentials quoted in this chapter are with respect to this electrode.

### CLEANING AND PREPARATION PROCEDURES

All glassware and Teflon and Kel-F components were rinsed in de-ionised water, soaked in pure nitric or sulphuric acid, and then rinsed thoroughly and soaked in milli-Q quality water.

The assembled working cell was steam cleaned without oven drying. All glassware other than the electrolysis cell was oven dried, while all Teflon and Kel-F components were air dried on clean Whatman No. 5, 11.0 cm filter papers.

The platinum wire auxiliary electrode and the platinum disc counter electrode were both soaked in pure nitric or sulphuric acid, and then rinsed and stored in milli-Q quality water until required.

## 5.7

The polycrystalline platinum disc electrode and the vitreous graphite rod were cleaned by rinsing in water, and then heating to 'red hot' in a flame. The platinum disc electrode was quenched in pure milli-Q quality water, and transferred into the working cell with a droplet of pure water covering its surface.

The other polycrystalline working electrodes had their surfaces polished to a mirror finish using conventional metallographic lap polishing techniques, using diamond or alumina paste. The finest finishes were obtained using 0.05  $\mu\text{m}$  alumina paste. The electrode surfaces were cleaned ultrasonically and by rinsing in water, and then etched for 30 seconds in aqua regia. The electrodes were further cleaned in pure sulphuric or nitric acid, rinsed, and left to soak in pure milli-Q water until required. From the acid cleaning stage until being placed into the electrolyte solution in the electrolysis cell, the working electrode surface was kept covered by pure water, or the electrolyte of interest.

The polycrystalline silver electrode was lap polished using alumina paste, and then further cleaned using a chemical procedure similar to those of Bewick and Thomas,<sup>9</sup> and Adzic, Hanson and Yeager.<sup>10</sup> Aqueous solutions of 20 volume percent of  $\text{H}_2\text{O}_2$  and 21 g/l of NaCN were mixed in a 1:1 ration, and used to chemically etch the silver surface. The electrode was held in this solution for a maximum of three seconds, or until gas evolution occurred. The electrode surface was then exposed to air for a brief period, to allow gas evolution to occur. The electrode was then transferred into an aqueous solution of 21 g/l NaCN until gas evolution ceased. The electrode was quickly rinsed in pure

water before its transfer into the second solution, to minimize contamination of it with  $H_2O_2$ . This whole procedure was repeated several times until a highly reflective surface was obtained.

Adzic, Hanson and Yeager<sup>10</sup> found that using such a procedure to polish silver single-crystals produced surfaces of high enough quality to yield low energy diffraction patterns without further treatment, suggestive of atomically flat, well ordered surfaces.

Further preparation of the silver electrode was carried out by maintaining the electrode at a potential of -1.40 volts for more than one hour in the solution of interest. This final stage electroreduction procedure was carried out in all silver studies reviewed by Hamelin, Vitanov, Sevastyanov and Popov.<sup>1</sup>

#### CHEMICALS

##### *Hydrochloric Acid (HCl)*

B.D.H. Aristar Ultrapure HCl was diluted to the desired concentration using milli-Q quality water.

##### *Potassium Nitrate (KNO<sub>3</sub>)*

B.D.H. Analytical reagent was used.

##### *Sodium Chloride (NaCl)*

B.D.H. Analytical reagent was used.

*Sodium Fluoride (NaF)*

B.D.H. Analytical reagent was used after heating to more than 450°C to remove volatile material.

*Sodium Nitrate (NaNO<sub>3</sub>)*

B.D.H. Analytical reagent was used.

*Water (H<sub>2</sub>O)*

Milli-Q quality water of >18 MΩ/cm<sup>2</sup> resistance with a final stage 0.22 μm Millipore filter was used.

**SOLUTION DE-OXYGENATION**

The solution to be investigated was flushed prior to measurements for a period of about one hour, using high purity argon gas. Argon gas was then continually passed over the solution surface for the duration of the measurements. An in-line vanadyl oxygen scrubbing system was used, as mentioned previously in Chapter 2. This system, however, did not appear to remove impurities, such as oxygen from the gas, nor did it appear to add impurities from the vanadyl solution to the electrolysis cell solution. As such, this oxygen scrubbing solution was not used in the latter measurements.

## RESULTS AND DISCUSSION

### PRELIMINARY RESULTS

Preliminary measurements of capacitance were made on systems using water of inferior quality to milli-Q water. The milli-Q system is described elsewhere,<sup>11</sup> and discussed by Rosen and Schuldiner.<sup>12</sup> The inferior water used was equivalent to triply distilled water.

For the polycrystalline platinum/1M HCl /H<sub>2</sub>O system, the lesser grade of water did not reflect itself noticeably in the measurements. The capacitance-potential curves were similar, and the capacitance showed a time dependence, whether milli-Q water was used or not. The results presented for this system in Figures 3 and 7 were made using lesser grade water, and hydrochloric acid stock that was only of Analytical, rather than Aristar, quality.

For the polycrystalline gold/0.010M NaF/H<sub>2</sub>O system, however, reproducible capacitance-potential curves could only consistently be obtained using milli-Q quality water. Although this system was not further studied beyond a preliminary stage, the effect of water quality on results was enough to convince the author of the necessity of using high quality milli-Q water in double layer capacitance studies.

SYSTEM I: Pt + 1M HCl + H<sub>2</sub>O

The Single Current Pulse Method was used to investigate the polycrystalline platinum/aqueous 1M HCl interface.

From Figures 3-7 it is evident that the Isaacs-Leach Log ( $\Delta V/\Delta t$ ) Plot Method and the Polynomial Least Squares Curve Fit Method give excellent agreement. The Two Point Linear Approximation Method, on the other hand, only produces fair agreement when utilizing the first 50  $\mu$ s. Over time ranges further removed from the origin, this latter method yields anomalously high capacitance values as the deviation from linearity of the potential-time transient becomes more accentuated. This effect is clearly shown in Figure 7. The Two Point Linear Approximation Method can be used to obtain relative differential capacitance values; however, the author sees no value in using this method, since the Isaacs-Leach Log ( $\Delta V/\Delta t$ ) Plot Method and the Polynomial Least Squares Curve Fit Method both yield absolute capacitances.

The results of the Single Current Pulse measurements agree favourably with those of Robertson,<sup>13</sup> who used an A.C. Bridge Method, and Riney, Schmidt and Hackerman,<sup>2</sup> who used a Single Current Pulse Method. The results presented here are more accurate than those published by Robertson, and Riney et al.

Table 1 gives a typical set of results achieved with the Single Current Pulse Method. For a single potential-time response curve, a number of evenly spaced sets of points were taken, and analysed using the Polynomial Least Squares Curve Fit Method (Polynomial Method) and the Isaacs-Leach Log ( $\Delta V/\Delta t$ ) Plot Method (Log ( $\Delta V/\Delta t$ ) Plot Method).

The calculated uncertainties in these measurements vary from 0.7% to 1.9% for the Polynomial Method, and from 0.7% to 3.2% for the Log ( $\Delta V/\Delta t$ ) Plot Method.

**Table 1**

Dependence of capacitance in  $\mu\text{F}/\text{cm}^2$   
determined by the Polynomial Method and the Log ( $\Delta V/\Delta t$ ) Plot Method  
on electrode potential

POLYNOMIAL METHOD

Potential/volts	Group A	Group B	Average
+0.30	$37.95 \pm 0.50$	$37.97 \pm 0.58$	$37.96 \pm 0.01$
+0.40	$32.27 \pm 0.23$	-	32.27
+0.50	$27.62 \pm 0.28$	-	27.62
+0.60	$23.83 \pm 0.23$	$23.35 \pm 0.19$	$23.59 \pm 0.34$
+0.70	$21.52 \pm 0.34$	$22.21 \pm 0.33$	$21.87 \pm 0.49$
+0.80	$21.74 \pm 0.42$	$21.75 \pm 0.30$	$21.75 \pm 0.01$
+0.90	$22.97 \pm 0.44$	$21.81 \pm 0.42$	$22.39 \pm 0.82$
+1.00	$30.08 \pm 0.34$	$30.46 \pm 0.39$	$30.27 \pm 0.27$

LOG ( $\Delta V/\Delta t$ ) PLOT METHOD

Potential/volts	Group A	Group B	Average
+0.30	$38.02 \pm 0.51$	$38.55 \pm 0.60$	$38.29 \pm 0.37$
+0.40	$32.66 \pm 0.24$	-	32.66
+0.50	$28.18 \pm 0.38$	-	28.18
+0.60	$23.77 \pm 0.23$	$23.77 \pm 0.23$	$23.77 \pm 0.00$
+0.70	$22.96 \pm 0.52$	$22.54 \pm 0.42$	$22.75 \pm 0.30$
+0.80	$20.99 \pm 0.60$	$21.58 \pm 0.38$	$21.29 \pm 0.42$
+0.90	$21.78 \pm 0.70$	$21.63 \pm 0.49$	$21.71 \pm 0.11$
+1.00	$29.24 \pm 0.37$	$29.11 \pm 0.31$	$29.18 \pm 0.09$

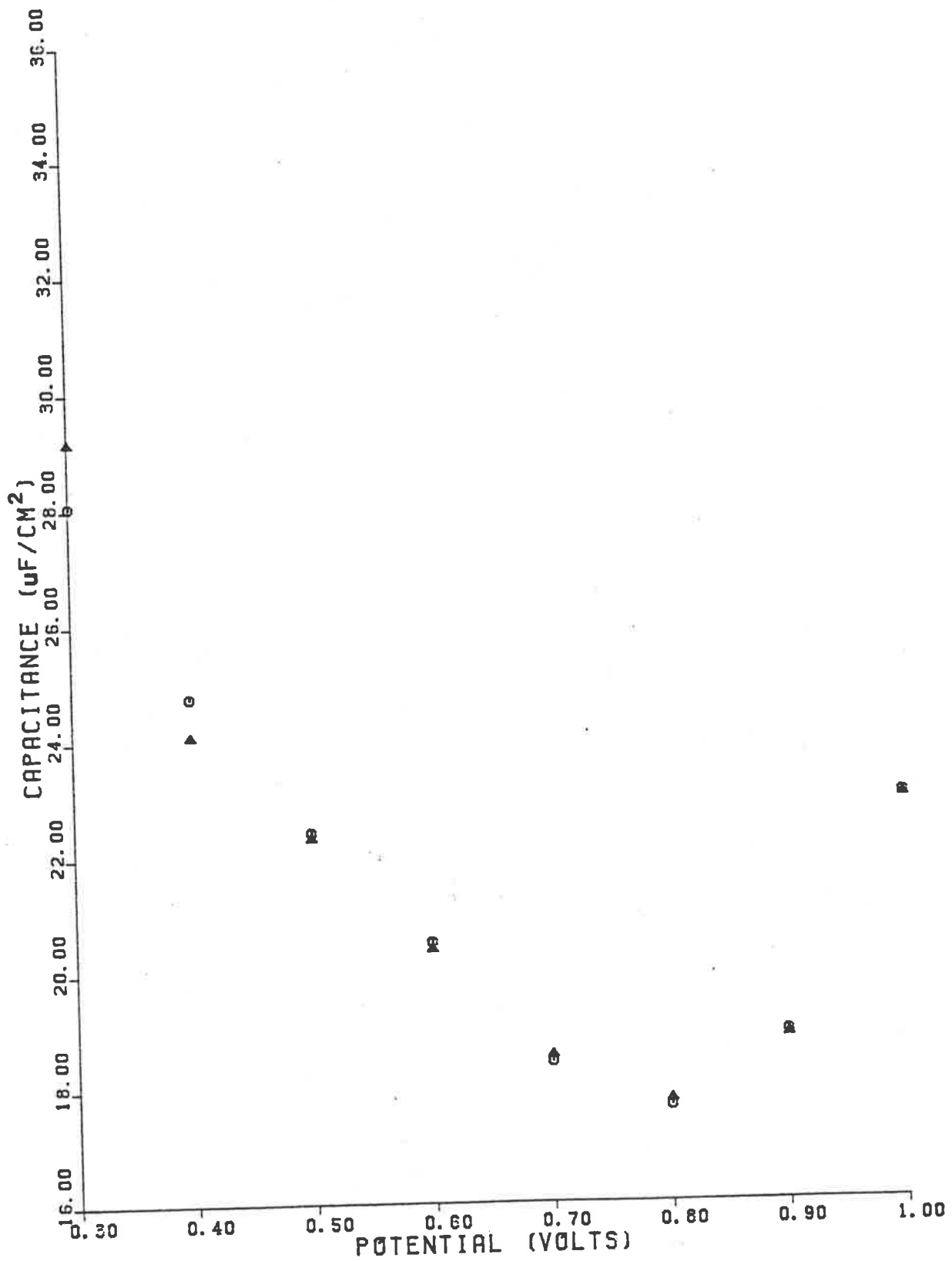


Figure 3. Capacitance - potential curves for polycrystalline platinum Cottrell Cell in 1.00M HCl: Polynomial Method (O); Log ( $\Delta V/\Delta t$ ) Plot Method ( $\Delta$ ).



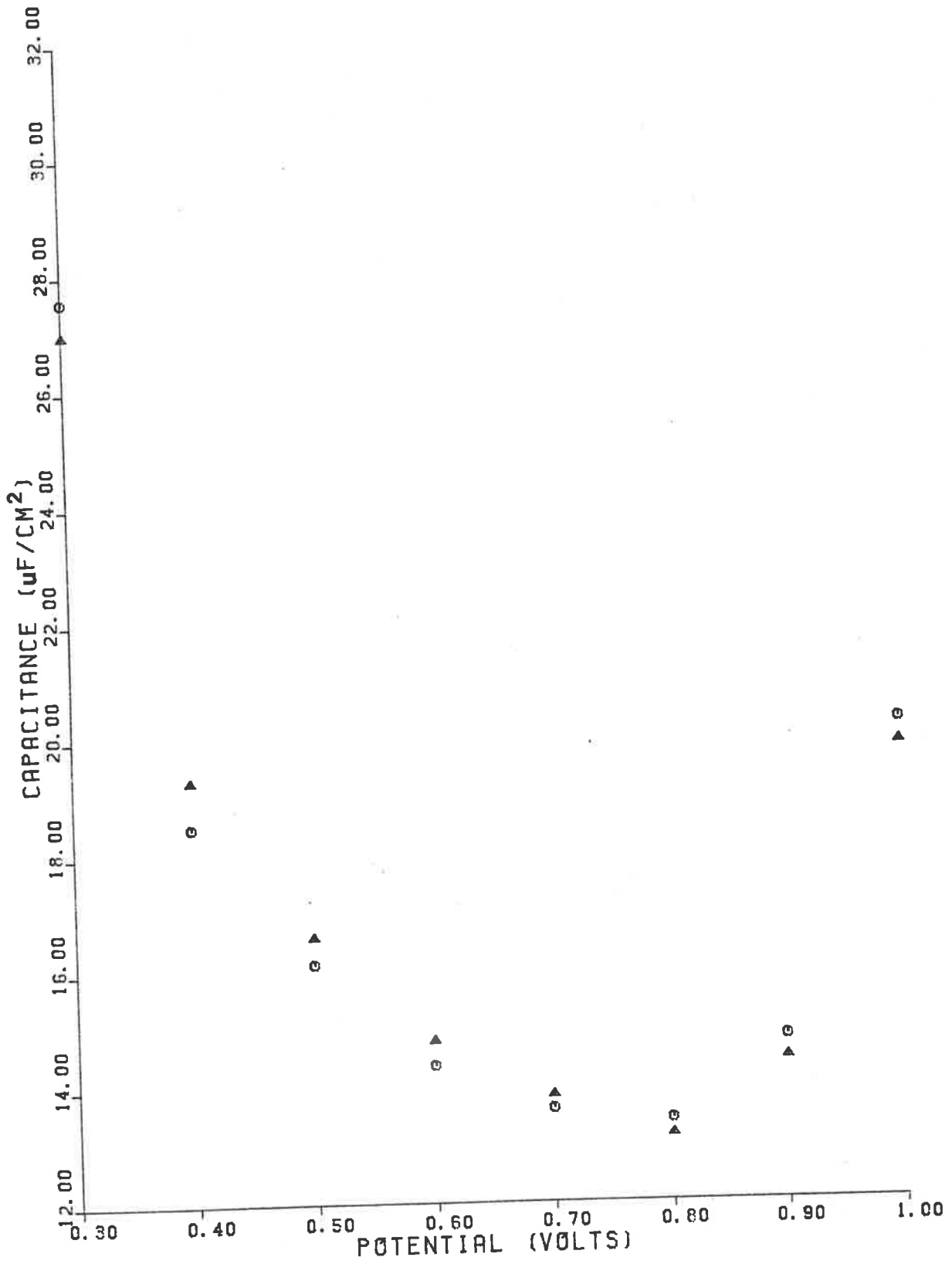


Figure 4. Capacitance - potential curves for polycrystalline platinum disc in 1.02M HCl: Polynomial Method (O); Log ( $\Delta V/\Delta t$ ) Plot Method ( $\Delta$ ).

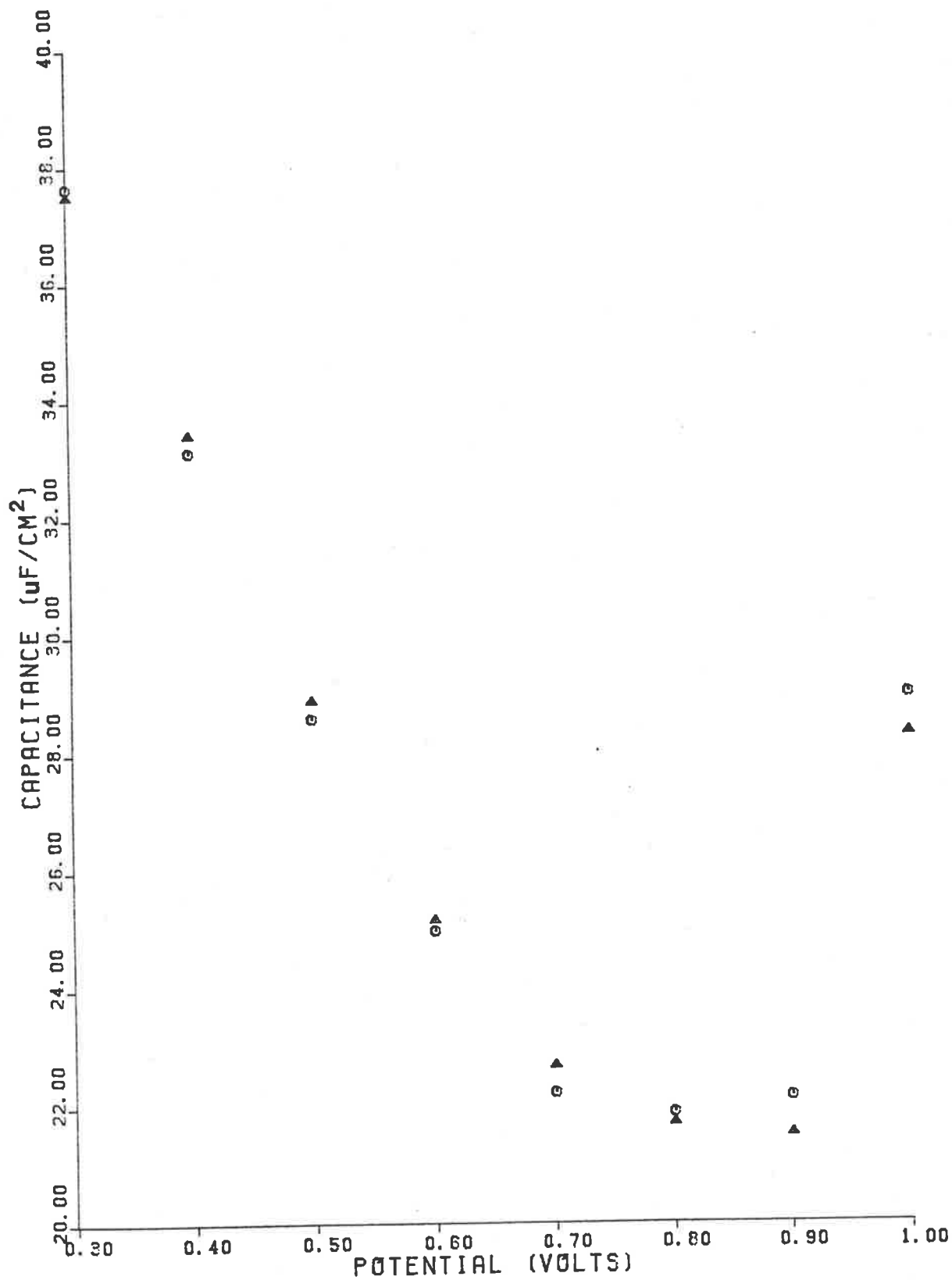


Figure 5. Capacitance - potential curves for teflon-encased polycrystalline platinum in 1.00M HCl: Polynomial Method (O); Log ( $\Delta V/\Delta t$ ) Plot Method ( $\Delta$ ).

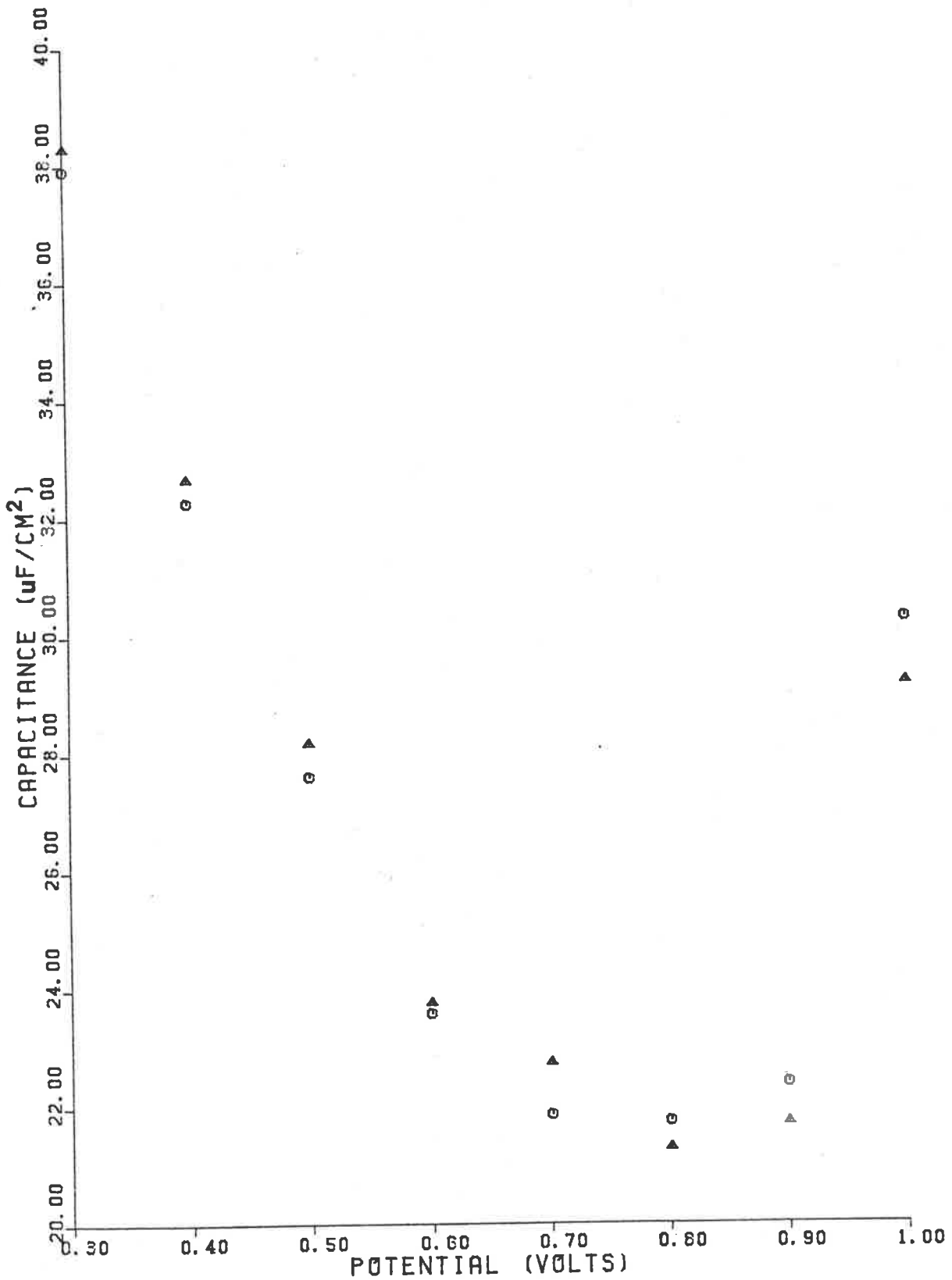


Figure 6. Capacitance - potential curves for Teflon-encased polycrystalline platinum in 1.00m HCl: Polynomial Method (O); Log ( $\Delta V/\Delta t$ ) Plot Method ( $\Delta$ ).

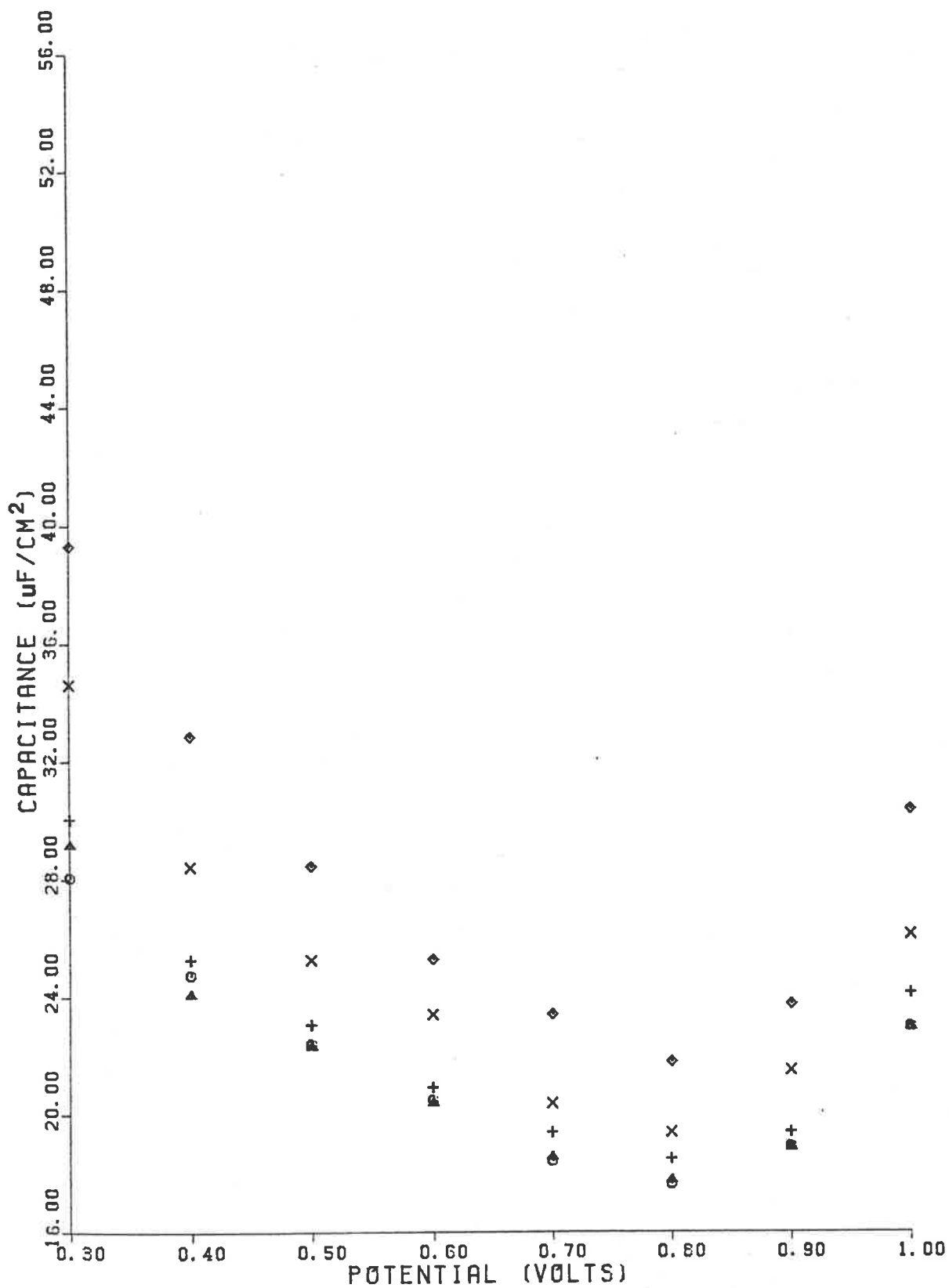


Figure 7. Capacitance-potential curves for polycrystalline platinum Cottrell Cell in 1.00M HCl: Polynomial Method (O); Log ( $\Delta V/\Delta t$ ) Plot Method ( $\Delta$ ); Two Point Linear Approximation Method using ranges: 0-50  $\mu$ s (+); 50-100  $\mu$ s (X); 90-190  $\mu$ s ( $\diamond$ ).

### 5.13

Selection and analysis of another group of evenly spaced sets of points for the same potential-time response curve provides an internal check on data accuracy. The results for two groups of points are presented in Table 1, and these are quite typical for all the results presented in this chapter for the Single Current Pulse Method.

In Table 1, the Group A calculations were made on a set of points selected at 250  $\mu\text{s}$  intervals over the range of 250  $\mu\text{s}$  to 5,000  $\mu\text{s}$ . The Group B calculations were made on a set of points selected at 250  $\mu\text{s}$  intervals over the range of 375  $\mu\text{s}$  to 4875  $\mu\text{s}$ . The average of Group A and Group B calculations is tabled, and the quoted uncertainty is the standard deviation between the calculations. This standard deviation is typically of the order of 1.5% or less.

The average of Group A and Group B calculations presented in Table 1 is presented graphically in Figure 6.

The capacitance-potential curves displayed in Figures 3-7 consistently display the same essentials. Each curve displays a capacitance minimum at +.80V. From this minimum the capacitance increases in both the anodic and cathodic directions. The increase in capacitance with change in potential is greatest at the potential range extremes.

From the cyclic voltammogram displayed in Figure 8, which is typical for this system, three major potential ranges can be observed. The extreme cathodic portion is a region of high current due to reduction of hydrogen ion producing atomic and then molecular hydrogen.

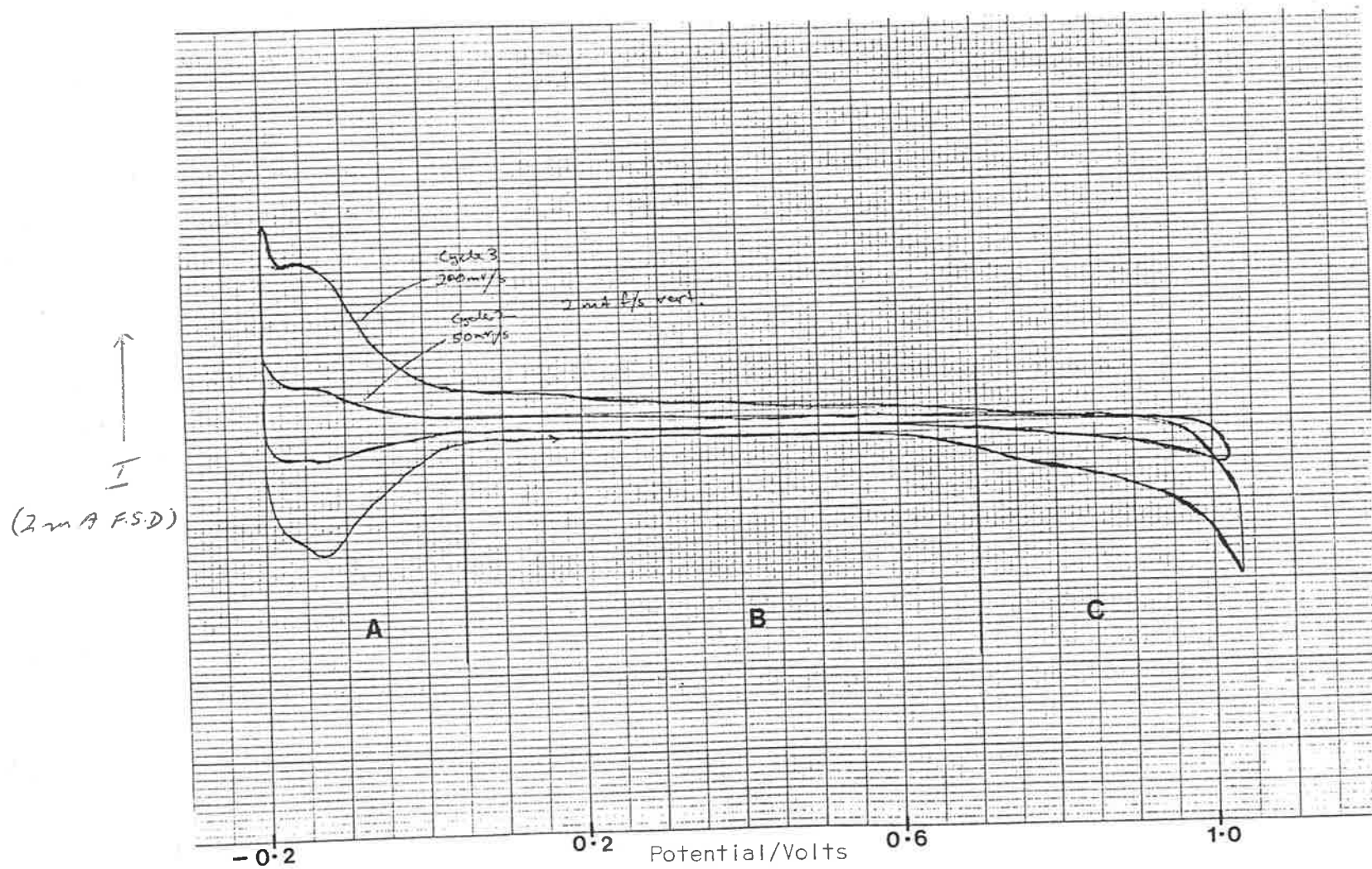


Figure 8. Cyclic voltammograms of polycrystalline platinum in 1M HCl showing: hydrogen adsorption region (A); double layer region (B); chlorine evolution region (C).

## 5.14

The extreme anodic portion is a region of high current due to oxidation of chloride to produce chlorine. The potential region in between the extremes is the so-called double layer region. In this latter region only would one expect to measure true double layer capacitance, unaffected by faradaic reaction.

The high capacitance extremes of the capacitance-potential curves can thus be correlated with the onset of chloride ion oxidation at anodic potentials, and hydrogen ion adsorption and reduction at more cathodic potentials.

Robertson noted a time dependence in his capacitance measurements at fixed potentials.<sup>13</sup> The author had previously noted that capacitance measurements were time dependent, often requiring 10 or 15 minutes before stable values were obtained when polycrystalline platinum electrodes were used.<sup>14</sup>

Figures 9 and 10 show the variation of the capacitance with time at a number of selected electrode potentials, determined by the Polynomial Method and the Log ( $\Delta V/\Delta t$ ) Plot Method, respectively. At the cathodic and anodic potential extremes of +.30 V and +1.00 V, respectively, the capacitance increased with time. In the vicinity of the capacitance minimum at +.80 V, the capacitance showed little tendency to vary at all. In the potential regions in between the extremes and the potential of the capacitance minimum, the capacitance tended to decrease with time. An example of this latter behaviour occurs at +.60 V.

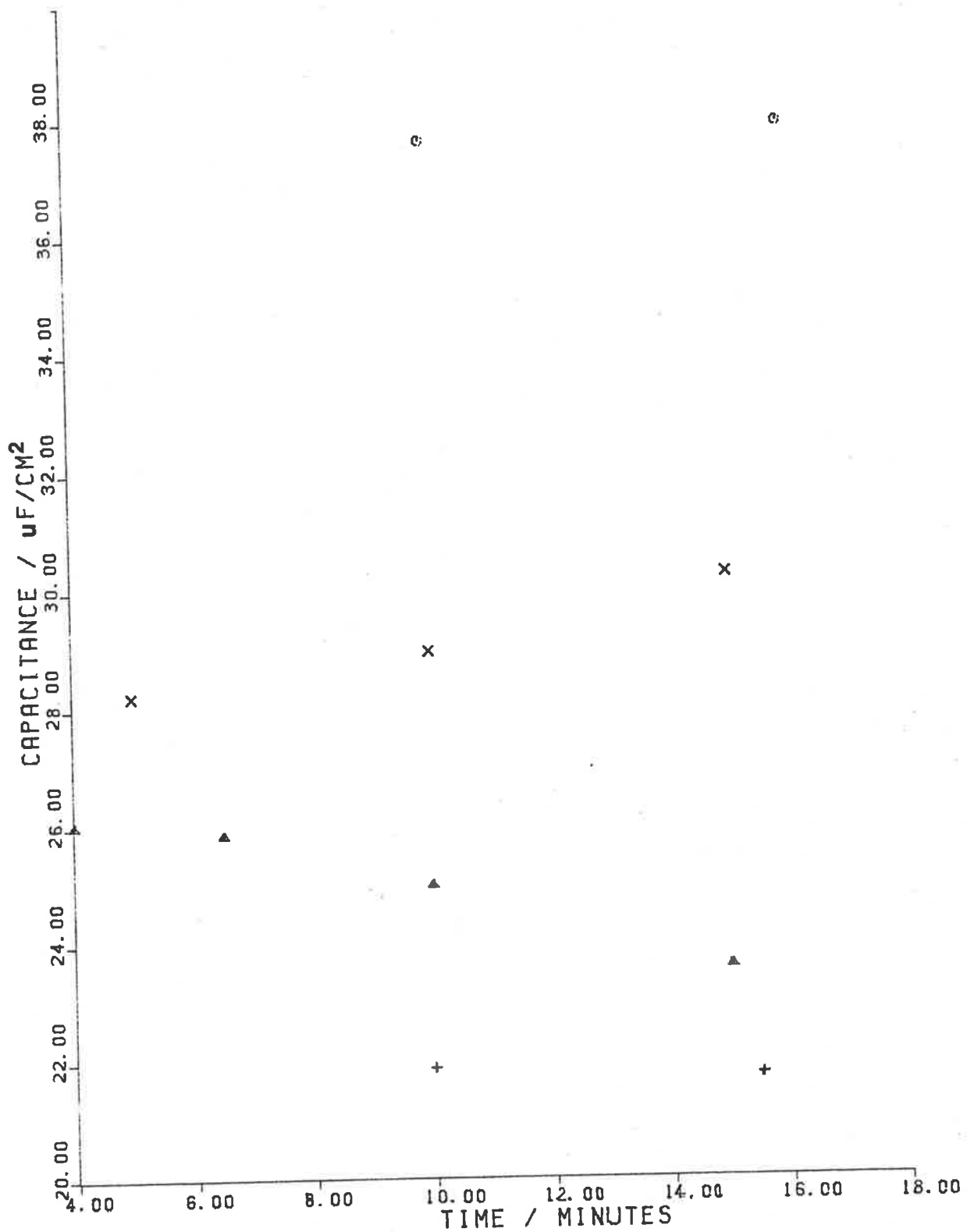


Figure 9. Dependence of capacitance of Teflon-encased polycrystalline platinum in 1.00m HCl (Polynomial Method) on time at selected electrode potentials: +0.30 V (O); +0.60 V (Δ); +0.80 V (+); +1.00 V (X).



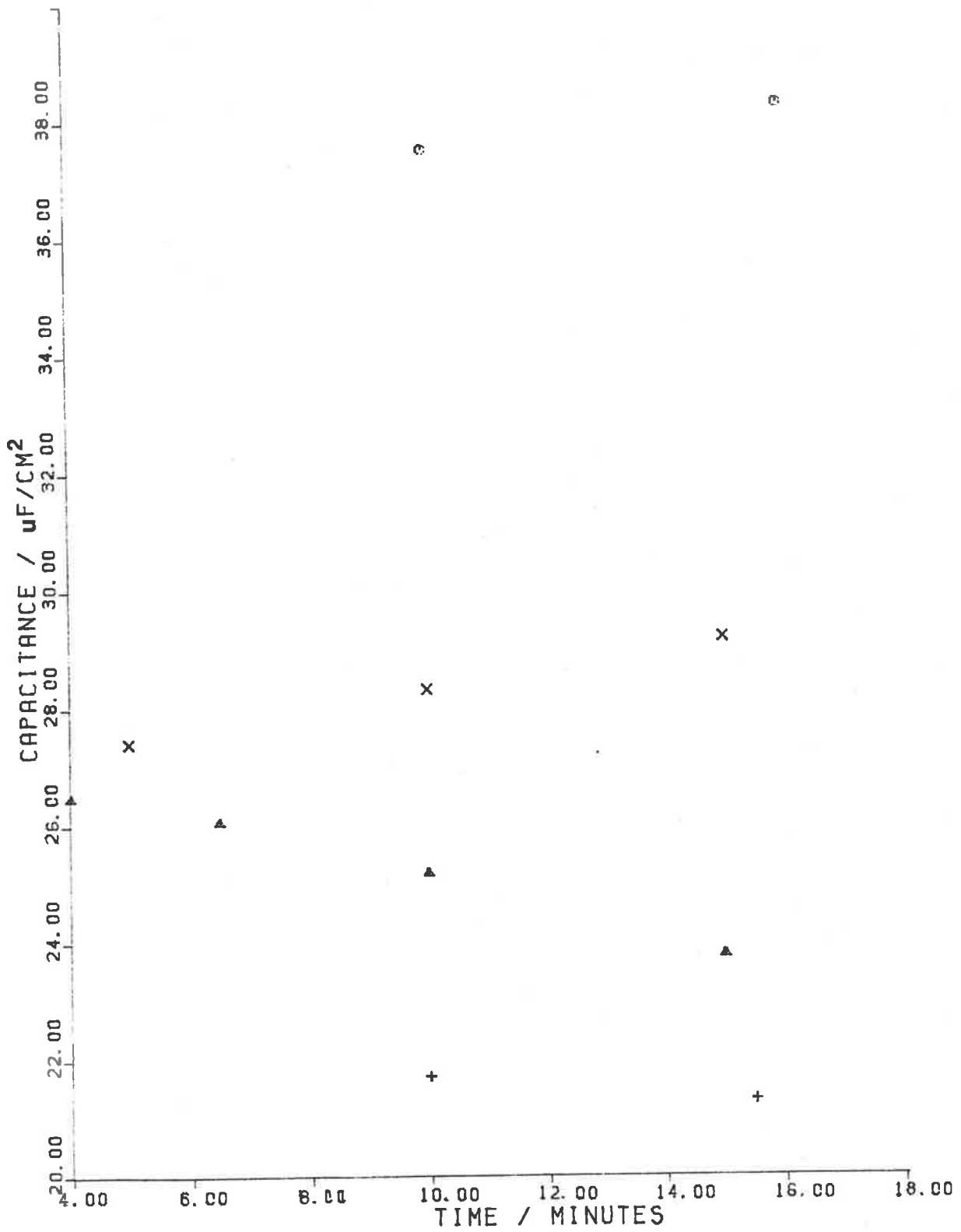


Figure 10. Dependence of capacitance of Teflon-encased polycrystalline platinum in 1.00m HCl (Log  $(\Delta V/\Delta t)$  Plot Method) on time at selected electrode potentials: +0.30 V (O); +0.60 V ( $\Delta$ ); +0.80 V (+); +1.00 V (X).

Table 2

Dependence of Parallel Resistance in ohms on time of measurement  
at selected electrode potentials

<i>Time/minutes</i>	4	5	6.5	10	15	15.5	16
<i>Potential/volts</i>							
+0.30	-	-	-	124	-	-	119
+0.60	168	-	170	167	164	-	-
+0.80	-	-	-	166	-	163	-
+1.00	-	178	-	176	180	-	-

## 5.15

The complex time dependence of the measured capacitance was not reflected in the associated parallel resistance measurements. Table 2 shows that the measured parallel resistance was independent of the time of measurement. The results presented in Table 2 correspond to the capacitance results presented in Figure 10. The resistance was, however, found to be dependent upon the electrode potential. The parallel resistance was found to be low, and increased with increasing anodic polarization.

The effect of the magnitude of the current pulse was tested by measuring the capacitance of an individual system using currents of 1 mA and 4 mA. The capacitance-potential curves were found to be identical, showing no dependence on the current pulse magnitude. This result shows that the capacitance determined using the Single Pulse Method is related to the electrode potential prior to the firing of the current pulse, and not related to some averaged potential due to a change in the electrode potential during the application of the current. If the latter were the case, then the capacitance-potential curve would be displaced along the potential axis as the current was increased.

The polycrystalline platinum/aqueous 1M HCl system was also investigated using the A.C. Impedance Method.

A typical anodic potential scan is displayed in Figure 11, showing the measured  $0^\circ$  and  $90^\circ$  components of the a.c. current. This data was used to determine the capacitance-potential and resistance-potential curves displayed in Figures 12 and 13,

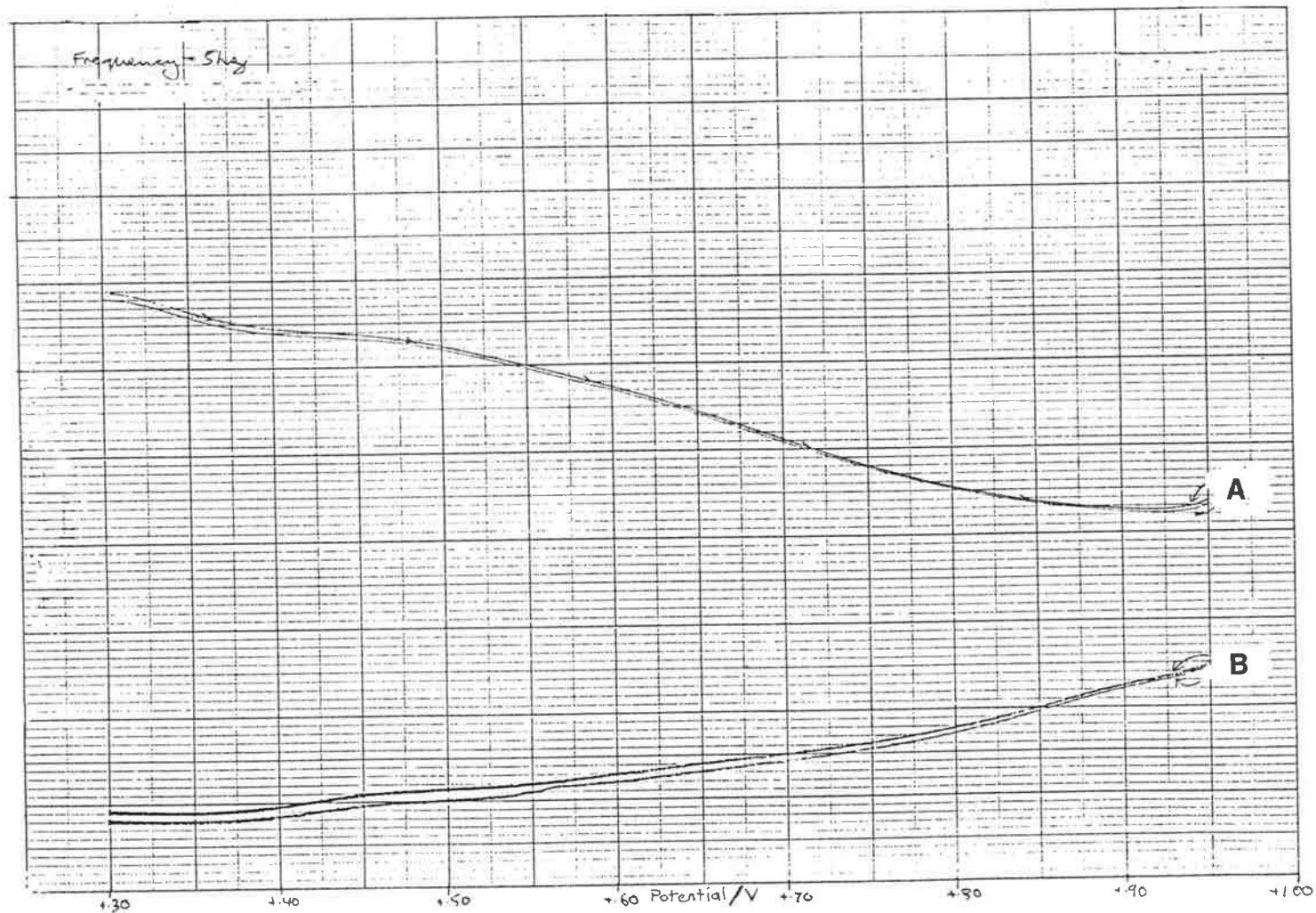


Figure 11. Current-potential curves recorded using the A.C. Impedance Method for the Teflon-encased polycrystalline platinum/1M HCl interface:

- A. imaginary current component with (upper) and without iR-compensation;
- B. real current component with (lower) and without iR-compensation.

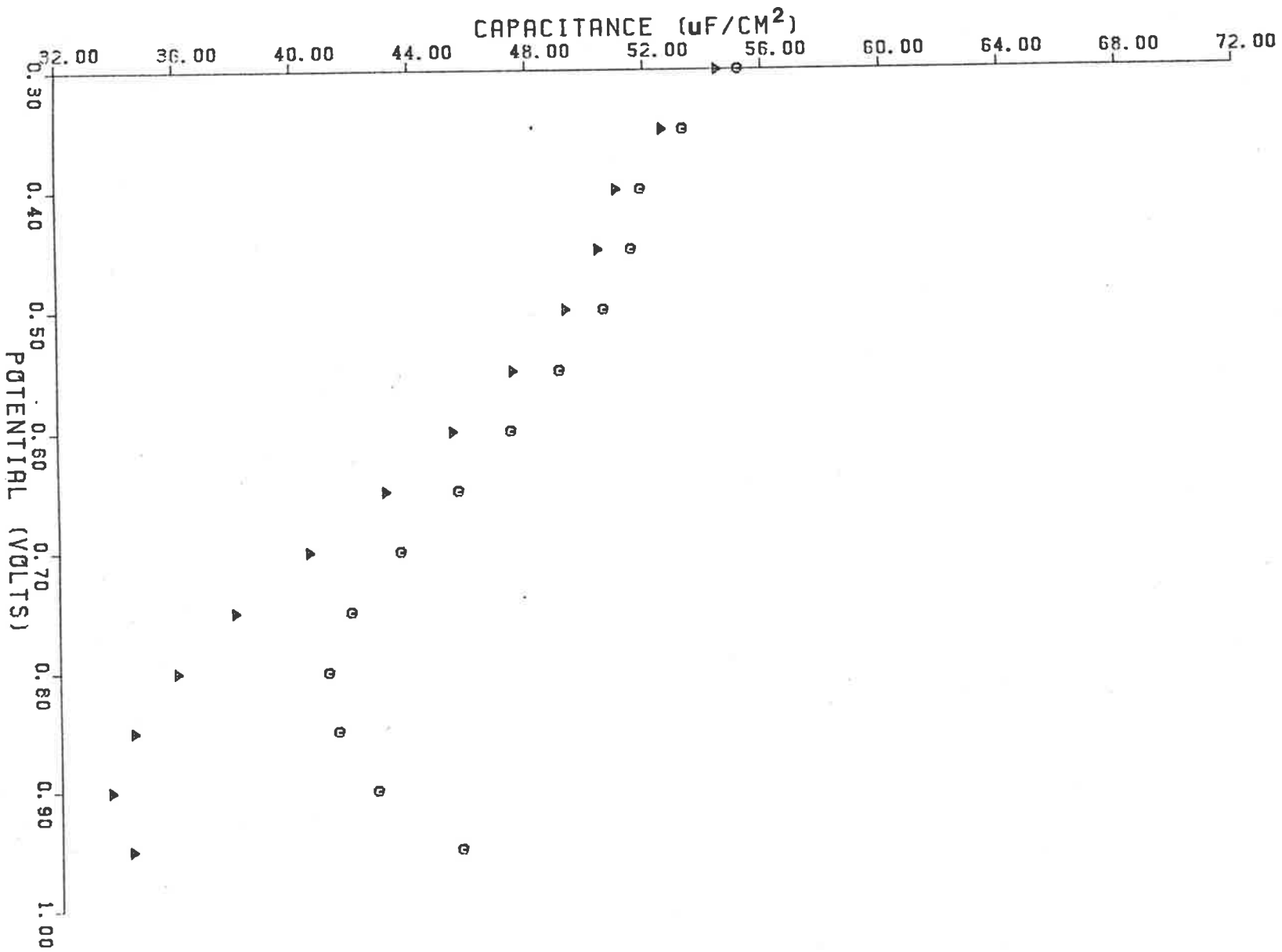


Figure 12. Capacitance-potential curves for Teflon-encased polycrystalline platinum in 1.04M HCl at 5 Hz: series capacitance (O); parallel capacitance ( $\Delta$ ). 10 mV/s scan rate.

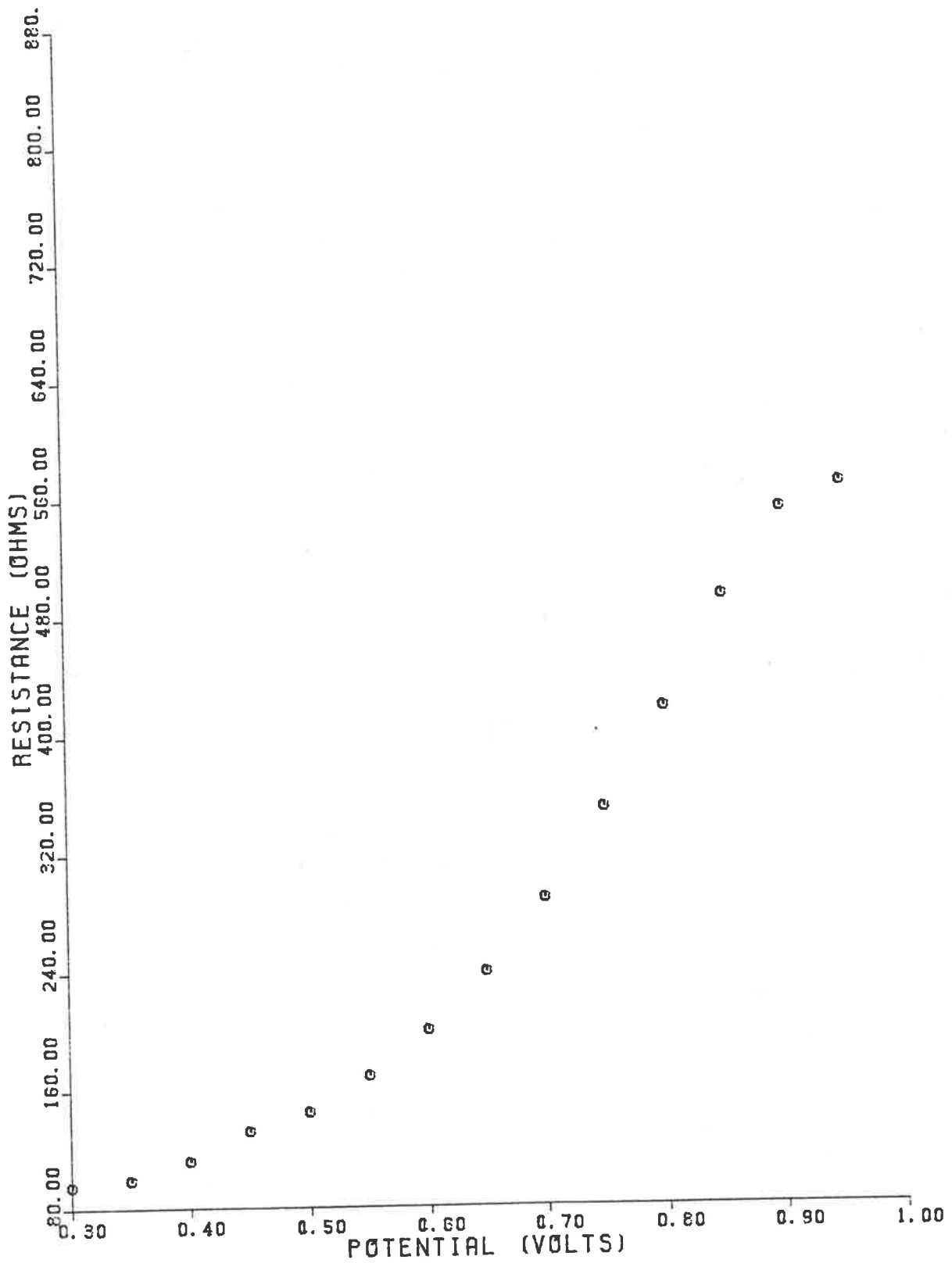


Figure 13. Series resistance-potential curve for Teflon-encased polycrystalline platinum in 1.04M HCl at 5 hz. 10 mV/s scan rate.

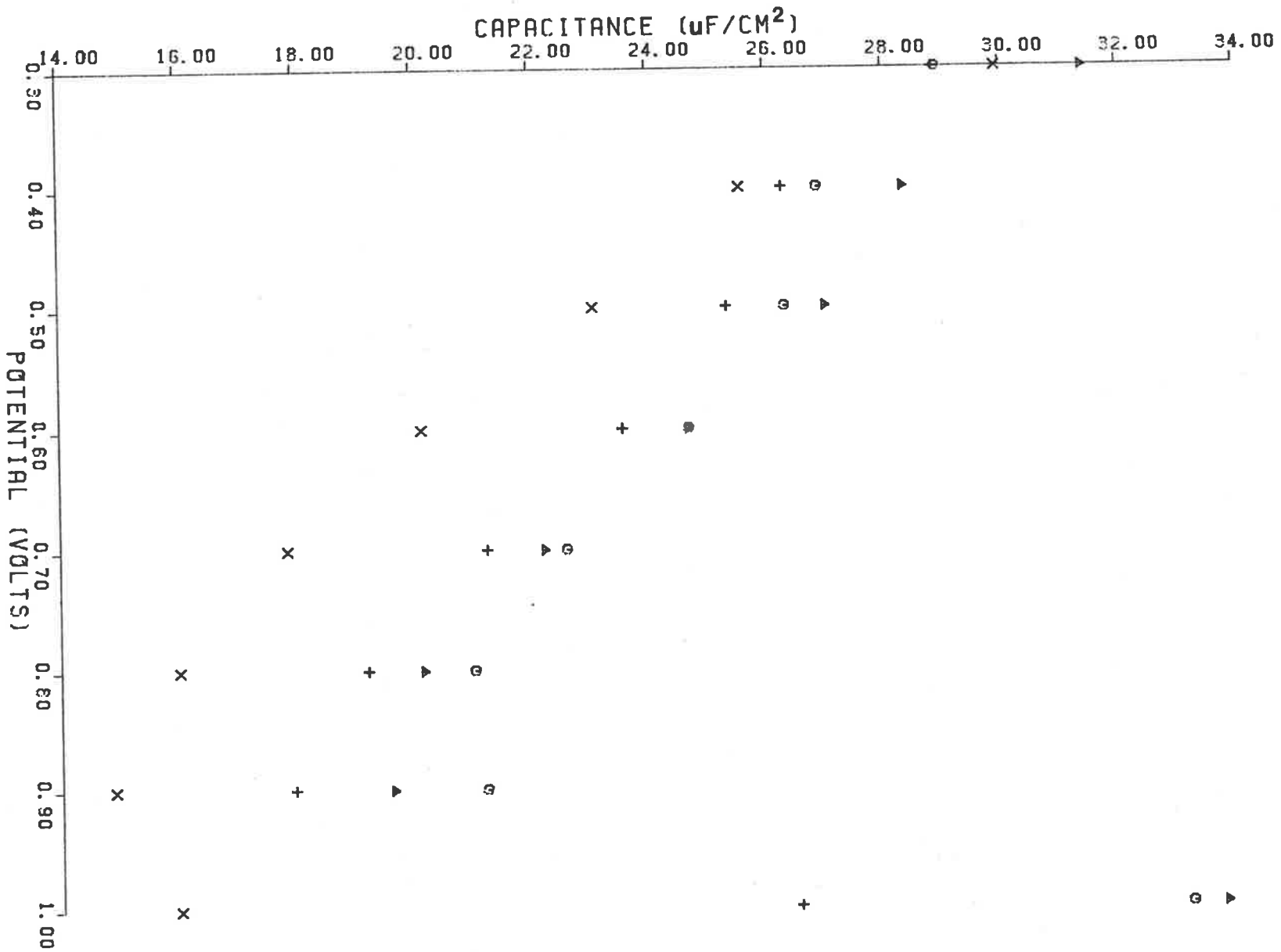


Figure 14. Frequency dependence of series capacitance-potential curves for polycrystalline platinum disc in 1.02M HCl: 5 Hz (O); 10 Hz ( $\Delta$ ); 20 Hz (+); 200 Hz (X). 10 mV/s scan rate.

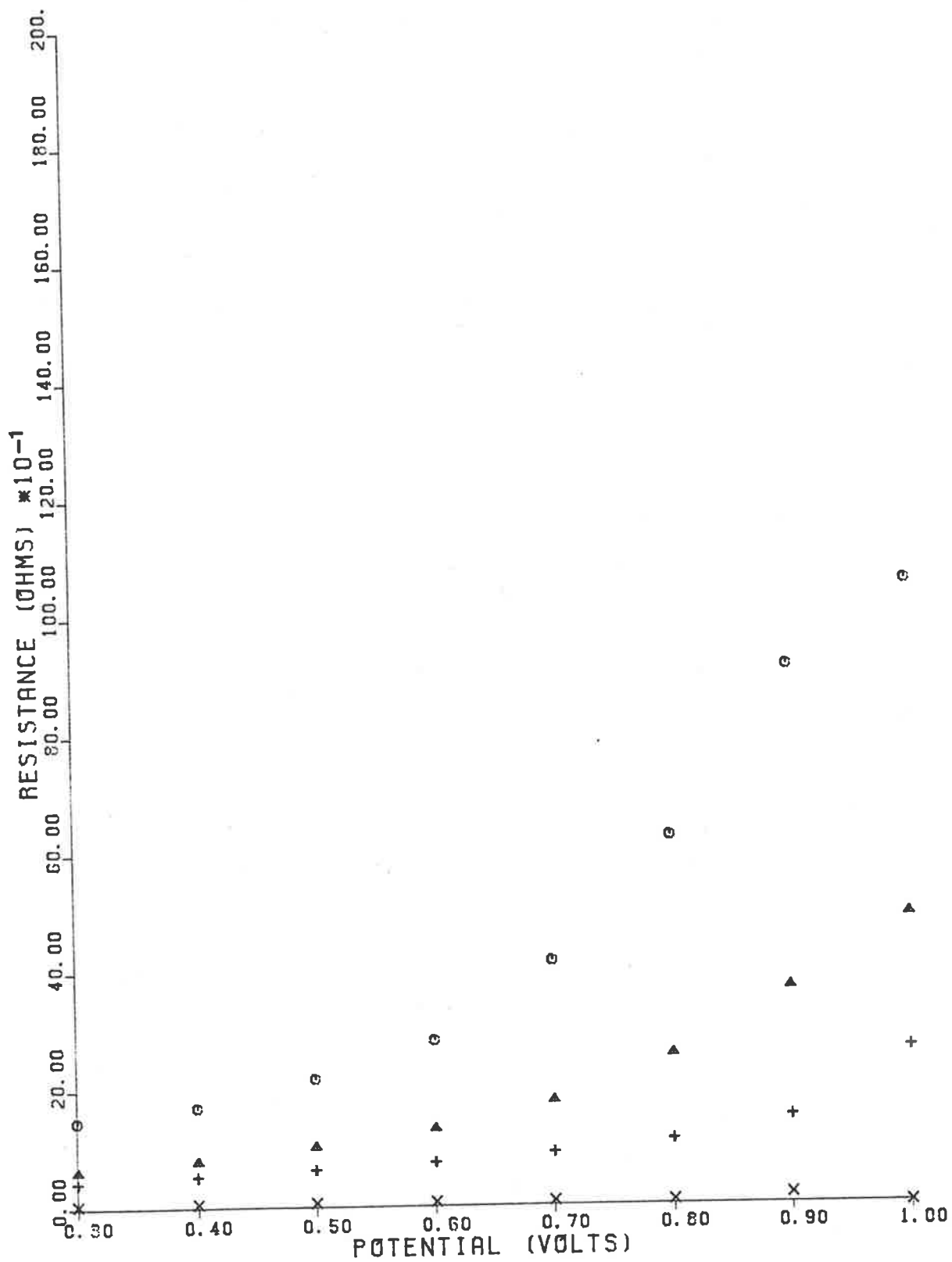


Figure 15. Frequency dependence of series resistance-potential curves for polycrystalline platinum disc in 1.02M HCl: 5 Hz (○); 10 Hz (△); 20 Hz (+); 200 Hz (×). 10 mV/s scan rate.



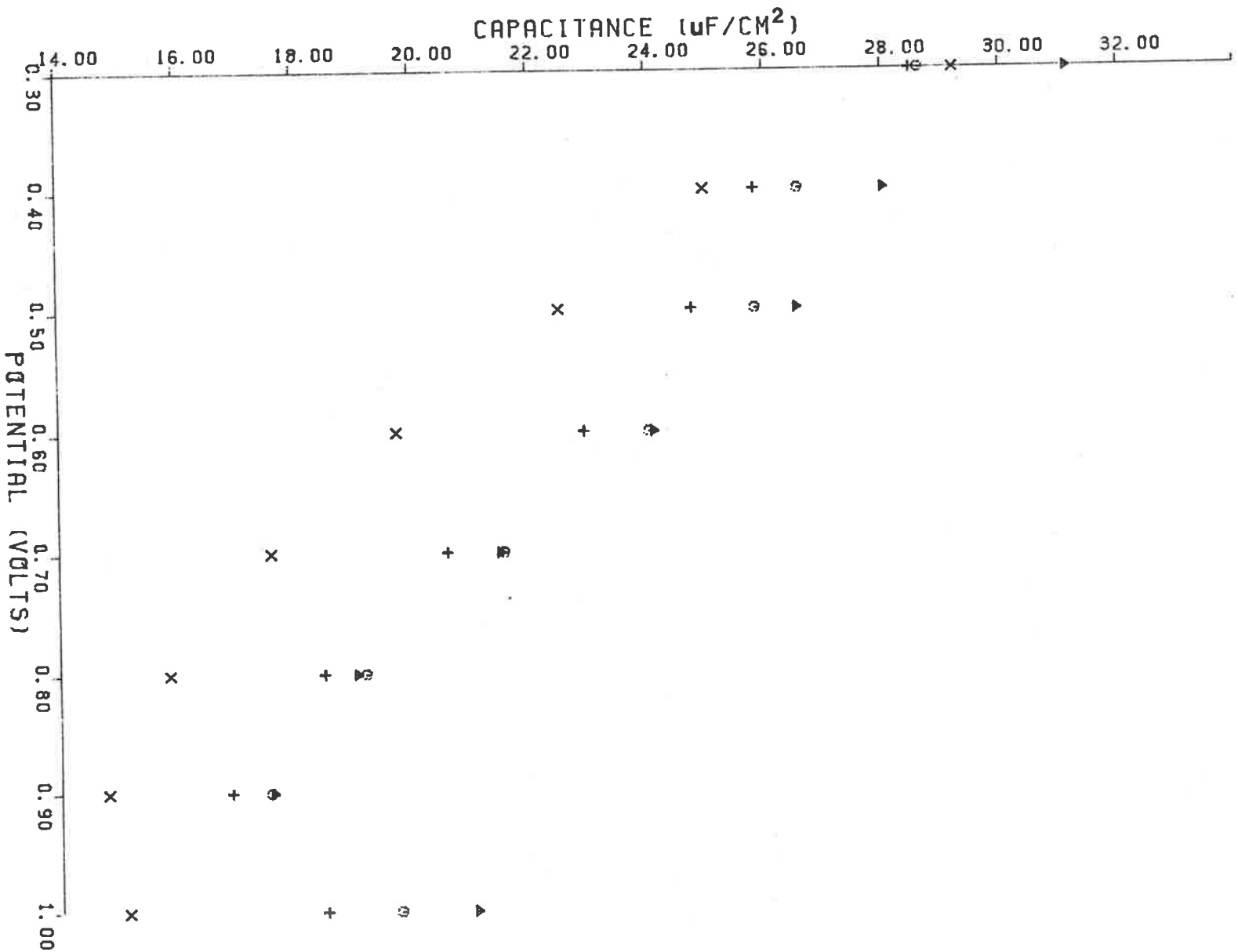


Figure 16. Frequency dependence of parallel capacitance-potential curves for polycrystalline platinum disc in 1.02M HCl: 5 Hz (O); 10 Hz (Δ); 20 Hz (+); 200 Hz (X). 10 mV/s scan rate.

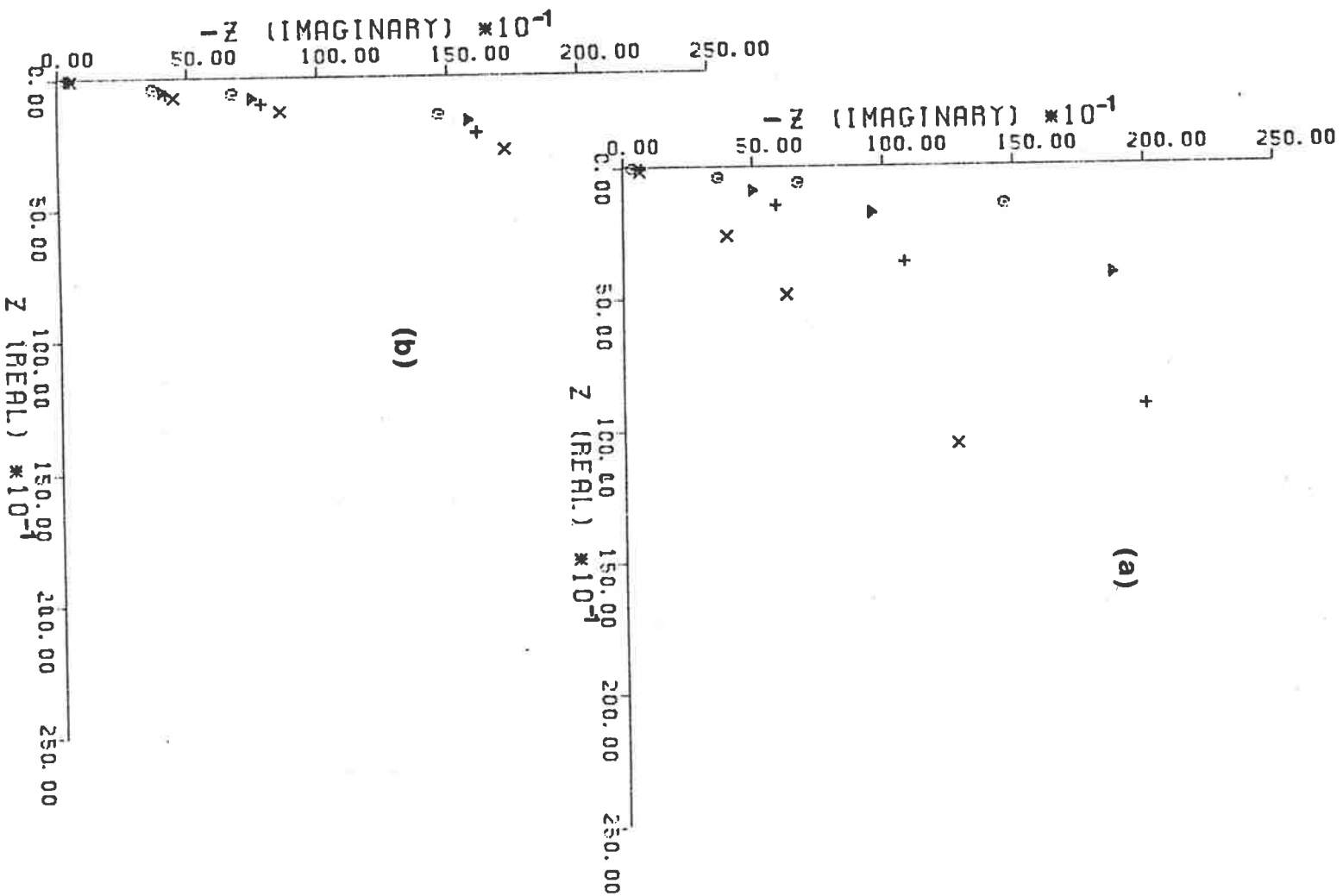


Figure 17.

Complex plane impedance spectra of the polycrystalline platinum disc/1.02M HCl interface at selected electrode potentials. (a) +0.30 V (O); +0.70 V ( $\Delta$ ); +0.90 V (+); +1.00 V (X). (b) +0.30 V (O); +0.40 V ( $\Delta$ ); +0.50 V (+); +0.60 V (X).

respectively. The results were obtained at a frequency of 5 hz using a potential scan rate fo 10 mV/s.

Interpretation of these results for the platinum/1M HCl interface in terms of a resistor and capacitor in series does not appear to conform to reality. The expected series resistance should be low in magnitude due to the high electrolyte concentration, and also independent of the polarizing potential. Figure 13 clearly shows that neither of these criteria are met as the calculated series resistance varies from 96 ohms at +0.30 volts up to 569 ohms at +0.95 volts.

Figures 14 and 15 were obtained using a different polycrystalline platinum electrode. The results show that both the series capacitance and series resistance are dependent on the fréquency of the applied a.c. signal. Figure 16 displays the equivalent parallel capacitance, which also shows some dependence upon frequency. The complex plane impedance spectra for these measurements are presented in Figure 17 for a selection of electrode potentials.

The impedance plane plots made at electrode potentials of +0.30 volts to +0.60 volts are shown in the lower plot in Figure 17. It can be seen that these plots can be approximated by straight lines making an acute angle  $\theta$  to the horizontal axis. The angle  $\theta$  was found to decrease from  $84^\circ$  to  $81^\circ$  upon changing the electrode potential from +0.30 volts to +0.60 volts.

At electrode potentials more anodic than +0.60 volts, the impedance plane plots become increasingly curved with increasing

anodic polarization. This behaviour is contrasted to the linear behaviour at +0.30 volts in the upper plot in Figure 17.

The intercept of the impedance plane curves with the real axis gives the true series resistance. The average intercept at electrode potentials of +0.30, +0.40, +0.50 and +0.60 volts is  $1.4 \pm 5.2$  ohms, corresponding to a very low series resistance through the solution between the working and reference electrodes. This virtual zero resistance is very reasonable, considering the concentration of the electrolyte and the physical nearness of the working and reference electrodes due to the use of a luggin capillary.

The frequency dependence of the series resistance shown in Figure 15 is only an artefact of the non-ideal behaviour of the system. It is evident from the impedance plane plots that the true series resistance can only be measured at high frequencies or found by extrapolation. The high apparent series resistance displayed in Figure 13 was determined using a low frequency of 5 hz. From the preceding discussion it is evident that these results do not reflect the true situation, but rather reflect the failure of the series resistor and capacitor analogue circuit to perfectly mimic the behaviour of the polycrystalline platinum/aqueous 1M HCl interface.

From the Single Current Pulse Method it was noted that capacitance measurements were time dependent. This time dependence was investigated by slowing the potential scan rate in the A.C. Impedance Method. The results were found to be dependent upon the potential scan rate selected.

Figure 18 shows the results obtained using the A.C. Impedance Method with a scan rate of 10 mV/s and a lower scan rate. The results are presented for both the simple series and parallel analogue circuits.

The potential scan took 70 seconds to complete at the moderate scan rate of 10 mV/s, and more than 120 minutes to complete at the lower scan rate. The low scan rate was achieved by maintaining the working electrode at a fixed potential for a period of 15 minutes before making measurements. The electrode potential was then advanced in 0.10 volt steps to more anodic potentials. This controlled potential stepping procedure enabled direct comparison of the A.C. Impedance results with those obtained from Single Current Pulse measurements using the same potential change procedure. This comparison is shown in Figure 19.

From Figure 18 it is clearly evident that there is a marked change with time in both the series and parallel capacitances determined using the A.C. Impedance Method.

From Figure 19 it can be seen that the capacitance-potential curve determined using the A.C. Impedance Method has a similar shape to that determined using the Single Current Pulse Method. All curves display a capacitance minimum at +0.80 volts. The magnitude of the capacitance minimum, however, is some 12% higher for the A.C. Impedance Method than for the Single Current Pulse Method.

Figure 20 shows the resistance-potential curves corresponding to the capacitance data displayed in Figure 18. The curves determined using the A.C. Impedance Method show the effect of time on the cal-

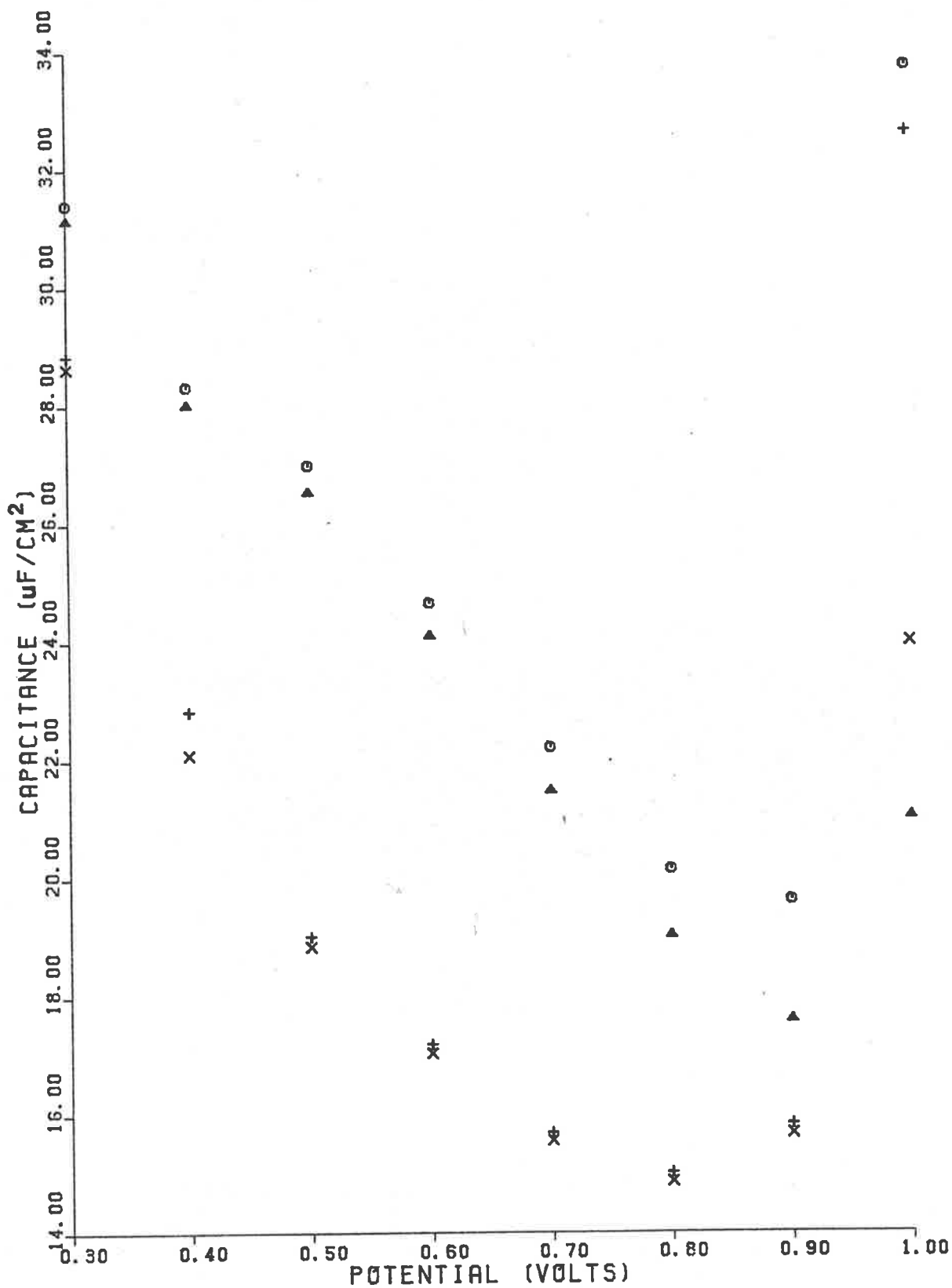


Figure 18. Scan rate dependence of capacitance-potential curves for polycrystalline platinum disc/1.02M HCl interface: series capacitance, 10 mV/s (O); parallel capacitance, 10 mV/s ( $\Delta$ ); series capacitance, slow scan rate (+); parallel capacitance, slow scan rate (X).

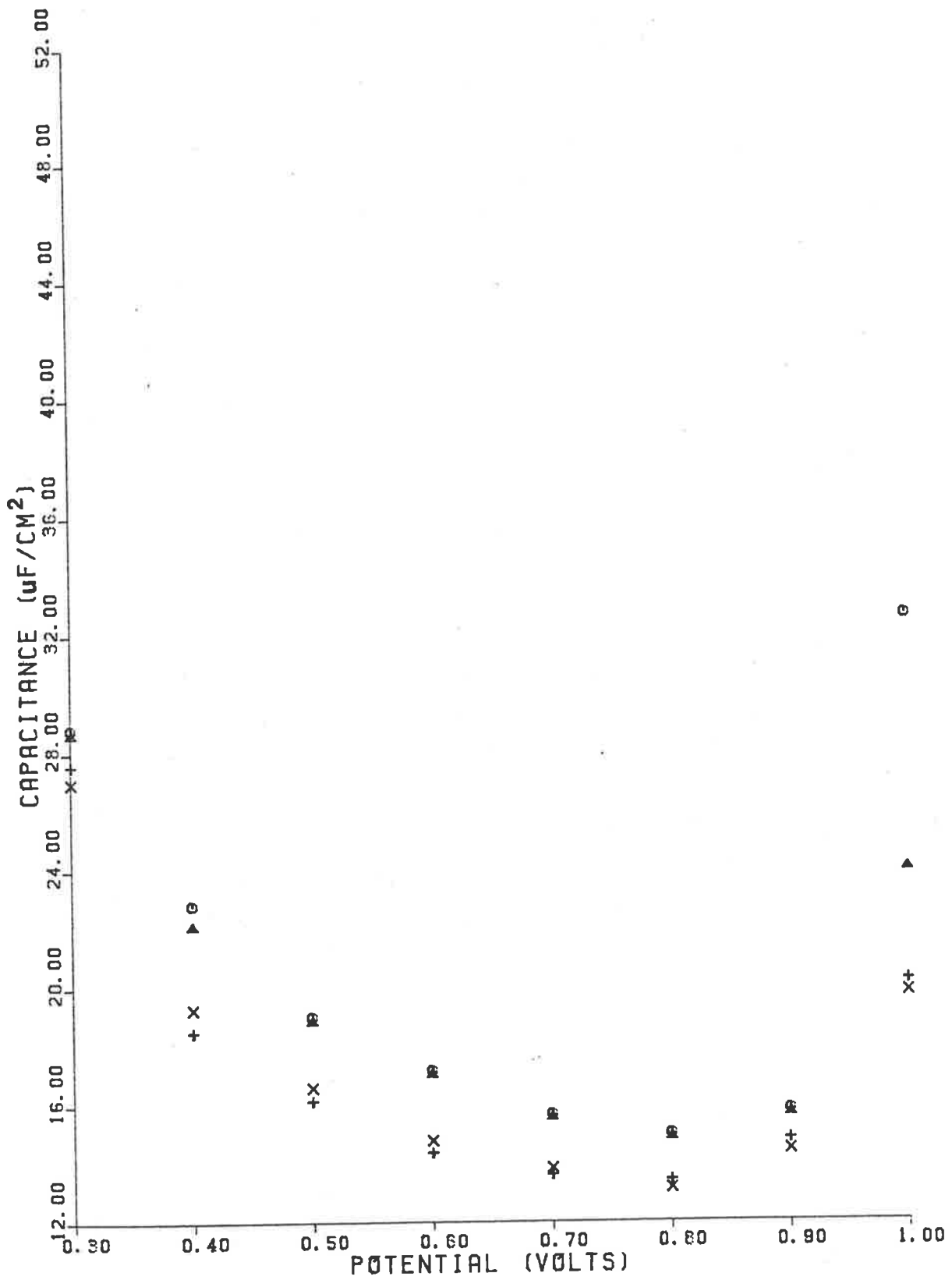


Figure 19. Capacitance-potential curves of polycrystalline platinum disc in 1.02M HCl: series capacitance (O); parallel capacitance (Δ); Polynomial Method (+); Log ( $\Delta V/\Delta t$ ) Plot Method (X). Slow scan rate.

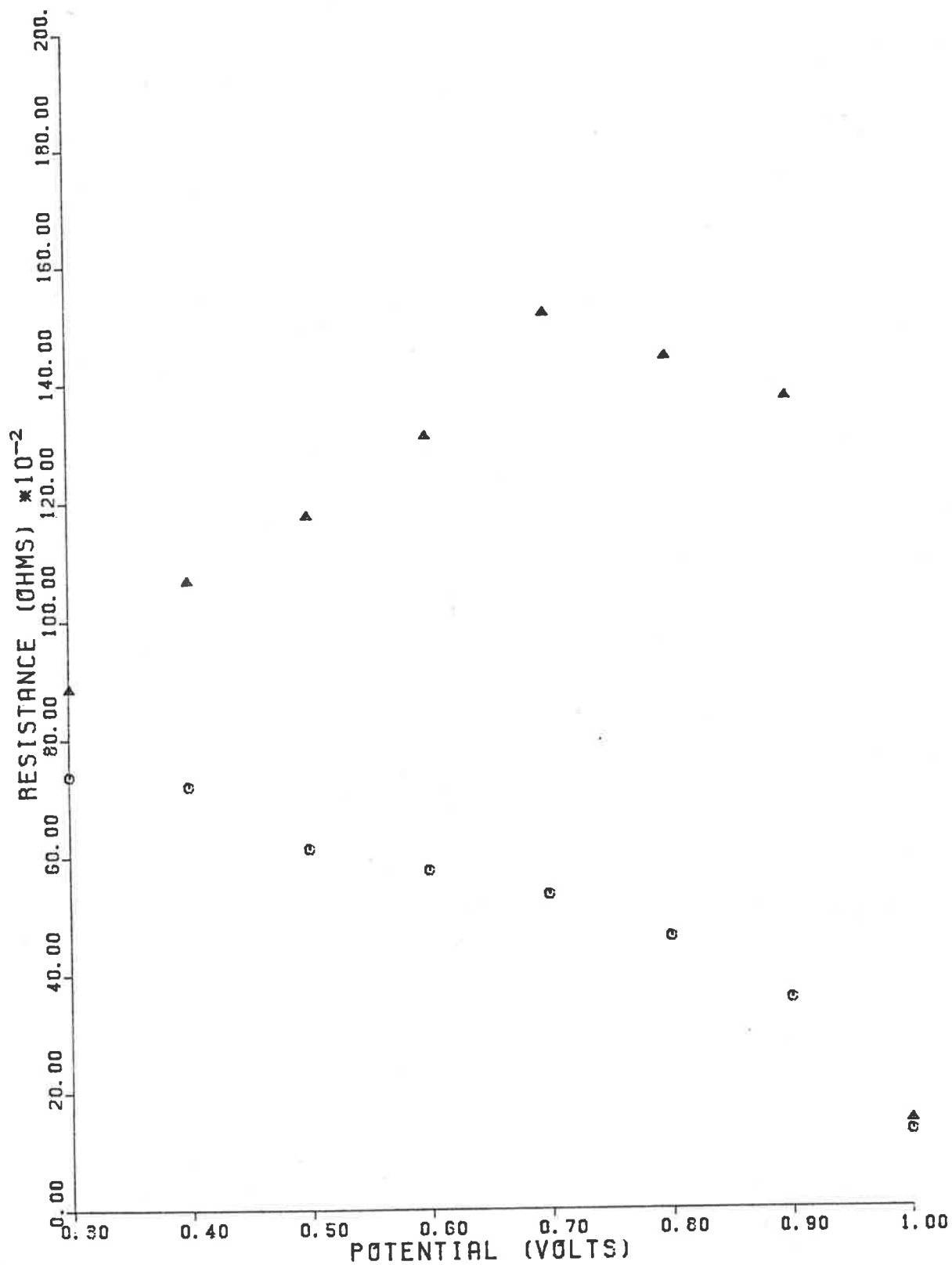


Figure 20. Scan rate dependence of parallel resistance-potential curves of polycrystalline platinum disc in 1.02M HCl: 10 mV/s (O); slow scan rate ( $\Delta$ ).



culated resistance, assuming a simple parallel analogue circuit. In the region of the potential extremes, where faradaic reaction is likely to be occurring, the parallel resistance showed low values, as one would expect. The parallel resistance increased from those regions to a maximum at +0.70 volts, where any faradaic reaction effects are likely to be a minimum.

The value of the parallel resistance determined from the Single Current Pulse Method, however, was very different from that determined using the A.C. Impedance Method.

From the above results and discussion, it is quite obvious that A.C. Impedance data collected for this system at even moderate scan rates will not be characteristic of a stabilized interface. If however, the interface was allowed time to stabilize, then the system showed a response that was more typical of what was expected.

Robertson<sup>13</sup> measured the capacitance in hydrochloric acid at the minimum with respect to potential, employing polished polycrystalline electrodes of different apparent areas varying by a factor of one hundred. He found that the measured capacitance plotted against the apparent electrode area could be fitted by a straight line intercepting the origin. He cited this as evidence that his polished electrode surfaces approximated true planes, within the technique limits to detect surface irregularities, and that the true electrode capacitance at the minimum was  $19 \pm 1 \mu\text{F}/\text{cm}^2$ . This value was used by Riney, Schmidt and Hackerman<sup>2</sup> to normalise their results obtained for the same system using a Single Current Pulse Method. It must be

pointed out, however, that the results of Robertson can also be interpreted as reflecting a consistent electrode surface roughness, due to the use of the same polishing technique to produce smooth electrode surfaces.

Table 3 shows the roughness factors obtained by the author using different methods for a number of polycrystalline platinum electrodes. The first two rows of results present the roughness factor as the ratio of the capacitance minimum at +0.80 volts and a normalising capacitance minimum of either  $19.0 \mu\text{F}/\text{cm}^2$  or  $13.3 \mu\text{F}/\text{cm}^2$ . The value of  $19.0 \mu\text{F}/\text{cm}^2$  is the value suggested by Robertson, whereas the minimum capacitance recorded by the author was found to be  $13.30 \mu\text{F}/\text{cm}^2$ . The final row in the table presents the roughness factor determined from cyclic voltammetry in sulphuric acid solution, as described in Chapter 3 of this thesis.

The capacitance minimum determined at +0.80 volts using the Single Current Pulse Method was  $13.30 \mu\text{F}/\text{cm}^2$ ,  $17.72 \mu\text{F}/\text{cm}^2$ ,  $21.80 \mu\text{F}/\text{cm}^2$  and  $21.52 \mu\text{F}/\text{cm}^2$  for electrodes A, B, C and D, respectively. The above capacitance minima were determined from the capacitance-potential curves displayed in Figures 3, 4, 5 and 6, respectively.

From Table 3 it can be seen that better correspondence of determined roughness factors occurs between the cyclic voltammetric results and the capacitance measurements using a normalising factor of 13.3. Even using this as the normalising factor, the agreement between the cyclic voltammetric and capacitance results is only moderate.

Table 3

Roughness factors determined by different methods  
for a number of polycrystalline platinum electrodes

Electrode	A Pt disc	B Pt Cottrell Cell	C Teflon-encased Pt	D Teflon-encased Pt
Method				
$C_{\min}/19.0$	0.70	0.93	1.15	1.13
$C_{\min}/13.3$	1.00	1.33	1.64	1.62
Cyclic Voltammetry	1.09	2.05	1.48	1.48

## 5.21

The lowest apparent roughness factor was determined for the platinum disc electrode, which was the only electrode to undergo a flame cleaning technique. The other electrodes, B, C, and D, all underwent standard polishing and etching techniques.

**CONCLUSION**

The capacitance of the polycrystalline platinum/1M HCl interface was determined using both the Single Current Pulse Method and the A.C. Impedance Method. The capacitance was found to have a time dependence that was also dependent on the polarizing potential. The resultant capacitance-potential curves were found to qualitatively agree with those previously determined by Robertson,<sup>13</sup> and Riney, Schmidt and Hackerman.<sup>2</sup>

For the Single Current Pulse measurements, the Polynomial Method and the Log ( $\Delta V/\Delta t$ ) Plot Method were found to give almost identical results. The apparent parallel capacitance determined via these methods was found to be independent of time, but dependent on the polarizing potential. The parallel capacitance was found to be low, and to increase with increasing anodic polarization.

The complex plane impedance plots determined using the A.C. Impedance Method fell into two basic groups. At cathodic potentials up to +0.60 volts, the data was best fitted by a straight line making an acute angle of more than  $80^\circ$  with the real axis. The interface at these potentials is equivalent to a pure capacitor, with distortion due to surface roughness. At potentials more anodic than +0.60 volts, the data was best fitted by an arc of a hemi-circle corresponding to the analogue circuit of a capacitor and resistor in parallel.

## 5.23

The capacitances determined by the Single Current Pulse Method and the A.C. Impedance Method were found to give reasonable qualitative agreement, but were consistently higher for the A.C. Impedance Method. The parallel resistances determined by the methods were dissimilar, with the resistance determined by the A.C. Impedance Method being considerably greater than that determined by the Single Current Pulse Method.

Roughness factors determined via the cyclic voltammetric method and a capacitance normalisation procedure were compared, and found to give poor to moderate agreement only. The platinum disc electrode, however, was found to have the lowest roughness factor using either method.

SYSTEM II: Pt + 0.100M X + H<sub>2</sub>O

*Pt/0.100M NaCl/H<sub>2</sub>O*

Figures 21 and 22 show the capacitance-potential curves determined from A.C. Impedance measurements for the polycrystalline platinum/ aqueous 0.100M NaCl interface at a frequency of 10 hz.

Figure 21 shows the series capacitance determined at a moderate scan rate of 10 mV/s and a much slower scan rate. The slow scan rate was obtained by holding the working electrode at a constant potential for a period of 15 minutes before stepping the electrode potential by 0.10 volts to a more anodic potential. At all potentials other than the initial potential at -0.50 volts, the capacitance determined at the slow scan rate was lower than that determined at the faster scan rate of 10 mV/s.

Figure 22 shows the capacitance-potential curves obtained at the slow scan rate, assuming the interface to behave as a series resistor and either a series capacitor or a capacitor and resistor in parallel. The capacitance determined as a parallel capacitance was quite similar to that determined as a series capacitance.

The general shape of all the capacitance-potential curves is similar. Each curve has a central capacitance hump with a maximum at about 0.00 volts, and high capacitance extremes.

*Pt/0.100M KNO<sub>3</sub>/H<sub>2</sub>O*

Figures 23-25 show the capacitance-potential curves determined assuming simple series and parallel equivalent circuits for the poly-

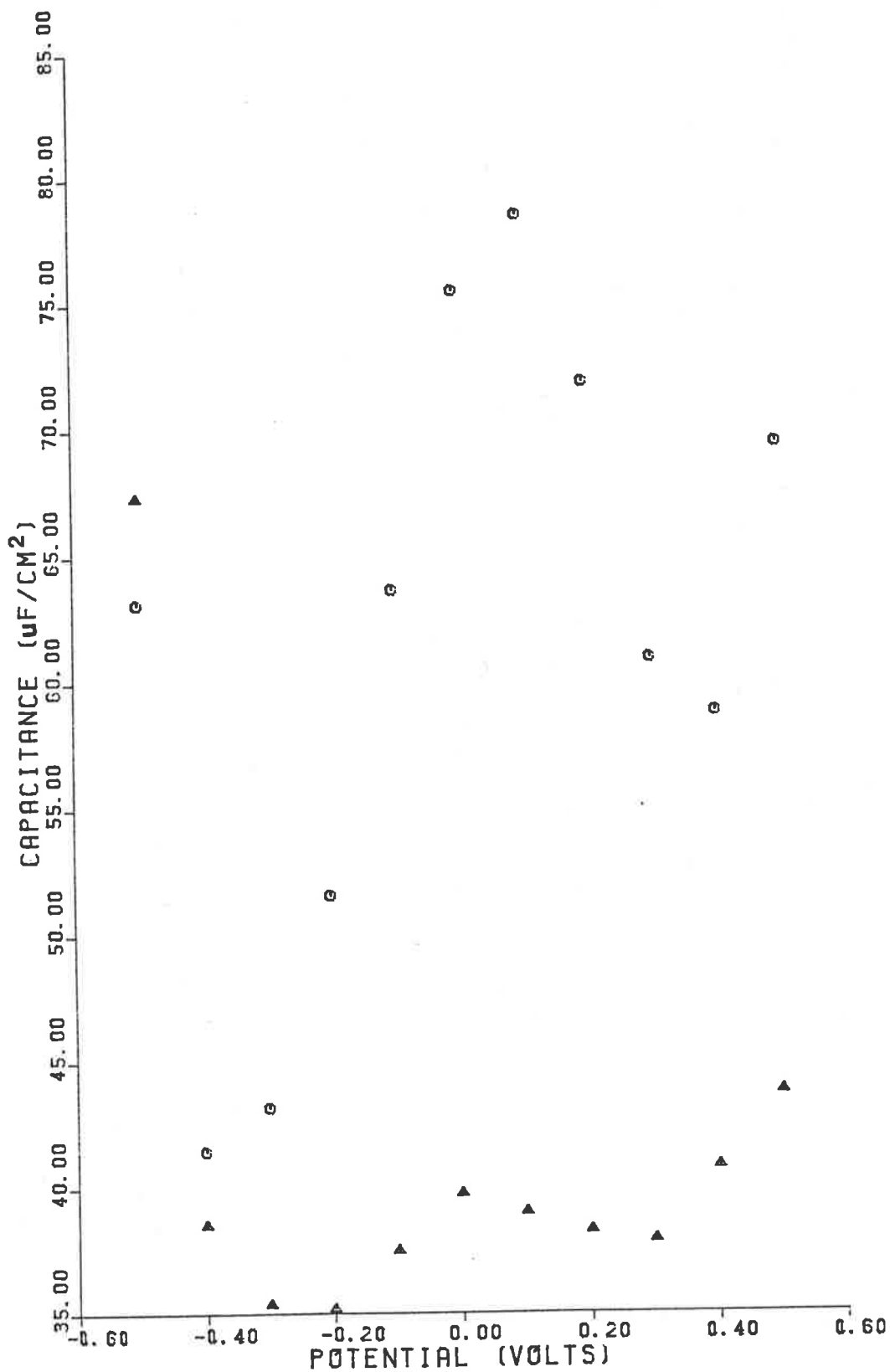


Figure 21. Scan rate dependence of series capacitance-potential curves of Teflon-encased polycrystalline platinum in 0.100M NaCl at 10 hz: 10 mV/s (O); slow scan rate (Δ).



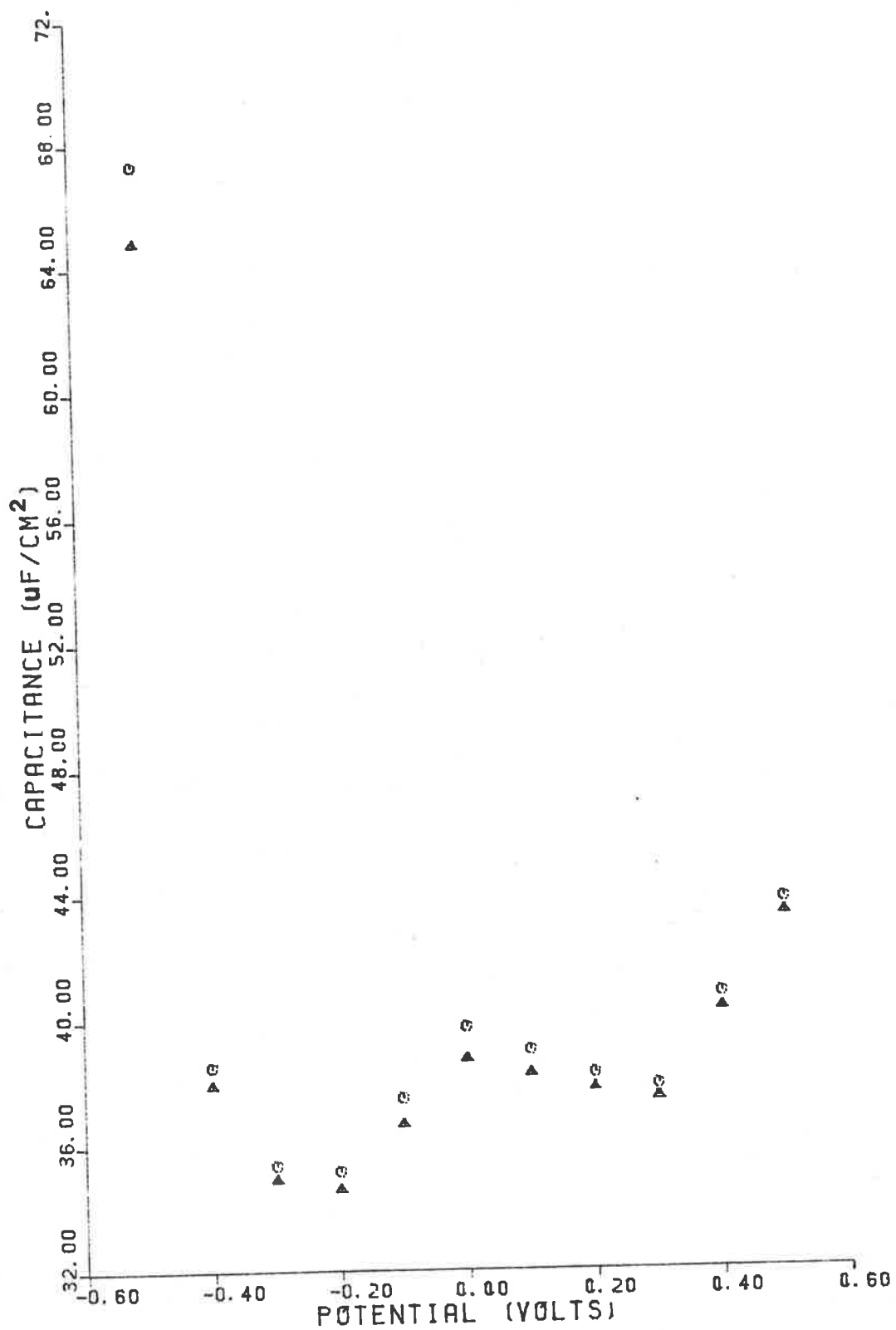


Figure 22. Capacitance-potential curves of Teflon-encased polycrystalline platinum in 0.100M NaCl at 10 Hz: series capacitance (O); parallel capacitance ( $\Delta$ ). Slow scan rate.

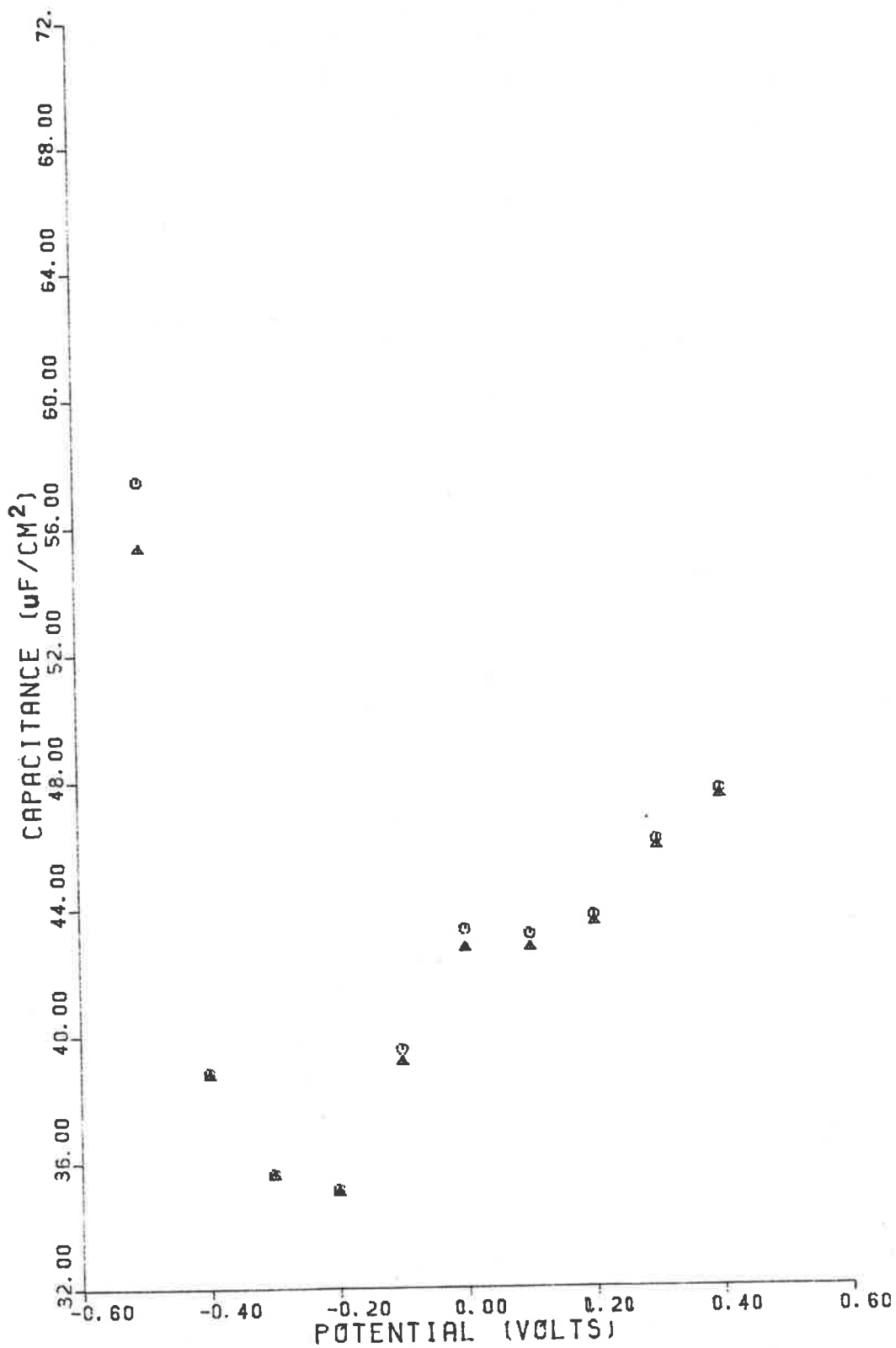


Figure 23. Capacitance-potential curves of Teflon-encased polycrystalline platinum in  $0.100\text{M KNO}_3$  at 20 Hz: series capacitance (O); parallel capacitance ( $\Delta$ ). Slow scan rate.

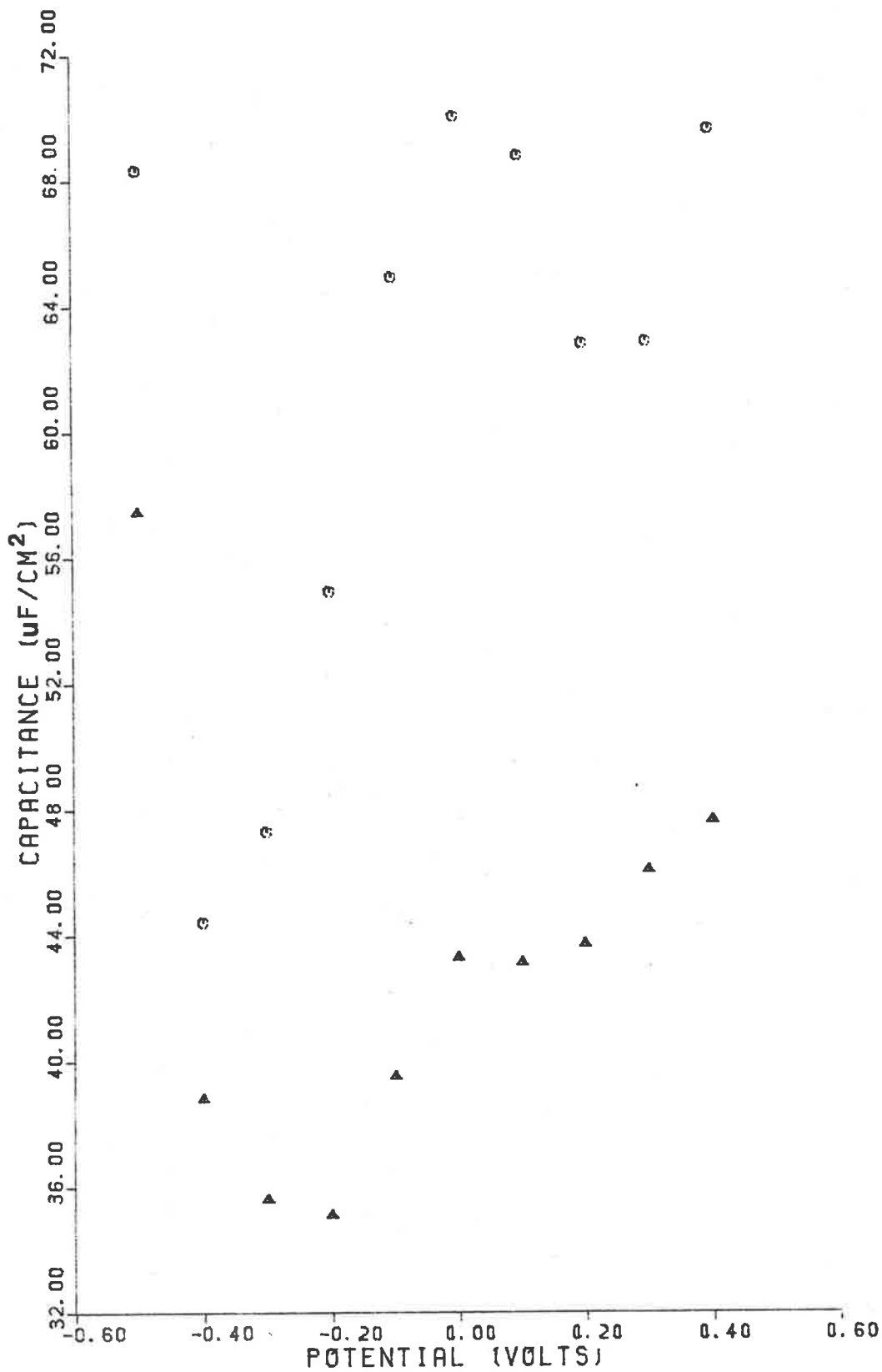


Figure 24. Scan rate dependence of series capacitance-potential curves of Teflon-encased polycrystalline platinum in 0.100M  $\text{KNO}_3$  at 20 Hz: 5 mV/s (O); slow scan rate ( $\Delta$ ).

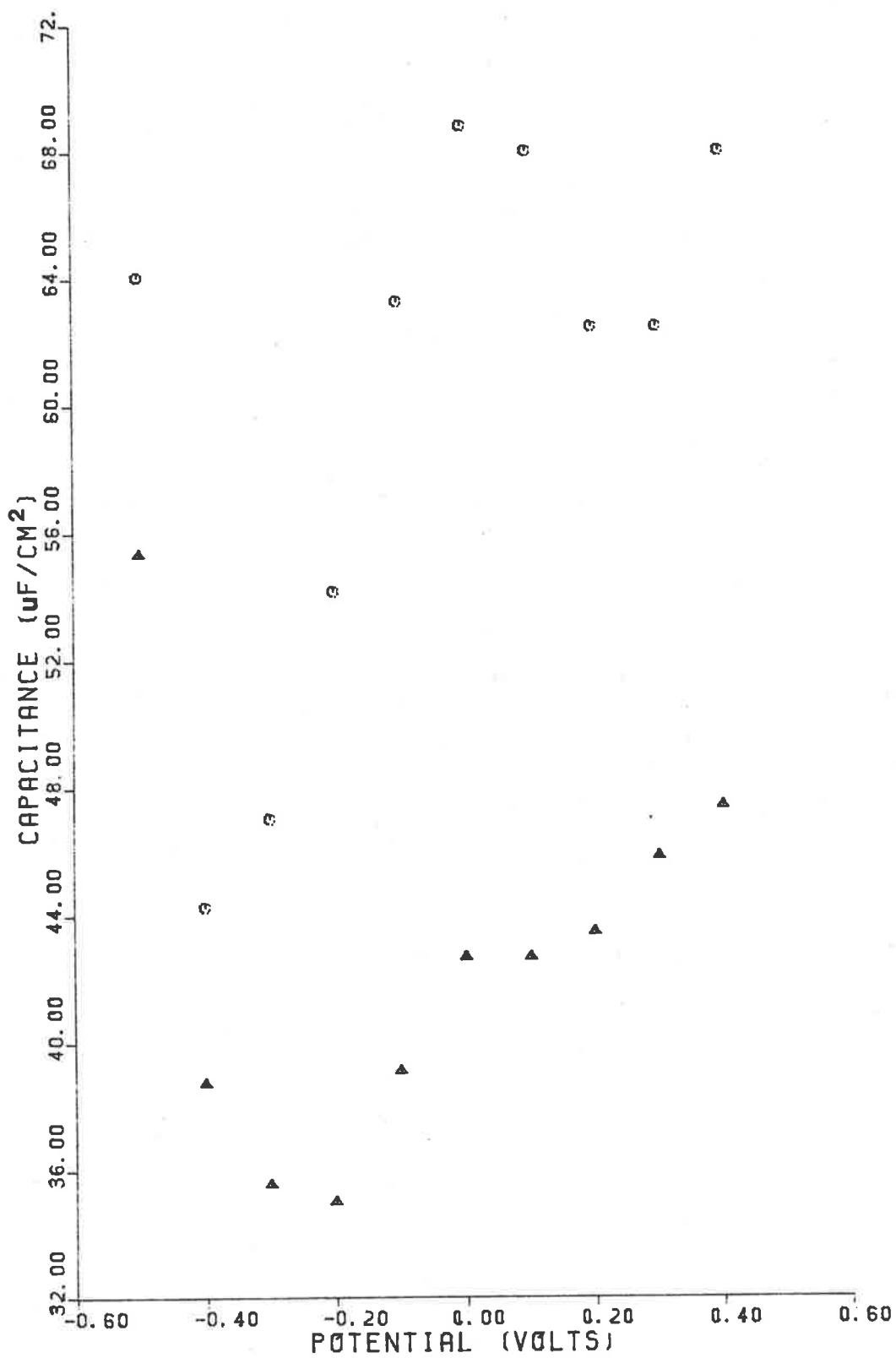


Figure 25. Scan rate dependence of parallel capacitance-potential curves of Teflon-encased polycrystalline platinum in 0.100M  $\text{KNO}_3$  at 20 Hz: 5 mV/s (O); slow scan rate ( $\Delta$ ).

crystalline platinum/aqueous 0.100M  $\text{KNO}_3$  interface using the A.C. Impedance Method. The results were obtained at a frequency of 20 hz.

The capacitance determined for the series and parallel analogue circuits is quite similar, except at the potential range extremes, where the ratio of the real current and the imaginary current becomes significant.

The capacitance-potential curves show marked differences between those obtained at a moderate scan rate of 5 mV/s and those obtained at a much slower scan rate. The slow scan rate was achieved by maintaining the working electrode at a fixed potential for a period of 12 minutes before taking measurements. The electrode potential was then stepped by 0.10 volts to a more anodic potential.

Figure 26 shows the capacitance-potential curves obtained using the A.C. Impedance Method and the Single Current Pulse Method. The curves were obtained by holding the working electrode at a potential for 12 minutes prior to making the measurements. After the measurements, the electrode potential was stepped to a new potential, 0.10 volts more anodic than the previous potential. From Figure 26 it can be seen that there is reasonable agreement, excepting between -0.40 volts and 0.00 volts, where the capacitance determined using the A.C. Impedance Method is considerably lower than that determined using the Single Current Pulse Method.

The parallel resistance determined for the simple analogue circuit of a capacitor and resistor in parallel is presented in Table 4. It

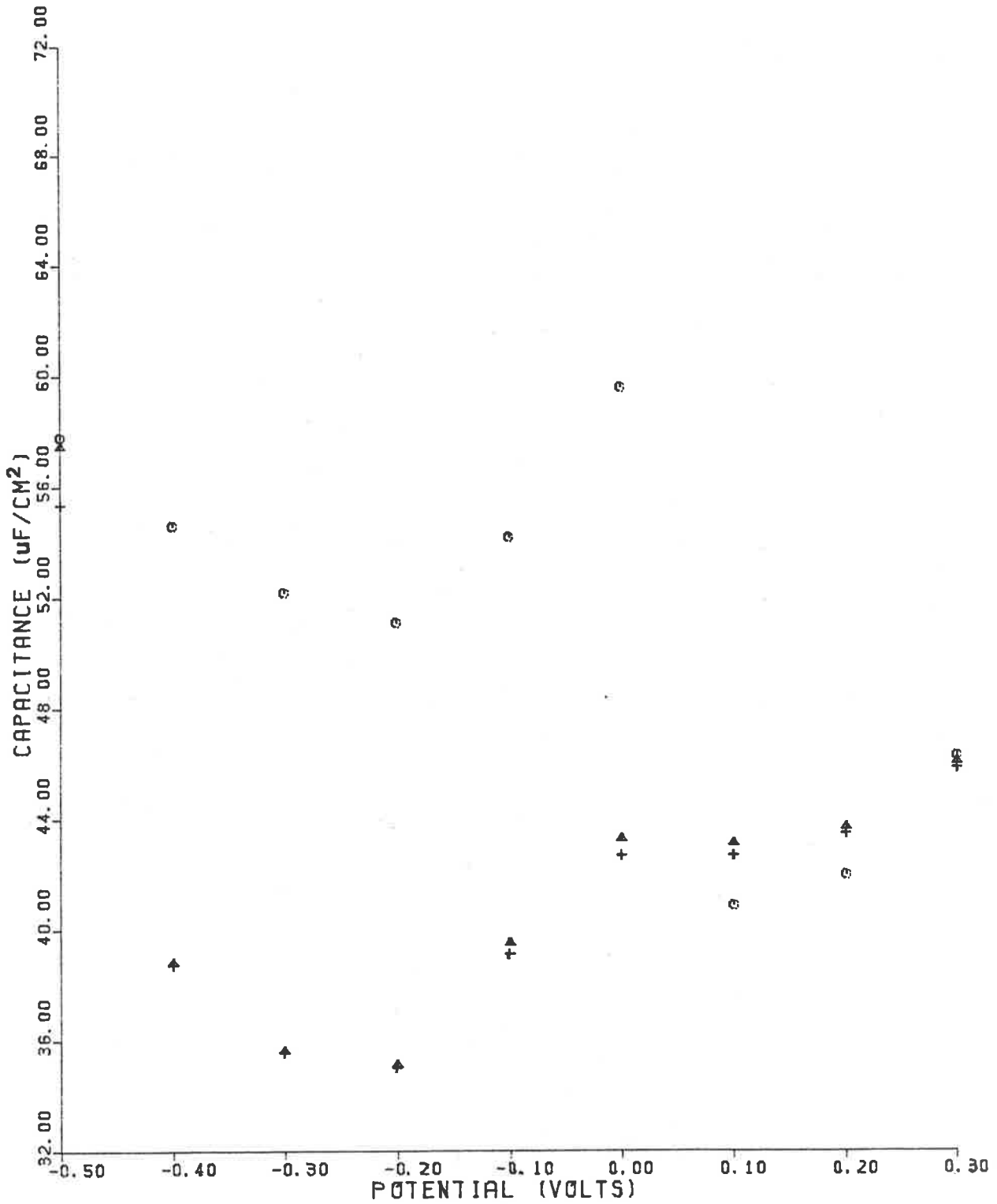


Figure 26. Capacitance-potential curves of teflon-encased polycrystalline platinum in 0.100M  $\text{KNO}_3$ : Single Current Pulse Method (○); series capacitance, 20 hz (△); parallel capacitance, 20 hz (+). Slow scan rate.

**Table 4**

Comparison of parallel resistance in ohms  
calculated from A.C. Impedance Method at 20 hz  
with Single Current Pulse Method at various electrode potentials

<i>Potential/volts</i>	-0.50	-0.40	-0.30	-0.20	-0.10	0.00	+0.10	+0.20	+0.30
<i>Method</i>									
<i>A.C. Impedance</i>	1049	5751	7987	5751	2875	2246	2614	3594	3594
<i>Single Current Pulse</i>	95	215	321	389	310	200	259	323	487

can clearly be seen that there is very poor agreement between the resistance determined by the A.C. Impedance Method and the Single Current Pulse Method. The results presented in Table 4 for the Single Current Pulse Method are those determined using the Isaacs-Leach Log ( $\Delta V/\Delta t$ ) Plot Method.

The general shape of the capacitance-potential curves presented in Figures 23-26 is similar to that presented for the Pt + 0.100M NaCl + H<sub>2</sub>O system, having a central capacitance hump with a maximum at 0.00 volts.

*Pt/0.100M NaNO<sub>3</sub>/H<sub>2</sub>O*

A typical cyclic voltammogram is displayed in Figure 27 for the polycrystalline platinum +0.100M NaNO<sub>3</sub> + H<sub>2</sub>O system. A scan rate of 20 mV/s was used. From the cyclic voltammogram it can be seen that the potential region between -0.60 volts and +0.60 volts is a region where little oxidation or reduction occurs, and thus was selected as the region for double layer capacitance measurements.

The A.C. Impedance Method was used to determine the capacitance-potential curves for the polycrystalline platinum/aqueous 0.100M NaNO<sub>3</sub> interface. Figures 28, 29 and 32 were obtained using a Teflon-encased polycrystalline platinum working electrode, and Figures 30, 31 and 33 were obtained using a polycrystalline platinum disk working electrode.

From Figures 28-31 it can be seen that the apparent series capacitance obtained using a moderate scan rate of 20 mV/s is markedly frequency dependent.



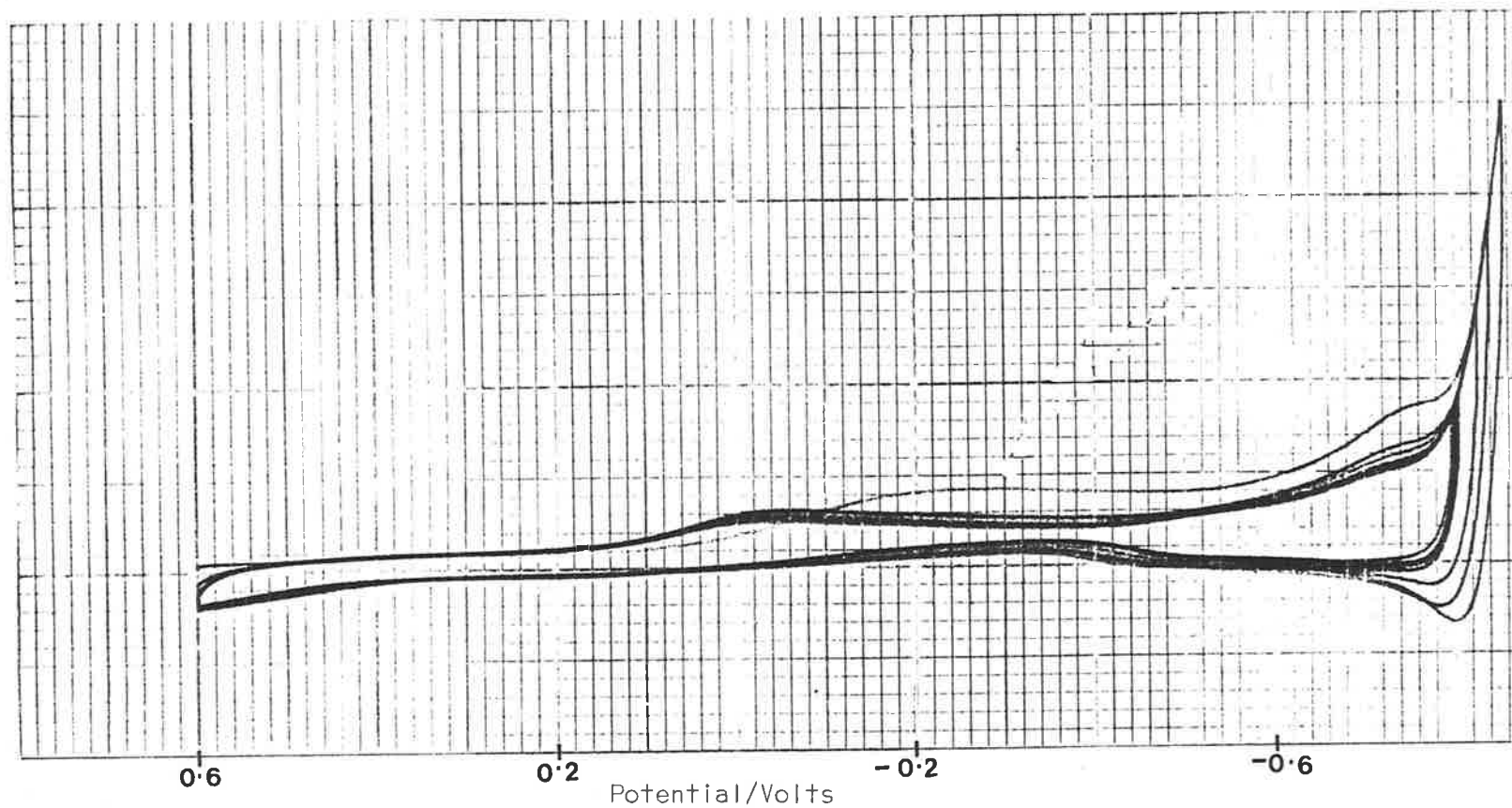


Figure 27. Cyclic voltammograms of polycrystalline platinum in 0.100M  $\text{NaNO}_3$ . Full scale vertical = 0.2 mA. 20 mV/s scan rate.

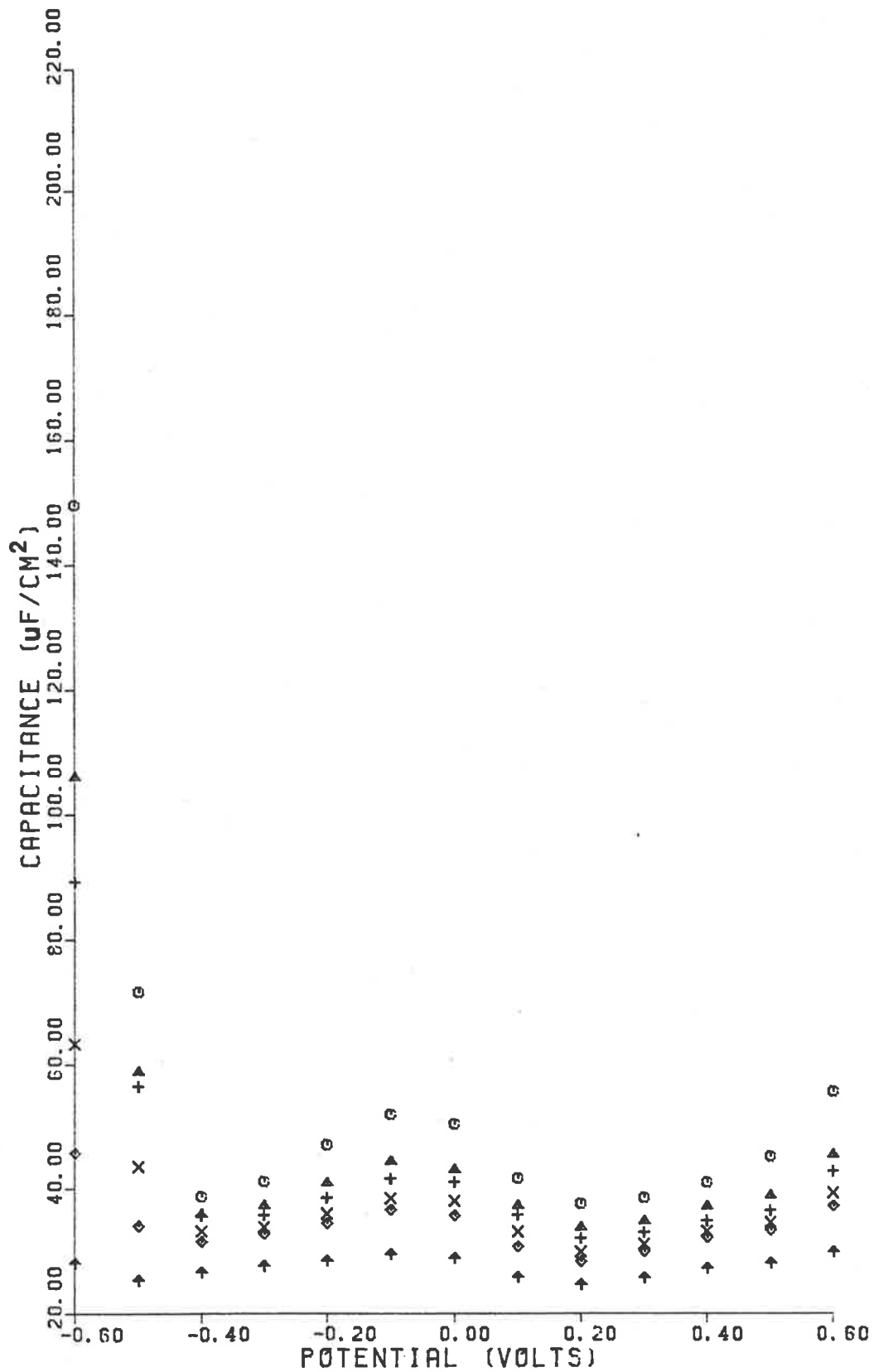


Figure 28. Frequency dependence of series capacitance-potential curves: 10 Hz (O); 30 Hz ( $\Delta$ ); 60 Hz (+); 140 Hz ( $\times$ ); 240 Hz ( $\diamond$ ); 400 Hz ( $\uparrow$ ). Cathodic scan. 20 mV/s scan rate.

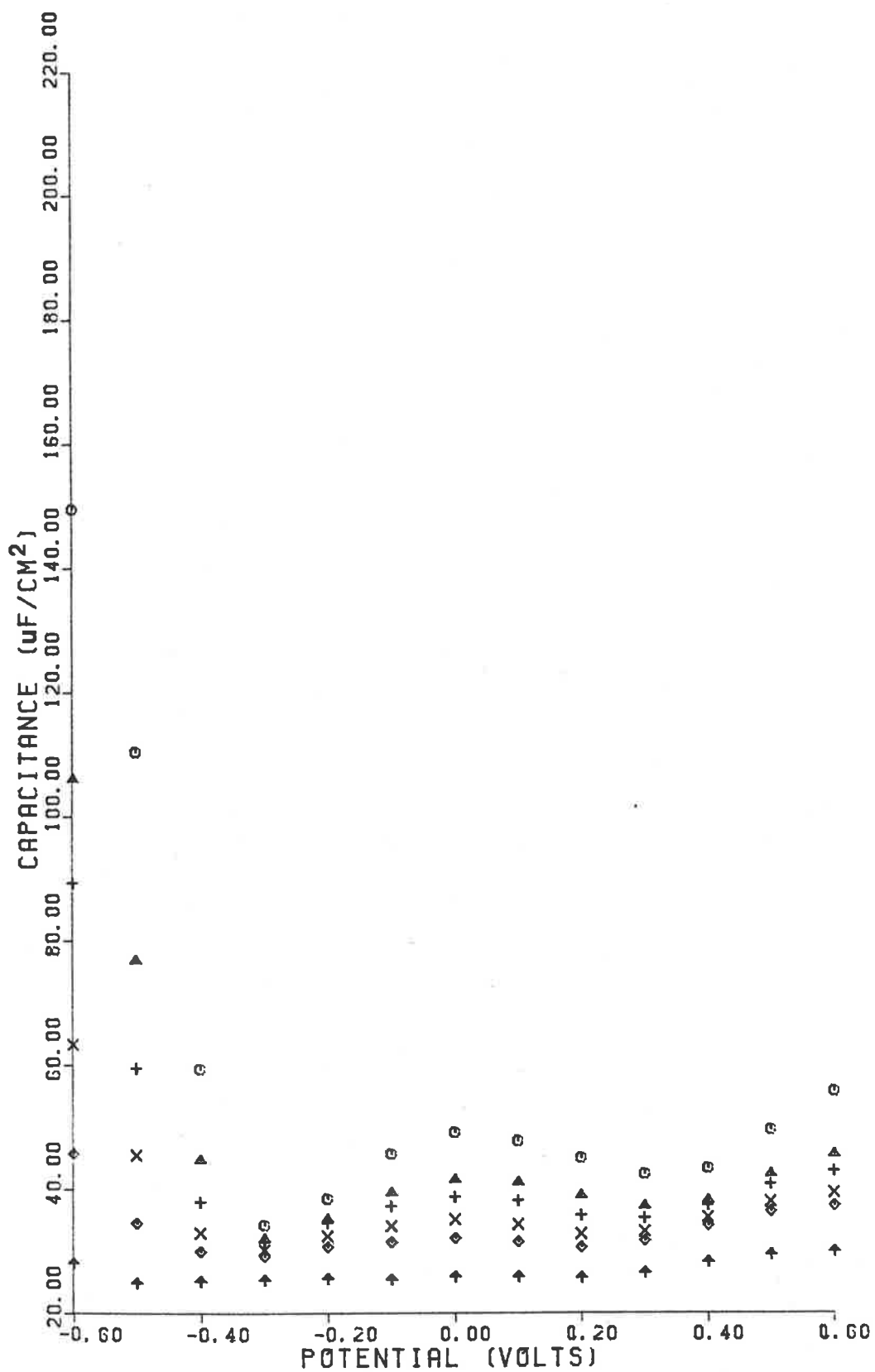


Figure 29. Frequency dependence of series capacitance-potential curves: 10 Hz (O); 30 Hz (Δ); 60 Hz (+); 140 Hz (X); 240 Hz (◇); 400 Hz (↑). Anodic scan. 20 mV/s scan rate.

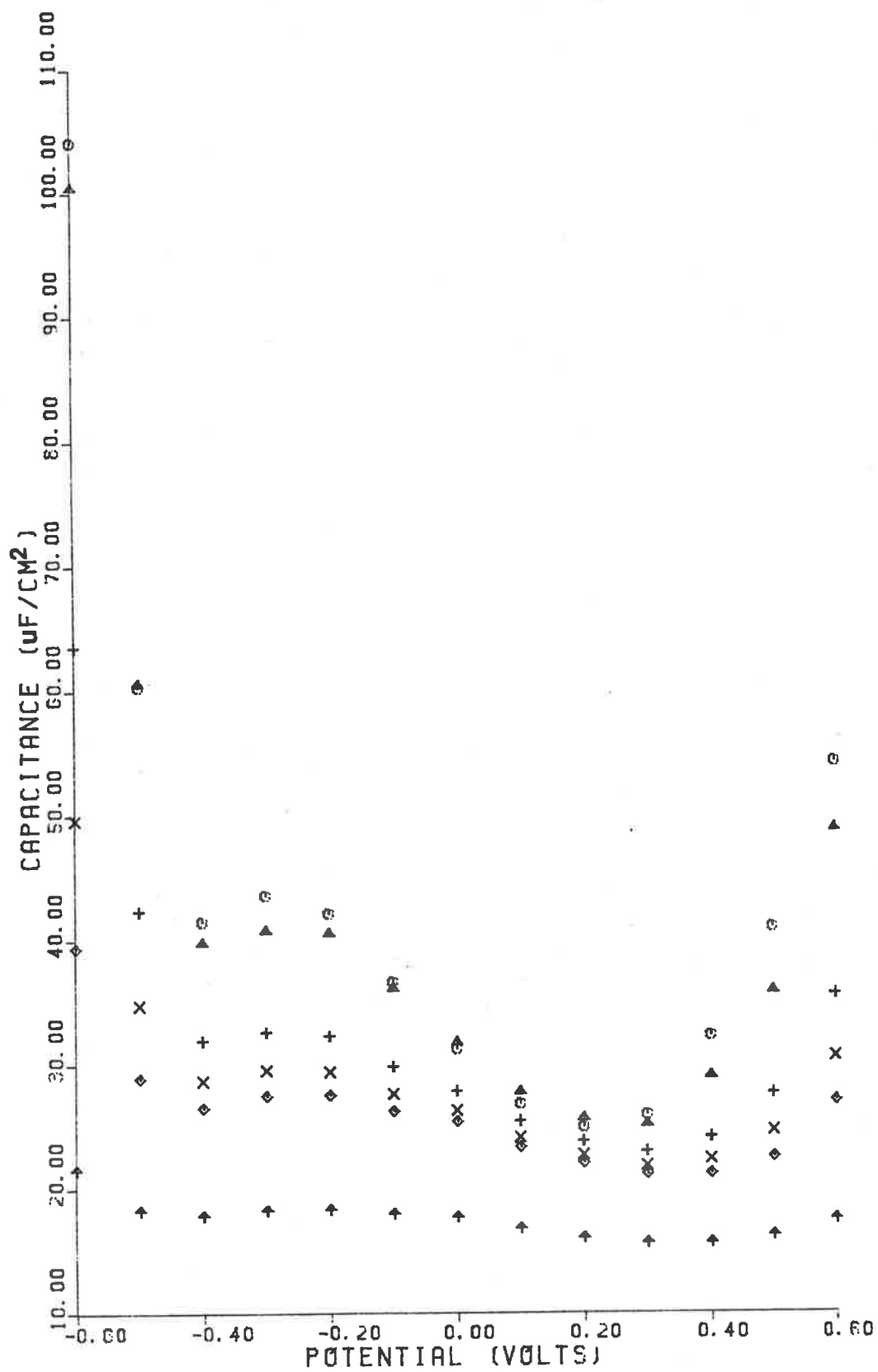


Figure 30. Frequency dependence of series capacitance-potential curves: 10 Hz (O); 20 Hz (Δ); 80 Hz (+); 140 Hz (X); 280 Hz (◇); 400 Hz (↑). Cathodic scan. 20 mV/s scan rate.

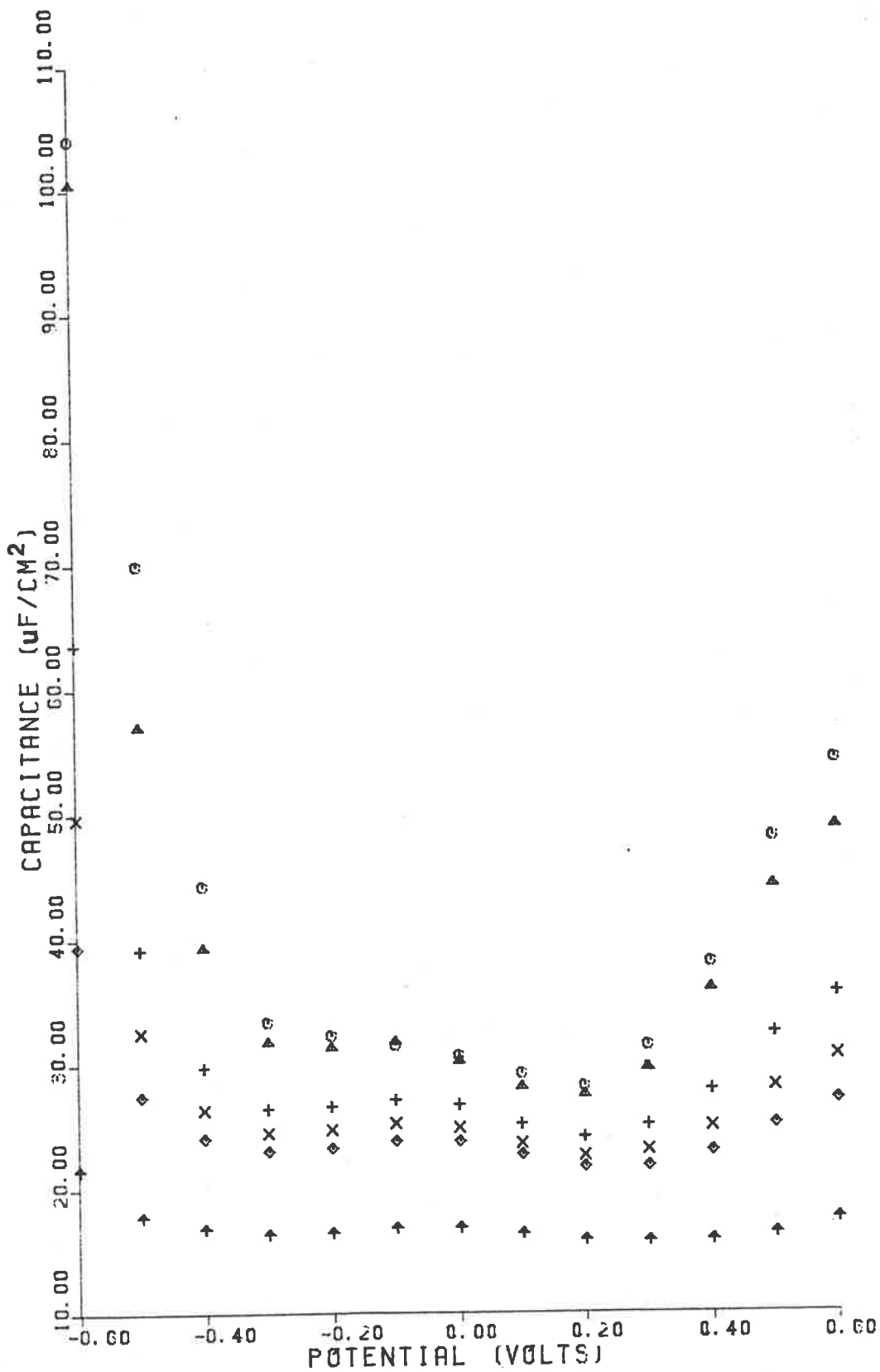


Figure 31. Frequency dependence of series capacitance-potential curves: 10 Hz (O); 20 Hz (Δ); 80 Hz (+); 140 Hz (X); 280 Hz (◇); 400 Hz (↑). Anodic scan. 20 mV/s scan rate.

## 5.27

Figures 32 and 33 show the series capacitance-potential curves determined at a moderate scan rate and at a much slower scan rate. The slow scan rate was achieved by maintaining the electrode potential constant for a fixed time period before making measurements. After the measurements, the electrode potential was stepped 0.10 volts increasingly in either a cathodic or anodic direction. The result displayed in Figure 32 for the slow scan rate was obtained by stepping the potential to an increasingly cathodic potential every 10 minutes. The results displayed in Figure 33 at the slow scan rate were obtained by stepping the potential 0.10 volts every 15 minutes to increasingly anodic potentials.

Figures 32 and 33 are not directly comparable, but both clearly show that determined series capacitance is time dependent. The capacitances determined at the slower scan rate are consistently lower than those determined at the faster scan rate.

Tables 5 and 6 show the effect of frequency on the capacitance determined, assuming a series capacitor or capacitor and resistance in parallel, for the Teflon-encased platinum and platinum disk working electrodes, respectively. The measurements were made for each electrode at +0.20 volts after the electrode had been maintained at that potential for more than 20 minutes. This ensured that the measurements reflected stable values that were independent of the time of measurement.

Figures 34 and 35 show the impedance plane plots corresponding to the results in Tables 5 and 6, respectively. The impedance plane plots

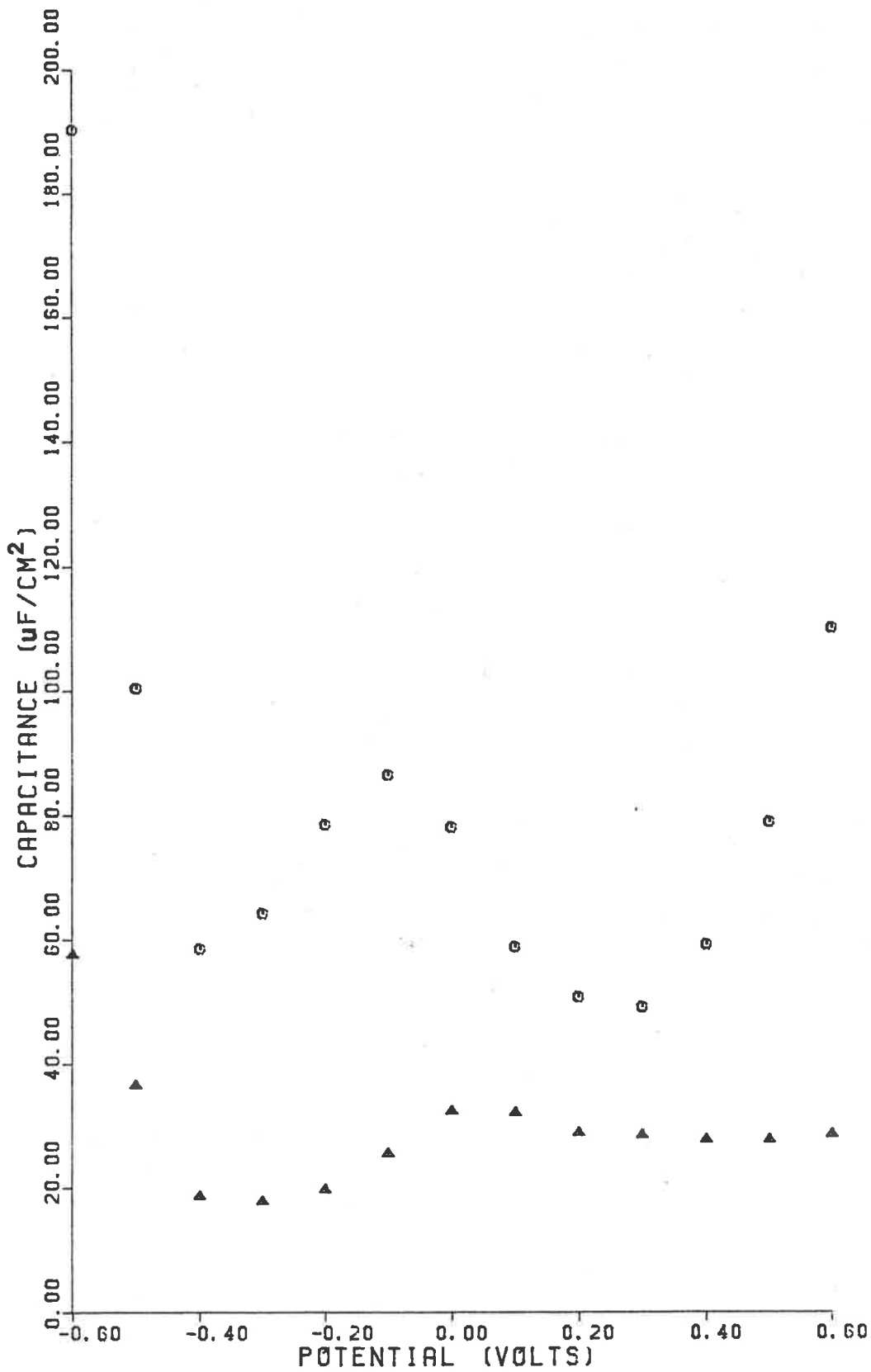


Figure 32. Scan rate dependence of series capacitance-potential curves at 10 Hz: 20 mV/s (O); slow scan rate ( $\Delta$ ). Cathodic sweep.

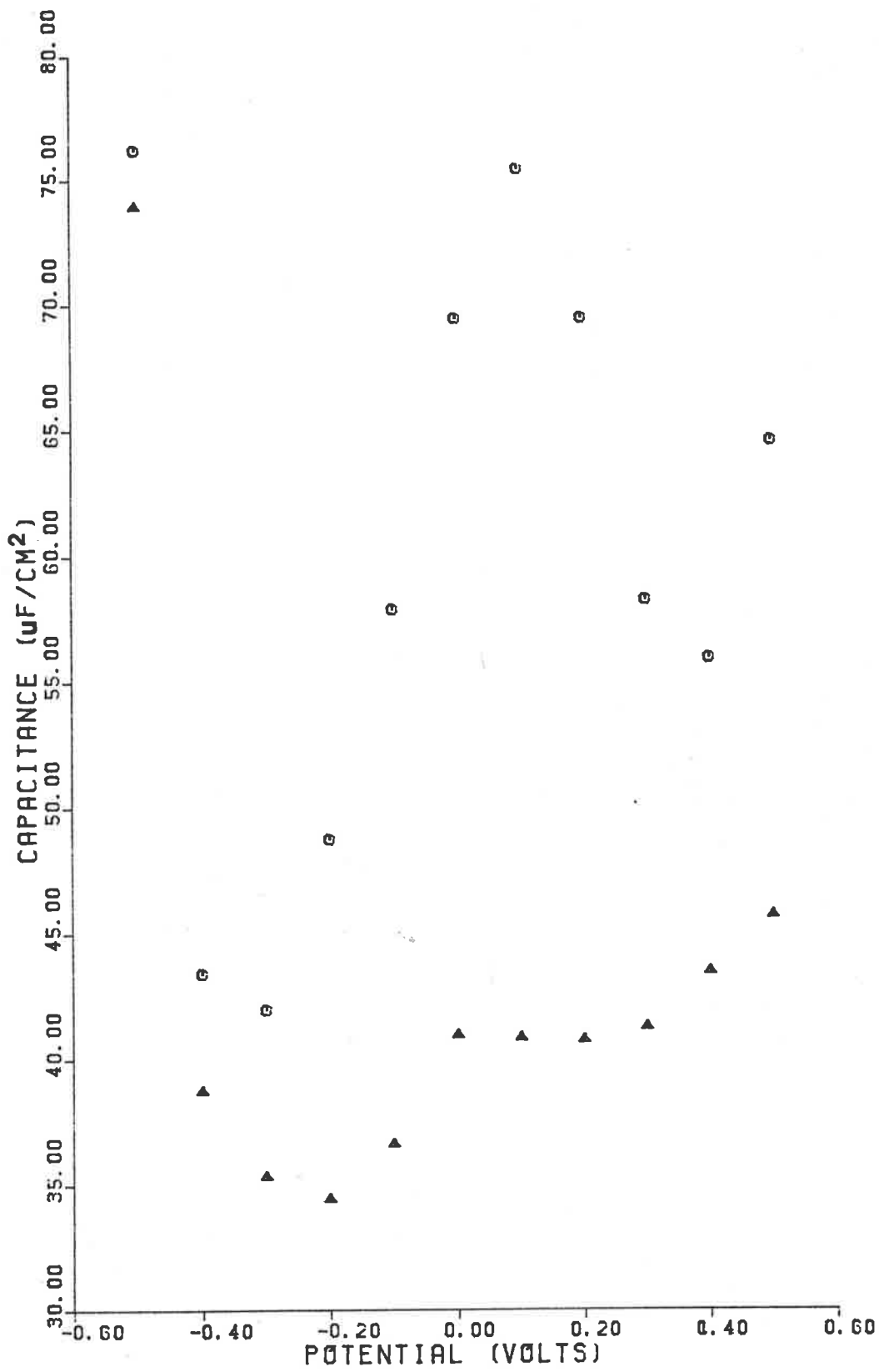


Figure 33. Scan rate dependence of series capacitance-potential curves at 10 Hz: 5 mV/s (O); slow scan rate (Δ). Anodic sweep.



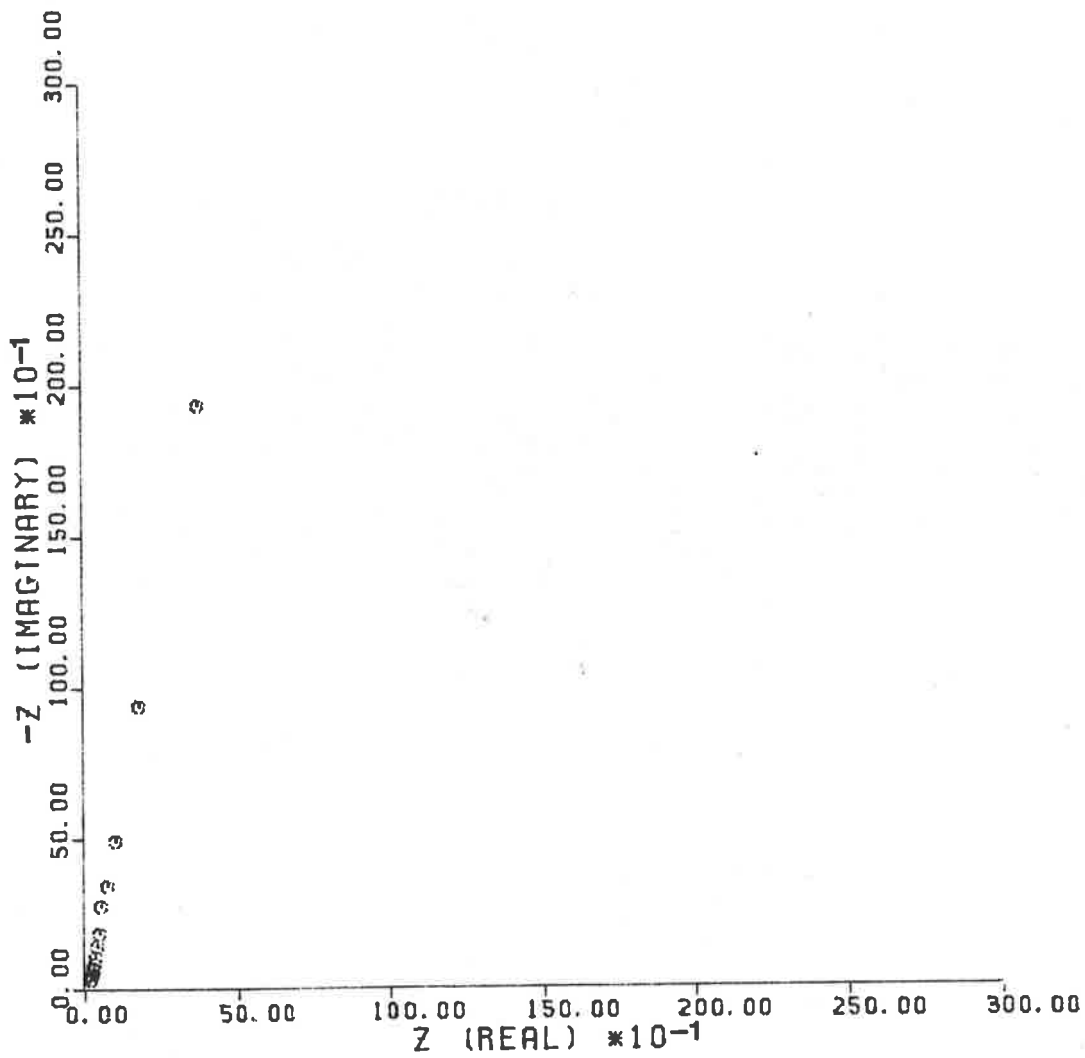


Figure 34. Complex plane impedance spectrum of Teflon-encased polycrystalline platinum in 0.100M  $\text{NaNO}_3$  at +0.20 V. Static measurement.

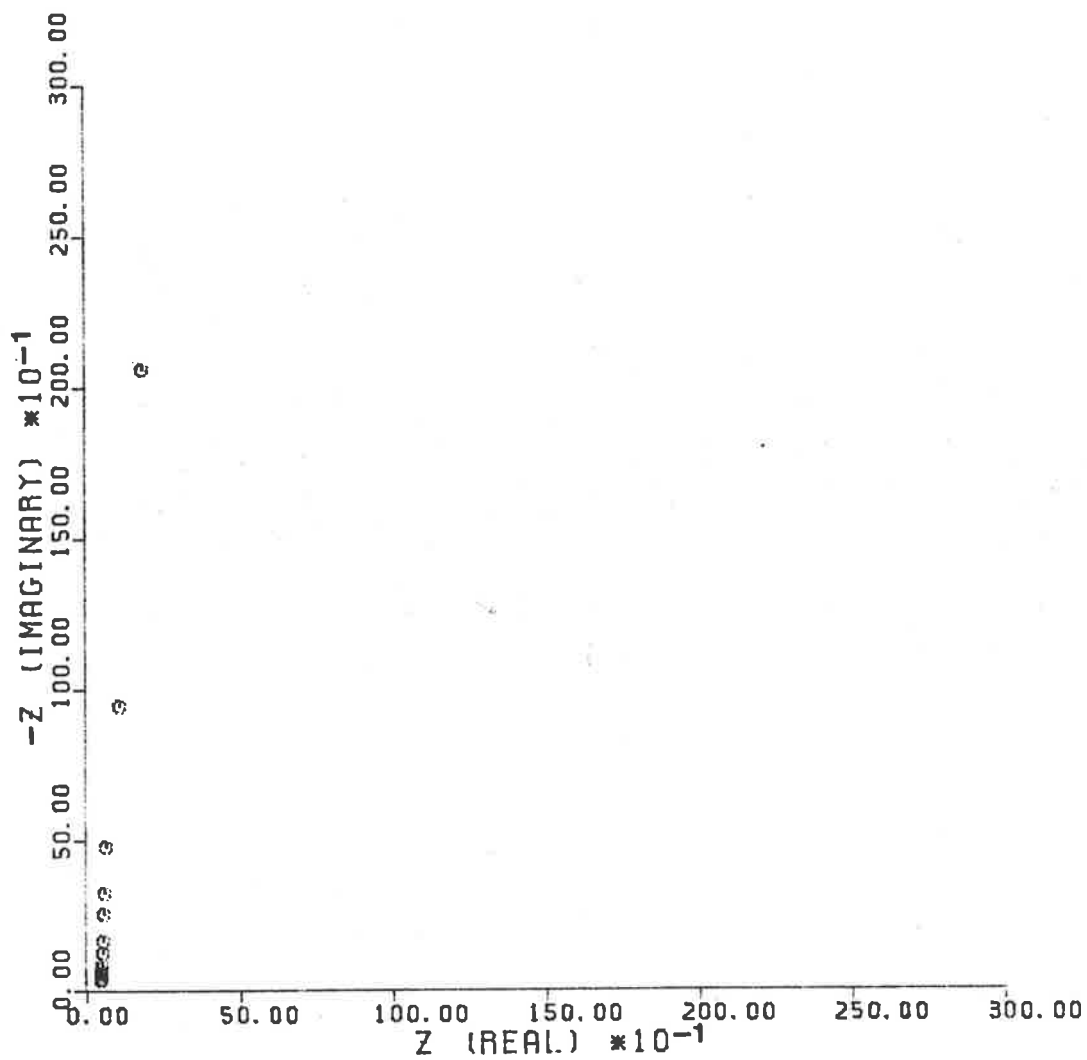


Figure 35. Complex plane impedance spectrum of polycrystalline platinum disc in 0.100M  $\text{NaNO}_3$  at +0.20 V. Static measurement.

Table 5

Dependence of capacitance in  $\mu\text{F}/\text{cm}^2$   
determined for the Teflon-encased  
polycrystalline platinum/aqueous 0.100M  $\text{NaNO}_3$  interface  
on frequency at a potential of +0.20 volts. Static method.

Frequency/hz	Series Capacitance	Parallel Capacitance
5	28.80	27.82
10	29.61	28.73
20	28.23	27.34
30	26.88	26.02
40	25.04	24.53
60	24.91	24.12
80	24.20	23.35
120	21.49	20.72
140	23.25	22.10
170	22.75	21.99
190	22.73	21.15
220	23.40	22.08
260	23.06	22.15
300	22.75	21.65
350	23.56	22.35
400	22.67	21.76

**Table 6**

Dependence of capacitance in  $\mu\text{F}/\text{cm}^2$   
determined for the polycrystalline  
platinum disk/aqueous 0.100M  $\text{NaNO}_3$  interface on frequency  
at a potential of +0.20 volts. Static method.

Frequency/hz	Series Capacitance	Parallel Capacitance
5	20.59	20.49
10	22.41	22.31
20	22.04	21.99
30	21.63	21.57
40	20.65	20.59
60	21.06	20.99
80	20.82	20.72
120	20.11	20.02
140	20.10	19.94
170	19.85	19.71
190	19.52	19.40
220	19.59	19.37
260	19.25	18.95
300	18.06	17.70
350	17.13	16.63
400	14.12	13.88

can be fitted by a straight line making an acute angle  $\theta$  with the real axis. This line intercepts the real axis at a value that corresponds to the true solution resistance between the working and reference electrodes, since no  $iR$ -compensation was used in this series of measurements. A linear least squares best fit of the data gave values for  $\theta$  of  $79.5^\circ$  and  $86.1^\circ$ , and values for the solution resistance of  $15.5 \pm 1.5$  ohms and  $44.5 \pm 2.0$  ohms for the data shown in Figures 34 and 35, respectively. The values for the parallel capacitance in Tables 5 and 6 were determined taking into account a constant series resistance taken to be equal to 15.5 ohms and 44.5 ohms, respectively.

It can be clearly seen that the measured capacitance does show frequency dependence in Tables 5 and 6. There are, however, some regions where the parallel and series capacitance is independent of the measuring frequency.

From Table 5, the series capacitance and parallel capacitance yielded averaged values of  $28.9 \pm 0.7 \mu\text{F}/\text{cm}^2$  and  $28.0 \pm 0.7 \mu\text{F}/\text{cm}^2$ , respectively, for the three lowest frequencies. Over the higher frequency range of 140 hz to 400 hz, the series capacitance and parallel capacitance had averaged values of  $23.0 \pm 0.35 \mu\text{F}/\text{cm}^2$  and  $21.9 \pm 0.4 \mu\text{F}/\text{cm}^2$ , respectively.

From Table 6, the series capacitance and parallel capacitance was determined over the low frequency range of 5 hz to 80 hz as  $21.3 \pm 0.7 \mu\text{F}/\text{cm}^2$  and  $21.2 \pm 0.7 \mu\text{F}/\text{cm}^2$ , respectively.

Figures 36-38 show the impedance plane plots for selected electrode potentials. These impedance measurements were made using a moderate scan rate of 20 mV/s. All the plots, typified by Figure 38, can be fitted by a straight line making an acute angle  $\theta$  with the real axis, having a real axis intercept corresponding to the value of the solution resistance.

The results at a potential of +0.20 volts from the dynamic method compare quite favourably with the static measurements made after holding the working electrode at +0.20 volts for more than 20 minutes. Measurements using the Teflon-encased platinum electrode yielded intercepts of  $14.9 \pm 2.0$  ohms and  $15.2 \pm 1.8$  ohms, and angles of  $78.0^\circ$  and  $75.8^\circ$  for the cathodic and anodic scans, respectively. These compare well with the static results made with the same electrode of  $15.5 \pm 1.5$  ohms and  $79.5^\circ$  for the intercept and angle, respectively. Measurements made with the platinum disk electrode yielded intercepts of  $44.2 \pm 2.8$  ohms and  $39.8 \pm 3.2$  ohms, and angles of  $84.3^\circ$  and  $79.3^\circ$  for the cathodic and anodic scans, respectively. The corresponding static results with the same electrode were  $44.5 \pm 2.0$  ohms and  $86.1^\circ$ . The angle the lines made with the real axis were a little greater for the static measurements than the dynamic measurements, reflecting a closer correspondence of the static measurements with the ideal behaviour of a series resistor and capacitor analogue circuit.

The intercepts of the impedance plane plots were found to be independent of the electrode potential and whether the measurements were made dynamically or statically. The intercepts differed for the different working electrodes due to change in physical parameters such as the closeness of the luggin tip to the working electrode. This

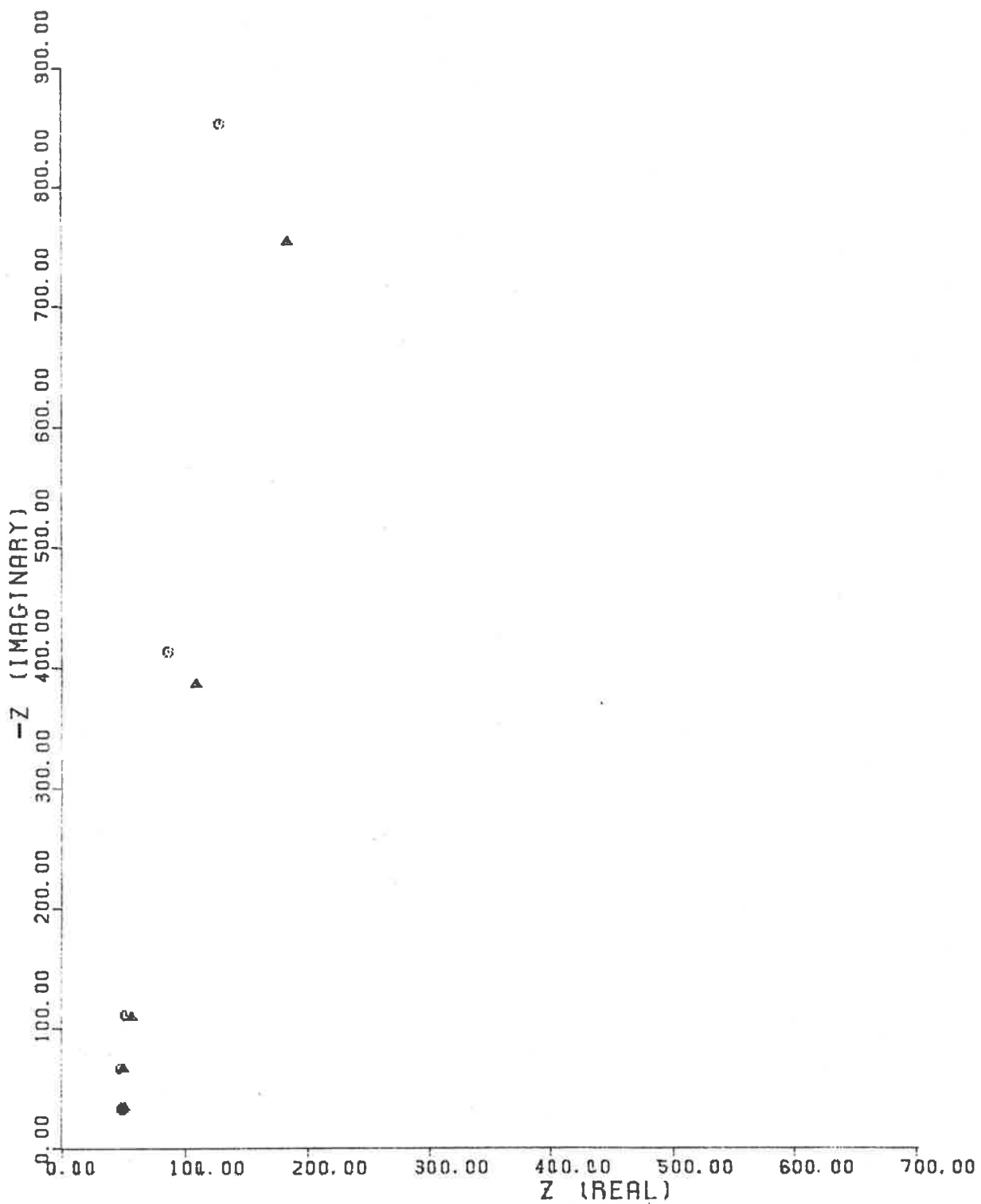


Figure 36. Complex plane impedance spectra of polycrystalline platinum disc in 0.100M  $\text{NaNO}_3$  at +0.20 V: cathodic scan (O); anodic scan ( $\Delta$ ); .20 mV/s scan rate.

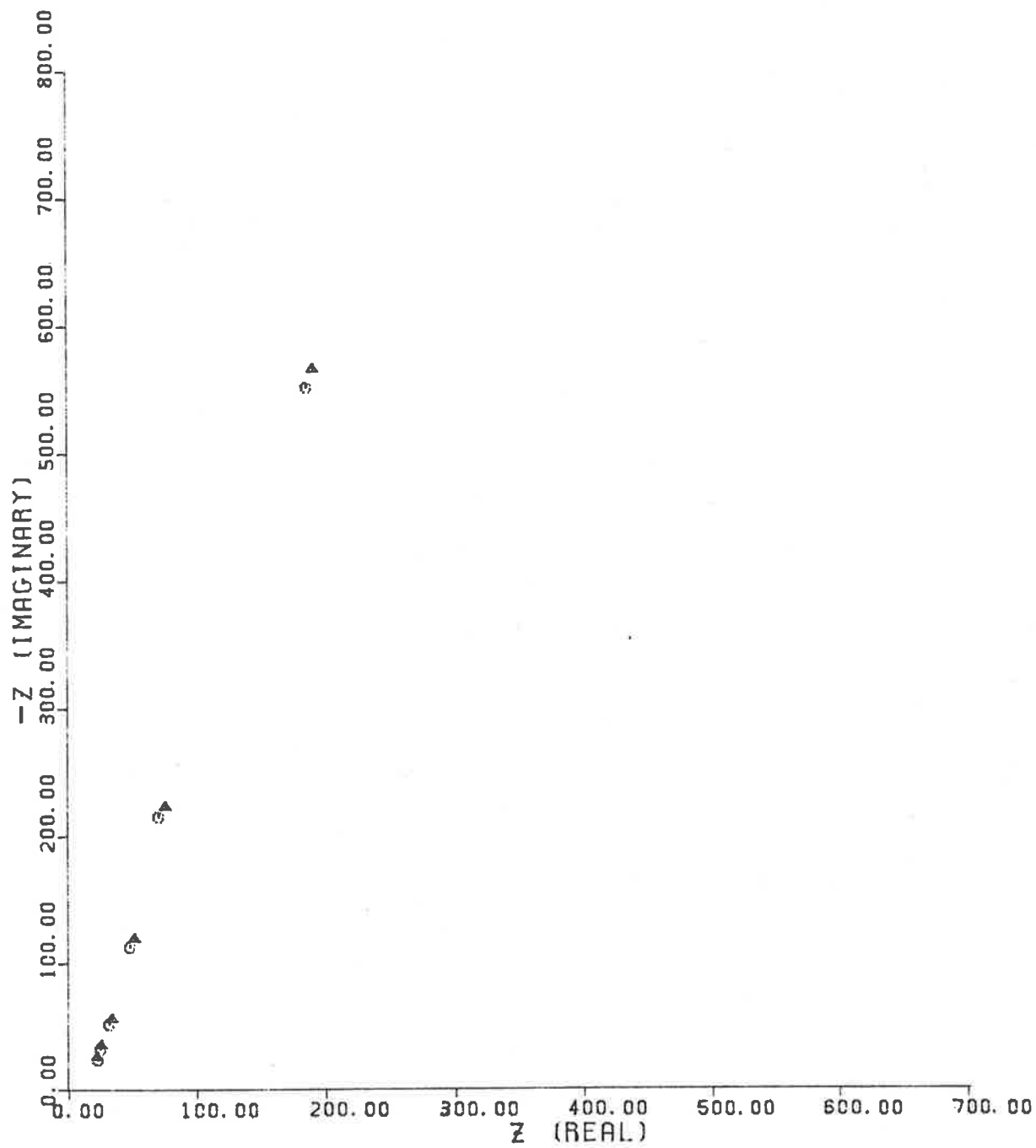


Figure 37. Complex plane impedance spectra of Teflon-encased polycrystalline platinum in 0.100M  $\text{NaNO}_3$  at 0.00 V: cathodic scan (O); anodic scan ( $\Delta$ ).  $\approx 20$  mV/s scan rate.



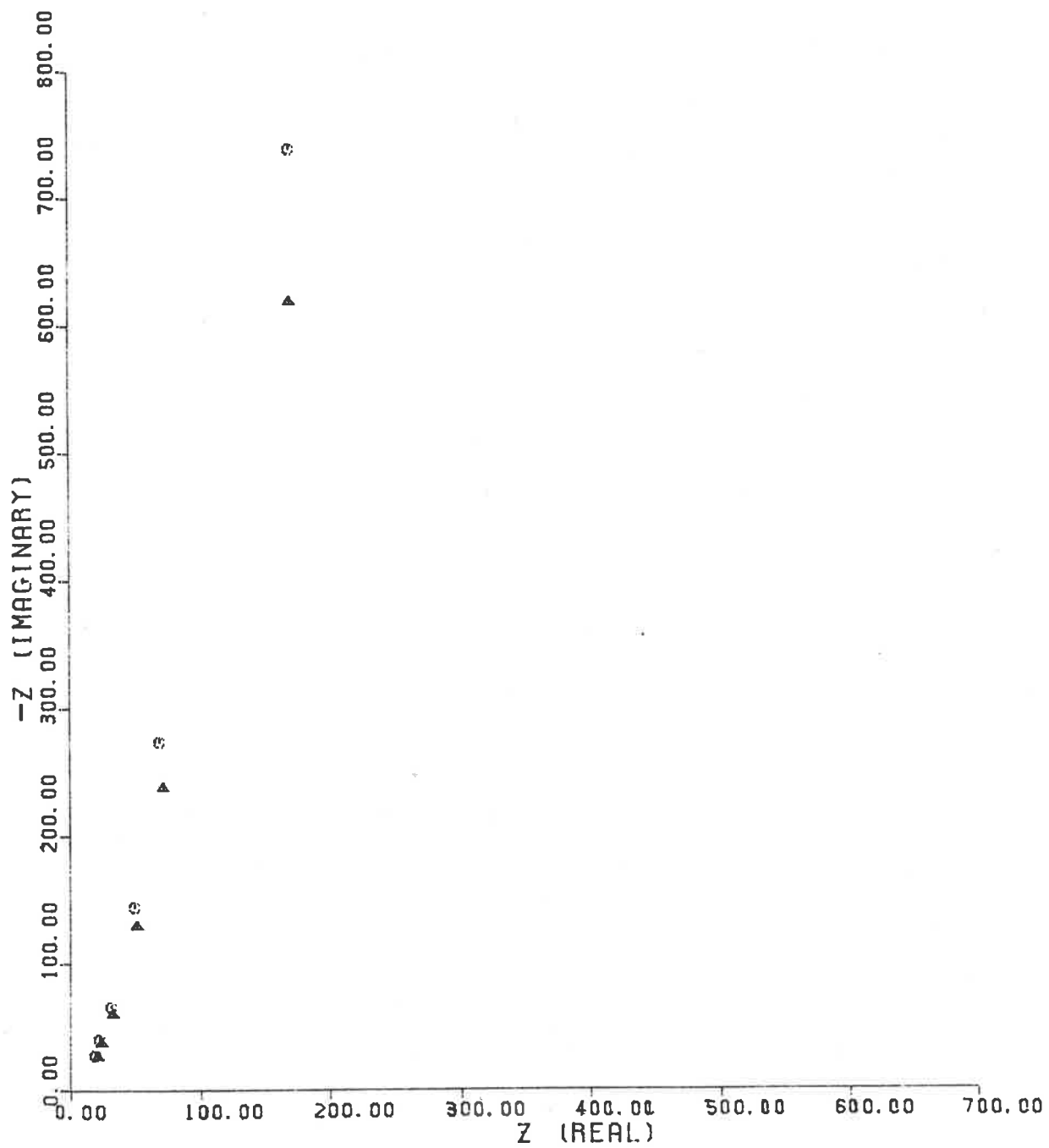


Figure 38. Complex plane impedance spectra of Teflon-encased polycrystalline platinum in 0.100M NaNO<sub>3</sub> at +0.20 V; cathodic scan (O); anodic scan (Δ). 20 mV/s scan rate.

strongly suggests that the intercepts determined by the above method do indeed correspond to the true solution resistance between the working and reference electrodes.

Figure 39 shows the capacitance determined as a function of potential using the Single Current Pulse Method. Figure 40 contrasts the capacitance determined using the Single Current Pulse Method with that determined using the A.C. Impedance Method at a frequency of 10 Hz.

Even though the results presented in Figure 40 were determined on separate occasions, the difference between the capacitance-potential curves determined via Single Current Pulse and A.C. Impedance Methods cannot be accounted for by experimental variation. The basic shape of the curves are distinctly different.

The results presented in Figures 39 and 40 were determined using a potential stepping technique, whereby the electrode potential was stepped 0.10 volt in an anodic direction after the electrode had been held at a set potential for a period of 15 minutes. The results presented, therefore, correspond to a stabilized electrode system.

The parallel resistance calculated using the Single Current Pulse Method was found to be low, and dependent upon the polarizing potential. For the capacitance results presented in Figure 39, the parallel resistance was found to vary from a minimum of 73 ohms to a maximum of 480 ohms. The parallel resistance determined from the A.C. Impedance measurements at 10 Hz varied from a minimum of 1310 ohms to a maximum of 5140 ohms.

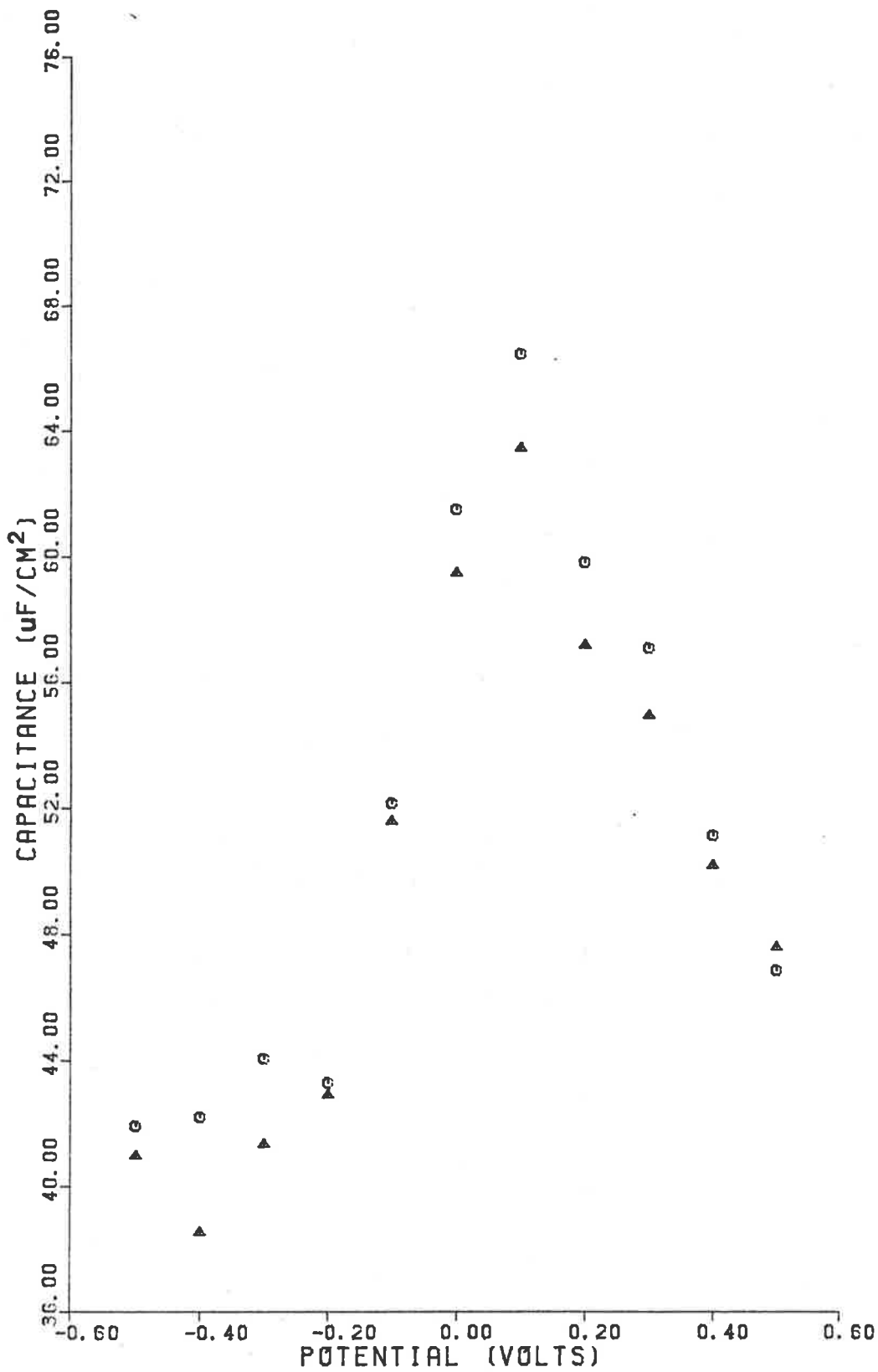


Figure 39. Capacitance-potential curves of Teflon-encased polycrystalline platinum in 0.100M NaNO<sub>3</sub>: Polynomial Method (O); Log (ΔV/Δt) Plot Method (Δ).

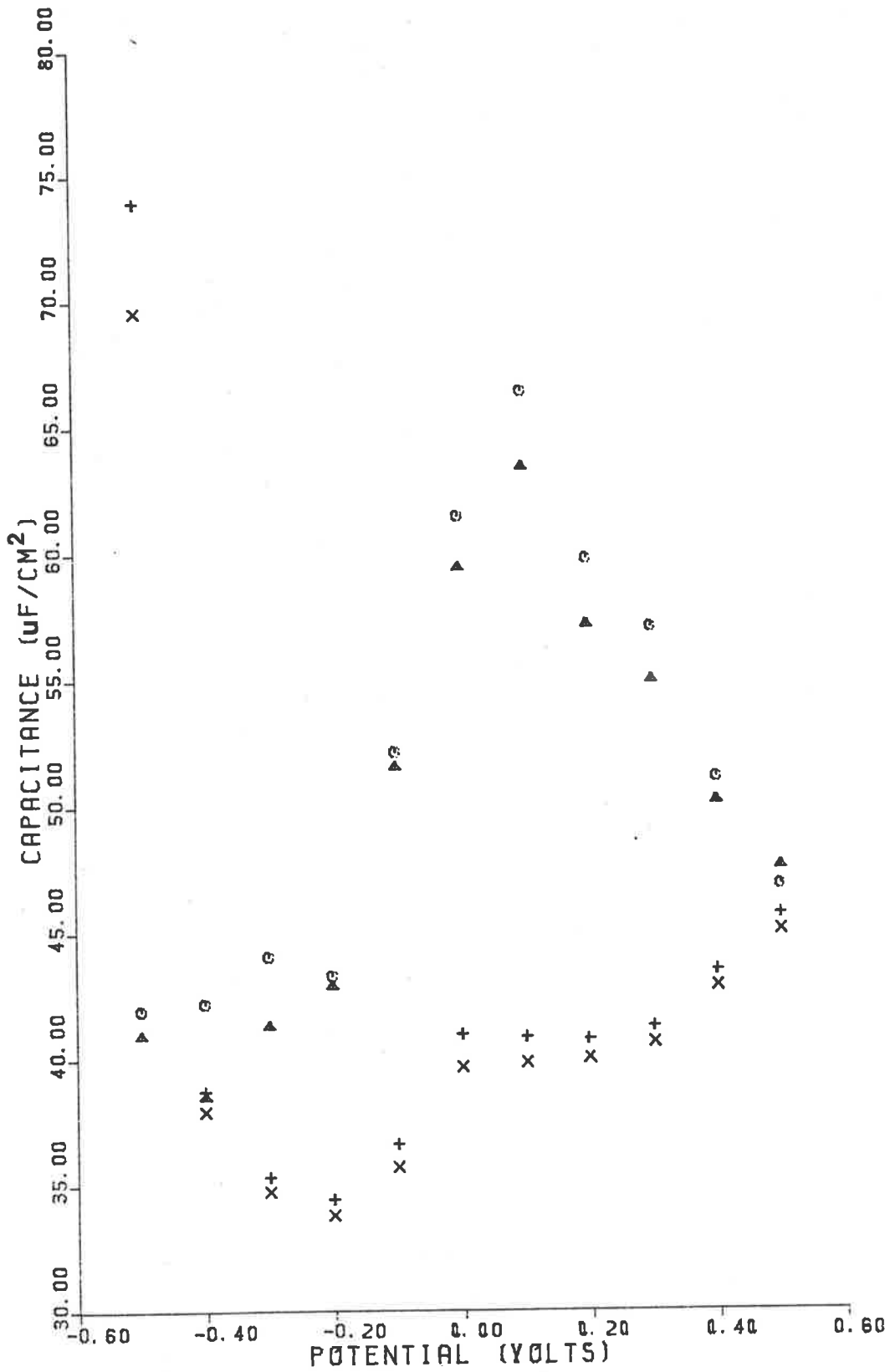


Figure 40. Capacitance-potential curves of Teflon-encased polycrystalline platinum in 0.100M NaNO<sub>3</sub>: series capacitance, 10 hz (O); parallel capacitance, 10 hz (Δ); Polynomial Method (+); Log (ΔV/Δt) Plot Method (x). Slow scan rate.

**CONCLUSION**

The polycrystalline platinum/0.100M X/H<sub>2</sub>O system was studied, and results were found to be similar whether the electrolyte, X, was NaCl, NaNO<sub>3</sub> or KNO<sub>3</sub>. The capacitance-potential curves for this system showed a central capacitance hump with a maximum in the vicinity of 0.0 volts, which is currently held to be due to solvent reorientation at the electrode surface.<sup>15</sup> This system was also found to consistently show time dependency, requiring a number of minutes before a stable interface could be obtained.

The complex plane spectra determined using the A.C. Impedance Method were best fitted by a straight line making an acute angle with the real axis of between 76° and 86°. The solution resistance, obtained from the real axis intercept, was independent of polarizing potential, and whether the results were obtained during potential cycling of the electrode or not. The spectra were best fitted by assuming the interface to behave as a pure capacitor in series with the solution resistance. The deviation of the angle from 90° is best thought of as being due to surface roughness of the electrodes.

The results obtained via the Single Current Pulse Method were consistent with the interface behaving as a capacitor in parallel with a resistor. The value of the apparent parallel resistance was found to be low, and potential dependent. There was poor agreement found between the results of the Single Current Pulse Method and those of the A.C. Impedance Method.

SYSTEM III: Pt + 0.001M NaNO<sub>3</sub> + H<sub>2</sub>O

The A.C. Impedance Method was used to determine the capacitance-potential curves displayed in Figures 41-46 for the polycrystalline platinum/aqueous 0.001M NaNO<sub>3</sub> interface. The data was measured at a moderate potential scan rate of 20 mV/s.

The effect of using iR-compensation was tested at a frequency of 10 Hz. The results are shown in Figures 41 and 42 for a cathodic and anodic potential scan, respectively, assuming the interface to behave as a resistor and capacitor in series. The results show that the determined capacitance was identical within experimental uncertainties whether iR-compensation was used or not.

At the highest frequencies used, however, the use of iR-compensation tended to increase the measured series capacitance. Since the use of iR-compensation decreased the degree of frequency dependence of the series capacitance, a constant level of iR-compensation was employed in the results presented in Figures 43-46.

The marked frequency dependence of the calculated series capacitance is clearly shown in Figures 43-46. Over the low frequency range, from 5 Hz to 30 Hz, the capacitance-potential curves show a minimum at +0.20 volts for a cathodic scan, and a minimum at +0.05 volts for an anodic scan using the Teflon-encased polycrystalline platinum working electrode (see Figures 43 and 44, respectively). At higher frequencies, the curves lessen in magnitude and become featureless.

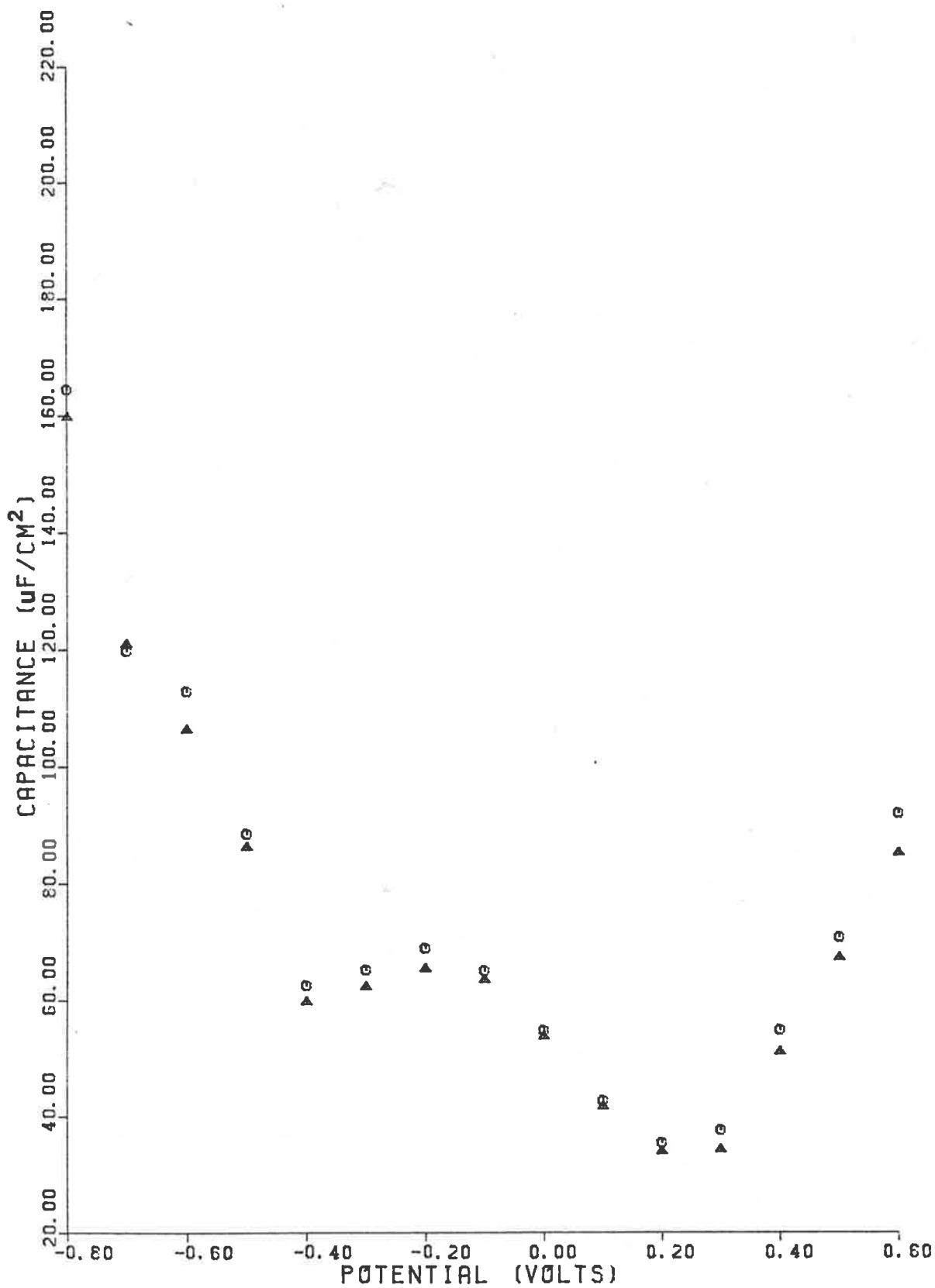


Figure 41. Series capacitance-potential curves for polycrystalline platinum disc in 0.001M NaNO<sub>3</sub> at 10 hz with (O) and without (Δ) iR-compensation. Cathodic scan. 20 mV/s scan rate.

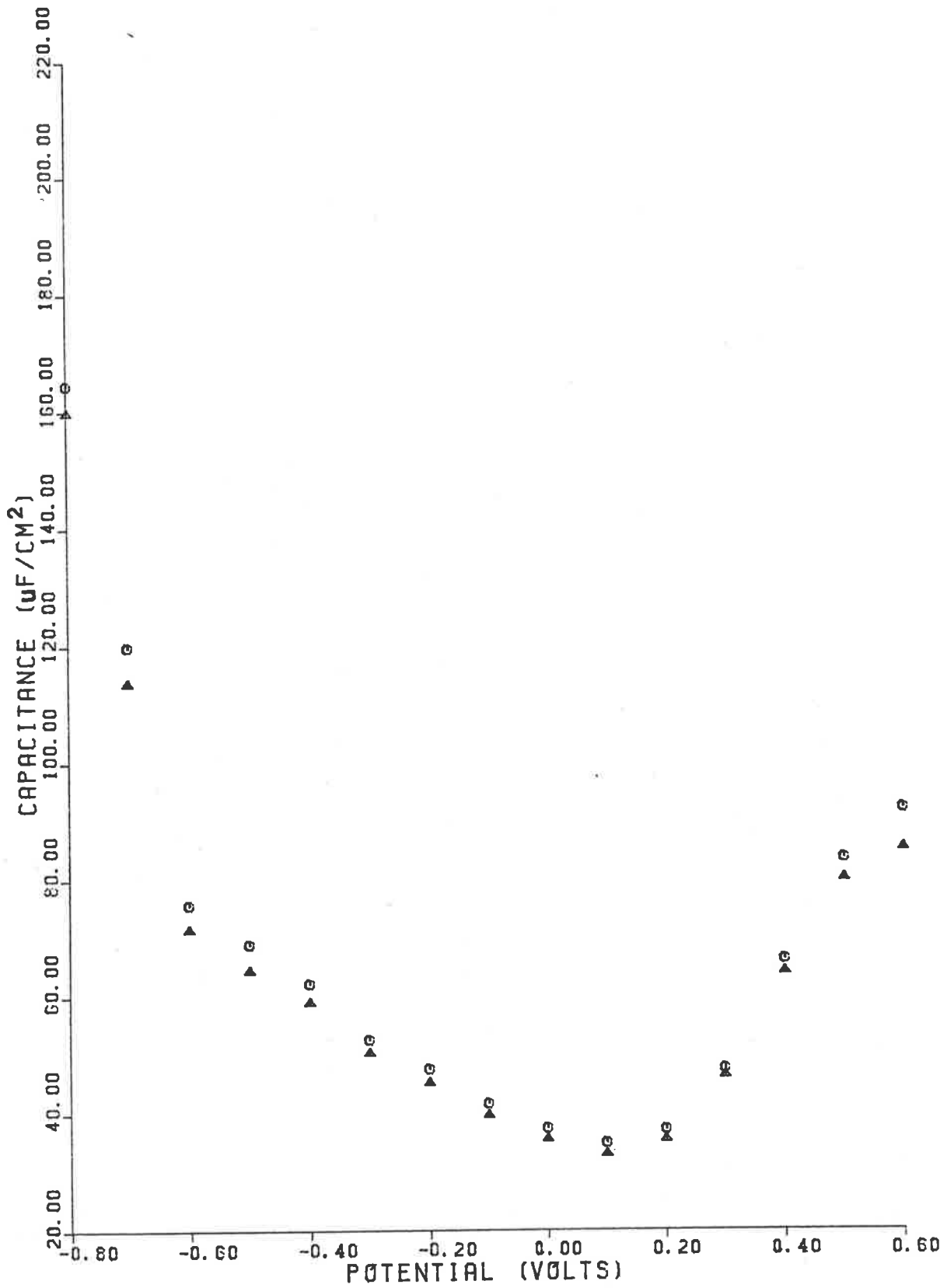


Figure 42. Series capacitance-potential curves for polycrystalline platinum disc in 0.001M NaNO<sub>3</sub> at 10 hz with (O) and without (Δ) IR-compensation. Anodic scan. 20 mV/s scan rate.



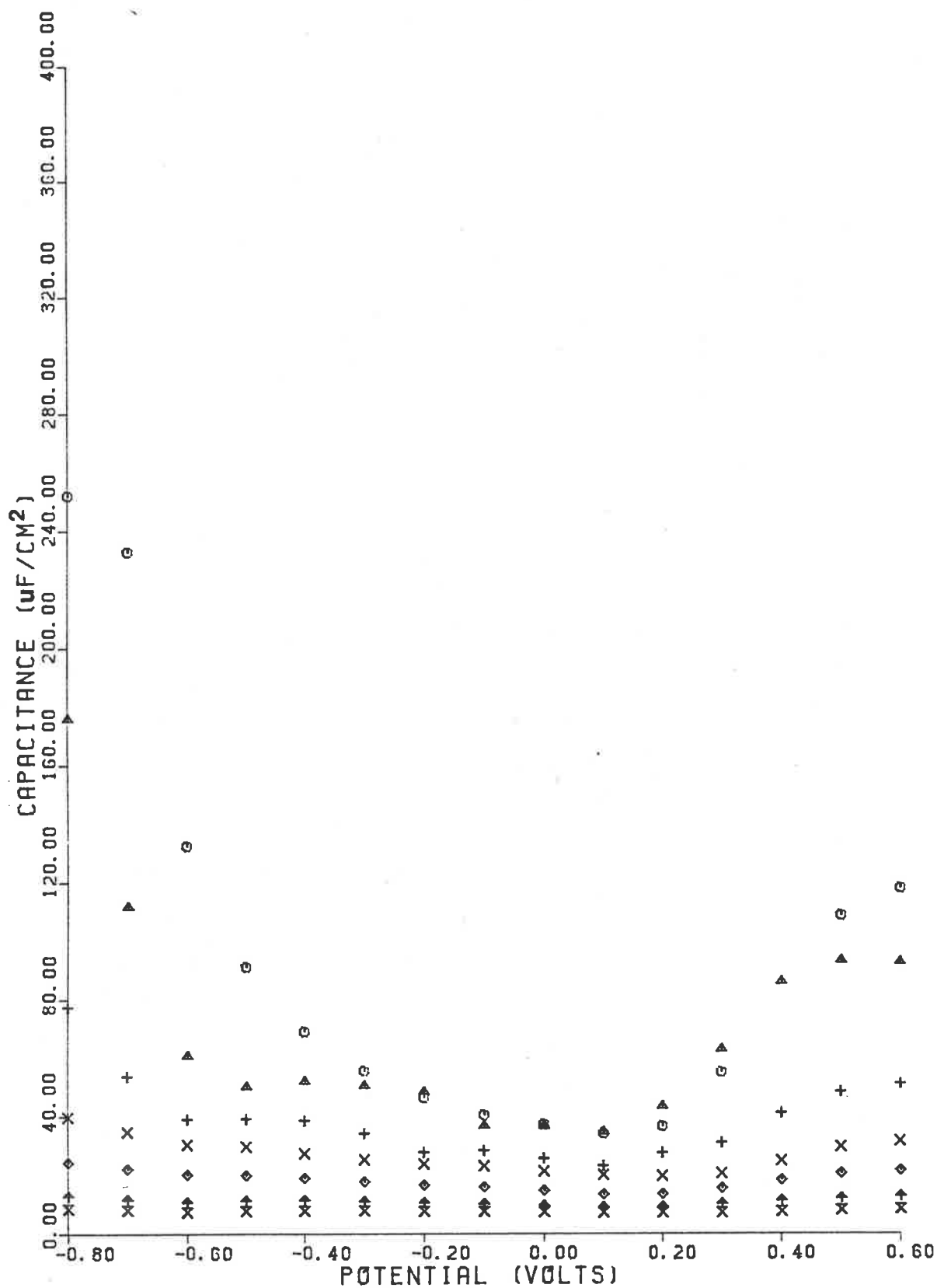


Figure 43. Frequency dependence of series capacitance-potential curves of Teflon-encased polycrystalline platinum in 0.001M NaNO<sub>3</sub>: 5 Hz (O); 10 Hz (Δ); 20 Hz (+); 30 Hz (X); 40 Hz (◇); 60 Hz (↑); 80 Hz (⊗). Cathodic scan.

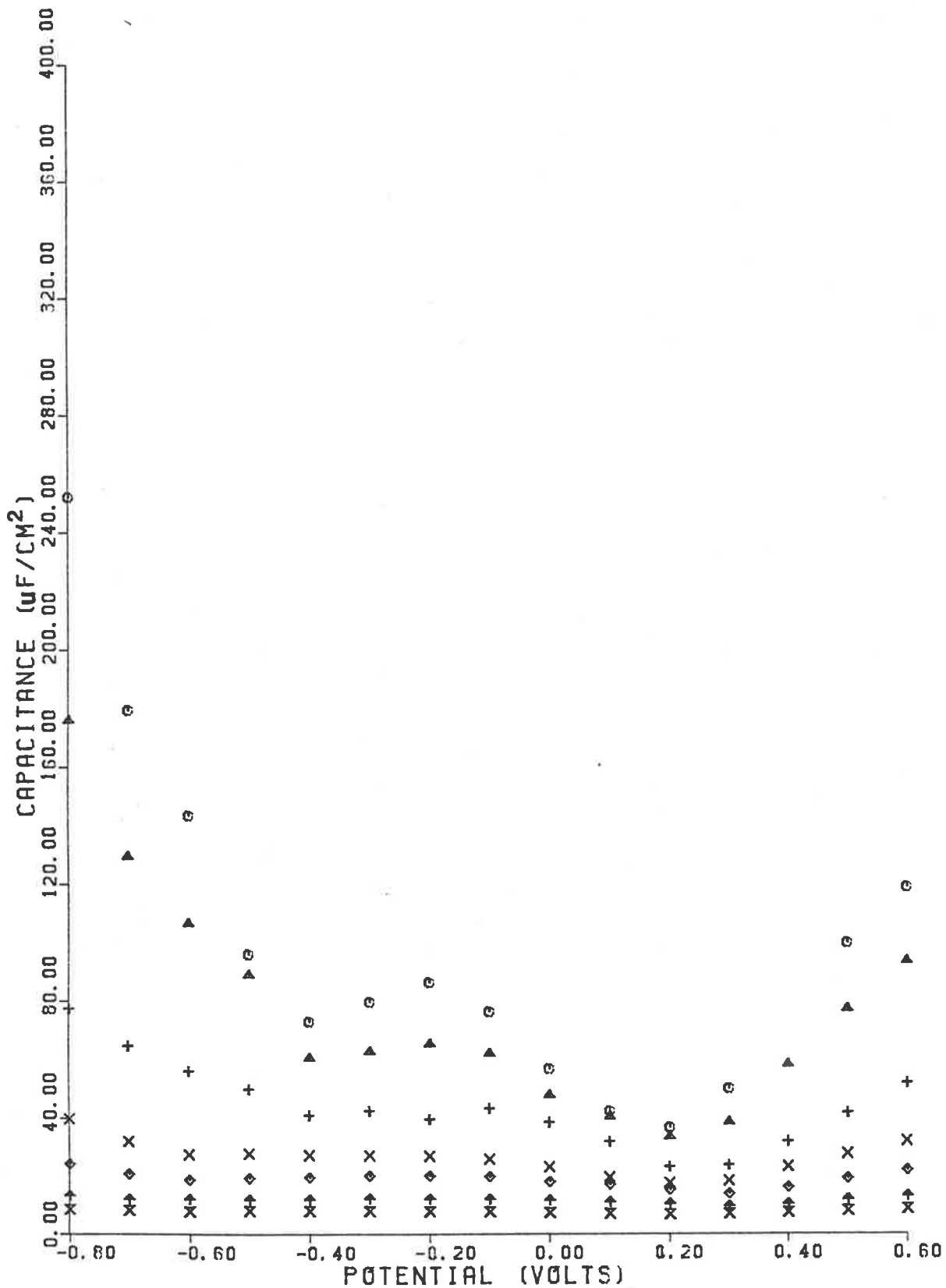


Figure 44. Frequency dependence of series capacitance-potential curves of Teflon-encased polycrystalline platinum in 0.001M NaNO<sub>3</sub>: 5 Hz (○); 10 Hz (△); 20 Hz (+); 30 Hz (×); 40 Hz (◇); 60 Hz (♣); 80 Hz (⊗).  
Anodic scan.

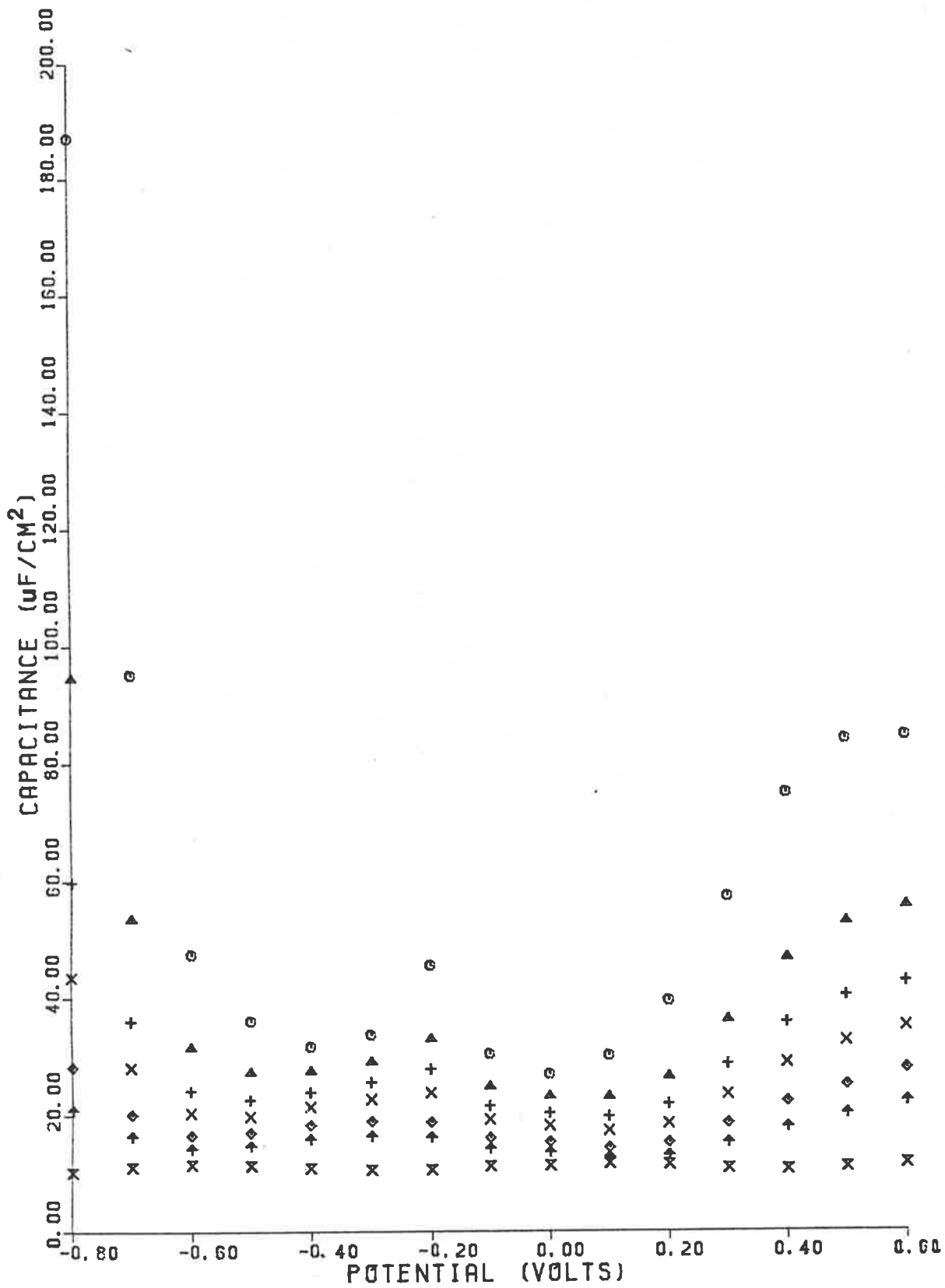


Figure 45. Frequency dependence of series capacitance-potential curves of polycrystalline platinum disc in 0.001M  $\text{NaNO}_3$ : 10 Hz (O); 20 Hz ( $\Delta$ ); 30 Hz (+); 40 Hz (X); 60 Hz ( $\diamond$ ); 80 Hz ( $\oplus$ ); 140 Hz ( $\otimes$ ). Cathodic scan. 20 mV/s scan rate.

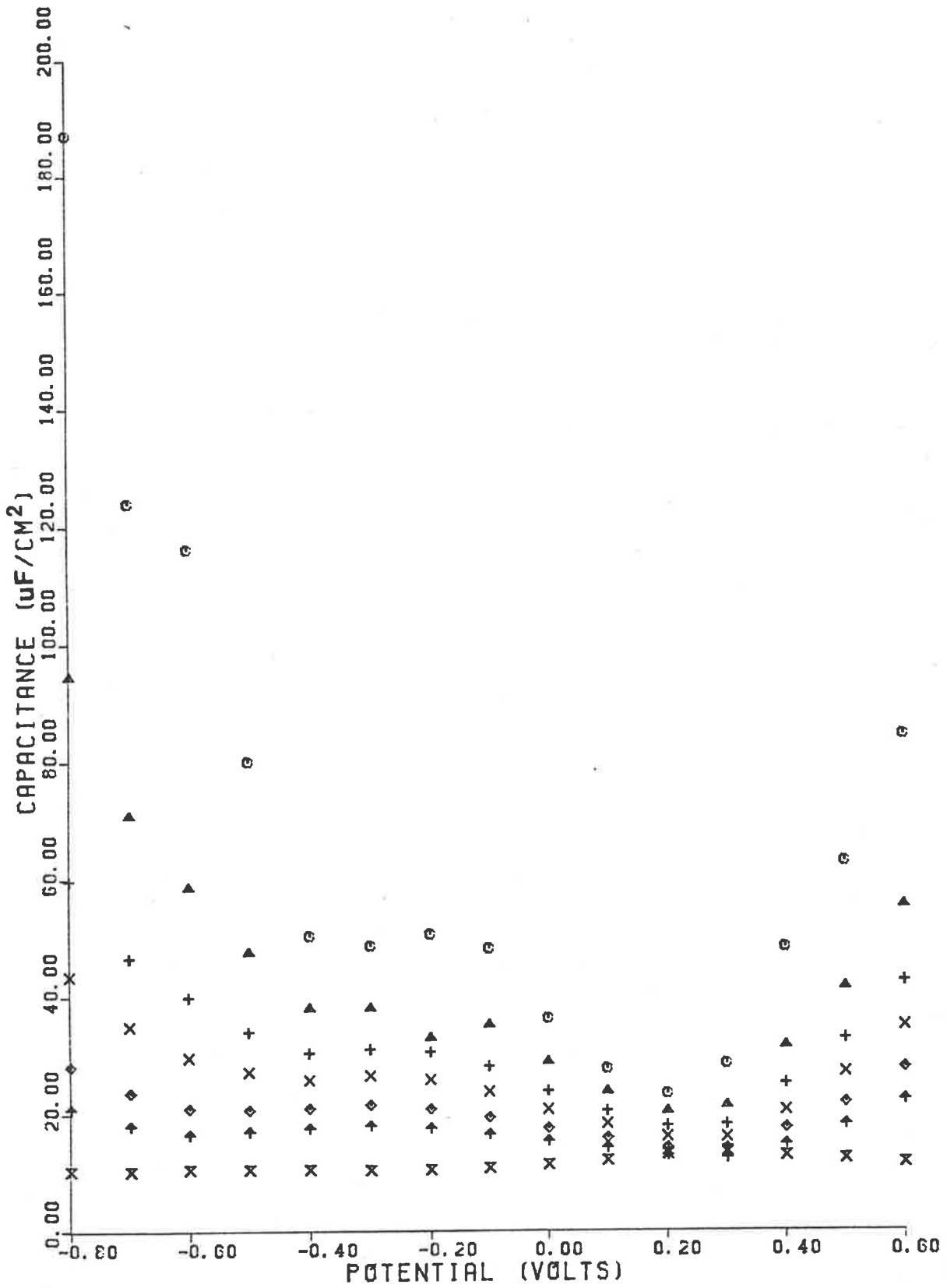


Figure 46. Fréquency dependence of series capacitance-potential curves of polycrystalline platinum disc in 0.001M NaNO<sub>3</sub>: 10 hz (O); 20 hz (Δ); 30 hz (+); 40 hz (X); 60 hz (◇); 80 hz (⋈); 140 hz (⊗). Anodic scan. 20 mV/s scan rate.

Similar behaviour was encountered using a polycrystalline platinum disk electrode, with a capacitance minimum at +0.20 volts for a cathodic scan, and at +0.10 volts for an anodic scan (see Figures 45 and 46).

This system not only shows a strong frequency dependence, but also a distinct difference between the capacitance-potential curves obtained in cathodic and anodic potential scans.

Figures 47 and 48 show the representative complex plane impedance spectra corresponding to the capacitance-potential curves presented in Figures 43 and 44, and Figures 45 and 46, respectively. Both spectra cannot be simply interpreted in terms of the simple analogue circuits discussed previously. The representative spectra show obvious differences between the response of the Teflon-encased platinum, and platinum disk electrodes.

An attempt was made to interpret the behaviour of the interface in terms of electrosorption of nitrate ion. The analogue circuit used to account for this behaviour<sup>16</sup> is shown in Figure 49a, and the expected complex plane impedance spectrum is shown in Figure 49b. The frequency corresponding to the position of maximum negative imaginary impedance on the hemi-circle,  $\omega_1$ , is given by the relation

$$\omega_1 = \frac{1}{C \cdot R_A}$$

It can be seen that a value for  $\omega_1$  and  $R_A$  determined from the impedance spectra will enable the determination of the double layer capacitance,  $C$ .

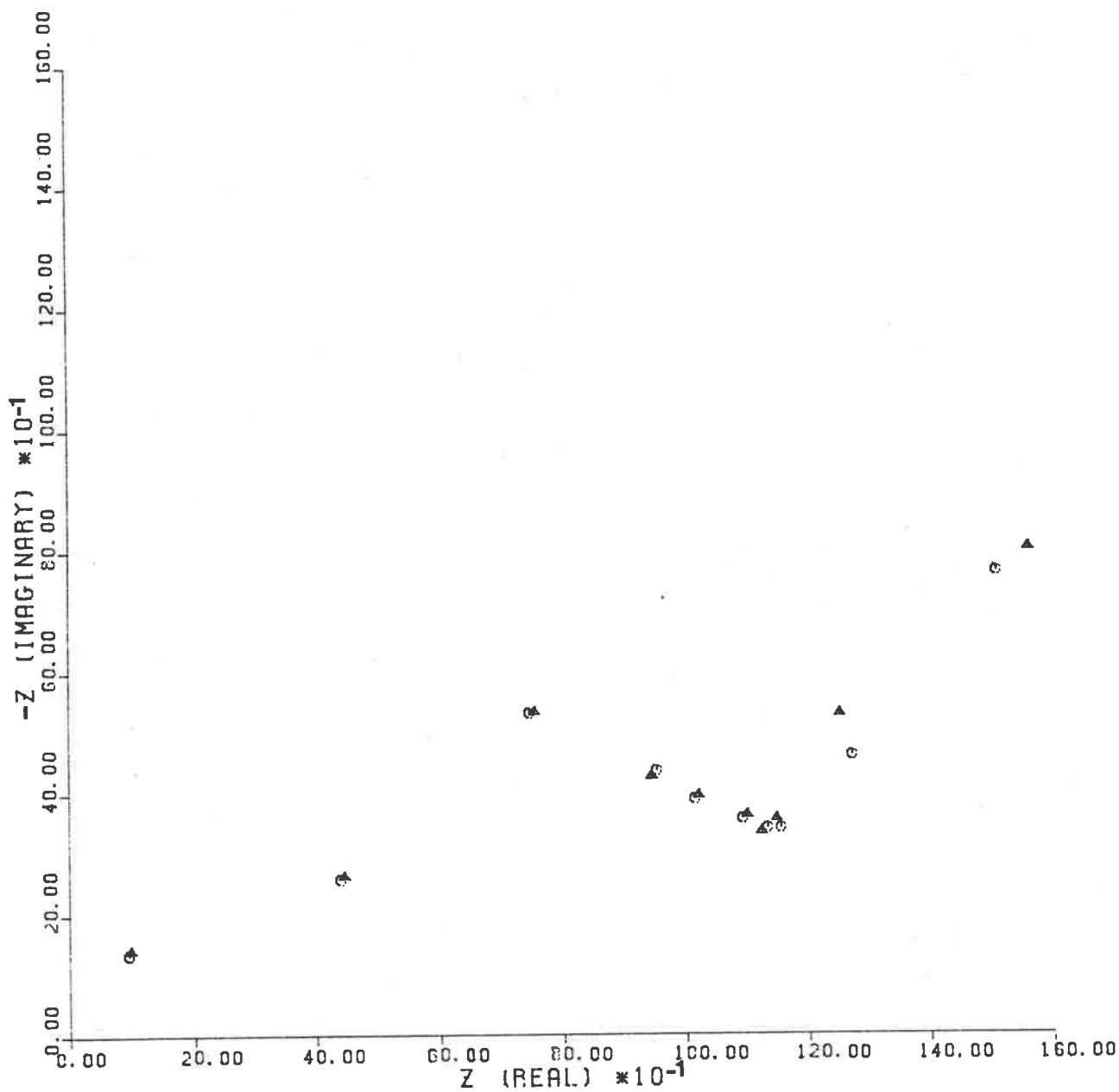


Figure 47 Complex plane impedance spectra of Teflon-encased polycrystalline platinum in 0.001M NaNO<sub>3</sub> at -0.40 volts: cathodic scan (O); anodic scan (Δ). 20 mV/s scan rate.

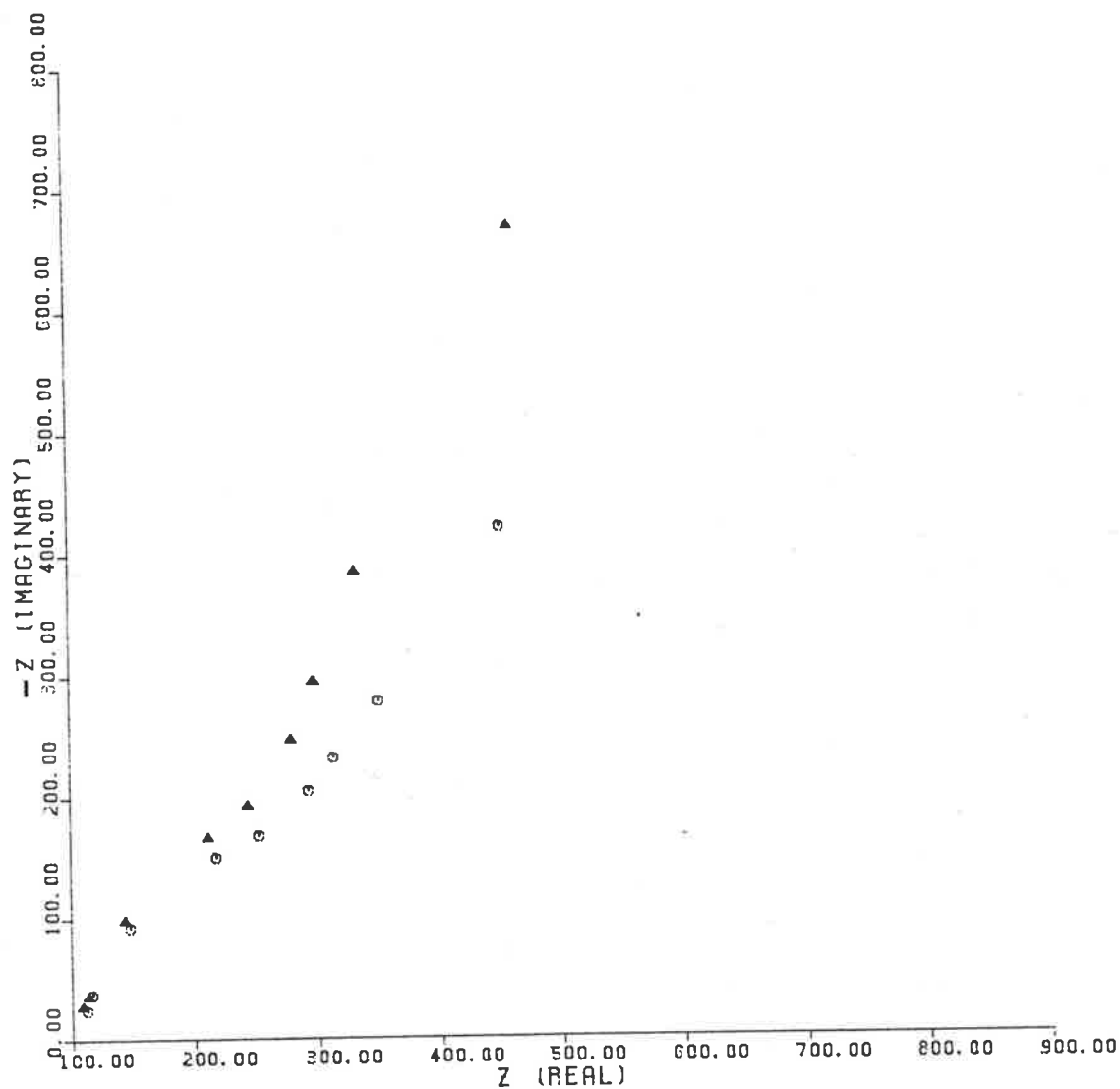


Figure 46 Complex plane impedance spectra of polycrystalline platinum disc in 0.001M  $\text{NaNO}_3$  at -0.40 volts: cathodic scan (○); anodic scan (△). 20 mV/s scan rate.

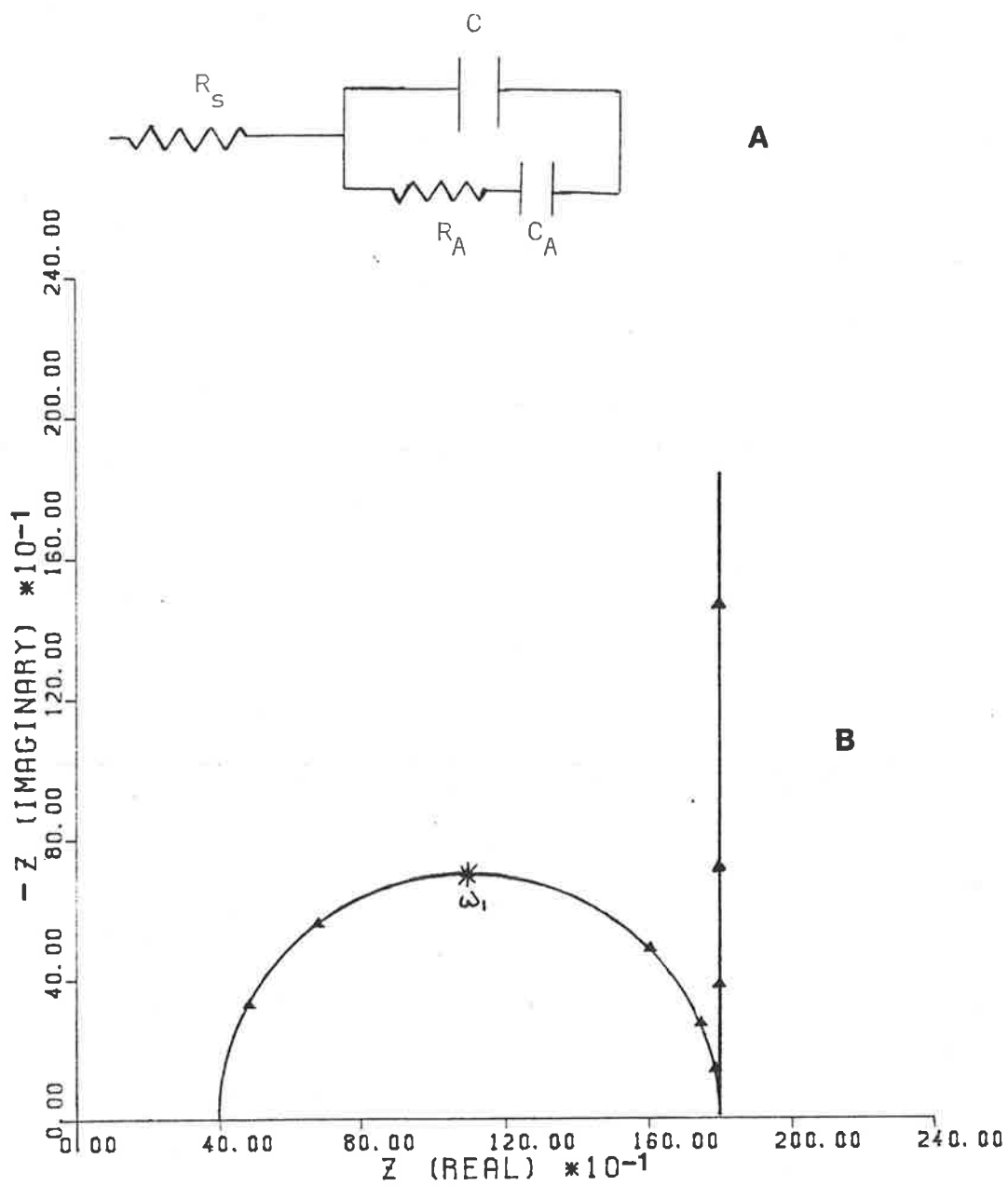


Figure 49. Analogue circuit (A) and complex plane impedance spectrum (B) for adsorption at the electrode/electrolyte solution interface.



Analysis of the impedance spectra presented in Figures 47 and 48 on this basis yielded a value of 140 Hz for  $\omega_1$  for both systems. The value of  $R_A$ , however, was approximated to be 1020  $\Omega$  and 30  $\Omega$  from Figures 47 and 48, respectively. The resultant capacitance was 1.9  $\mu\text{F}/\text{cm}^2$  and 50.5  $\mu\text{F}/\text{cm}^2$  for the results presented in Figures 47 and 48, respectively.

The very large difference in the capacitance determined for two polycrystalline platinum electrodes suggests that the model presented in Figure 49 does not correspond at all well to the observed behaviour of the platinum/aqueous 0.001M  $\text{NaNO}_3$  interface. While a value of 50.5  $\mu\text{F}/\text{cm}^2$  is not unreasonable, a value of 1.9  $\mu\text{F}/\text{cm}^2$  would appear much too low to be the true double layer capacitance.

#### CONCLUSION

Preliminary investigations of the polycrystalline platinum + 0.001M  $\text{NaNO}_3$  +  $\text{H}_2\text{O}$  system have been presented using the A.C. Impedance Method. The response of this system was complex, and could not be correlated with the simple analogue circuits previously discussed in Chapter 4 of this thesis. An attempt to interpret the complex behaviour of this system in terms of nitrate ion electrosorption did not prove to be adequate.

De Levie<sup>5</sup> attempted to quantitatively describe the effects of surface roughness on double layer capacitance measurements. In his treatment he used a v-shaped groove model to approximate the roughness of solid metal surfaces. From such a treatment, de Levie concluded

that surface roughness effects would become more pronounced in more dilute solutions. A comparison between the results obtained for 0.001M  $\text{NaNO}_3$  and 0.100M  $\text{NaNO}_3$  would suggest that some of the complex behaviour of the dilute electrolyte system was a problem related to surface roughness. The difference in the impedance spectra for the platinum disk and Teflon-encased platinum electrodes may be a reflection of the apparent differences in the roughness of the electrode surfaces. From the results already presented in Systems I and II of this chapter, the platinum disk electrode consistently behaved as if it had a lower surface roughness than the Teflon-encased platinum electrode. This, again, is not inconsistent with the results presented here, since the results obtained with the platinum disk show the lesser deviation from what might be expected as roughness distortion of the response of a capacitor in series with the solution resistance.

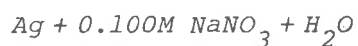
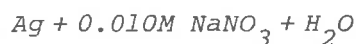
SYSTEM IV:  $\text{Ag} + \text{X} + \text{H}_2\text{O}$ 

Figure 50 contrasts the capacitance-potential curve obtained via the Single Current Pulse Method with those obtained via the A.C. Impedance Method, assuming simple analogue circuits of a resistor and capacitor in series or parallel. The A.C. Impedance measurements were made using a frequency of 5 hz, and a potential scan rate of 10 mV/s. The Single Current Pulse measurements were made by the standard potential stepping technique, holding the electrode potential constant for a period of 10 minutes before stepping 0.10 volts to a more anodic potential.

The results displayed in Figure 50 for the polycrystalline silver/aqueous 0.100M  $\text{NaNO}_3$  interface clearly show poor agreement between the capacitance determined using the Single Current Pulse Method and the A.C. Impedance Method, assuming either a simple series or parallel analogue circuit.



Figures 51 and 52 show the capacitance-potential curves of the polycrystalline silver/aqueous 0.010M  $\text{NaNO}_3$  interface obtained from A.C. Impedance measurements assuming a simple analogue circuit of a capacitor and resistor in series. Measurements were made at frequencies of 5, 10 and 20 hz using a constant potential scan of 10 mV/s.

A number of features are evident in these curves. The general trend of the capacitance-potential curve is a decrease in capacitance from -1.20 volts to -0.9 volts, followed by an increase in the capaci-

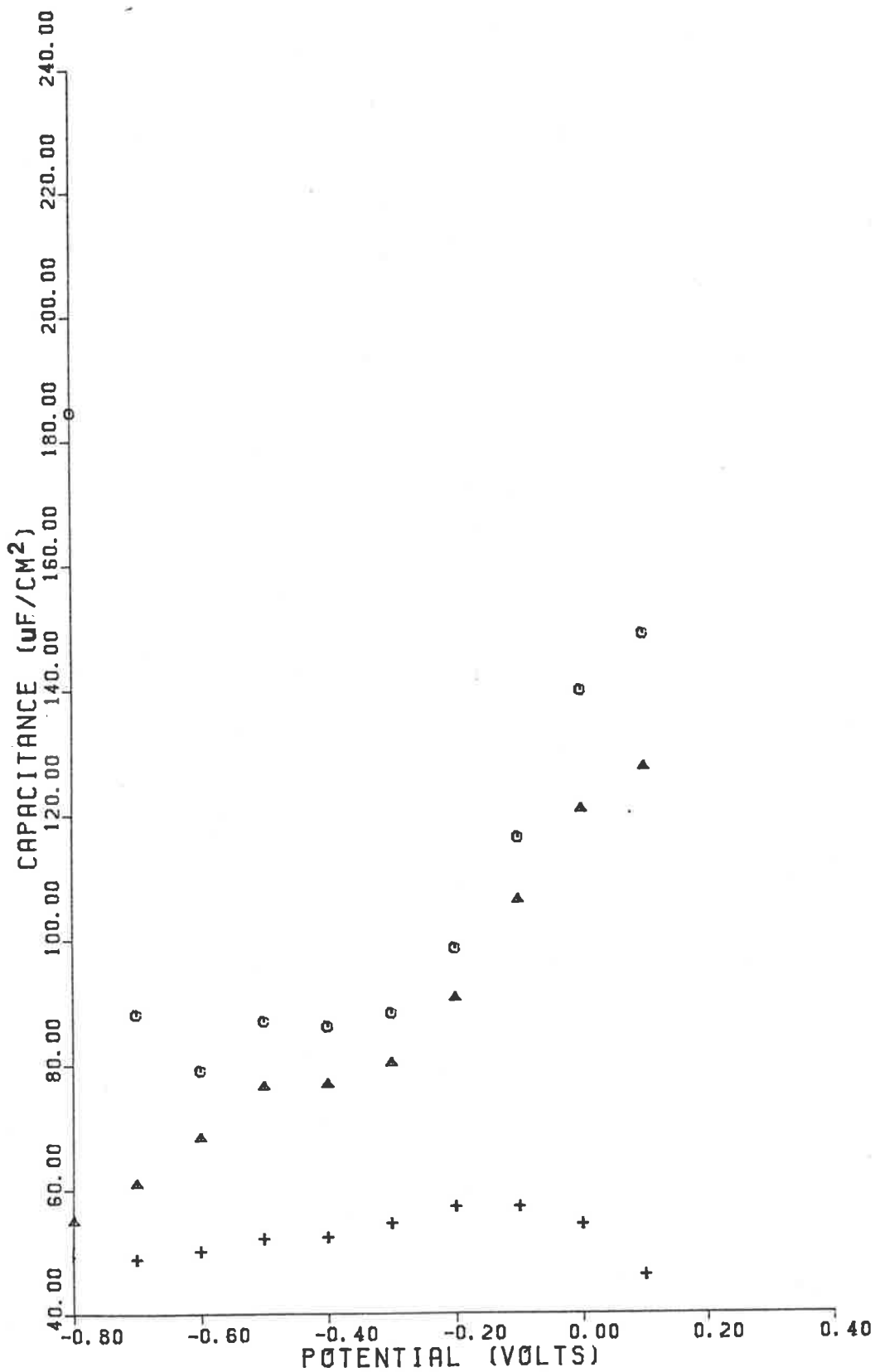


Figure 50 Capacitance-potential curves for the polycrystalline silver/0.100M NaNO<sub>3</sub> interface: Single Current Pulse Method, slow scan rate (+); series capacitance, 10 mV/s scan rate (O); parallel capacitance, 10 mV/s scan rate (Δ).

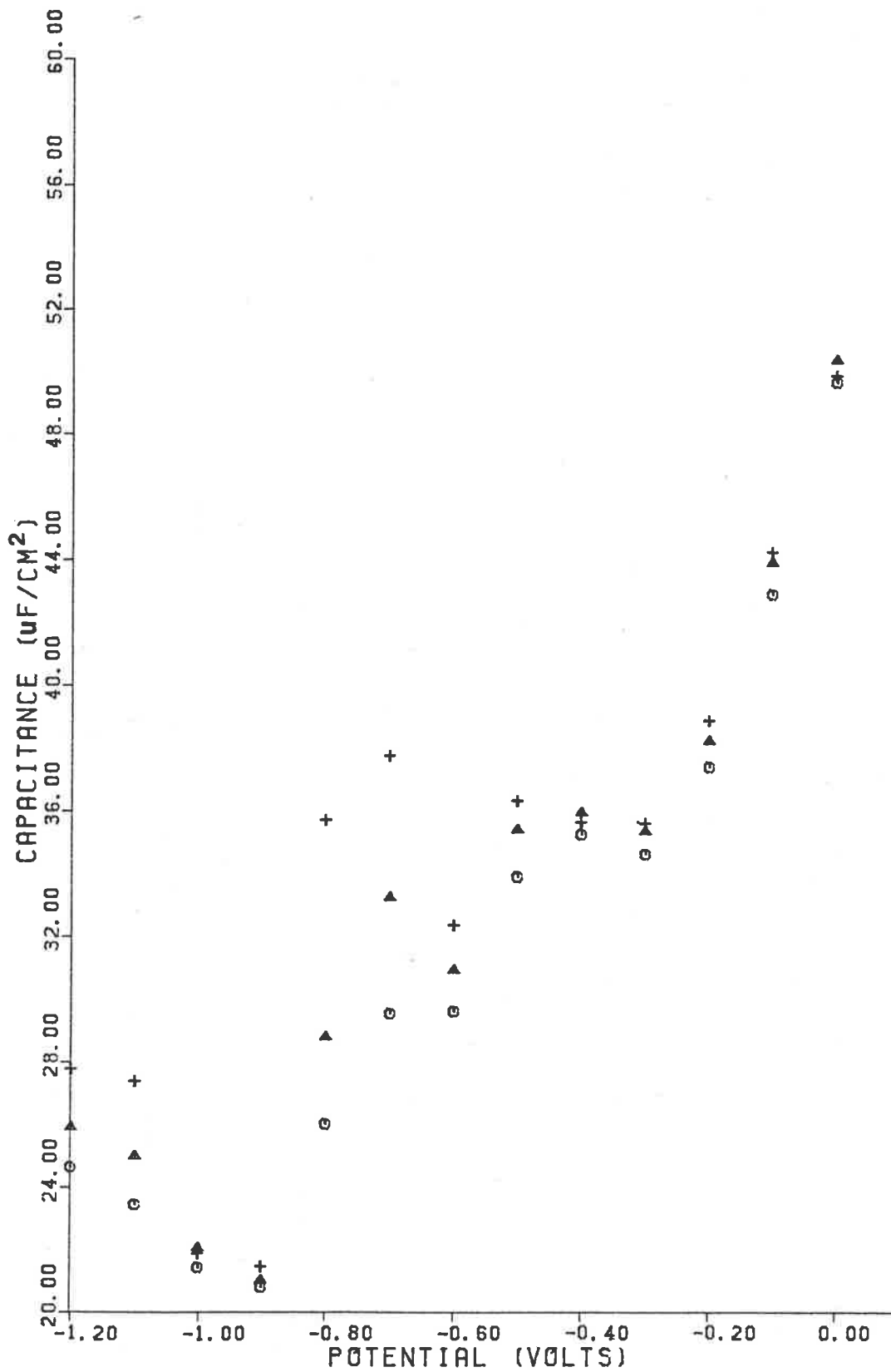


Figure 51 Frequency dependence of series capacitance-potential curves for polycrystalline silver in 0.010M NaNO<sub>3</sub>: 5 Hz (+); 10 Hz (Δ); 20 Hz (O). Cathodic scan. 10 mV/s scan rate.

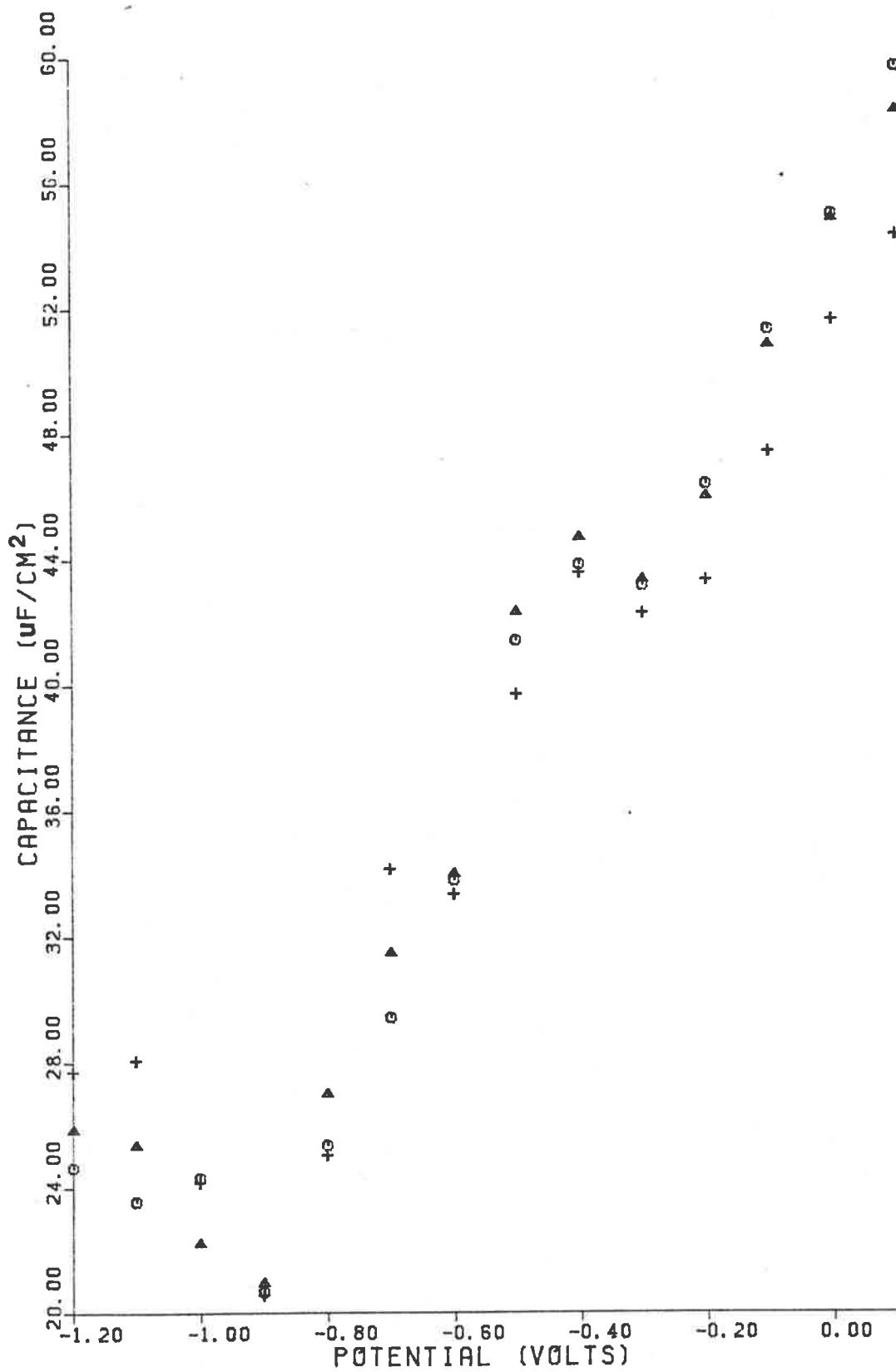


Figure 52 Frequency dependence of series capacitance-potential curves for polycrystalline silver in 0.010M NaNO<sub>3</sub>: 5 Hz (+); 10 Hz (Δ); 20 Hz (O). Anodic scan. 10<sup>-3</sup> mV/s scan rate.

tance from -0.9 volts to +0.10 volts. The determined capacitance shows some frequency dependence at the limits of the potential range scanned. The other obvious features are a capacitance minimum at -0.9 volts, and two capacitance humps at more anodic potentials. The capacitance hump with a maximum at -0.7 volts shows a marked frequency dependence. This frequency dependence is more evident in the cathodic scan shown in Figure 51. The other capacitance hump, having a maximum at about -0.4 volts, shows no frequency dependence. The cathodic and anodic series capacitance-potential curves are similar, but not superimposable.

Figures 53 and 54 show the complex plane impedance plots of the cathodic and anodic scans, respectively, for the polycrystalline silver/aqueous 0.010M  $\text{NaNO}_3$  interface at a number of selected electrode potentials. Although measurements were made only at frequencies of 5, 10 and 20 hz, it is obvious that the complex plane impedance plots are best fitted by a semicircle offset along the real axis. This corresponds to the analogue circuit of a series resistor combined with a resistor and capacitor in parallel. A number of representative arcs have been drawn in the figures to indicate appropriate values of the parallel resistance. In Figure 53, the parallel resistance has values of 3260, 2060, 4050, 4050 and more than 11,200 ohms at electrode potentials of -1.20, -0.70, -0.40, -0.10 and -0.90 volts, respectively. In Figure 54, the parallel resistance has values of 7400 and 4770 ohms at potentials of -0.90 volts and -0.10 volts, respectively. A best estimate of the real axis intercept of the arcs is 170 ohms. This corresponds to the value of the solution resistance between the working and reference electrodes, since no iR-compensation was used in these experiments.

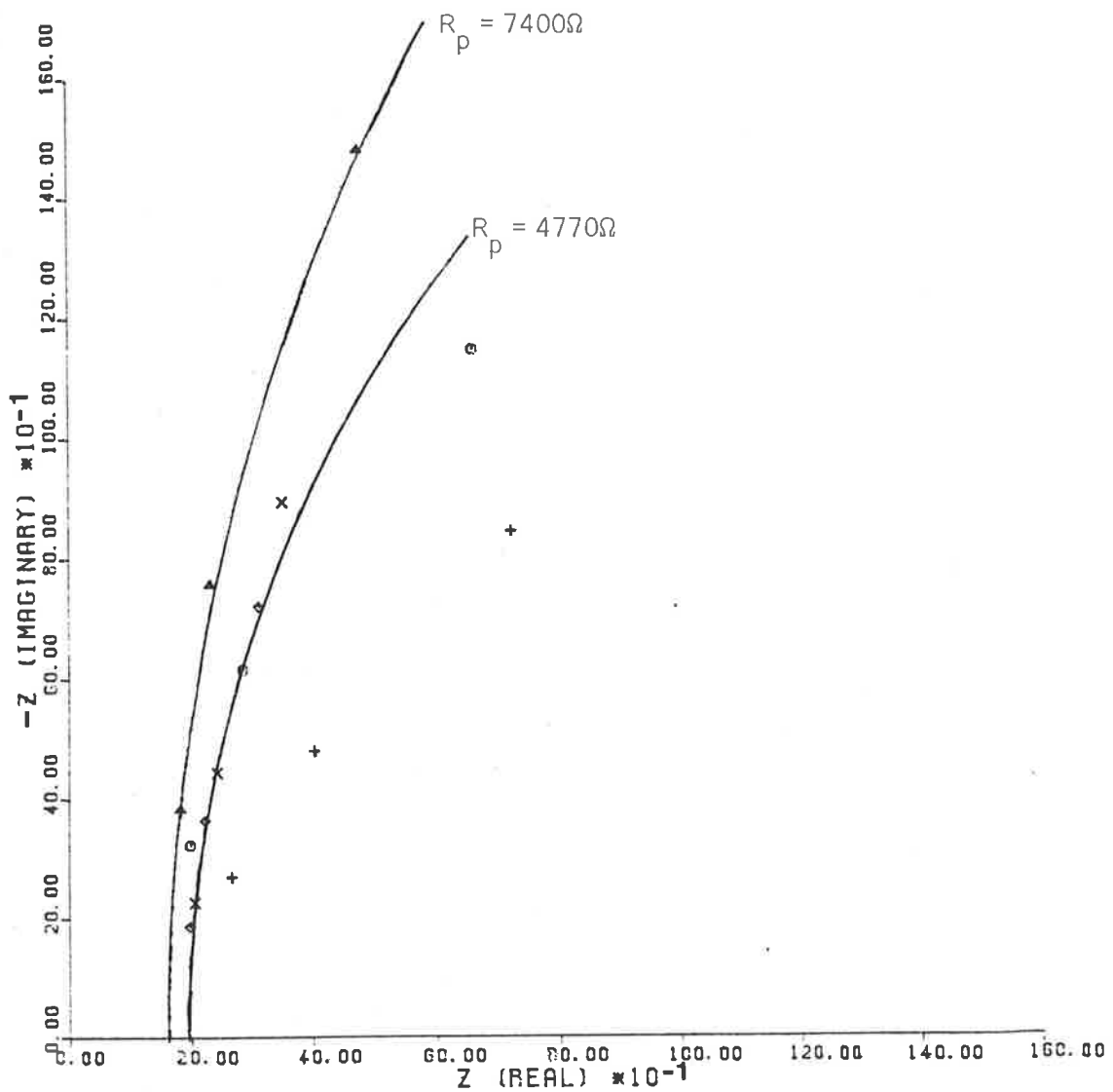


Figure 53. Complex plane impedance spectra for the polycrystalline silver/0.010M  $\text{NaNO}_3$  interface at selected electrode potentials:  $-1.20\text{ V}$  (○);  $-0.90\text{ V}$  (△);  $-0.70\text{ V}$  (+);  $-0.40\text{ V}$  (×);  $-0.10\text{ V}$  (◇). Cathodic scan. 10 mV scan rate.



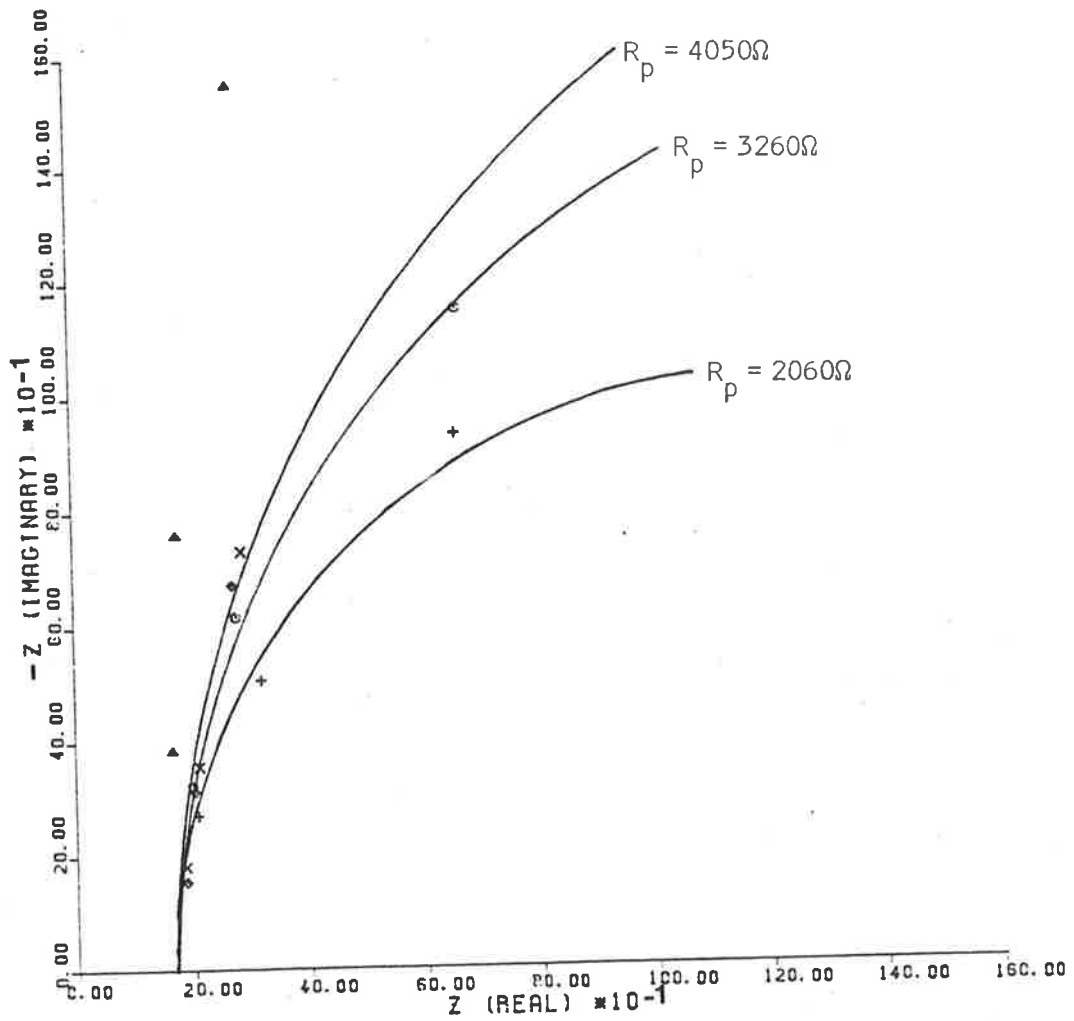


Figure 54. Complex plane impedance spectra for the polycrystalline silver/0.010M  $\text{NaNO}_3$  interface at selected electrode potentials:  $-1.20 \text{ V}$  (O);  $-0.90 \text{ V}$  ( $\Delta$ );  $-0.70 \text{ V}$  (+);  $-0.40 \text{ V}$  (X);  $-0.10 \text{ V}$  ( $\diamond$ ). Anodic scan.  $10 \text{ mV/s}$  scan rate.

Figures 55 and 56 show the parallel capacitance-potential curves calculated assuming a constant series resistance of 170 ohms. Measurements were made at frequencies of 5, 10 and 20 hz using a constant potential scan rate of 10 mV/s. The general trend in the capacitance-potential curves is a decrease in capacitance from -1.20 volts to -0.90 volts, followed by an increase in the capacitance from -0.90 volts to +0.10 volts. Both the cathodic and anodic curves show a capacitance minimum at -0.90 volts, and a capacitance hump with a maximum at -0.40 volts. The frequency dependent capacitance hump with a maximum at -0.70 volts apparent in the series capacitance-potential curves is obviously an artefact of the wrong analogue circuit being selected. There is no hint of such a peak in the parallel capacitance-potential curves.

The curves displayed in Figures 55 and 56 also show very little dependence on frequency. The cathodic curves shown in Figure 55 show no evidence of frequency dependence, excepting at the anodic extreme at +0.10 volts. The anodic capacitance-potential curves are identical at frequencies of 10 hz and 20 hz to within experimental error. The anodic curve at 5 hz is slightly lower in magnitude than those at 10 hz and 20 hz for potentials more anodic than the potential of the capacitance minimum.

The capacitance minimum at -0.90 volts for this system is independent of frequency and the scan rate direction. Convention would suggest that this potential corresponds to the true potential of zero charge. However, the cyclic voltammogram depicted for this system in Figure 57 clearly shows that this system is in a constant state of re-

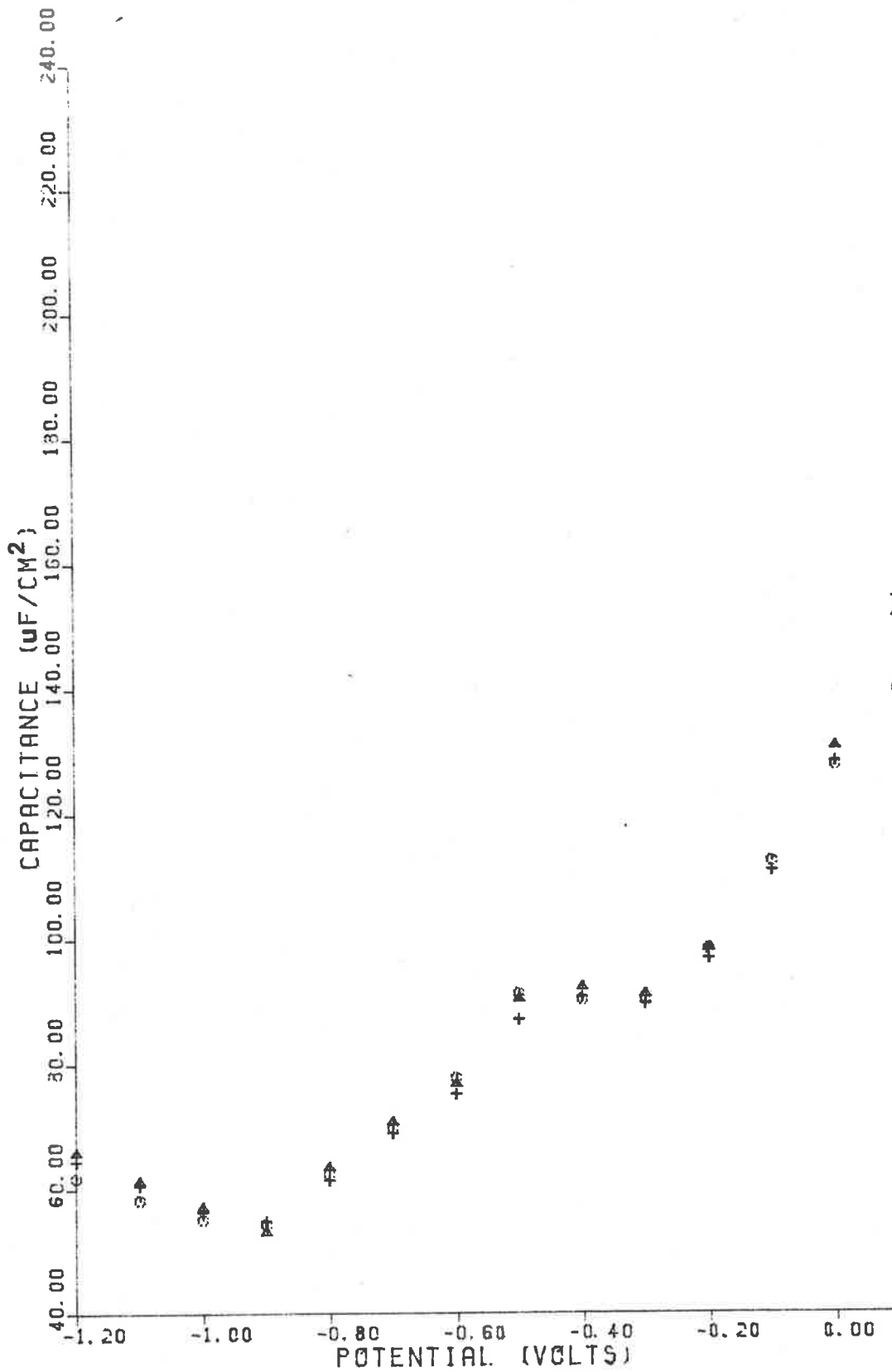


Figure 55 Frequency dependence of parallel capacitance-potential curves for polycrystalline silver in 0.010M NaNO<sub>3</sub>: 5 Hz (O); 10 Hz (Δ); 20 Hz (+). Cathodic scan. 10 mV/s scan rate.

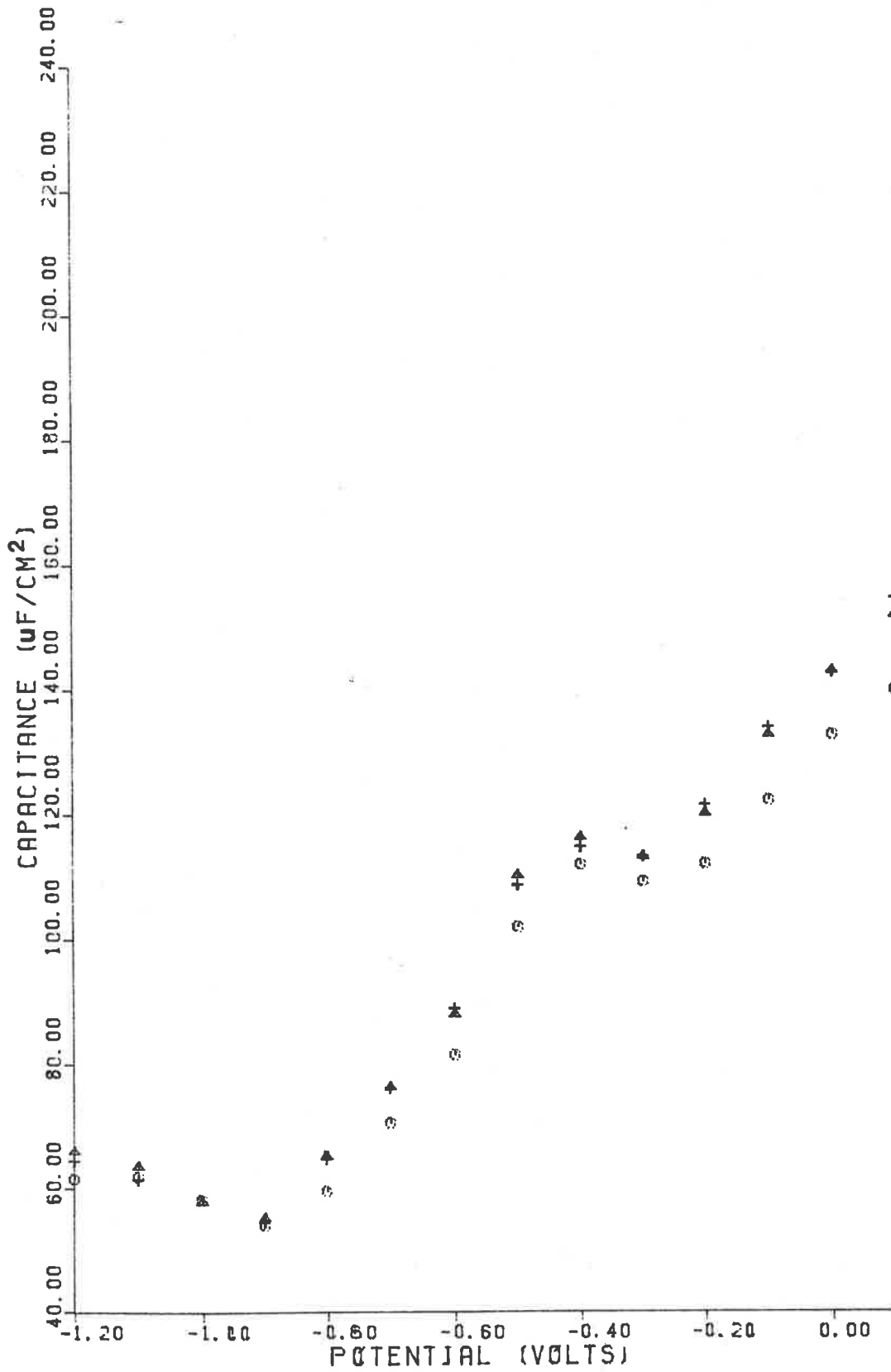


Figure 56 Frequency dependence of parallel capacitance-potential curves for polycrystalline silver in 0.010M NaNO<sub>3</sub>: 5 Hz (○); 10 Hz (△); 20 Hz (+). Anodic scan. 10 mV/s scan rate.

duction at potentials more cathodic than  $-0.60$  volts. The high reduction current at cathodic potentials is most probably due to nitrate ion reduction. From this evidence, it must be doubtful whether the potential of the capacitance minimum at  $-0.90$  volts truly corresponds to the potential of zero charge.

Vitanov and Popov determined the potential of zero charge to be at  $-0.90$  volts for the single-crystal silver (100)/aqueous  $1-10\text{mM}$   $\text{NaNO}_3$  interface. However, they found a marked concentration dependence of the potential of zero charge. This same dependence was also observed by Sevastyanov, Shlepacov and Kozlov for the polycrystalline silver/aqueous  $\text{NaNO}_3$  interface. The concentration dependence of the capacitance minimum observed by these authors is consistent with the considerable adsorption or reduction of nitrate that is evidently occurring in the vicinity of the capacitance minimum, as clearly shown in the cyclic voltammogram in Figure 57.

Figure 58 portrays the dependence of the electrode charge on the polarization potential for the polycrystalline silver/ $0.010\text{M}$   $\text{NaNO}_3/\text{H}_2\text{O}$  system. The shape of this curve is not affected by the author's assumption that the capacitance minimum corresponds to the potential of zero charge, but the true position of the curve along the potential axis must be regarded as somewhat uncertain.

Figure 59 compares the parallel capacitance-potential curves determined for the cathodic and anodic scans at a frequency of  $10$  hz. There is an evident hysteresis in the curves between the extreme anodic potential at  $+0.10$  volts and the potential of the capacitance

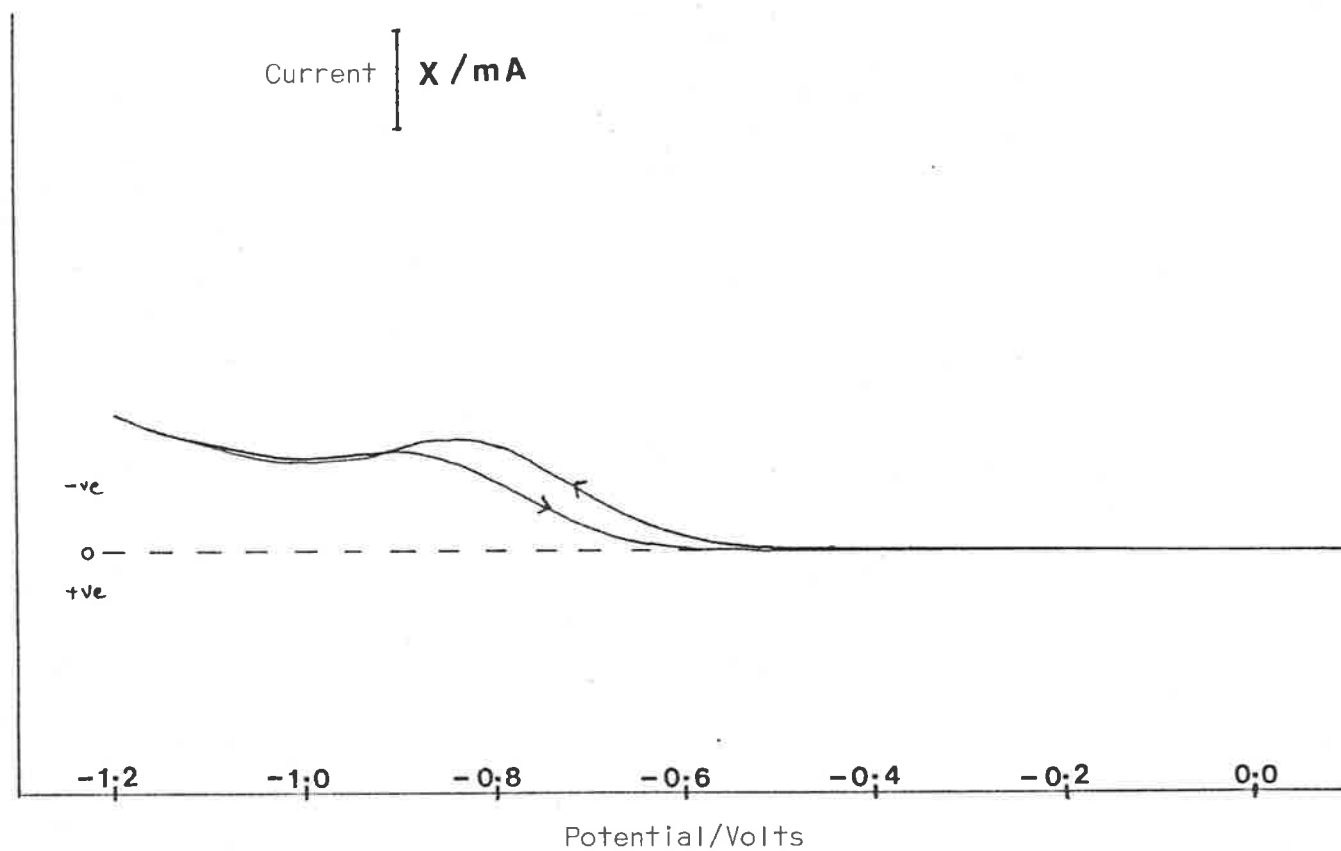


Figure 57. Cyclic voltammogram of polycrystalline silver in aqueous 0.010M  $\text{NaNO}_3$ .  $X = 0.1$ . Scan rate = 10 mV/s.

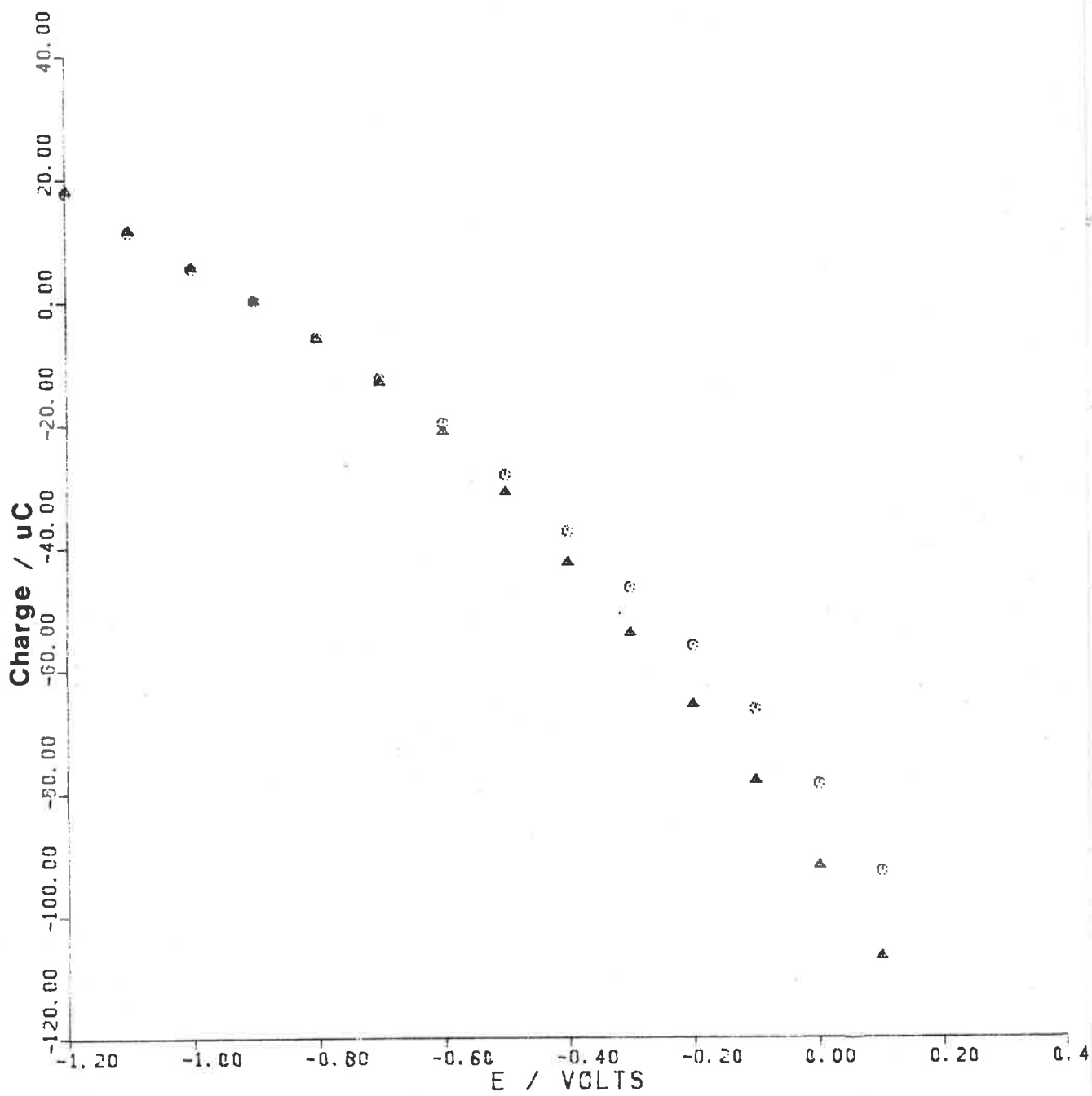


Figure 58 Dependence of electrode charge on potential for the polycrystalline silver/0.010M NaNO<sub>3</sub> interface: cathodic scan (O); anodic scan (Δ). - 10 mV/s scan rate.

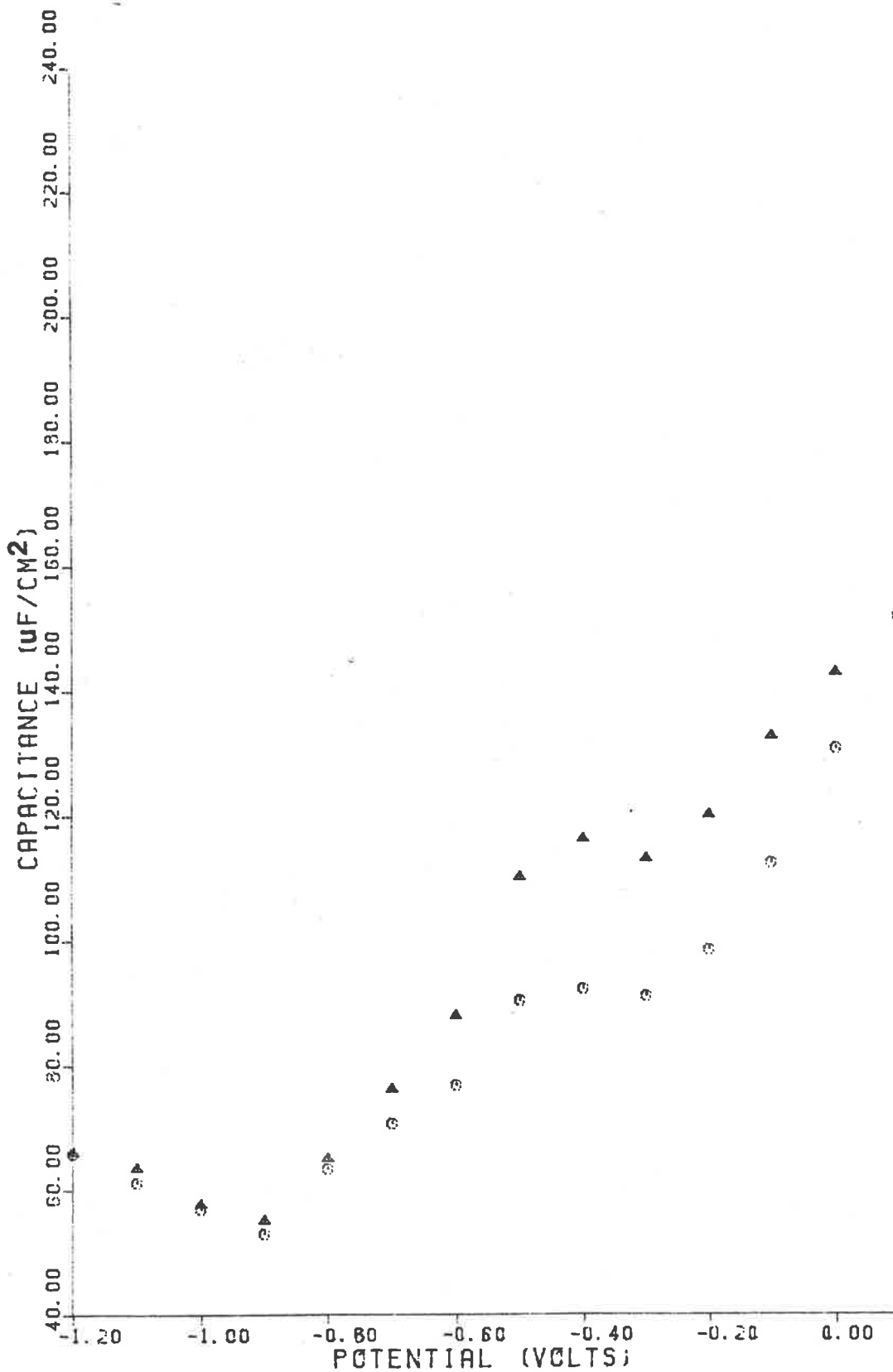


Figure 59 Hysteresis in parallel capacitance-potential curve for the polycrystalline silver/0.010M NaNO<sub>3</sub> interface at 10 hz: cathodic scan (O); anodic scan (Δ). 10 mV/s scan rate.



minimum at -0.90 volts. This is also evident from electrode charge-potential curves displayed in Figure 58.

Hysteresis in capacitance-potential curves is a well-known phenomenon in solid electrode studies. It has been found that the choice of the potential range has an effect on the amount of hysteresis.<sup>17</sup> In a recent article by Hamelin<sup>17</sup> the phenomena of hysteresis is linked by the author to restructuring of the electrode surface atomic structure. Surface reconstruction is known to occur for gold and platinum.<sup>18</sup> Hamelin,<sup>17</sup> however, maintained that no reconstruction had been observed for silver, as both the cathodic and anodic capacitance-potential curves coincided, and there was no great frequency dispersion for all media studied to that date (1982). The fact that no silver surface reconstruction had been observed in ultra-high vacuum studies<sup>18</sup> was also used as supportive evidence of the unlikelihood of silver surface reconstruction.

The results presented here in Figure 59, however, clearly show that hysteresis does occur for the polycrystalline Ag/0.010M NaNO<sub>3</sub>/H<sub>2</sub>O system, and that this phenomenon is likely to be connected with the reduction current found at potentials more cathodic than -0.6 volts, as shown in the cyclic voltammogram of Figure 57.



Figures 60-63 show the series capacitance-potential curves for the polycrystalline silver/aqueous 0.01M NaF interface obtained from A.C. Impedance measurements, assuming a simple analogue circuit of a capacitor and resistor in series.

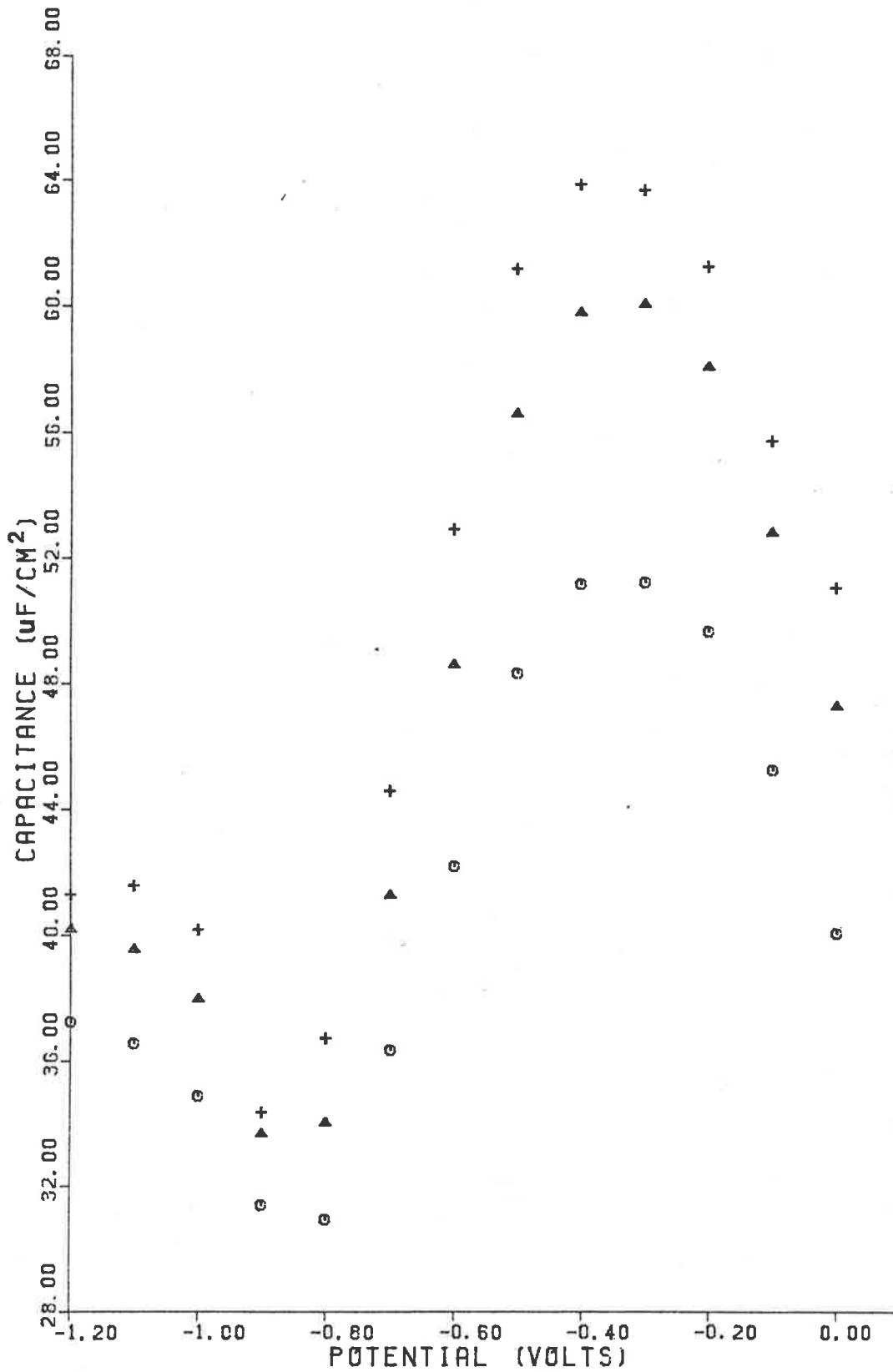


Figure 60 Frequency dependence of series capacitance-potential curves for the polycrystalline silver/0.010M NaF interface: 5 Hz (+); 10 Hz (Δ); 20 Hz (○). Cathodic scan. 10 mV/s scan rate.

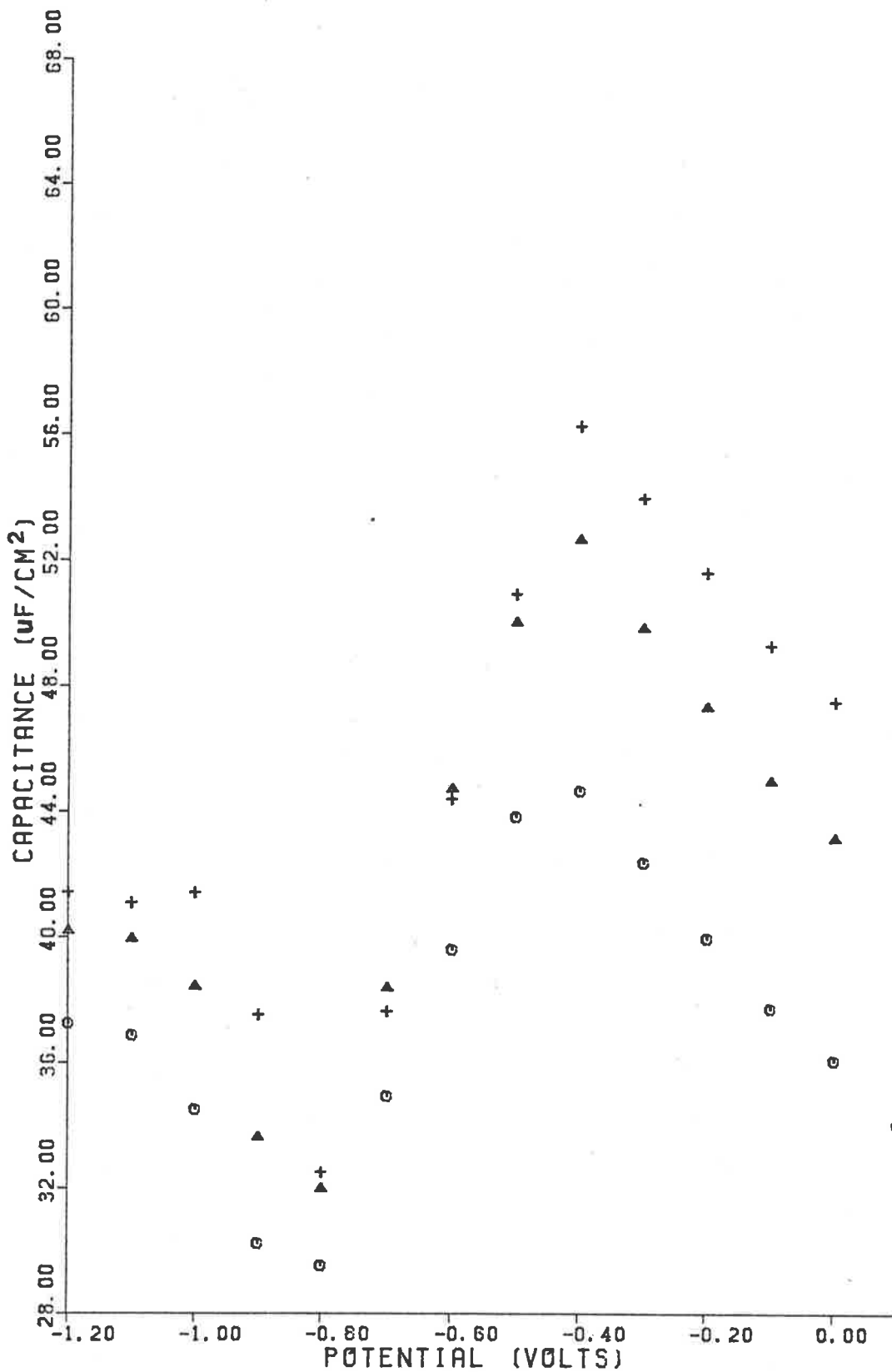


Figure 61 Frequency dependence of series capacitance-potential curves for the polycrystalline silver/0.010M NaF interface: 5 Hz (+); 10 Hz ( $\Delta$ ); 20 Hz (O). Anodic scan. 10 mV/s scan rate.

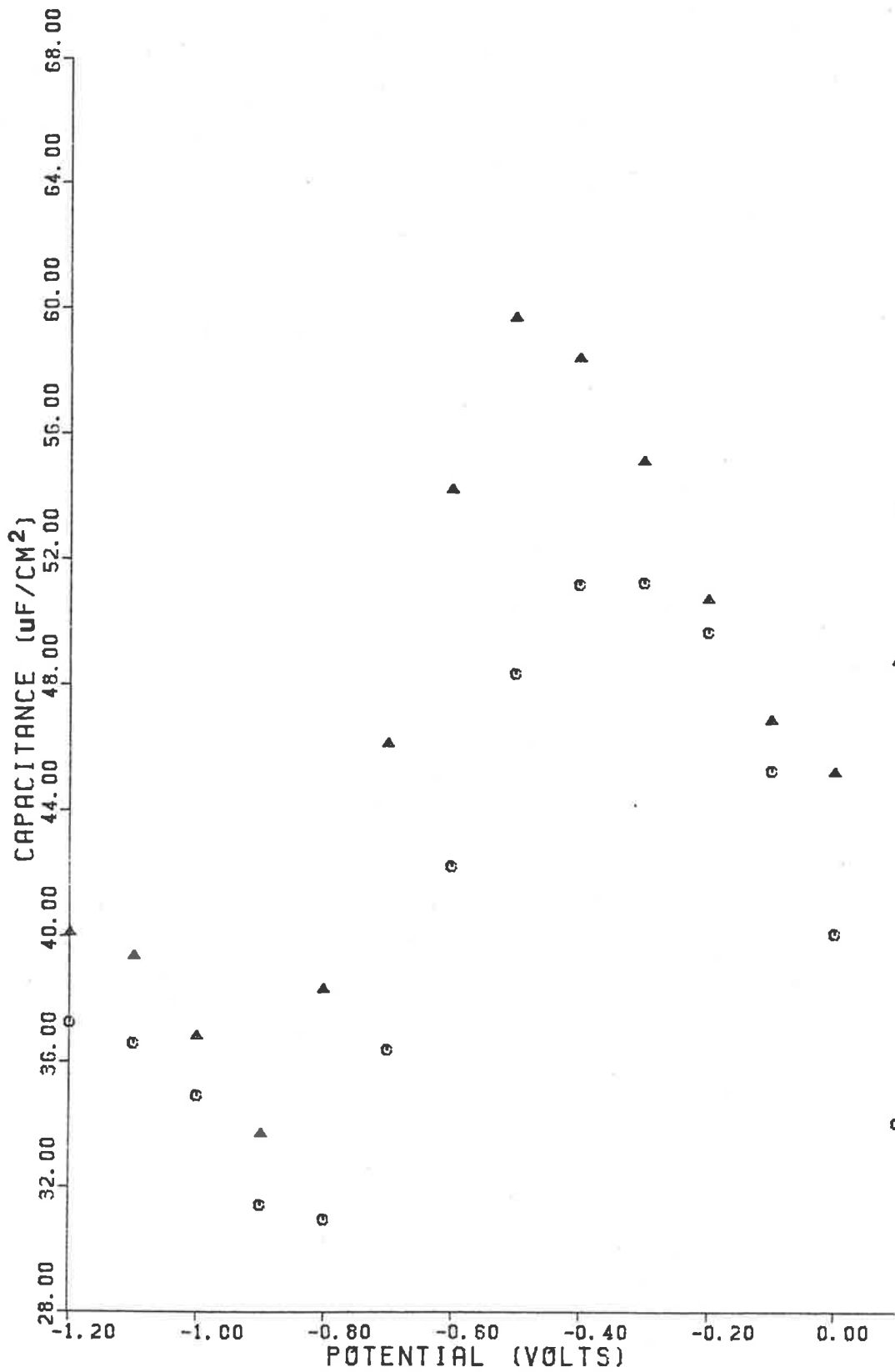


Figure 62 Scan rate dependence of series capacitance-potential curves for the polycrystalline silver/0.010M NaF interface at 20 Hz: 10 mV/s (O); 100 mV/s (Δ). Cathodic scan.

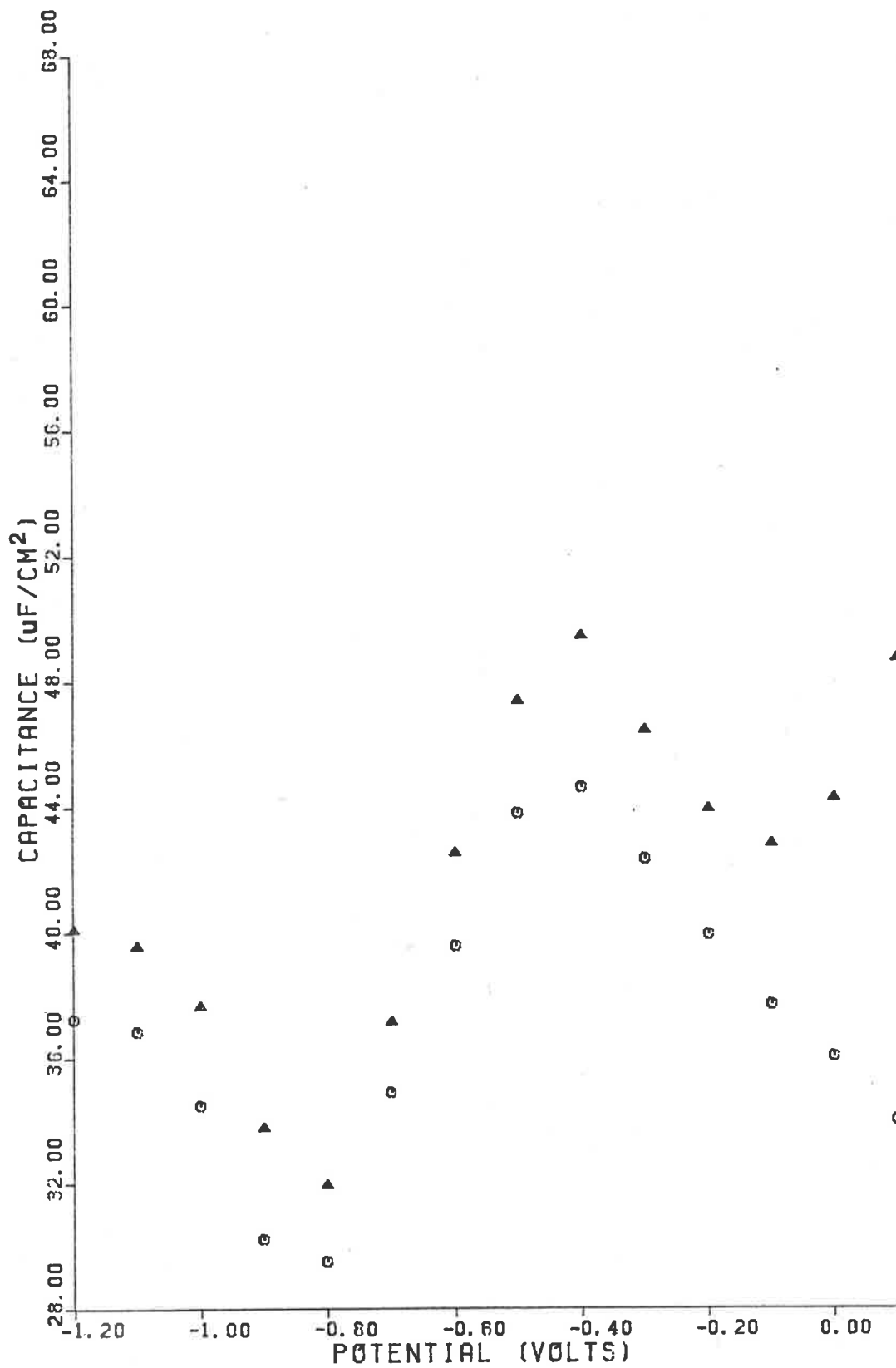


Figure 63 Scan rate dependence of series capacitance-potential curves for the polycrystalline silver/0.010M NaF interface at 20 hz: 10 mV/s (O); 100 mV/s (Δ). Anodic scan.

This system was found to show considerable dependence upon frequency. This is evident in the cathodic and anodic capacitance-potential curves presented in Figures 60 and 61, respectively, for frequencies of 5, 10 and 20 hz. A moderate scan rate of 10 mV/s was used in these measurements.

The general trend in the capacitance-potential curves is a decreasing capacitance from -1.2 V to -0.8 V, followed by an increasing capacitance from -0.8 V to -0.4 V, and a decreasing capacitance from -0.4 V to +0.1 V.

Figures 62 and 63 show the cathodic and anodic capacitance-potential curves, respectively, obtained at a frequency of 20 hz using two different potential scan rates. It can be seen that changing the potential scan rate from 10 mV/s to 100 mV/s resulted in generally higher capacitances, as well as a shape change in the capacitance-potential curve.

Based on the above observation, one might be tempted to presume that this system will yield capacitances that show a time dependence akin to that found for the polycrystalline platinum/aqueous electrolyte interface. Upon holding the electrode potential steady at -0.90 volts, however, the capacitance measured at 20 hz was found to be independent of the time of measurement. If the polycrystalline silver/aqueous 0.010M NaF interface did require an amount of time to stabilize, this time must be limited to the few seconds required to make the first measurement.

Figure 64 shows the complex impedance plot obtained for this system maintained at a constant potential of  $-0.90$  volts. The plot of the imaginary impedance against the real impedance can be fitted by a straight line intercepting the real axis at a value of  $237 \pm 11$  ohms. The acute angle made by the line with the real axis is  $73.6^\circ$ . The intercept made with the real axis corresponds to the series resistance through the solution between the working and reference electrodes. Adjustment to impedance measurements for the amount of the solution resistance simply moves the line to the origin without affecting its slope.

The data shown in Figure 64 can also be fitted by an arc of a semicircle. This would correspond to the analogue circuit of a series resistor combined with a resistor and capacitor in parallel. This is more clearly borne out in Figures 79 and 80.

Figures 65 and 66 show the complex plane impedance plots of the cathodic and anodic scans, respectively, for the polycrystalline silver/aqueous  $0.010M$  NaF interface at a number of selected electrode potentials. Although measurements were made only at frequencies of 5, 10 and 20 hz, it is obvious that the complex plane impedance plots are best fitted by a semicircle offset along the real axis. A number of representative arcs have been drawn in the figures to indicate appropriate values of the parallel resistance. In Figure 65, the parallel resistance has values of 8750, 5820, 5080, 5080 and more than 8800 ohms at electrode potentials of  $-1.20$ ,  $-0.70$ ,  $-0.40$ ,  $-0.10$  and  $-0.90$  volts, respectively. In Figure 66, the parallel resistance has values of 8600, 8600, 5750 and 5750 ohms at potentials of  $-1.20$ ,  $-0.90$ ,  $-0.40$

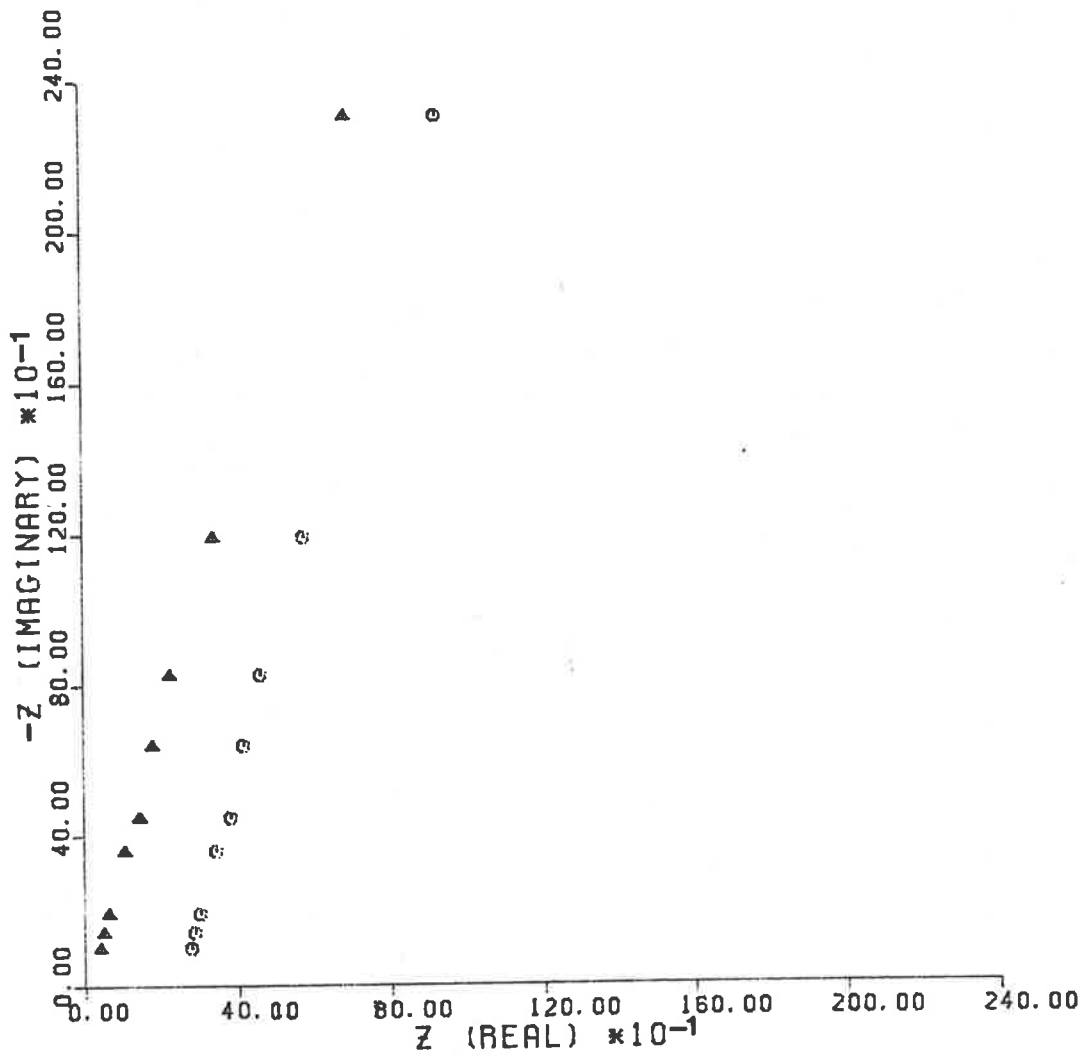


Figure 64 Complex plane impedance spectra of the polycrystalline silver/0.010M NaF interface at +0.20 volts: unadjusted data (O); series resistance adjusted data (Δ). Static measurement.



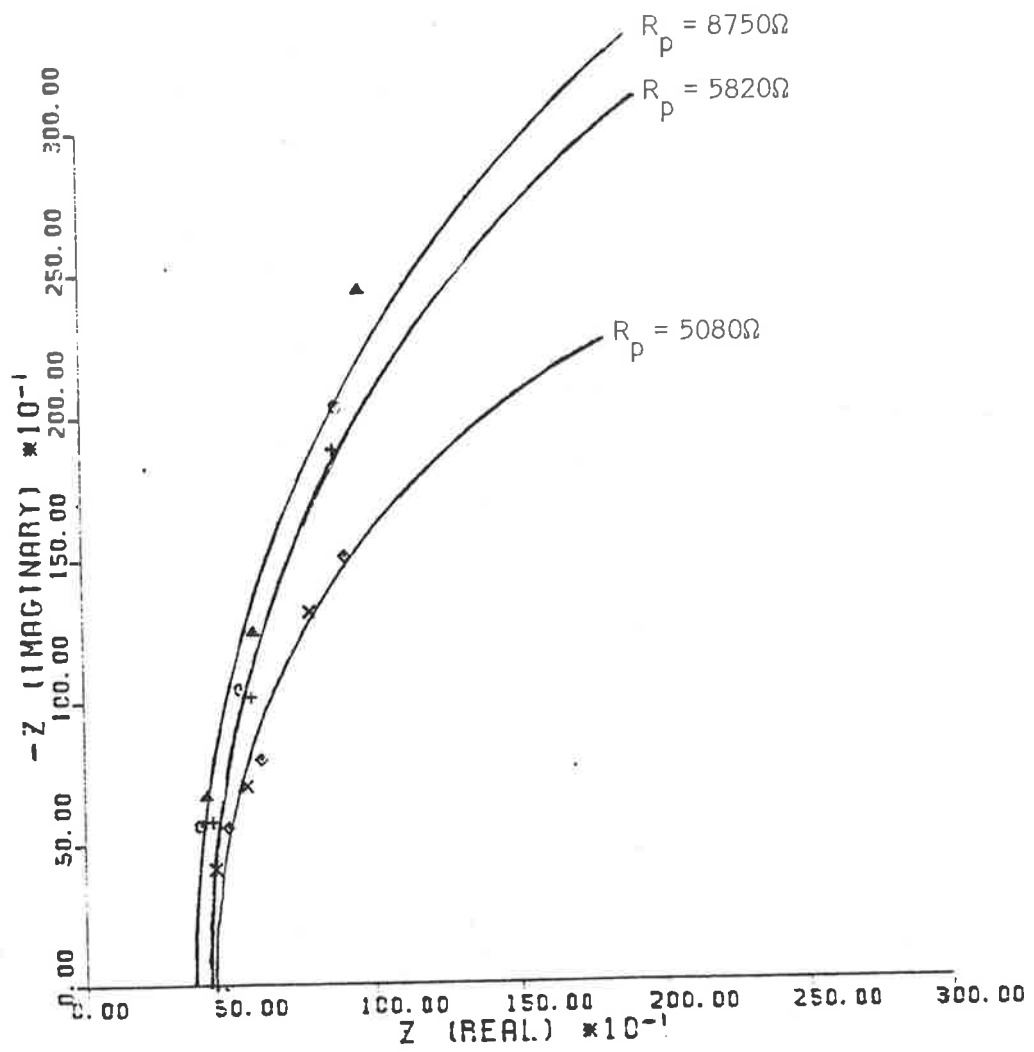


Figure 65. Complex plane impedance spectra for the polycrystalline silver/0.010M NaF interface at selected electrode potentials: -1.20 V ( $\circ$ ); -0.90 V ( $\Delta$ ); -0.70 V ( $+$ ); -0.40 V ( $\times$ ); -0.10 V ( $\diamond$ ). Cathodic scan. 10 mV/s scan rate.

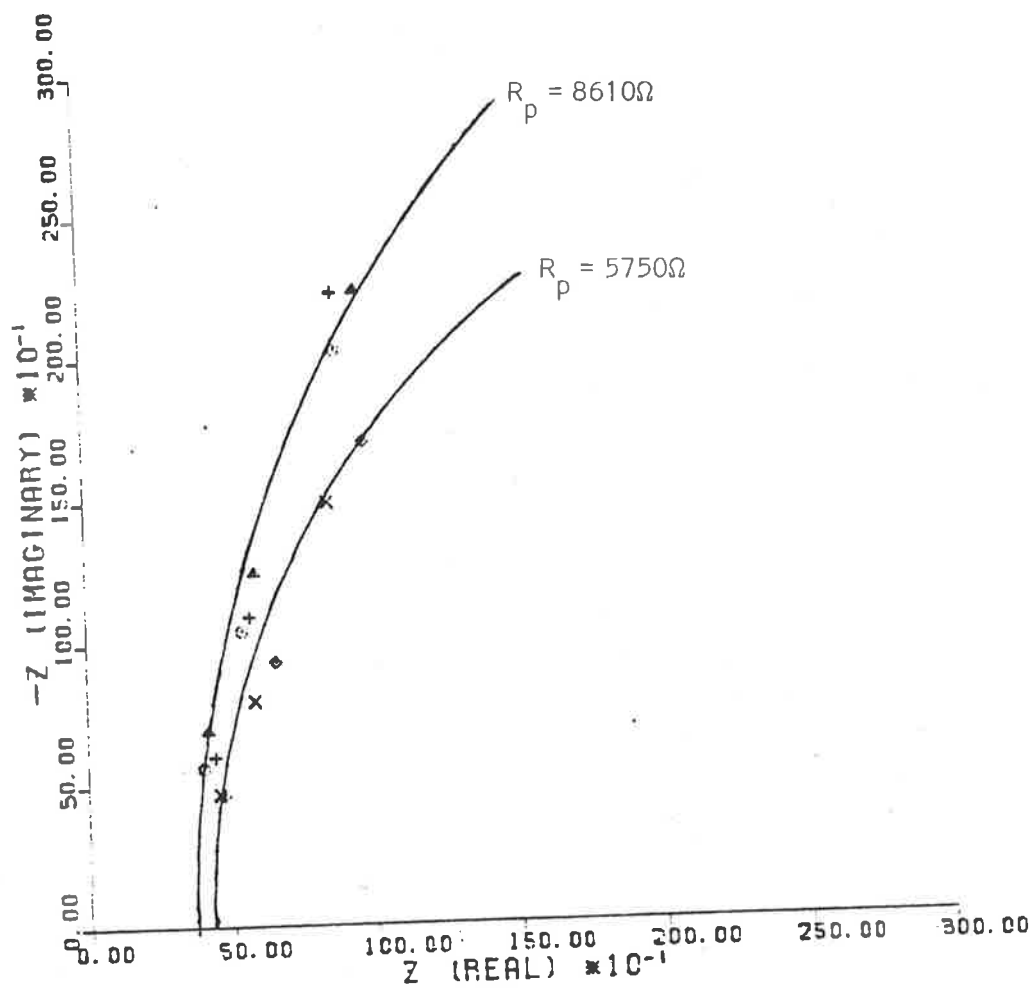


Figure 66. Complex plane impedance spectra for the polycrystalline silver/0.010M NaF interface at selected electrode potentials: -1.20 V ( $\circ$ ); -0.90 V ( $\Delta$ ); -0.70 V ( $+$ ); -0.40 V ( $\times$ ); -0.10 V ( $\diamond$ ). Anodic scan. 10 mV/s scan rate.

and -0.10 volts, respectively. A best estimate of the real axis intercept of the arcs is  $415 \pm 35$  ohms. Since no iR-compensation was used in this series of measurements, the real axis intercept corresponds to the solution resistance between the working and reference electrodes.

Fitting the impedance data at -0.90 volts with a straight line for the dynamic measurements yields slopes of  $72.7^\circ$  and  $70.2^\circ$ , and real axis intercepts of  $212 \pm 16$  ohms and  $160 \pm 35$  ohms for the cathodic and anodic scans, respectively. The cathodic scan results compare favourably with the static results of an angle of  $73.6^\circ$  and a real axis intercept of  $237 \pm 11$  ohms. These real axis intercepts are much lower than the potential independent 415 ohm intercept determined by fitting the data to part of a semicircle. Obviously, the measurement of the complex plane impedance spectrum at a single potential could by itself be misleading as to the appropriateness of a particular analogue circuit.

Figures 67 and 68 show the parallel capacitance-potential curves calculated assuming a constant series resistance of 415 ohms. Measurements were made at frequencies of 5, 10 and 20 hz using a constant potential scan rate of 10 mV/s. The curves have the same general features as the series capacitance-potential curves displayed in Figures 60 and 61. The curves show the parallel capacitance to be frequency dependent, though the curves determined at 5 hz and 10 hz are reasonably similar. There is no clearly defined capacitance minimum in the capacitance-potential curves. The capacitance minimum was found at potentials of -0.80 volts to -0.90 volts, showing a dependence upon both frequency and the potential scan direction.

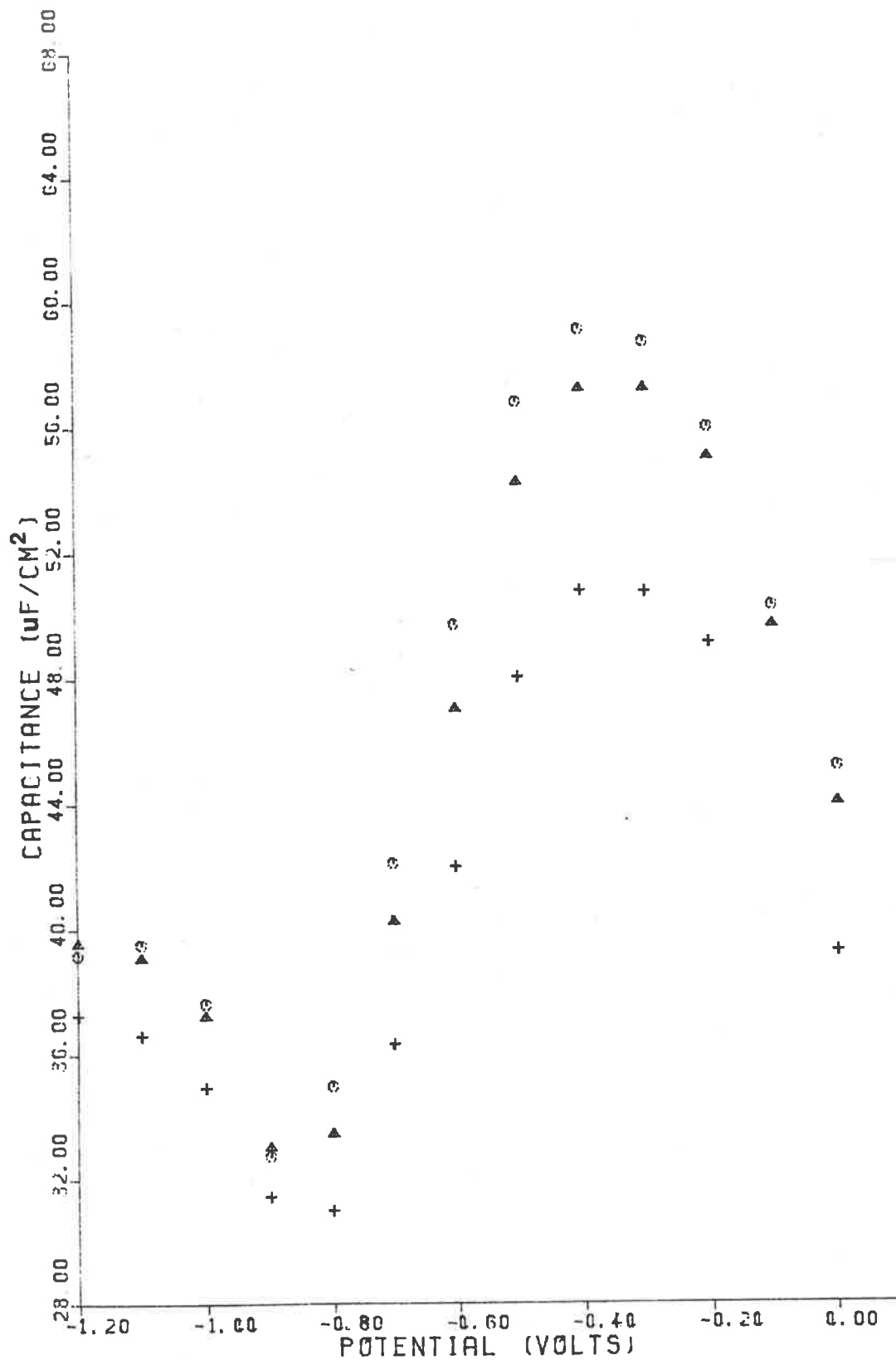


Figure 67 Frequency dependence of parallel capacitance-potential curves for the polycrystalline silver/0.010M NaF interface: 5 Hz (○); 10 Hz (△); 20 Hz (+). Cathodic scan. 10 mV/s scan rate.

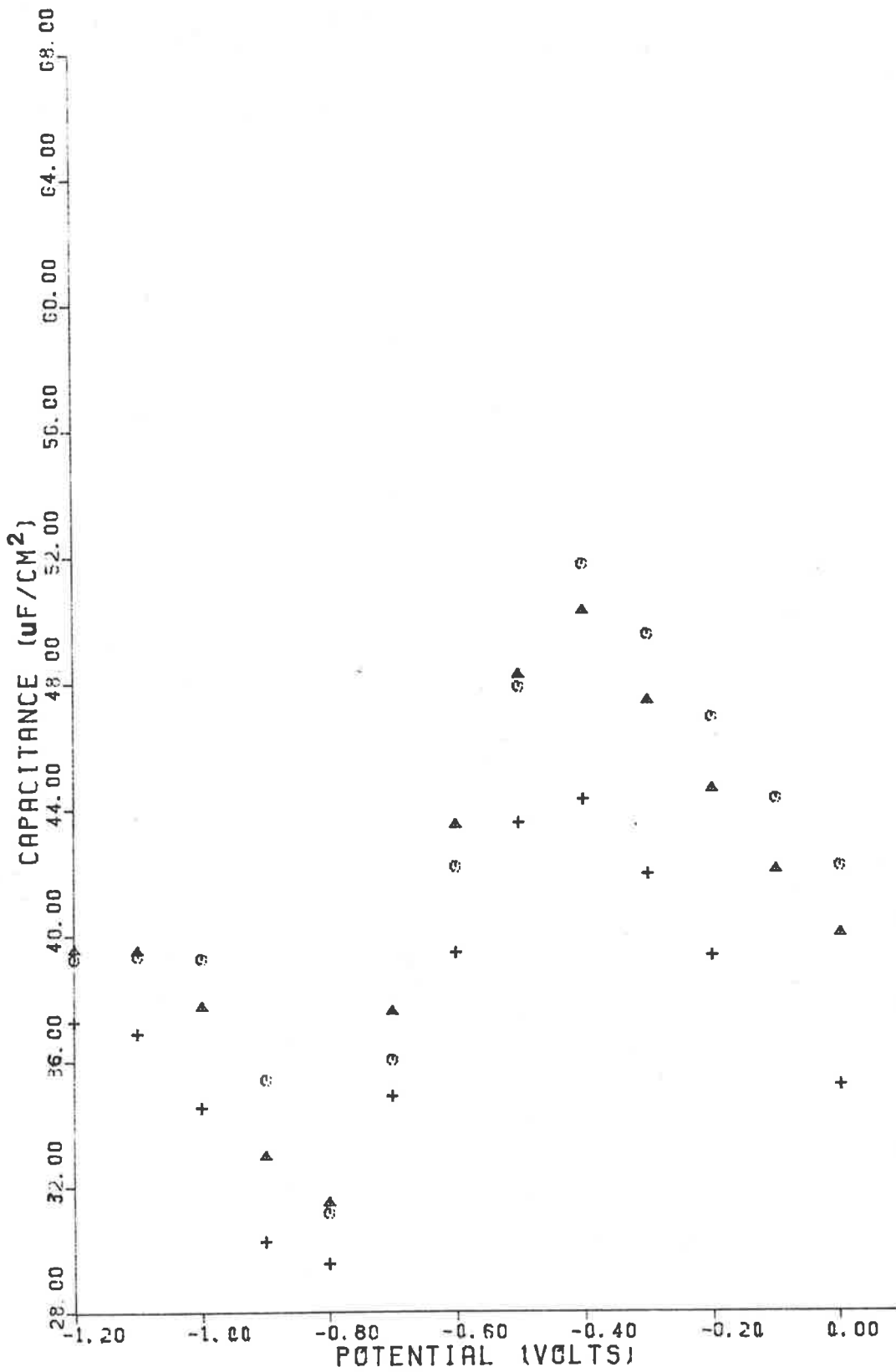


Figure 68 Frequency dependence of parallel capacitance-potential curves for the polycrystalline silver/0.010M NaF interface: 5 Hz (○); 10 Hz (△); 20 Hz (+). Anodic scan. 10 mV/s scan rate.

Figure 69 compares cyclic voltammograms obtained with the polycrystalline silver electrode in aqueous 0.010M NaF and aqueous 0.010M NaNO<sub>3</sub>. It can be seen that the general current level is low in 0.010M NaF, and that there is no apparent region of anionic reduction, as there is in aqueous 0.010M NaNO<sub>3</sub>.

Valette and Hamelin<sup>19</sup> studied the polycrystalline Ag/0.040M NaF/H<sub>2</sub>O system. Their capacitance-potential curves show some frequency dependence, and have a capacitance minimum at -0.94 volts. These authors assumed a simple analogue circuit of a capacitor and resistor in series, which has been shown in these studies to not be the best analogue circuit. In this case, however, the use of series capacitance rather than parallel capacitance is not likely to drastically alter the results. This can be seen from the work presented here for the polycrystalline Ag/0.010M NaF/H<sub>2</sub>O system by comparing the series capacitance in Figures 60 and 61 with the parallel capacitance shown in Figures 67 and 68. The general shape of the capacitance-potential curves obtained by the author is similar to that of Valette and Hamelin, with the capacitance minimum at -0.80 volts to -0.90 volts, which is slightly anodic of the -0.94 volts claimed by Valette and Hamelin.

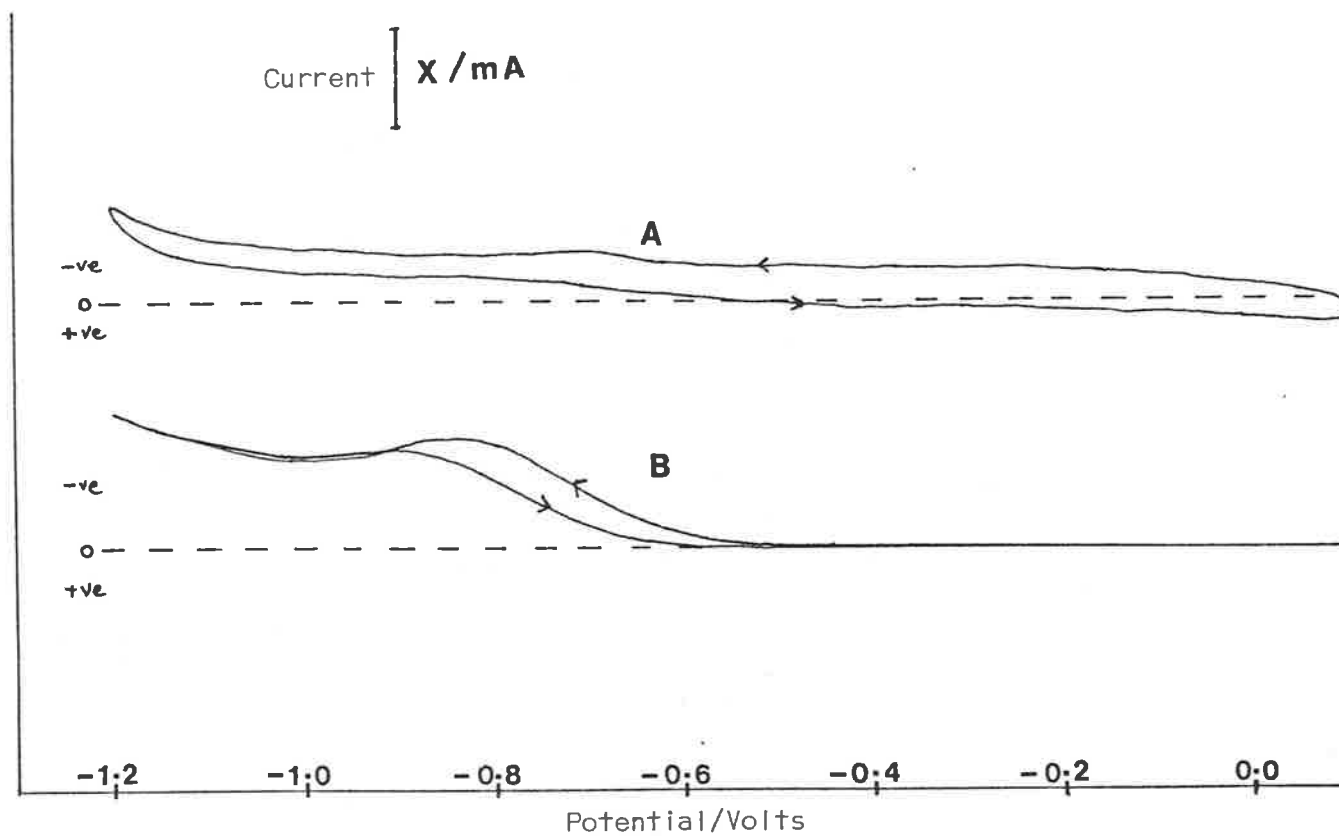


Figure 69. Cyclic voltammograms of polycrystalline silver in aqueous electrolyte solutions:

A. 0.010M NaF,  $X = 0.005$ ;

B. 0.010M NaNO<sub>3</sub>,  $X = 0.1$ .

Scan rate = 10 mV/s.

**CONCLUSION**

The polycrystalline silver/0.100M NaNO<sub>3</sub>/H<sub>2</sub>O system was briefly investigated using the Single Current Pulse Method and the A.C. Impedance Method. It was found that there was poor agreement between the capacitance-potential curves determined using the Single Current Pulse Method and the A.C. Impedance Method, assuming either a simple series or parallel analogue circuit.

Typically, the silver/aqueous electrolyte interface is assumed to be equivalent to a capacitor and resistor in series. From the complex plane impedance spectra presented here, however, it was observed that the polycrystalline silver/aqueous 0.010M NaNO<sub>3</sub> and polycrystalline silver/aqueous 0.010M NaF interfaces were best fitted by the analogue circuit of a series resistor and a resistor and capacitor in parallel. It was only by using such an analogue circuit that one could obtain a value for the solution resistance that was independent of both the potential and direction of potential scan.

The capacitance in aqueous 0.010M NaNO<sub>3</sub> was found to show very little frequency dependence, but clearly showed hysteresis over a portion of the potential range scanned. For this system, a capacitance minimum was found at -0.90 volts that was independent of frequency and the scan direction. Conventionally, this would be forwarded as the potential of zero charge; however, cyclic voltammetric evidence shows that the electrode appears to be irreversibly reducing nitrate ion at this potential. The current flowing at this potential due to reaction surely will serve to confuse the true position of the potential of zero charge on the electrode in the absence of reaction,



and so the author does not put forward  $-0.90$  volts as unambiguously being the potential of zero charge.

No known hysteresis in capacitance-potential curves for silver/ aqueous electrolyte systems had been observed prior to the observation of such a phenomenon in this work on the polycrystalline silver/ $0.010M$   $NaNO_3/H_2O$  system. The observed hysteresis is likely to be related to the transition found in the nature of this system as observed using cyclic voltammetry.

Recently, the author found that Sevastyanov et al<sup>20</sup> had investigated adsorption and electroreduction of nitrate and nitrite ions on polycrystalline silver. These authors found that appreciable reduction of nitrate ions on silver began at considerably more positive potentials than the reduction of nitrite ions which began at around  $-1.00$  volts. These electroreduction results are consistent with the results of the writer. Sevastyanov et al also concluded that because the measured resistance component at a given frequency was not dependent on the polarizing potential over a particular range in nitrite solution, then the capacitance component of the measured impedance corresponded to double layer capacitance for the polycrystalline silver +  $NaNO_2 + H_2O$  system. The measured parallel resistance for the polycrystalline silver +  $NaNO_3 + H_2O$  system, however, was found by the writer to vary significantly enough for the capacitance component not to be unequivocally equated with the double layer capacitance.

During the progress of the writer's work, Milkowska and Minc<sup>21</sup> investigated the adsorption of nitrate ion at the polycrystalline

silver/aqueous electrolyte solution interface. These authors measured the differential capacitance of this interface for a number of different concentrations of  $\text{LiNO}_3$ . They used the method of Grahame and Soderberg,<sup>22</sup> modified by Damaskin et al,<sup>23</sup> to determine adsorption parameters from the differential capacitance results. No mention, however, was made of the actual reduction of nitrate on silver in the potential range of interest as found by the writer using  $\text{NaNO}_3$ , and by others using  $\text{KNO}_3$ <sup>20</sup> and  $\text{AgNO}_3$ .<sup>24</sup> Milkowska and Minc claimed that nitrate adsorption was weaker at low positive charge on silver than on mercury or gold, but stronger than in the case of mercury at high positive charge.

In the light of these claims, the writer used cyclic voltammetry to investigate the potential range used by Milkowska and Minc, and found that the cyclic voltammogram showed that nitrate was reduced from an aqueous solution of  $\text{LiNO}_3$  as it was for the sodium and potassium nitrate salts. The writer would therefore regard the calculations and conclusions presented by Milkowska and Minc to be of questionable value.

The capacitance-potential curves obtained for the polycrystalline silver/ $0.010\text{M NaF/H}_2\text{O}$  system were found to be frequency dependent, and gave a poorly defined cathodic capacitance minimum at a potential slightly anodic of the minimum at  $-0.94$  volts found for this system by Valette and Hamelin.<sup>19</sup> The general shape and frequency dependence of the capacitance-potential curves obtained by the author were similar to those obtained by Valette and Hamelin. Cyclic voltammograms for this system were basically featureless over the entire potential range scanned, indicating no obvious adsorption or reduction of fluoride

on silver. A number of other studies have also been made using silver single-crystal and polycrystalline electrodes in aqueous NaF or KF solutions.<sup>25-28</sup> The conclusion derived from those studies was that specific adsorption of fluoride ion is weak or absent.

It is of interest to note here that, in the vicinity of the potential of zero charge, fluoride and nitrate are only weakly specifically adsorbed on mercury,<sup>29</sup> fluoride is only weakly adsorbed on silver, whereas nitrate is readily adsorbed and reduced on silver. Cadmium is another metal that displays the same duality as silver with regard to fluoride and nitrate.<sup>30</sup> Certainly, the specific nature of the metal must be an important part of future theories concerning the metal/electrolyte solution interface.

The polycrystalline silver/dilute electrolyte/H<sub>2</sub>O systems yielded capacitances that showed little time dependence, unlike the polycrystalline platinum/aqueous electrolyte systems. Obviously, maintaining the electrode potential constant within the region of hysteresis would result in an averaged capacitance being measured once the system had quickly equilibrated. At a potential outside this region, such as at -0.90 volts, the capacitance determined was found to be independent of time.

## CONCLUSION

The solid metal/aqueous electrolyte solution interface was investigated using double layer capacitance measurements derived from an A.C. Impedance Method and a Single Current Pulse Method. Capacitance-potential curves were obtained in 1M and 1m HCl, 0.1M NaCl, 0.1M KNO<sub>3</sub>, 0.1M NaNO<sub>3</sub> and 0.001M NaNO<sub>3</sub> using polycrystalline platinum, and in 0.1M NaNO<sub>3</sub>, 0.010M NaNO<sub>3</sub> and 0.010M NaF using polycrystalline silver.

The Single Current Pulse measurements showed that the interfaces studied were the equivalent of a capacitor and resistor in parallel. The measured resistance was consistently found to be quite low. The capacitance was found to show a consistent marked time dependence using polycrystalline platinum which was not present when using polycrystalline silver.

In a study of this time dependency of the polycrystalline platinum/HCl interface, the writer found that, although the capacitance showed a complex time dependency, the parallel resistance was shown to be independent of time. In a recent article, McNicol et al<sup>31</sup> looked at the influence of electrolyte purity on electrochemical measurements using platinum electrodes. They concluded from hydrogen adsorption studies in sulphuric acid that platinum electrodes adsorbed impurities from the electrolyte solution, no matter how pure the solution was, if the electrode was maintained at a potential within the double layer region for a period of minutes. The accumulation of surface active impurities on the platinum electrode with time, however, does not appear to be consistent with the time dependency found in these capacitance measurements. If surface accumulation of impurities

were a dominating influence, then all capacitance measurements would be expected to decrease with time. The parallel resistance component would also be expected to decrease with time. Neither of these effects was observed. The parallel resistance was found to be independent of time, while the capacitance increased, decreased, or remained the same with time, depending on the particular polarizing potential.

The writer found a time dependence in the capacitance measurements for polycrystalline platinum in all the electrolytes studied, for both the Single Current Pulse Method and the A.C. Impedance Method. This time dependence is likely to be related to the influence of the particular metal on the electrolyte, rather than due to the accumulation of surface active impurities.

The use of complex plane impedance spectra was found to be invaluable in determining the appropriate double layer analogue circuits. Neglecting the series solution resistance, the A.C. Impedance data were consistent with the interface behaving as a resistor and capacitor in parallel, or as a capacitor with distortion due to surface roughness effects. Only the polycrystalline platinum/aqueous 0.001M  $\text{NaNO}_3$  interface was found to behave in a complex manner that was not resolved in the present research. It is believed by the writer that the complex behaviour of this system is compounded by surface roughness effects, which should be more pronounced in dilute electrolyte solutions, as discussed by de Levie.<sup>5</sup>

All capacitance data presented here, and also in Chapter 7, were given in terms of the geometric surface area without correction using

apparent roughness factors. A number of researchers<sup>1,5,19,32</sup> have discussed the problems involved in using the concept of a roughness factor for polycrystalline metal electrodes. An attempt to correlate roughness factors determined from capacitance and hydrogen adsorption measurements for polycrystalline platinum electrodes gave only poor to moderate success.

The capacitance minimum at +0.80 volts for the polycrystalline platinum/HCl system was determined by the writer to be considerably lower than the  $19 \mu\text{F}/\text{cm}^2$  forwarded by Robertson<sup>13</sup> for both the platinum disc and platinum Cottrell Cell electrodes. This would tend to suggest that the surfaces prepared by Robertson all had a consistent roughness factor greater than unity, since the platinum Cottrell Cell electrode had its surface prepared by mechanical polishing.

The platinum disc electrode consistently gave results that were consistent with it having a lower apparent roughness than the other platinum electrodes. The disc electrode underwent a flame cleaning process, whereas the other platinum electrodes were mechanically polished and then etched. The results may indicate that the latter process was not as efficient in decreasing surface roughness as the flame cleaning technique. Another possible interpretation, discussed in Chapter 3, is that the flame cleaning procedure results in residual carbonaceous material being left on the electrode surface, which effectively blocks portions of the electrode surface, and thus gives it an apparently low surface roughness. The writer cannot definitely say that the platinum disc electrode was perfectly clean of carbonaceous material; however, the results obtained using the platinum disc elec-

trode and the Teflon-encased platinum electrode were qualitatively very similar in all but the dilute  $\text{NaNO}_3$  solution. This would suggest that the amount of carbonaceous material was not significant enough to greatly influence double layer capacitance measurements.

Of most fundamental importance was the finding by the writer that there was only poor to moderate agreement in the results determined by the Single Current Pulse Method and the A.C. Impedance Method. The measured capacitance was often found to be higher using the A.C. Impedance Method than for the Single Current Pulse Method. In the case where the interface was best described by a capacitor and resistor in parallel, the parallel resistance determined by the A.C. Impedance Method was always significantly greater than that determined by the Single Current Pulse Method. Both methods have been used to measure the differential capacitance of solid metal/electrolyte solution interfaces. The A.C. Impedance Method has been most commonly used, while the Single Current Pulse Method has also been significantly used.<sup>2,14,33-38</sup>

It was shown in Chapter 4 that both methods were able to accurately measure analogue circuits composed of resistors and capacitors. There also appeared to be no inconsistencies in each method when used to measure properties of the solid metal/electrolyte solution interface. Then, why do the results obtained by each method fail to yield the same capacitance and resistance values? And, does the parallel resistance determined using the Single Current Pulse Method actually correspond to the true parallel resistance?

## 5.53

The above two questions have been posed by the outcome of this research, but satisfactory answers will come only with further research. An area of interest may be a detailed study of how surface roughness affects the parallel resistance determined by the Single Current Pulse Method. De Vries<sup>5</sup> and Lorenz<sup>39</sup> both state that surface roughness should affect the results obtained with pulse techniques. In posing the second question above, the writer desires to know whether the apparently low parallel resistance values are real or an artefact induced by surface roughness.



## REFERENCES

- 1 HAMELIN, A., VITANOV, T., SEVASTYANOV, E. and POPOV, A., *J. Electroanal. Chem.*, 145(1983) 225.
- 2 RINEY, J. S., SCHMID, G. M. and HACKERMAN, N., *Rev. Sci. Instr.*, 32(1961) 588.
- 3 BREITER, M. W., *J. Electroanal. Chem.*, 7(1964) 38.
- 4 BORISOVA, T. and ERSHLER, B., *Zh. Fiz. Khim.*, 24(1950) 337.
- 5 DE LEVIE, R., *Electrochim. Acta*, 10(1965) 113.
- 6 DE LEVIE, R., *Adv. Electrochem. Electrochem. Eng.*, 6(1967) 329.
- 7 ARMSTRONG, R. D. and BURNHAM, R. A., *J. Electroanal. Chem.*, 72(1976) 257.
- 8 ARMSTRONG, R. D., DICKINSON, T. and WILLIS, P. M., *J. Electroanal. Chem.*, 53(1974) 389.
- 9 BEWICK, A. and THOMAS, B., *J. Electroanal. Chem.*, 65(1975) 911.
- 10 ADZIC, R. R., HANSON, M. E. and YEAGER, E. B., *J. Electrochem. Soc.*, 131(1984) 1730.
- 11 *The Super-Q System*, Catalog No. LTPB062BA and Catalog MC/1. Millipore Corporation, Bedford, Mass.
- 12 ROSEN, M. and SCHULDINER, S., *Electrochim. Acta*, 18(1973) 687.
- 13 ROBERTSON, W. D., *J. Electrochem. Soc.*, 100(1953) 194.
- 14 CURRIE, N., Honours Thesis, University of Adelaide (1978).
- 15 FAWCETT, W. R. and LOUTFY, R. O., *J. Electroanal. Chem.*, 39(1972) 185.
- 16 ARCHER, W. I. and ARMSTRONG, R. D., *Electrochemistry*, 7(1980) 169.
- 17 HAMELIN, A., *J. Electroanal. Chem.*, 142(1982) 299.
- 18 VAN HOVE, M. A., KOESTNER, R. J., STAIR, P. C., BIBERIAN, J. P., KESMODEL, L. L., BARTOS, I. and SOMORJAI, G. A., *Surf. Sci.*, 103(1981) 189, 218.
- 19 VALETTE, G. and HAMELIN, A., *J. Electroanal. Chem.*, 45(1973) 301.
- 20 SEVASTYANOV, E. S., TER-AKOPYAN, M. N., LEIKIS, D. I., KVARATSKHELIYA, R. K. and MACHAVARIANI, T. Sh., *Soviet Electrochem.*, 19(1983) 1125.
- 21 MILKOWSKA, M. and MINC, S., *Electrochim. Acta*, 29(1984) 257.
- 22 GRAHAME, D. C. and SODERBERG, B. A., *J. Chem. Phys.*, 22(1954) 449.

- 23 DAMASKIN, B. B., SEVEROVA, T. A. and IVANOVA, R. V., *Elektrokhimiya*, 12(1976) 646.
- 24 VITANOV, T. and POPOV, A., *Elektrokhimiya*, 10(1974) 1372.
- 25 VITANOV, T. and POPOV, A., *Trans. S.A.E.S.T.*, 10(1975) 5.
- 26 VITANOV, T., POPOV, A. and SEVASTYANOV, E., *Elektrokhimiya*, 12(1976) 582.
- 27 SCHLEPAKOV, A. and SEVASTYANOV, E., *Elektrokhimiya*, 14(1978) 287.
- 28 ZELINSKII, A. and BEK, R., *Elektrokhimiya*, 14(1978) 1825.
- 29 PAYNE, R., *J. Electrochem. Soc.*, 113(1966) 999.
- 30 PANKINA, G. V., LEIKIS, D. I. and SEVASTYANOV, E. S., *Soviet Electrochem.*, 16(1980) 183.
- 31 McNICOL, B. D., MILES, R. and SHORT, R. T., *Electrochim. Acta*, 28(1983) 1285.
- 32 HAMELIN, A., *Soviet Electrochem.*, 18(1981) 1259.
- 33 DYER, C. K. and LEACH, J. S. L., *Electrochim. Acta*, 20(1975) 151.
- 34 KATOH, K. and KOSEKI, M., *J. Electrochem. Soc.*, 131(1984) 303.
- 35 KATOH, K. and SCHMID, G. M., *Bull. Chem. Soc. Japan*, 44(1971) 2007.
- 36 SCHMID, G. M. and HACKERMAN, N., *J. Electrochem. Soc.*, 110(1963) 440.
- 37 SCHMID, G. M. and HACKERMAN, N., *J. Electrochem. Soc.*, 109(1962) 243.
- 38 LAITINEN, H. A. and CHAO, M. S., *J. Electrochem. Soc.*, 108(1961) 726.
- 39 LORENZ, W., *Z. Phys. Chem.*, 205(1956) 311.

## CHAPTER 6

### DETERMINATION OF ELECTROLYTE ACTIVITY IN H<sub>2</sub>O + NMF SOLVENT MIXTURES FROM EMF MEASUREMENTS AT 25°C

INTRODUCTION	6.1
DETERMINATION OF ELECTROLYTE CONCENTRATION REQUIRED TO MAINTAIN CONSTANT ELECTROLYTE ACTIVITY IN H <sub>2</sub> O + ORGANIC SOLVENT MIXTURES	6.3
DETERMINATION OF THE FREE ENERGY OF TRANSFER OF ONE MOLE OF SUBSTANCE FROM WATER TO MIXED H <sub>2</sub> O + ORGANIC SOLVENTS	6.5
INVESTIGATION OF THE H <sub>2</sub> O + NMF + NaCl SYSTEM AT 25°C	6.7
EXPERIMENTAL	6.7
RESULTS AND DISCUSSION	6.8
INVESTIGATION OF THE H <sub>2</sub> O + NMF + NaNO <sub>3</sub> SYSTEM AT 25°C	6.10
EXPERIMENTAL	6.10
RESULTS AND DISCUSSION	6.12
RESPONSE OF THE NITRATE ION SELECTIVE ELECTRODE TO NaNO <sub>3</sub> IN PURE WATER AT 25°C	6.15
INTRODUCTION	6.15
EXPERIMENTAL	6.15
RESULTS AND DISCUSSION	6.16
CONCLUSION	6.18
REFERENCES	6.20

## INTRODUCTION

The knowledge of the response of electrolyte activity to solvent composition is important in electrochemical studies of electrolyte solutions. A strictly thermodynamic study of adsorption from mixed solvents at constant temperature and pressure, for example, requires the electrolyte activity for such a study to be kept constant while the solvent composition is changed.<sup>1</sup>

Various authors<sup>1-5</sup> have used electromotive force (emf) measurements from appropriate galvanic cells to study the response of electrolyte activity to changes in solvent composition. These authors used the method of Mohilner and Nakadomari<sup>1</sup> to determine the electrolyte concentration required to maintain constant electrolyte activity in various H<sub>2</sub>O+organic solvent mixtures. The method assumes that the emf of the galvanic cell in the presence of an organic phase will be the same as that in pure water when the electrolyte activities of the two solutions are equal. The H<sub>2</sub>O+NMF+NaNO<sub>3</sub> system has been studied by the author using this technique. This system was compared with the H<sub>2</sub>O+NMF+NaCl system, which has been previously studied.<sup>5</sup>

The concentration of NaNO<sub>3</sub> required to maintain the same electrolyte activity as 0.100M NaNO<sub>3</sub> in pure water was found to decrease with increasing mole fraction of NMF, to a value of  $5 \times 10^{-4}$ M NaNO<sub>3</sub> in pure NMF.

The standard free energy of transfer of one mole of NaNO<sub>3</sub> from pure water to mixed H<sub>2</sub>O+NMF solvents was also determined by the author from emf measurements. The standard free energies of trans-

## 6.2

fer were found to be 7.3, 10.4, 12.3 and 13.8  $\text{kJmole}^{-1}$  for solvents of 0.250, 0.500, 0.750 and 1.000 NMF mole fraction, respectively.

The concentration of NaCl required to maintain the same electrolyte activity as 0.100M NaCl in pure water was found to decrease to  $6.3 \times 10^{-3}$  M NaCl in pure NMF. This is in good agreement with the results of Kozminska, Borkowska and Behr.<sup>5</sup>

The author also records the development of a novel nitrate ion selective electrode, and its response in  $\text{H}_2\text{O} + \text{NMF} + \text{NaNO}_3$  solutions. The novel nitrate ion selective electrode presented here uses a solid state electrode activated by nitron nitrate in a similar manner to the Selectrode developed by Ruzicka, Lamm and Tjell.<sup>6</sup> It differs from the conventional liquid ion exchanger based nitrate ion selective electrode<sup>7,8</sup> in that it possesses no liquid ion exchanger membrane.

DETERMINATION OF ELECTROLYTE CONCENTRATION REQUIRED TO MAINTAIN  
CONSTANT ELECTROLYTE ACTIVITY IN  $H_2O$  + ORGANIC SOLVENT MIXTURES

Mohilner and Nakadomari<sup>1</sup> devised a method to determine electrolyte concentration required to maintain constant electrolyte activity in a series of  $H_2O$  + organic solvent mixtures. They determined the effect of organic compound on the electrolyte activity from emf measurements of a reversible galvanic cell without liquid junctions in the presence and absence of the organic compound. The requirement for such a cell was that one of the electrodes was reversible to the cation, while the other was reversible to the anion of the electrolyte. They reasoned that, if the emf of such a cell in the presence of the organic compound was the same as the emf of the cell with a certain concentration of the electrolyte with no organic compound, then it would follow that the electrolyte activities in the two solutions would be equal.

The method firstly selects the desired activity to be equal to that of a particular electrolyte concentration in pure water. Then, for a series of solvent mixtures, emf's were measured for a range of electrolyte concentrations such that the emf's of the cell were close to and bracketed the emf of the cell in the absence of organic compound. For each solvent composition, the measured cell emf's were plotted against the electrolyte concentration, and the resulting curve interpolated to the emf of the cell without any organic compound. The corresponding interpolated electrolyte concentration is the concentration required for a particular solvent to maintain the electrolyte activity constant at the chosen value.

#### 6.4

This method was employed by the author in determining the concentration of electrolyte in  $\text{H}_2\text{O} + \text{NMF}$  solvent mixtures necessary to maintain the same activity as 0.100M electrolyte in pure water.

DETERMINATION OF THE FREE ENERGY OF TRANSFER OF ONE MOLE OF SUBSTANCE FROM WATER TO MIXED  $H_2O$  + ORGANIC SOLVENTS

Conventionally, the activity coefficient  ${}_s\gamma_i$  is set at 1.000 at infinite electrolyte dilution in a particular solvent. This activity coefficient essentially characterises the interionic and ion-molecule forces in that solvent, and other effects dependent on the concentration of solute in that solvent. This may be termed the concentration effect or salt effect, and is usually estimated from the Debye-Huckel equation.<sup>9</sup> The salt effect characterises the departure from ideal behaviour brought about largely by the electrostatic interactions among the ions.

The activity coefficient of species  $i$ ,  $\gamma_i$ , in different solvents referred to the standard state in water, will approach a value different from unity in solvents other than water as the concentration of solute is decreased. The limit is a measure of the medium effect  ${}_m\gamma_i$ .<sup>9</sup> The activity coefficient of species  $i$  is given by the product

$$\gamma_i = ({}_s\gamma_i) \times ({}_m\gamma_i)$$

The medium effect is a measure of the free energy change on transfer of one mole of species  $i$  from the standard state in water to the standard state in a different solvent,  $s$ .

The standard free energy of transfer of one mole of species  $i$ ,  $\Delta G_{\pm}^0$ , was calculated using the following equations

$$\begin{aligned} \Delta G_{\pm}^0 &= G_{\pm}^0(s) - G_{\pm}^0(H_2O) \\ &= RT \ln({}_m\gamma_{\pm}) \\ &= 2RT \ln({}_m\gamma_{\pm}) \quad \text{for 1:1 electrolyte} \\ &= -F\Delta E^0 = -F(E^0(H_2O) - E^0(s)) \end{aligned}$$



## 6.6

The electrostatic part of the free energy of transfer can be estimated from the Born equation<sup>10</sup> if the ions are treated as spheres of finite radius immersed in a continuum of uniform electrolyte of uniform dielectric constant. The Born treatment makes no allowance for specific chemical interactions between the ions and the solvent, which do, however, make an important contribution to the nonelectrostatic part of the free energy change. As such, there is often poor agreement between the predictions of the Born equation and the experimentally determined activity coefficients. This poor agreement is discussed for hydrochloric acid in mixtures of water and low dielectric solvents such as methanol, ethanol and dioxan.<sup>9</sup> A general prediction of the Born equation is that the medium effect activity coefficient will increase with decreasing solvent dielectric constant.

Even though the Born equation is inadequate to explain the medium effect, it is still used as a reference point, simply because there has not yet been developed a more comprehensive theoretical treatment to explain the medium effect.

INVESTIGATION OF THE  $\text{H}_2\text{O} + \text{NMF} + \text{NaCl}$  SYSTEM AT  $25^\circ\text{C}$ 

## EXPERIMENTAL

*Reagents*

Analytical grade B.D.H. NaCl, milli-Q water and distilled purum Fluka NMF were used, as previously described.

*Sodium Ion Glass Electrode*

A commercially available Radiometer G502Na Sodium Selectrode was employed in measurements, and was conditioned by storage in 0.1M NaCl in pure water.

*Ruzicka Chloride Selectrode*

The Ruzicka solid state Selectrode is an ion-selective basic electrode essentially consisting of a Teflon-hydrophobised graphite rod. The Selectrode can be made selective to a particular ionic species by applying a superficial layer of an electroactive compound sensitive to the particular ion. The selectrode surface can be renewed by simply trimming off the activated section.<sup>6</sup>

A Ruzicka solid state Chloride Selectrode was prepared and used by the author by activating an F3012 Selectrode with S42315 Chloride Selectrode Powder.

*Emf Measurements*

The emf was measured for the following cell

Chloride Selectrode/ $\text{XNMF} + (1-\text{X})\text{H}_2\text{O} + \text{YNaCl}/\text{Na}^+$  glass electrode

where  $X$  is the mole fraction of NMF and  $Y$  is the molar concentration of sodium chloride.

All emf measurements were made at 25°C in stirred solutions using an Orion 701A digital ionalyzer.

The emf measurements were carried out on individually prepared solutions into which the electrodes were dipped. Cell response times were around 5 minutes and 10 minutes in pure water and pure NMF solutions, respectively; before emf values were  $\leq \pm 1$  mV from the final value.

#### RESULTS AND DISCUSSION

Figure 1 records the results of the emf of the cell measured as a function of concentration of NaCl in pure water and pure NMF at 25°C. Applying the method of Mohilner and Nakadomari,<sup>1</sup> it is evident that a concentration of  $6.3 \times 10^{-3}$  M NaCl in pure NMF has the same electrolyte activity as 0.100M NaCl in pure water.

The  $H_2O + NMF + NaCl$  system was studied by Kozminska, Borkowska and Behr,<sup>5</sup> who reported that the concentration of NaCl required to maintain the same electrolyte activity decreased with increasing NMF mole fraction, from 0.100M in pure water to  $7 \times 10^{-3}$  M in pure NMF. The results presented here are in good agreement with those of Kozminska et al.

The emf of the cell is related to the activity of ionic species, in accordance with the Nernst equation

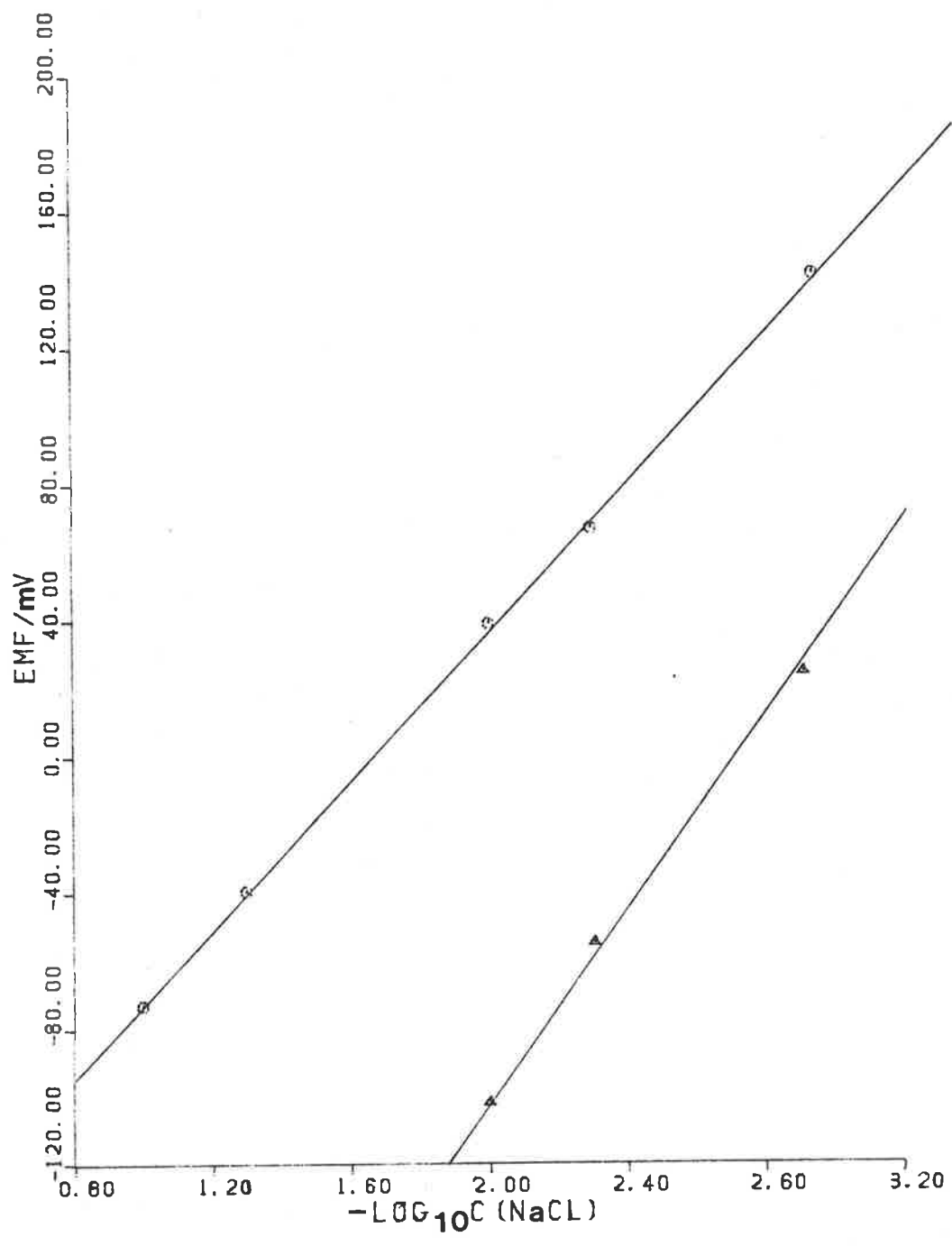


Figure 1. Dependence of EMF on  $\text{Log } (C_{\text{NaCl}})$  in pure water (O) and pure NMF (Δ).

6.9

$$\begin{aligned} E_{\text{cell}} &= E' + \frac{2.303RT}{F} \log (a_{\text{Na}^+} \cdot a_{\text{Cl}^-}) \\ &= E' + \frac{4.606RT}{F} \log a_{\pm} \\ &= E' + \frac{4.606RT}{F} (\log c_{\pm} + \log \gamma_{\pm}) \end{aligned}$$

where  $\gamma_{\pm}$  is the activity coefficient of the electrolyte. Using the activity coefficient data previously tabled,<sup>11</sup> the theoretical Nernstian response for the cell is plotted as a dashed line in Figure 1. It is evident that the cell response is quite close to the expected Nernstian behaviour, giving confidence in the use of the  $\text{Na}^+$  glass electrode.

INVESTIGATION OF THE  $\text{H}_2\text{O} + \text{NMF} + \text{NaNO}_3$  SYSTEM AT  $25^\circ\text{C}$ 

## EXPERIMENTAL

*Reagents*

Previously described Analytical grade B.D.H.  $\text{NaNO}_3$ , milli-Q water and distilled purum Fluka NMF were used.

Nitron nitrate was prepared by a method similar to that used by Lal, Chattopadhyaya and Dey,<sup>12</sup> and Cope and Barab.<sup>13</sup> Reagent grade B.D.H. nitron was dissolved in dilute acetic acid, and nitron nitrate precipitated on the addition of Analytical grade B.D.H. sodium nitrate. The filtered dry precipitate was white, and went faintly fawn during storage. The infra red spectrum of the precipitate showed a characteristic absorption due to nitrate at  $1350\text{ cm}^{-1}$ . The precipitate was white, and not black, as claimed by Lal et al.

*Sodium Ion Glass Electrode*

A commercially available Radiometer G502Na Sodium Selectrode was employed in measurements, and was conditioned by storage in  $0.1\text{M NaNO}_3$  in pure water.

*Nitrate Ion Selective Electrode*

The electrode used consisted of a 75%/25% w/w Teflon-graphite rod of 0.95 cm diameter that was trimmed and encased in a teflon jacket. The teflon-graphite rod, available from John Crane Mauri Pty. Ltd., had been successfully used to fabricate an electrode of the Ruzicka Selectrode type by Mellor, Haskard and Mulcahy.<sup>14</sup> Electrical contact with the teflon-graphite was made via a brass connecting rod screwed into the teflon-graphite rod.

## 6.11

The exposed teflon-graphite surface was made active to nitrate ion by grinding dry nitron nitrate into it using a glass rod. Any loose nitron nitrate was rinsed off in water.

### *Emf Measurements*

The emf was measured for the following cell

$\text{NO}_3^-$  selective electrode /  $X\text{NMF} + (1-X)\text{H}_2\text{O} + Y\text{NaNO}_3 / \text{Na}^+$  glass electrode

where X is the mole fraction of NMF and Y is the molar concentration of sodium nitrate.

All emf measurements were made at 25°C in stirred solutions using an Orion 701A digital Ionalyzer.

The electrolyte concentration was varied by successive additions of known volumes of the electrolyte dissolved in the solvent of interest.

Stable emf values were obtained after 1 to 20 minutes, depending upon the concentration of sodium nitrate and the NMF mole fraction. The system was progressively more stable with increasing NMF mole fraction. All emf values were normalised to the emf of  $10^{-3}\text{M NaNO}_3$  in pure NMF. This normalisation was achieved by measuring the emf difference between  $10^{-3}\text{M NaNO}_3$  in pure NMF and  $10^{-3}\text{M NaNO}_3$  in each  $\text{H}_2\text{O} + \text{NMF}$  solvent mixture. These emf differences were then used to adjust the position of the emf- $\log C_{\text{NaNO}_3}$  curves relative to the emf- $\log C_{\text{NaNO}_3}$  curve obtained in pure NMF.

## RESULTS AND DISCUSSION

Figure 2 records the results of the emf of the cell measured as a function of concentration of  $\text{NaNO}_3$  for NMF mole fractions of 0.000, 0.250, 0.500, 0.750 and 1.000 at 25°C.

Other researchers have noted that the higher the solvent mole fraction of organic compound, the higher the ionic activity for a given electrolyte concentration in the solution.<sup>1-5</sup> This effect for the  $\text{H}_2\text{O} + \text{NMF} + \text{NaNO}_3$  system is evident in Table 1, where the electrolyte concentration required to maintain the same activity as 0.100M  $\text{NaNO}_3$  in pure water is given as a function of mole fraction of NMF. To maintain the same electrolyte activity, the electrolyte concentration must be reduced with increasing NMF concentration; from 0.100M  $\text{NaNO}_3$  in pure water to  $5.2 \times 10^{-4}$  M  $\text{NaNO}_3$  in pure NMF. The largest change in the electrolyte activity is evident at low NMF mole fractions.

The emf of the cell is related to the activity of the ionic species in accordance with the Nernst equation

$$\begin{aligned} E_{\text{cell}} &= E' + \frac{2.303RT}{F} \log (a_{\text{Na}^+} \cdot a_{\text{NO}_3^-}) \\ &= E' + \frac{4.606RT}{F} \log a_{\pm} \end{aligned}$$

The theoretical Nernstian slope should be 118 mv/decade activity at 25°C when emf is plotted against  $\log a_{\pm}$ . From Figure 3 it is evident that the response of the cell is less than the theoretical slope. The activity of  $\text{NaNO}_3$  was calculated as the product of the known



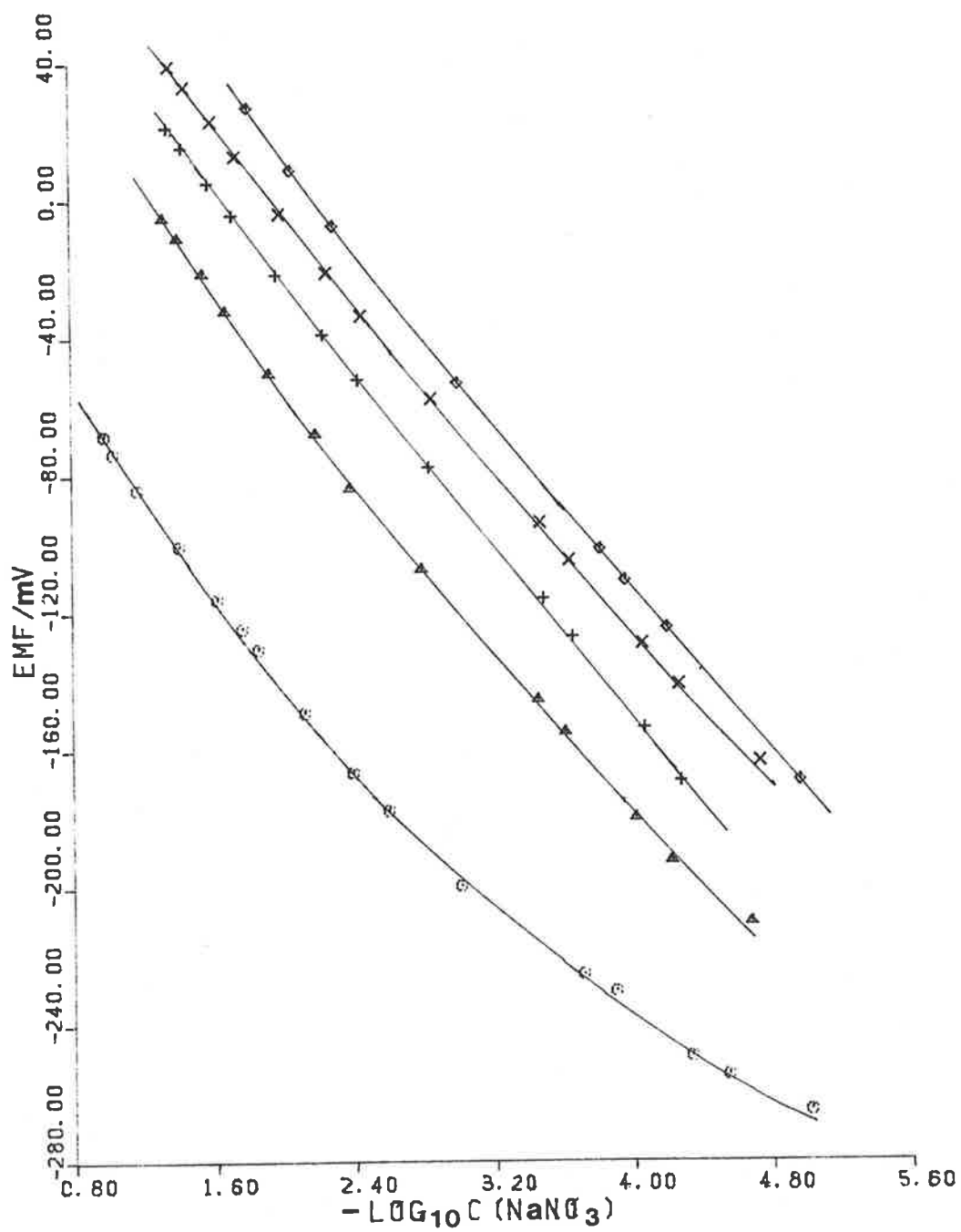


Figure 2. Dependence of EMF on  $\text{Log}(C_{\text{NaNO}_3})$  for various NMF mole fractions: 0.000 (O); 0.250 ( $\Delta$ ); 0.500 (+); 0.750 (x); 1.000 ( $\diamond$ ).

**Table 1**

Concentrations of  $\text{NaNO}_3$  required  
to maintain the same electrolyte activity as 0.100M  $\text{NaNO}_3$   
in pure water at 25°C

$X_{\text{NMF}}$	$\log_{10} C_{\text{NaNO}_3}$	$C_{\text{NaNO}_3} / \text{M}$
0.000	-1.000	$1.00 \times 10^{-1}$
0.250	-2.221	$6.01 \times 10^{-3}$
0.500	-2.713	$1.94 \times 10^{-3}$
0.750	-3.106	$7.83 \times 10^{-4}$
1.000	-3.287	$5.16 \times 10^{-4}$

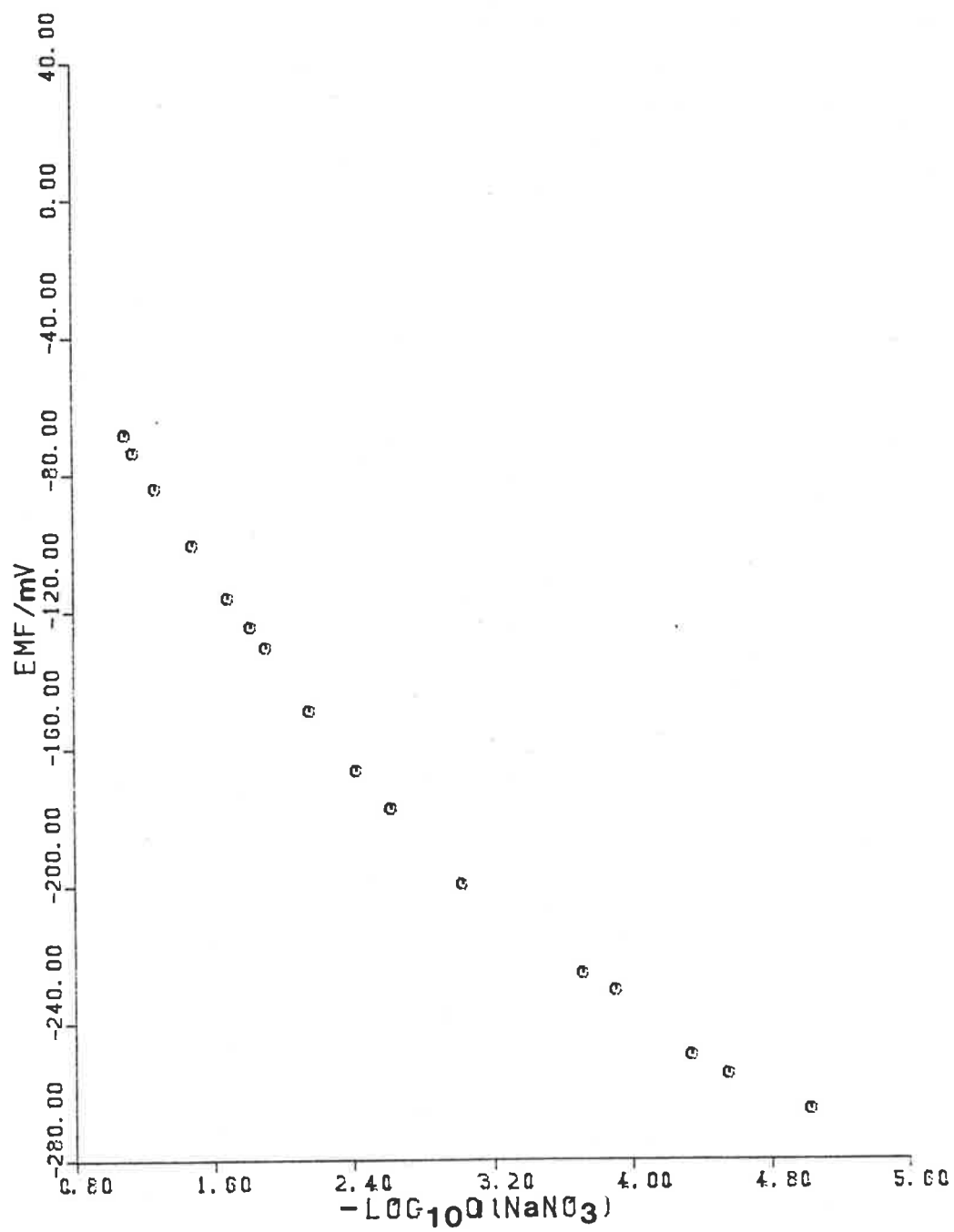


Figure 3. Dependence of EMF on  $\text{Log}(a_{\text{NaNO}_3})$  in pure water.

electrolyte concentration and the appropriate activity coefficient determined at the solution freezing point by Scatchard, Prentiss and Jones.<sup>15</sup> The freezing point activity coefficient data was used because no appropriate low concentration data at 25°C has yet been determined for NaNO<sub>3</sub>, and because the activity coefficient determined by Scatchard et al<sup>15</sup> for 0.1M NaNO<sub>3</sub> is almost identical to that determined for the same concentration at 25°C.<sup>11</sup>

For the cell

NO<sub>3</sub><sup>-</sup> selective electrode/XNMF + (1-X)H<sub>2</sub>O + YNaNO<sub>3</sub>/Na<sup>+</sup> glass electrode

we can define

$$\Delta E = E_w - E_s$$

where  $E_w$  and  $E_s$  are the measured cell emf's at a concentration Y of sodium nitrate in pure water and mixed H<sub>2</sub>O+NMF solvent, respectively.

The free energy of transfer of 1 mole of sodium nitrate from water to the mixed solvent,  $\Delta G_{\dagger}$ , can be calculated using the equation

$$\Delta G_{\dagger} = -F\Delta E$$

Values of  $\Delta E$  and  $\Delta G_{\dagger}$  are recorded in Table 2 as a function of sodium nitrate concentration and solvent mole fraction of NMF.

Extrapolating values of  $\Delta G_{\dagger}$  to infinite dilution as a function of  $\sqrt{c}$  yields standard free energies of transfer of  $7.3 \pm 0.1$ ,  $10.4 \pm 0.2$ ,  $12.3 \pm 0.1$  and  $13.8 \pm 0.2$  kJmole<sup>-1</sup> for solvent mole fractions of NMF of 0.250, 0.500, 0.750 and 1.000, respectively.

Table 2a

Dependence of  $\Delta E$  in mV on  $\sqrt{C}$  for  $\text{NaNO}_3$   
in mixed  $\text{H}_2\text{O} + \text{NMF}$  solvents

$X_{\text{NMF}}$	0.250	0.500	0.750	1.000
$\sqrt{C}$				
.0200	-76	-107	-127	-143
.0316	-80	-113	-132	-148
.0501	-81	-115	-134	-150
.1000	-86	-119	-137	-155
.1259	-87	-119	-138	-156

Table 2b

Dependence of  $\Delta G_{\ddagger}$  in  $\text{kJmol}^{-1}$  on  $\sqrt{C}$  for  $\text{NaNO}_3$   
in mixed  $\text{H}_2\text{O} + \text{NMF}$  solvents

$X_{\text{NMF}}$	0.250	0.500	0.750	1.000
$\sqrt{C}$				
.0200	7.3	10.3	12.3	13.8
.0316	7.7	10.9	12.7	14.3
.0501	7.8	11.0	12.9	14.5
.1000	8.3	11.5	13.2	15.0
.1259	8.4	11.5	13.3	15.1

There is quite a large dependence of  $\Delta G_{\pm}$  on  $\sqrt{c}$ ; however, this dependence is consistent with the data of Kozminska et al<sup>5</sup> for the  $H_2O + NMF + NaCl$  system. Reworking of their data using the author's method for  $0.002M \leq \text{concentration of NaCl} \leq 0.05M$  in pure NMF yielded a standard free energy of transfer of one mole of NaCl of  $10.8 \pm 0.14 \text{ kJmole}^{-1}$ , and a slope of  $7 \text{ kJmole}^{-1} \text{ molarity}^{-\frac{1}{2}}$ . These values are lower, but of comparable magnitude to the standard free energy of transfer of one mole of  $NaNO_3$  from water to pure NMF of  $13.8 \pm 0.2 \text{ kJmole}^{-1}$ , and the dependence of  $\Delta G_{\pm}$  on  $\sqrt{c}$  of  $11 \text{ kJmole}^{-1} \text{ molarity}^{-\frac{1}{2}}$ .

The Born equation<sup>10</sup> predicts that for the  $H_2O + NMF$  system the medium effect activity coefficient should decrease with increasing NMF concentration as the solvent dielectric constant increases.<sup>16,17</sup> Since

$$\Delta G_{\pm}^0 = 2RT \ln(\gamma_{\pm})$$

it can be seen from the large positive values of  $\Delta G_{\pm}^0$  presented here that the converse is true, that the medium effect activity coefficient increases with increasing solvent mole fraction of NMF. The treatment by Born takes no account of specific chemical interactions between the ions and the solvent, which obviously make a very important contribution to the nonelectrostatic part of the free energy change for the  $H_2O + NMF + NaNO_3$  and  $H_2O + NMF + NaCl$  systems.

## RESPONSE OF THE NITRATE ION SELECTIVE ELECTRODE TO $\text{NaNO}_3$ IN PURE WATER AT 25°C

### INTRODUCTION

The main interest to the author in the development and use of the previously described nitrate ion selective electrode was in the determination of  $\text{NaNO}_3$  activity in mixed  $\text{H}_2\text{O} + \text{NMF}$  solvents. The ion selective electrode, however, can also be used as an analytical tool.

Preliminary investigations are presented by the author for the use of the nitrate ion selective electrode as an analytical sensor for nitrate ions in aqueous solutions.

### EXPERIMENTAL

#### *Reagents*

Analytical grade B.D.H. sodium nitrate and milli-Q quality water were used to prepare solutions, as previously described.

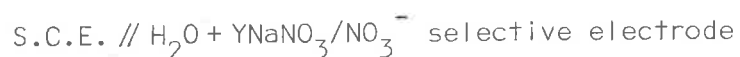
#### *Electrodes*

A commercially available saturated calomel electrode (S.C.E.) with a low leakage glass frit was used as the fixed potential reference electrode.

The nitrate ion selective electrode has been described previously.

*Emf Measurements*

The emf was measured for the following cell



where Y is the molar concentration of sodium nitrate.

All emf measurements were made at 25°C in stirred solutions using an Orion 701A digital Ionalyzer. A standard addition method was employed to change the electrolyte concentration.

The emf of the above cell is related to the activity of nitrate, in accordance with the Nernst equation

$$\begin{aligned} E &= E' - E_{\text{Cal}} + E_{\text{LJ}} - \frac{2.303RT}{F} \log a_{\text{NO}_3^-} \\ &\equiv E'' - \frac{2.303RT}{F} \log a_{\text{NO}_3^-} \end{aligned}$$

where  $E_{\text{Cal}}$  and  $E_{\text{LJ}}$  are the potential drops associated with the calomel reference electrode and liquid junction, respectively.

**RESULTS AND DISCUSSION**

The nitrate ion selective electrode without a liquid junction, coupled with a sodium glass selectrode, has proved useful in determining the activity of  $\text{NaNO}_3$  in  $\text{H}_2\text{O} + \text{NMF}$  solvent mixtures. The nitrate ion selective electrode also has an analytical application as a means of determining nitrate ion content of solutions.



The emf response of the nitrate ion selective electrode with respect to a fixed potential reference electrode is recorded as a function of concentration of  $\text{NaNO}_3$  in pure water at  $25^\circ\text{C}$  in Figures 4 and 5. The response of the cell on these two separate occasions yielded slopes of  $38.0 \pm 2.1$  mV/decade  $\text{NaNO}_3$  concentration, and  $25.4 \pm 0.6$  mV/decade  $\text{NaNO}_3$  concentration.

The nitrate ion selective electrode was responsive to nitrate ion, but not to the expected theoretical Nernstian response of 59 mV/decade activity at  $25^\circ\text{C}$ . The responses of the two experiments recorded in Figures 4 and 5 are significantly different. The response, however, for each experiment was internally reproducible. This can be seen in Figure 4, where the curve of emf versus  $\log c_{\text{NaNO}_3}$  derived upon steadily increasing the electrolyte concentration was retraced upon dilution.

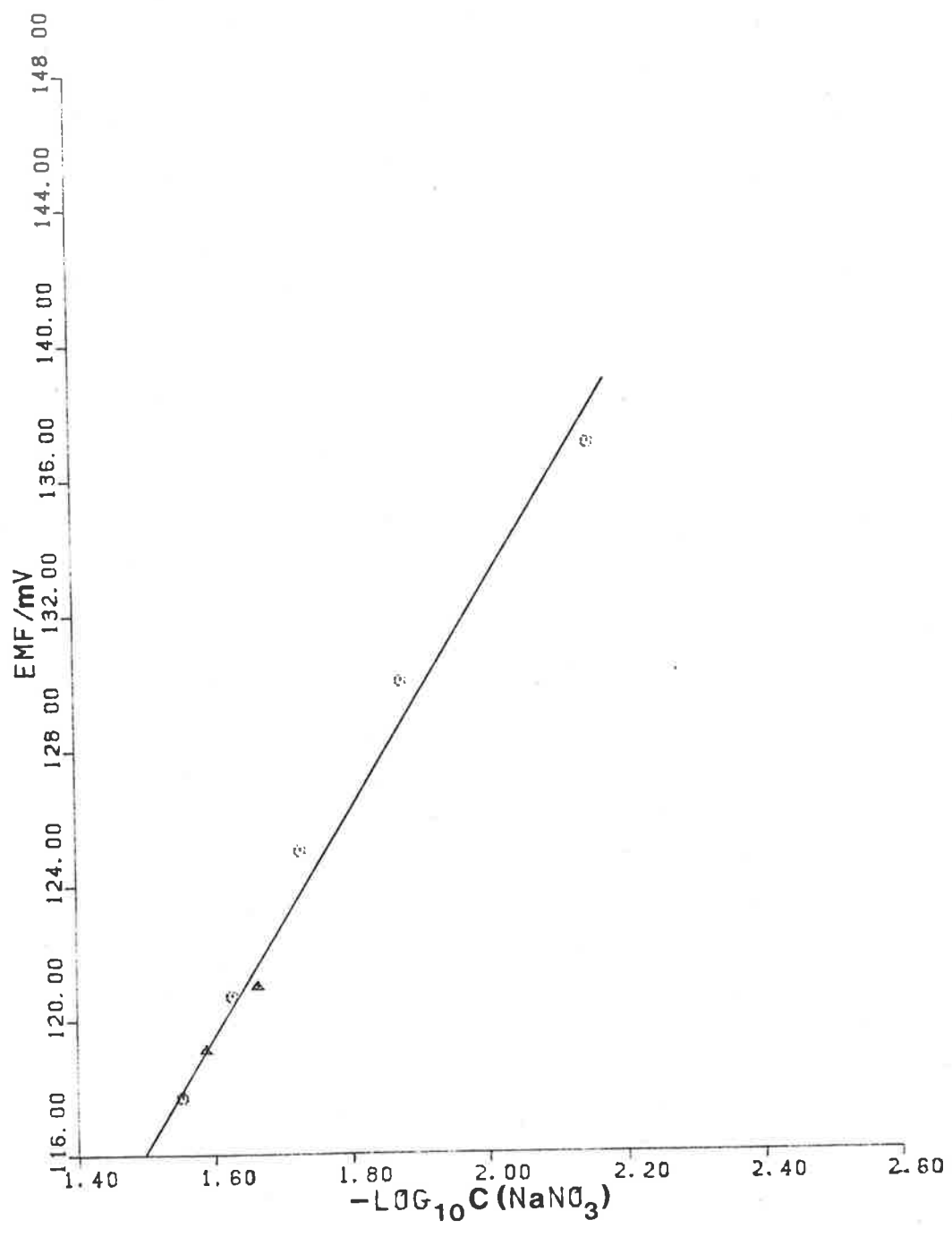


Figure 4. Dependence of EMF on  $\text{Log}(c_{\text{NaNO}_3})$  in pure water: increasing  $c_{\text{NaNO}_3}$  (O); decreasing  $c_{\text{NaNO}_3}$  (Δ).

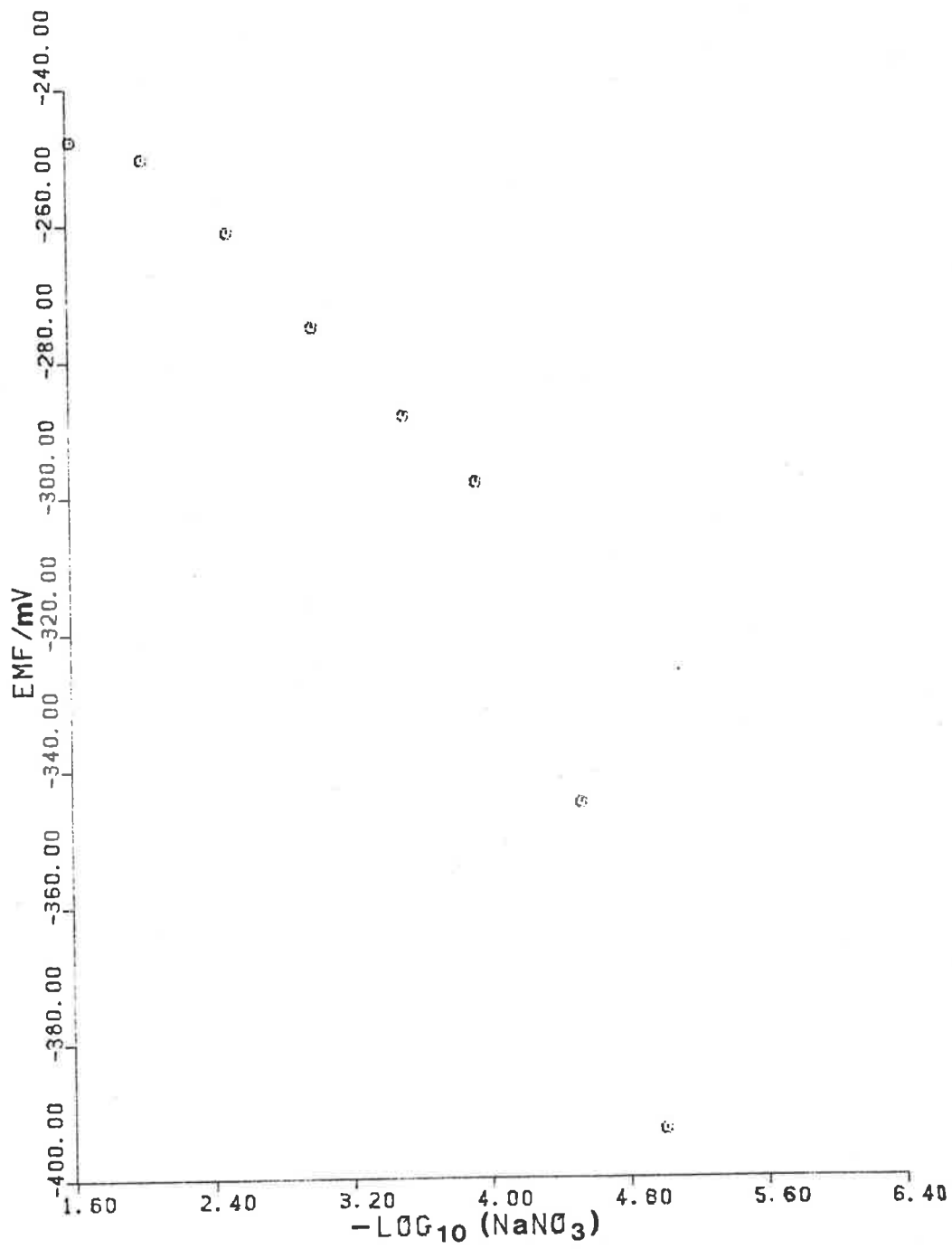


Figure 5. Dependence of EMF on  $\text{Log}(c_{\text{NaNO}_3})$  in pure water.

## CONCLUSION

The practice of using constant electrolyte concentration instead of constant electrolyte activity in adsorption studies would lead to serious errors for the  $\text{H}_2\text{O} + \text{NMF} + \text{NaNO}_3$  and  $\text{H}_2\text{O} + \text{NMF} + \text{NaCl}$  systems. For these systems,  $5.2 \times 10^{-4} \text{M NaNO}_3$  and  $6.3 \times 10^{-3} \text{M NaCl}$  have the same electrolyte activity in pure NMF as  $0.100 \text{M NaNO}_3$  and  $0.100 \text{M NaCl}$ , respectively, in pure water. The increase in the electrolyte activity with increasing NMF mole fraction corresponds to an increase in the solvent dielectric constant. This effect cannot be explained by any current theoretical treatment, such as that by Born,<sup>10</sup> and reflects the importance of the nonelectrostatic ion-solvent interactions.

The development of a novel nitrate ion selective electrode without liquid junctions was necessary before the activity of  $\text{NaNO}_3$  could be determined from emf measurements using the method of Mohilner and Nakadomari.<sup>1</sup> No other nitrate ion selective electrode without liquid junctions has been successfully developed. The delay in developing a successful nitrate ion selective electrode without liquid junctions is, in part, related to the high solubility of most nitrate salts. Nitron nitrate, on the other hand, has a moderately low solubility of 1 part in 60,000 in water,<sup>18</sup> making it suitable for use as an activating agent in conjunction with a simple Ruzicka type solid state electrode.

The emf response of the electrode to nitrate ion was found to be below the expected Nernstian response. This was also found to be the case by Lal et al,<sup>12</sup> who incorporated nitron nitrate into a membrane for a nitrate ion selective electrode.

The preliminary analytical investigations show that the response of the nitrate ion selective electrode presented here is sensitive to the preparation and ageing of the electrode. This sensitivity, and the sub-Nerstian electrode response may be indicative of some solubility problems associated with the use of nitron nitrate. Further investigations, beyond the present scope of this work, need to be carried out to see whether the electrode response can be improved. The incorporation of the nitron nitrate into the electrode Teflon-graphite matrix, the stabilizing of the nitron nitrate by an inorganic compound, or the use of nitron nitrate in a different crystalline form may be means whereby this could be achieved.

Many ion selective electrodes were developed for use in aqueous solutions, and are of dubious usability in the presence of organic compounds. Other electrodes, such as the Ruzicka Chloride Selectrode used here, show a lower stability in organic solvents compared with that in aqueous solutions. The nitrate ion selective electrode developed by the author is unusual in this regard, in that it behaves better in pure NMF and mixed  $H_2O + NMF$  solvents than in pure water.

## REFERENCES

- 1 MOHILNER, D. M. and NAKADOMARI, H., *J. Electroanal. Chem.*, 65(1975) 843.
- 2 NAKADOMARI, H., MOHILNER, D. M. and MOHILNER, P. R., *J. Phys. Chem.*, 80(1976) 1761.
- 3 MOHILNER, D. M., KAKIUCHI, T. and TARASZEWSKA, J., *Can. J. Chem.*, 59(1981) 1872.
- 4 BORKOWSKA, Z., *J. Electroanal. Chem.*, 63(1975) 379.
- 5 KOZMINSKA, D., BORKOWSKA, Z. and BEHR, B., *Can. J. Chem.*, 59(1981) 2043.
- 6 RUZICKA, J., LAMM, C. G. and TJELL, J. Chr., *Anal. Chim. Acta*, 62(1972) 15.
- 7 DURST, R. A. (Ed.), *Ion Selective Electrodes*, N.B.S. Special Publication 314, National Bureau of Standards, 1969.
- 8 MIDGLEY, D. and TORRANCE, K., *Potentiometric Water Analysis*. Wiley-Interscience Publication, 1978.
- 9 BATES, R., *Determination of pH. Theory and Practice*. John Wiley and Sons Inc., 1964.
- 10 BORN, M., *Z Physik.*, 1(1920) 45.
- 11 ROBINSON, R. A. and STOKES, R. H., *Electrolyte Solutions*, 2nd edition. Butterworths, London, 1959.
- 12 LAL, U. S., CHATTOPADHYAYA, M. C. and DEY, A. K., *Mikrochimica Acta II*, 1980, 417.
- 13 COPE, W. C. and BARAB, J., *J. Am. Chem. Soc.*, 39(1917) 504.
- 14 MELLOR, T. J., HASKARD, M. and MULCAHY, D. E., *Analytical Letters*, 15(1982) 1549.
- 15 SCATCHARD, G. PRENTISS, S. S. and JONES, P. T., *J. Am. Chem. Soc.*, 54(1932) 2690.
- 16 ROHDEWALD, P. and MOLDNER, M., *J. Phys. Chem.*, 77(1973) 373.
- 17 MALMBERG, C. G. and MARYOTT, A. A., *J. Res. Nat. Bur. Stand.*, 56(1956) 1.
- 18 BUSCH, M., *J. Chem. Soc.*, 88(1905) 282.

## CHAPTER 7

### DOUBLE LAYER CAPACITANCE OF THE SOLID ELECTRODE/ ELECTROLYTE SOLUTION INTERFACE IN NMF AT 25°C

INTRODUCTION	7.1
EXPERIMENTAL	7.3
RESULTS AND DISCUSSION	7.4
System I. Pt/NaNO <sub>3</sub> /NMF	7.4
System II. Ag/NaNO <sub>3</sub> /NMF	7.5
STANDARDISATION OF POTENTIAL SCALES	7.6
CONCLUSION	7.9
REFERENCES	7.15

## INTRODUCTION

Double layer capacitance studies have previously been carried out using mercury electrodes for a number of electrolytes dissolved in n-methylformamide (NMF).<sup>1-8</sup> The general shape of the capacitance-potential curves obtained was similar to the shape of those obtained in water, with a central capacitance hump that is generally accepted as being caused by solvent rearrangement at the electrode surface.<sup>4,7,9</sup>

The double layer capacitance in NMF was generally found to be smaller than in water, even though the bulk dielectric constant of NMF is greater than that of water. The smaller values of the double layer capacitance in NMF were suggested as indicating that the effective dielectric constant of NMF is much smaller in the vicinity of the electrode surface than in the bulk of the solution.<sup>1,2</sup>

A number of NMF adsorption studies have been made from mixed  $H_2O$ +NMF solutions from double layer capacitance studies at mercury electrodes.<sup>3,6</sup> The work of Payne<sup>6</sup> considered mixed solvents containing low concentrations of NMF, whereas Kozminska, Borkowska and Behr<sup>3</sup> investigated the adsorption of NMF over the entire solvent range.

The work of Kozminska, Borkowska and Behr<sup>3</sup> looked at how the use of constant electrolyte concentration, instead of constant electrolyte chemical potential, would affect the adsorption studies. These authors found that the chemical potential of NaCl increased markedly with increasing NMF mole fraction. To maintain the same electrolyte chemical potential in  $H_2O$ +NMF solutions, the concen-



## 7.2

tration of NaCl had to be decreased with increasing NMF mole fraction. In Chapter 6 of this thesis, the writer found a similar observation using  $\text{NaNO}_3$  as the electrolyte instead of NaCl, but to an even more marked degree. The writer found that the concentration of  $\text{NaNO}_3$  had to be as low as  $5.2 \times 10^{-4} \text{M}$  in pure NMF to maintain the same electrolyte chemical potential as 0.100M  $\text{NaNO}_3$  in pure water.

The writer determined the capacitance-potential curves for the polycrystalline platinum/ $\text{NaNO}_3$ /NMF system, and the polycrystalline silver/ $\text{NaNO}_3$ /NMF system. To the writer's knowledge, no other double layer capacitance measurements in NMF have been made using solid electrodes. The capacitance results have been discussed in terms of the usability of such data to investigate NMF adsorption from mixed  $\text{H}_2\text{O} + \text{NMF}$  solutions.

## EXPERIMENTAL

The electrodes, chemicals, cells, instruments and procedures have been discussed elsewhere in this thesis, and need not be discussed here.

The only deviation from previous procedures involved the electroreduction of the silver electrode in aqueous 0.1M  $\text{NaNO}_3$  for a period of hours before the electrode was rinsed in NMF solution, and then placed into the  $5 \times 10^{-4}$  M  $\text{NaNO}_3$  + NMF solution. The silver electrode was polarized in the aqueous solution because of the uncertainty as to the equivalent polarizing potential in the NMF solution.

All potentials quoted in this chapter, unless otherwise stated, are with respect to a low leakage, saturated calomel reference electrode placed in a luggin capillary containing the solution under study.

## RESULTS AND DISCUSSION

System I. Pt/NaNO<sub>3</sub>/NMF

Figure 1 shows cyclic voltammograms obtained for polycrystalline platinum in pure NMF with 0.100M NaNO<sub>3</sub> and  $5 \times 10^{-4}$  M NaNO<sub>3</sub>. The cyclic voltammograms were similar, with the cathodic reduction current peak occurring at about 0.2 volts more cathodic in the case of the dilute electrolyte. The reduction peak was found to be insensitive to the presence of deliberately added amounts of water. Over the scanned potential range of +0.80 volts to -0.80 volts the cyclic voltammograms were generally featureless, with increasing reduction current at potentials more cathodic than -0.4 volts.

From the representative complex plane impedance diagram in Figure 2, it can be seen that the polycrystalline platinum/NaNO<sub>3</sub> + NMF interface is best described by a resistor and capacitor in parallel. It can also be seen that the representative arcs drawn through the data points intersect the real axis at the origin. This shows that the iR-compensation used in these experiments was 100% efficient in removing the effect of the solution resistance, and that the parallel capacitance could be determined directly from the A.C. Impedance data.

Figures 3 and 4 show the cathodic and anodic parallel capacitance-potential curves determined for the polycrystalline platinum/0.100M NaNO<sub>3</sub>/NMF system. The curves show little frequency dependence over the range of 10 hz to 200 hz. The curves show few features other than an increase in the capacitance from

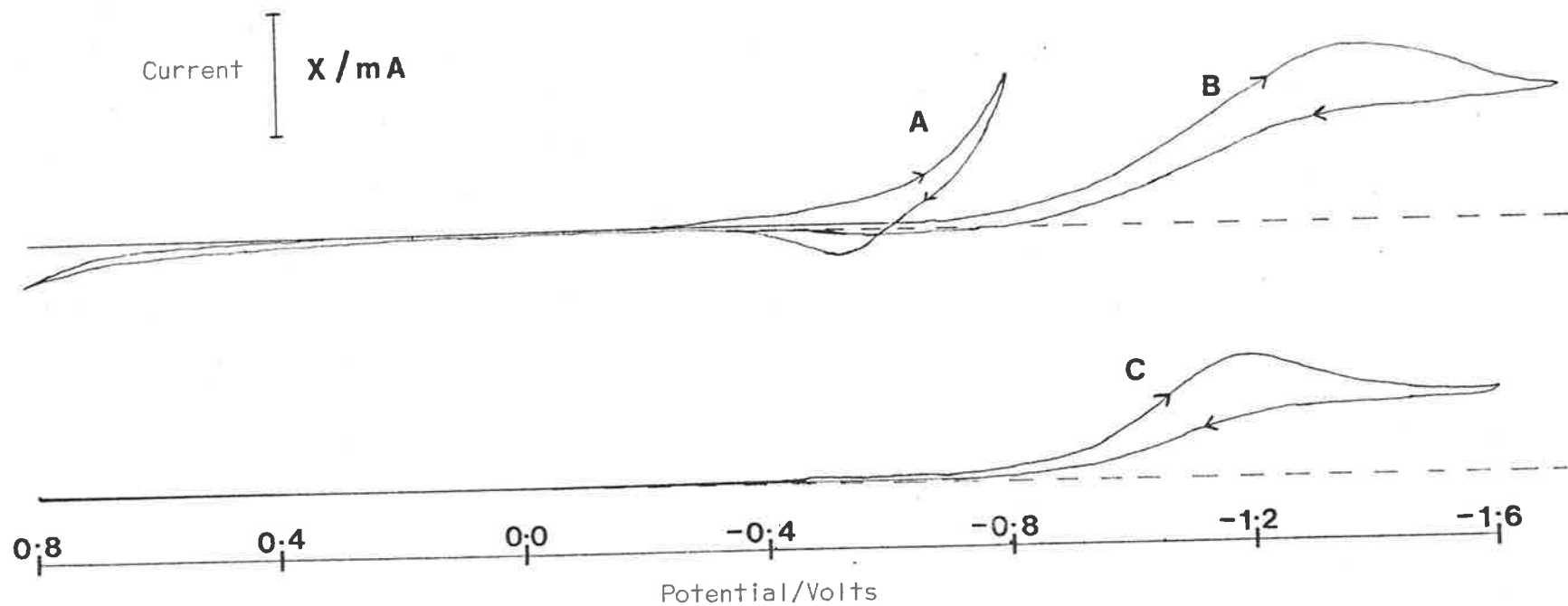


Figure 1. Cyclic voltammograms of polycrystalline platinum in NaNO<sub>3</sub> + NMF solutions.

A.  $5 \times 10^{-4}$  M NaNO<sub>3</sub>; X = 0.05; 20 mV/s scan rate.

B.  $5 \times 10^{-4}$  M NaNO<sub>3</sub>; X = 0.5; 20 mV/s scan rate.

C. 0.100M NaNO<sub>3</sub>; X = 0.5; 20 mV/s scan rate.

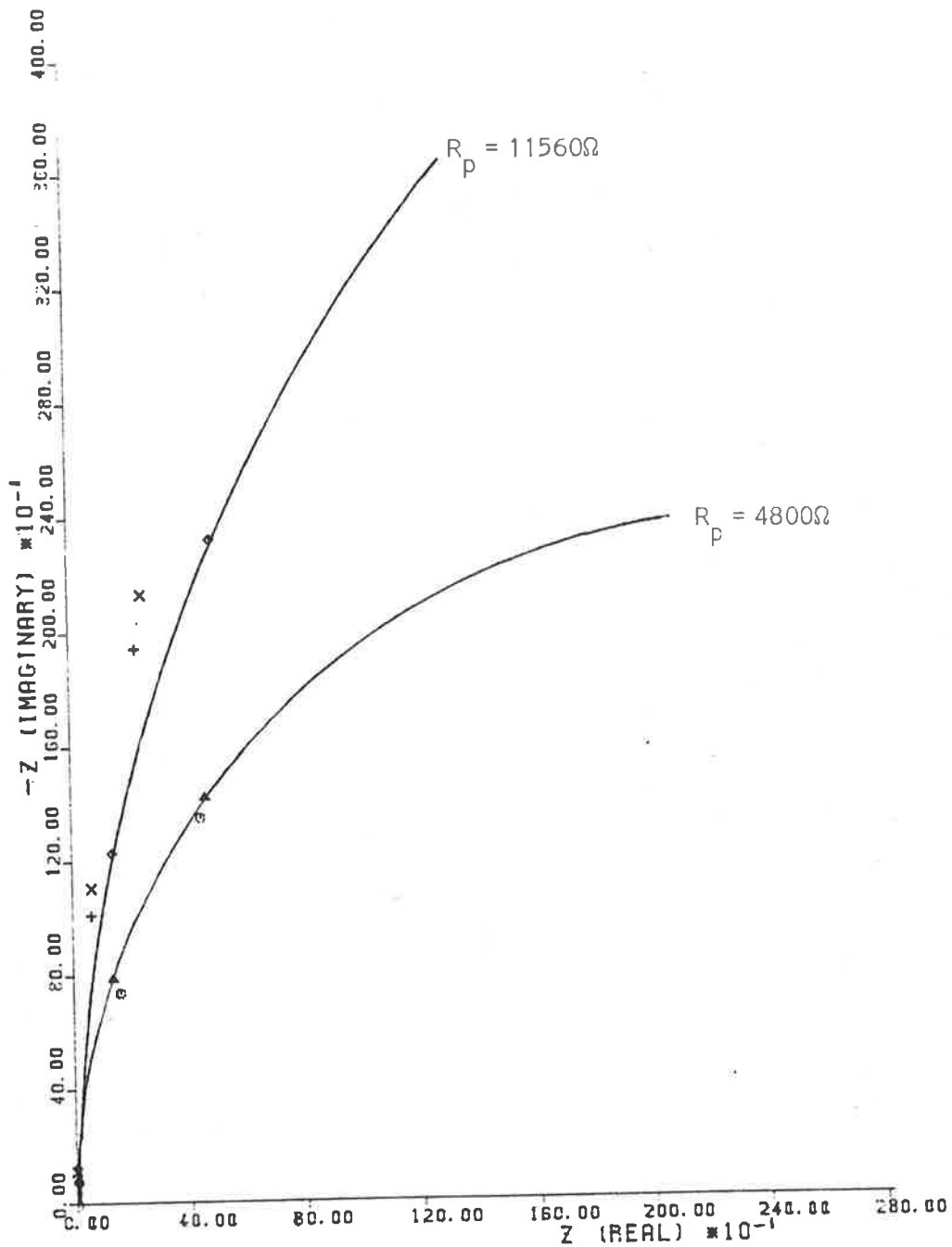


Figure 2. Complex plane impedance spectra for polycrystalline platinum/0.100M NaNO<sub>3</sub>/NMF at selected electrode potentials: -0.60 V (○); -0.40 V (Δ); 0.00 V (+); +0.20 V (×); +0.60 V (◇). Anodic scan. 10 mV/s scan rate.

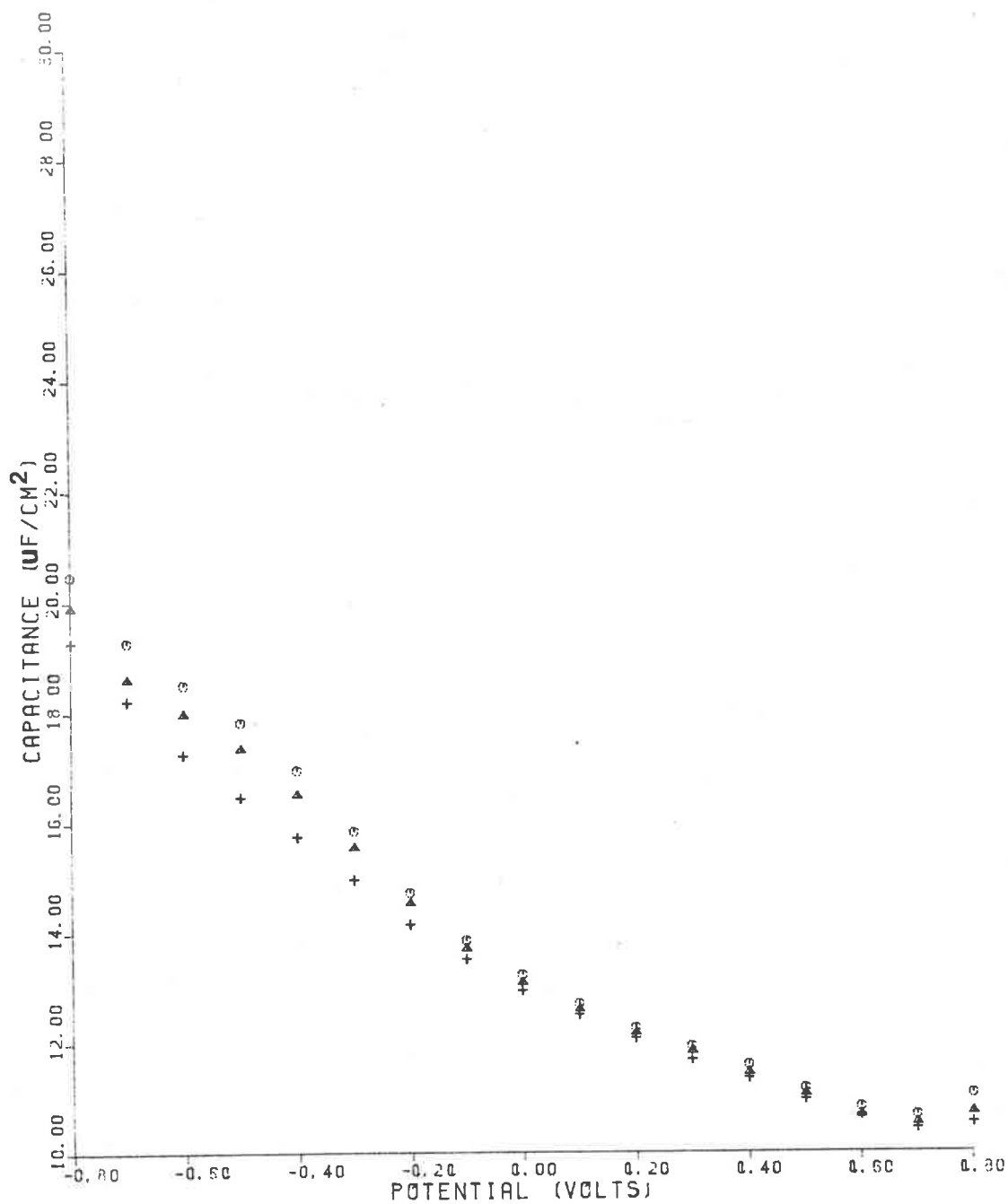


Figure 3. Frequency dependence of parallel capacitance-potential curves of teflon-encased polycrystalline platinum electrode in 0.100M NaNO<sub>3</sub> in NMF: 10 Hz (○); 20 Hz (△); 200 Hz (+). Cathode scan. 10 mV/s scan rate.

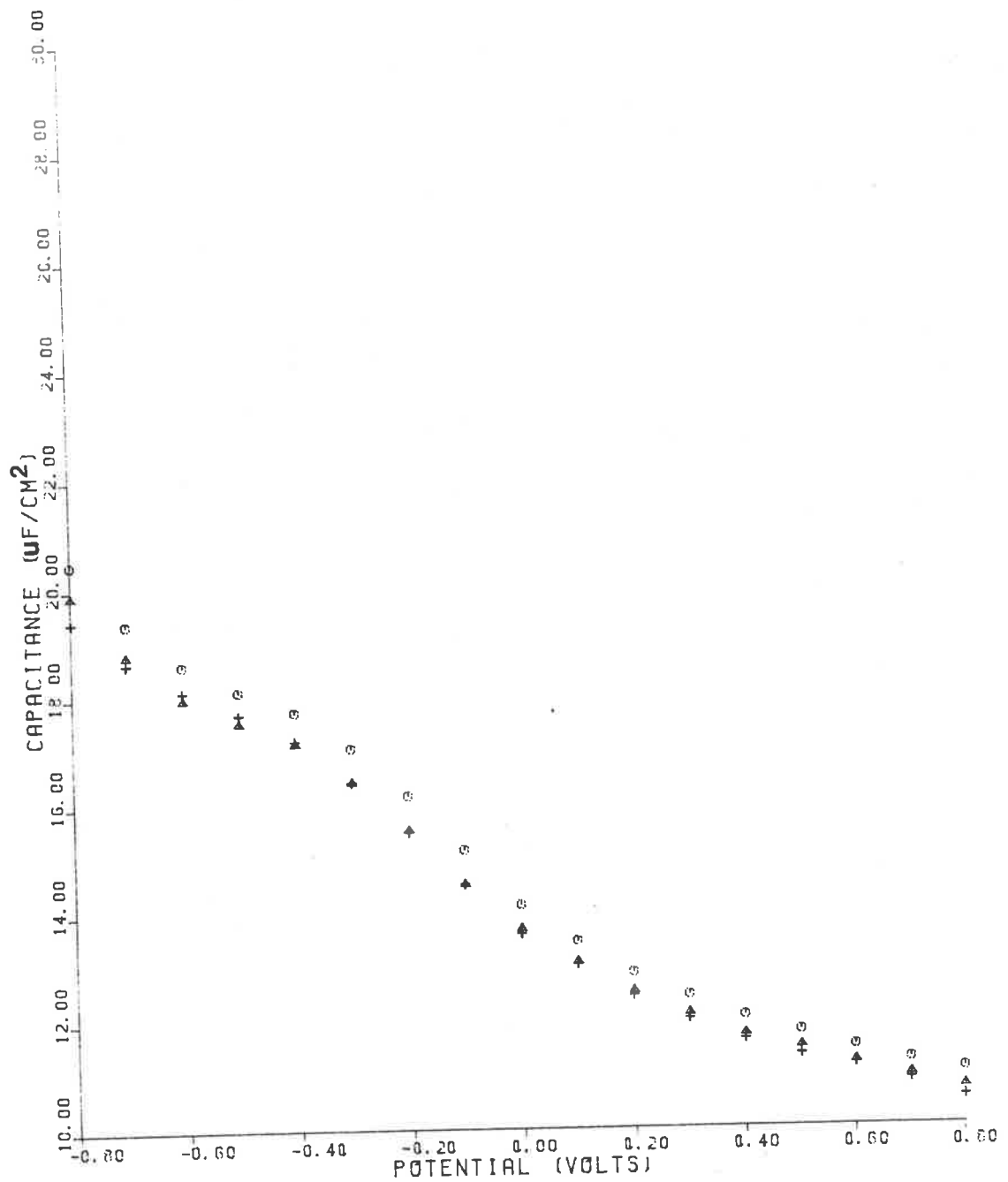


Figure 4. Frequency dependence of parallel capacitance-potential curves of teflon-encased polycrystalline platinum electrode in 0.100M  $\text{NaNO}_3$  in NMF: 10 Hz (○); 20 Hz (△); 200 Hz (+). Anodic scan. 10 mV/s scan rate.

a low value of  $10\frac{1}{2} \mu\text{F}/\text{cm}^2$  at +0.80 volts to a value of  $20 \mu\text{F}/\text{cm}^2$  at -0.80 volts.

Figures 5 and 6 show the parallel capacitance-potential curves determined for the polycrystalline platinum/ $5 \times 10^{-4}\text{M}$   $\text{NaNO}_3/\text{NMF}$  system. The general shape of these curves are similar to those in  $0.100\text{M}$   $\text{NaNO}_3$ , but at a frequency of 10 hz vary from about  $10 \mu\text{F}/\text{cm}^2$  at +0.80 volts up to a value of  $14\frac{1}{2} \mu\text{F}/\text{cm}^2$  at -0.80 volts. From Figures 5 and 6 it can be seen that the capacitance-potential curves show great frequency dependence, and possess no unambiguous capacitance minimum at a potential that could be equated with the potential of zero charge.

The general increase in the capacitance with increasing cathodic polarization can simply be correlated with the increasing reduction current observed in the cyclic voltammogram shown in Figure 1.

#### System II. $\text{Ag}/\text{NaNO}_3/\text{NMF}$

From the representative complex plane impedance diagram shown in Figure 7 it can be seen that the polycrystalline silver/ $5 \times 10^{-4}\text{M}$   $\text{NaNO}_3 + \text{NMF}$  interface is best described by the analogue circuit of a capacitor and resistor in parallel, combined with a series solution resistance of 960 ohms.

The parallel capacitance, calculated assuming a constant series resistance of 960 ohms, is displayed in Figures 8 and 9



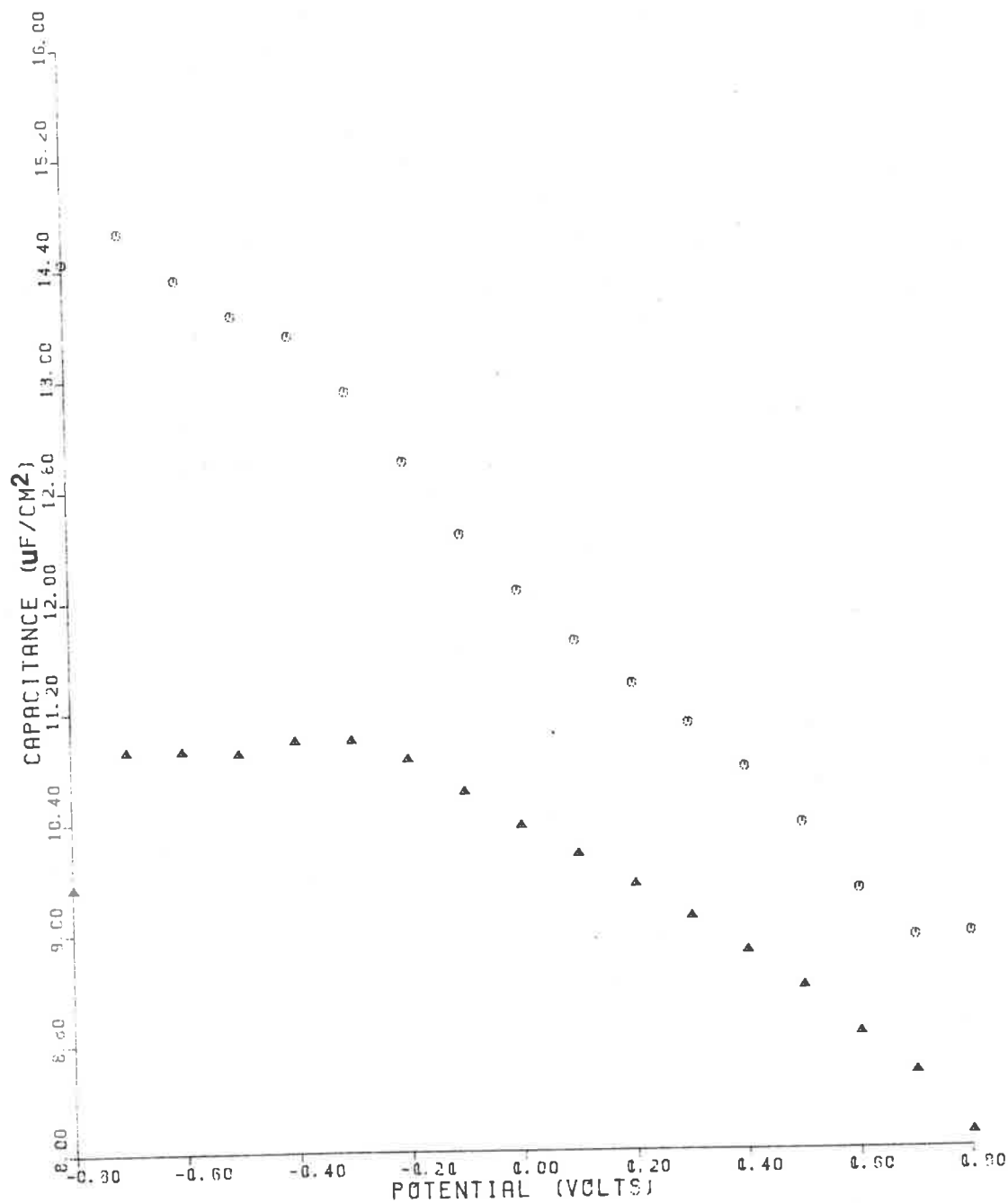


Figure 5. Frequency dependence of parallel capacitance-potential curves of teflon-encased polycrystalline platinum electrode in  $5 \times 10^{-4} \text{M NaNO}_3$  in NMF: 10 Hz (O); 20 Hz ( $\Delta$ ). Cathodic scan. 10 mV/s scan rate.

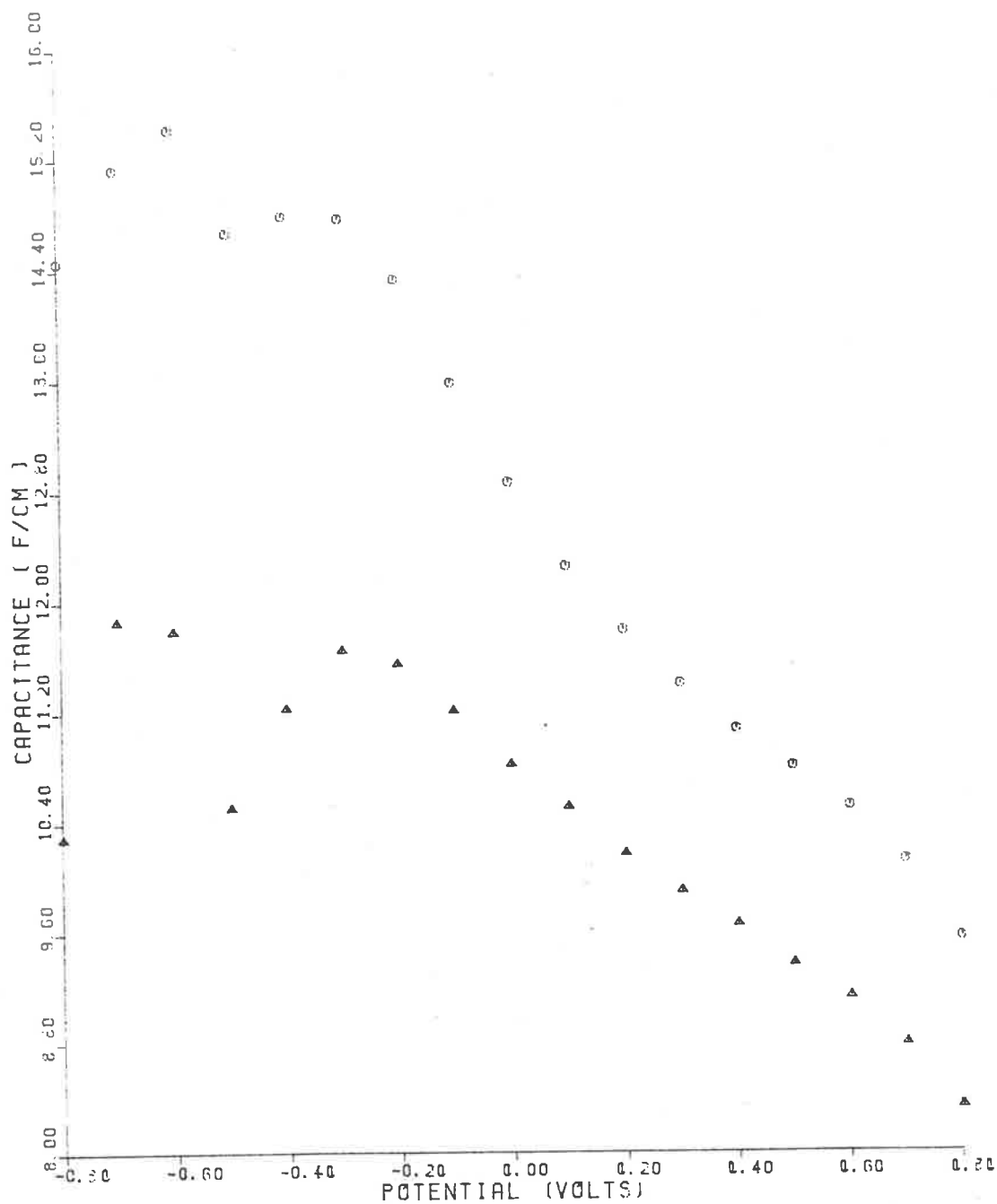


Figure 6. Frequency dependence of parallel capacitance-potential curves of teflon-encased polycrystalline platinum electrode in  $5 \times 10^{-4} \text{M NaNO}_3$  in NMF: 10 Hz (O); 20 Hz ( $\Delta$ ). Anodic scan.  $10 \text{ mV/s}$  scan rate.

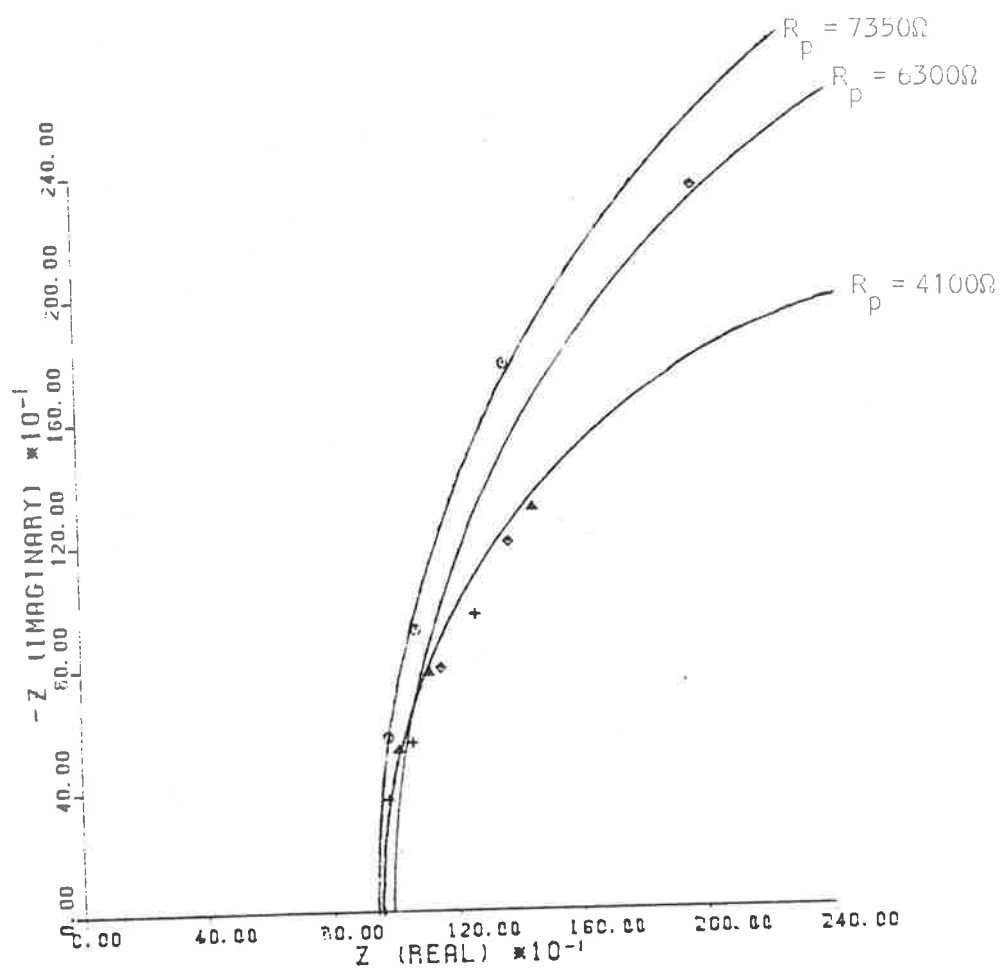


Figure 7. Complex plane impedance spectra for polycrystalline silver/  
 $5 \times 10^{-4}$  M  $\text{NaNO}_3$ /NMF at selected electrode potentials:  
 $-1.20$  V ( $\circ$ );  $-0.90$  V ( $\Delta$ );  $-0.70$  V ( $+$ );  $-0.40$  V ( $\times$ );  
 $-0.10$  V ( $\diamond$ ). Cathodic scan.  $10$  mV/s scan rate.

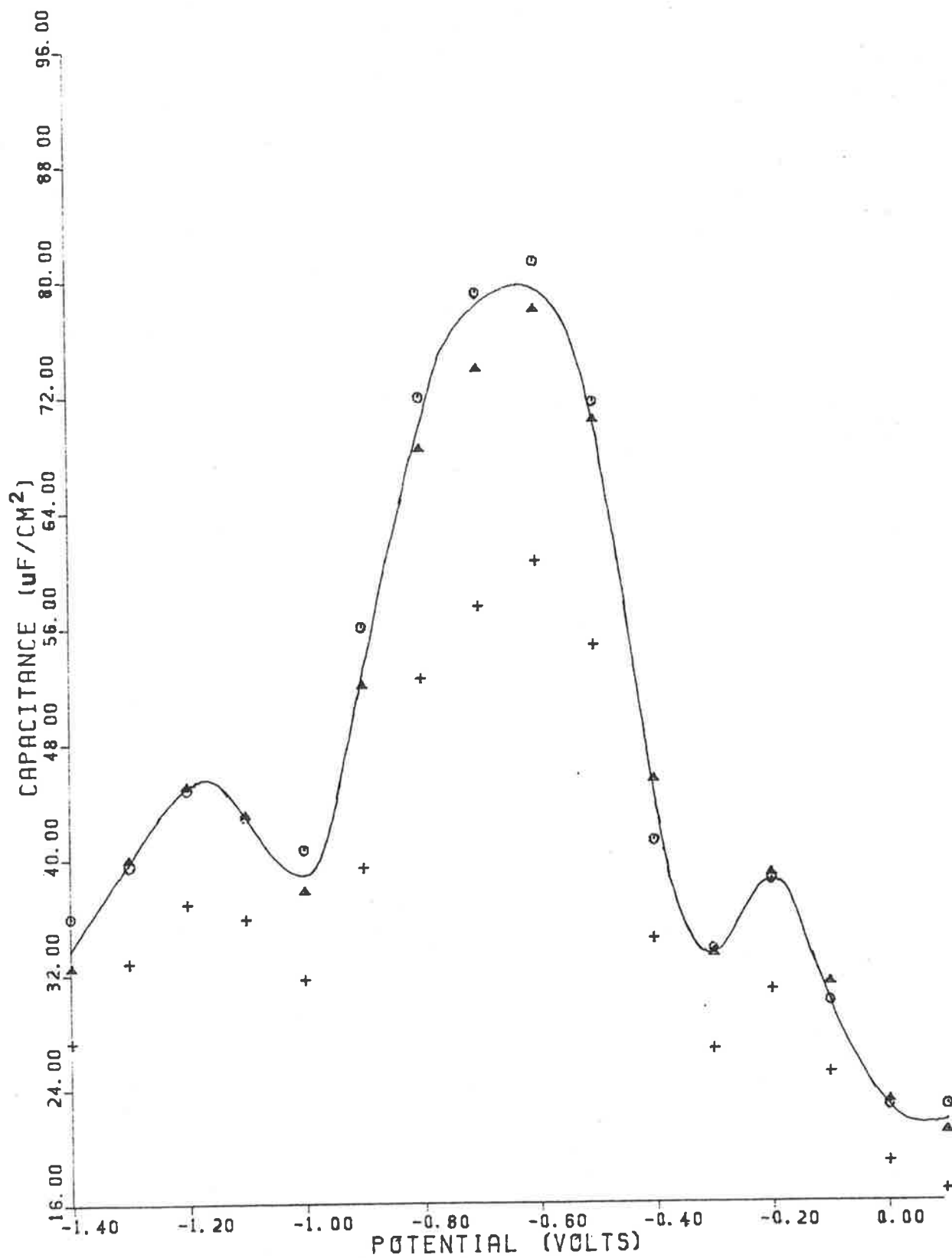


Figure 8. Frequency dependence of parallel capacitance-potential curves of the polycrystalline silver/ $5 \times 10^{-4} \text{M NaNO}_3 + \text{NMF}$  interface: 5 Hz (○); 10 Hz (△); 20 Hz (+). Cathodic scan. 10 mV/s scan rate.

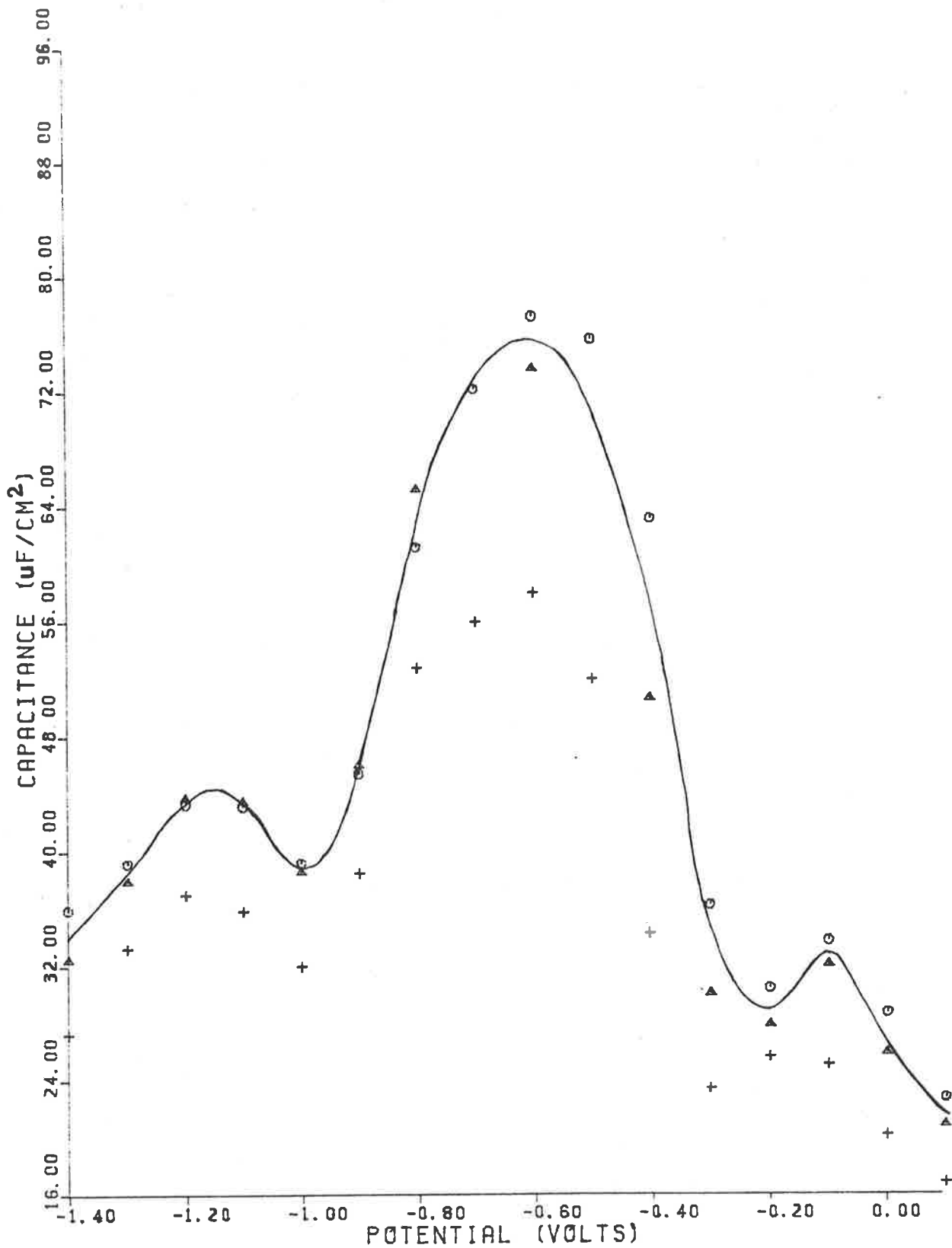


Figure 9. Frequency dependence of parallel capacitance-potential curves of the polycrystalline silver/ $5 \times 10^{-4} \text{M NaNO}_3 + \text{NMF}$  interface: 5 Hz (O); 10 Hz ( $\Delta$ ); 20 Hz (+). Anodic scan. 10 mV/s scan rate.

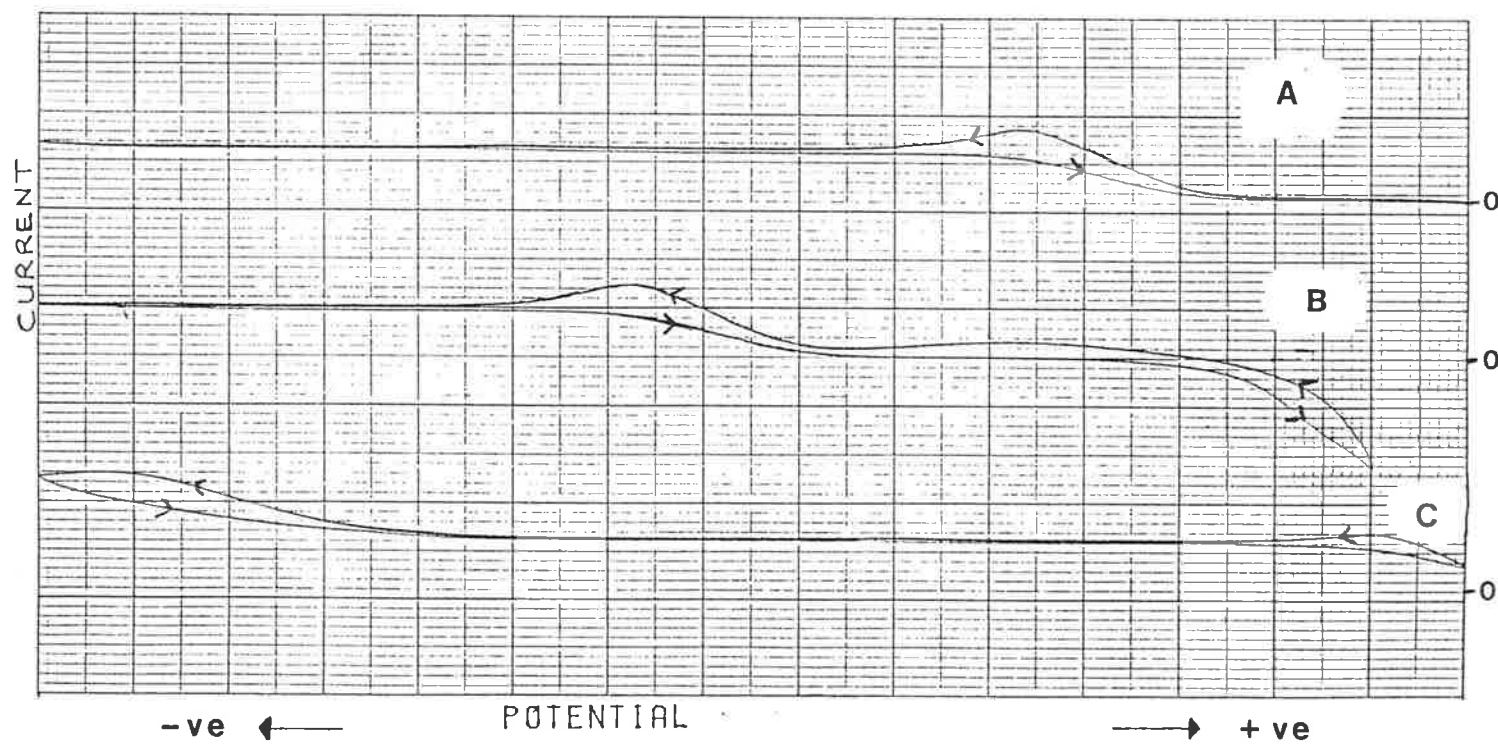


Figure 10. Cyclic voltammograms of the polycrystalline silver +  $5 \times 10^{-4}$  M  $\text{NaNO}_3$  + NMF system over various potential ranges:

A. -1.40 volts to +0.10 volts;

B. -1.00 volts to +0.40 volts;

C. -1.80 volts to -0.30 volts.

Horizontal fullscale = 1.50 volts. Vertical fullscale = 0.35 mA. 10 mV/s scan rate.

## 7.6

as a function of electrode potential. The curves show some frequency dependence, but the capacitance determined at the lowest frequencies of 5 hz and 10 hz are quite similar. The curves display the general features of a central capacitance maximum at about -0.7 volts, with capacitance minimum and maximums on either side.

Figure 10 shows a series of cyclic voltammograms for the above system cycled over different potential ranges. At potentials more cathodic than +0.20 volts, to avoid oxidation of the silver electrode, up to -0.20 volts is a featureless region of low current. At potentials more cathodic than about -0.30 volts, a constant degree of irreversible reduction occurs up to about -1.50 volts, where a second level of irreversible reduction occurs. The second reduction region is likely to be the onset of solvent reduction, whereas the earlier reduction current is likely to be associated with the electrolyte,  $\text{NaNO}_3$ .

### STANDARDISATION OF POTENTIAL SCALES

As was previously mentioned, the potential scales used in Figures 1-10 are with respect to a saturated calomel reference electrode in a luggin capillary filled with the solution under study. For a strictly thermodynamic study of adsorption from mixed solvent solutions, the reference electrode needs to be reversible to the cation or anion in the mixed solvent.<sup>3</sup>

## 7.7

The novel nitrate ion selective electrode, discussed by the author in Chapter 6 of thesis, was tested as a suitable reference electrode in NMF + NaNO<sub>3</sub> and H<sub>2</sub>O + NaNO<sub>3</sub> solutions. As was discussed in Chapter 6, the nitrate ion selective electrode responded to the nitrate ion present in both the pure NMF and pure H<sub>2</sub>O solvents. It was found that the electrode potential drifted, and required some 30 or so minutes to stabilize.

The capacitance-potential curves determined using the nitrate ion selective electrode as the reference electrode could be transposed on to those obtained using the calomel reference electrode by moving the curves along the potential axis. The author preferred to measure the capacitance-potential curves with respect to the calomel reference electrode because of its superior potential stability. The amount, however, that the potential scale needed to be altered by to give a correspondence with the nitrate electrode scale was found to be a simple matter that could be determined from cyclic voltammograms after the capacitance-potential curves had been obtained. Characteristic features in the cyclic voltammograms were used to calibrate the potential difference between the reference electrodes.

The nitrate ion selective electrode was found to have a potential 0.20 volts more negative than the saturated calomel electrode in a solution containing  $5 \times 10^{-4}$  M NaNO<sub>3</sub> + NMF.



7.8

The nitrate ion selective electrode was found to have a potential 0.35 volts more negative than the saturated calomel electrode in a solution containing 0.100M  $\text{NaNO}_3$  in pure water.

## CONCLUSION

The determination of the relative surface excess of an organic compound on a metal electrode from an aqueous solution containing a single electrolyte is based on the electrocapillary equation.<sup>3,10-13</sup> For a thermodynamically rigorous treatment of data at constant temperature and pressure, the electrocapillary equation needs to be differentiated with respect to solvent composition at constant activity of the electrolyte and constant electrode potential.<sup>11,12</sup>

From the writer's previous discussion in Chapter 6, it can be seen that it is possible to obtain data at constant electrolyte activity and constant electrode potential for the  $\text{H}_2\text{O} + \text{NMF} + \text{NaNO}_3$  system. The electrode potential for adsorption studies must be measured versus an electrode immersed in the same solution which is reversible either to the cation or the anion of the electrolyte. From earlier discussion, it was concluded by the writer that the novel nitrate ion selective electrode discussed in Chapter 6 could be used to establish a standardised potential scale for the  $\text{H}_2\text{O} + \text{NMF} + \text{NaNO}_3$  system.

The determination of adsorption data from double layer capacitance measurements further requires the knowledge of the variation of the charge density on the metal with respect to the electrode potential. The charge density on the metal electrode can be obtained from integration of capacitance-potential curves with respect to the potential of zero charge. This requires an accurate knowledge of the potential of zero charge.

The determination of the potential of zero charge is a fairly straightforward matter using mercury electrodes using a streaming mercury electrode technique.<sup>6</sup> However, this technique cannot be applied to solid electrodes. A number of methods have been attempted to determine the potential of zero charge on solid electrodes;<sup>14-20</sup> however, only the capacitance minimum technique appears to have found universal acceptance. In this latter technique, the potential of zero charge is equated with the potential of the capacitance minimum found in a capacitance-potential curve obtained in dilute electrolyte solutions. This technique does not, however, necessarily result in the finding of an unambiguous potential of zero charge, since specific ion adsorption can affect the results. This technique also has limited usability because in many moderate to high concentration electrolyte solutions there is no evidence of a capacitance minimum.

The writer's initial investigation of  $H_2O + NMF$  systems using double layer capacitance measurements attempted to use an electrolyte that was known to be only weakly specifically adsorbed on mercury in the vicinity of the potential of zero charge, and was very soluble in pure NMF. It was further hoped that a potential of zero charge could be found using such an electrolyte. It was known that  $NaF$  and  $NaNO_3$  were two electrolytes that fulfilled the first criteria.<sup>21</sup> It was found, however, that  $NaF$  was almost insoluble in pure NMF, whereas  $NaNO_3$  had a high solubility in NMF.

Polycrystalline silver and platinum electrodes were used by the writer to determine capacitance-potential curves in  $NaNO_3 + H_2O$  and  $NaNO_3 + NMF$  solutions. To maintain the same electrolyte activity as

## 7.11

0.100M  $\text{NaNO}_3$  in pure water, it was necessary to use  $5 \times 10^{-4}$  M  $\text{NaNO}_3$  in pure NMF.

Capcitanace minima were observed in dilute electrolyte solutions using the polycrystalline silver electrode. However, these capacitance minima could not be simply equated with the position of the potential of zero charge because the electrolyte at these potentials was undergoing irreversible reduction. There was also a further problem in the assigning of a potential of zero charge in aqueous 0.100M  $\text{NaNO}_3$ , since no capacitance minimum was found for that system. Though there are some problems, the use of silver electrodes to investigate NMF adsorption from mixed  $\text{H}_2\text{O} + \text{NMF}$  solutions appears quite plausible with a better choice of electrolyte.

The use of polycrystalline platinum electrodes to measure capacitance in pure water and NMF was found to be a reasonably simple matter only in moderately concentrated solutions. In dilute  $\text{NaNO}_3$  solutions, the selection of an appropriate analogue circuit to represent the polycrystalline platinum/electrolyte solution interface was not resolved in the present research. The consistent time dependence of capacitance measurements using polycrystalline platinum was also found to be a further complication that requires further attention. The writer realises that more detailed measurements of the capacitance using polycrystalline and single-crystal platinum electrodes are necessary in dilute electrolytes in mixed  $\text{H}_2\text{O} + \text{NMF}$  solutions. The usefulness of such studies to determine NMF adsorption data cannot be gauged at this stage.

Khomchenko and others<sup>22-26</sup> have recently measured the double layer capacitance of polycrystalline platinum in acetonitrile solutions. These workers found that the cation selected had a considerable bearing on the capacitance-potential curves. They found it possible to detect a capacitance minimum, corresponding to the maximum diffuseness of the electrical double layer, using  $\text{LiClO}_4$ ,<sup>22</sup>  $(\text{C}_2\text{H}_5)_4\text{NClO}_4$  and  $(\text{C}_2\text{H}_5)_4\text{NBF}_4$ ,<sup>23,24</sup> but not in  $\text{NaClO}_4$  solutions.<sup>25</sup> Khomchenko and Zelinskii<sup>26</sup> concluded from these results that the specific interaction of cations with platinum in acetonitrile was in the order:  $\text{Na}^+ > (\text{C}_2\text{H}_5)_4\text{N}^+ > \text{Li}^+$ .

From the conclusions of Khomchenko et al concerning cation interaction, and problems encountered in using nitrates with silver, the writer envisages that future work in mixed  $\text{H}_2\text{O} + \text{NMF}$  solutions using platinum and silver electrodes will involve a more thorough study of electrolytes to discern what electrolytes will enable the most adsorption information to be obtained.

The common practice in adsorption studies using metal electrodes has been to supplement the thermodynamic approach with model assumptions, in particular by the assumption of congruence of the adsorption isotherm with respect to one of the electric variables, charge or potential. Standard equations have been derived that enable one to determine adsorption data from double layer capacitance measurements assuming the adsorption isotherm to be congruent with respect to charge or with respect to potential. This is well discussed by Frumkin et al.<sup>27</sup>

### 7.13

Katoh and co-workers, for example, used such a method to study the adsorption of organic molecules on polycrystalline gold in perchlorate<sup>28</sup> and perchloric acid solutions<sup>29</sup> from capacitance measurements made using rectangular single pulse techniques. In deriving adsorption data, Katoh et al assumed the adsorption isotherm to be congruent with respect to potential.

A vigorous debate has been carried on over the last 30 years as to whether congruence with respect to electrode potential or excess charge density was the better approximation to the behaviour of organic sorbates on metal electrodes. Recently, however, Mohilner and Karolczak<sup>30</sup> concluded that there was no theoretical justification in using the concept of congruence of an organic electrosorption isotherm with respect to electric variable. From this finding, Karolczak and Mohilner<sup>31</sup> concluded that the equation most commonly used to determine electrosorption isotherms from differential capacitance measurements is, in general, incorrect. They did state, however, that in certain cases the most commonly used equation may be approximately valid.

On a more positive note, Karolczak and Mohilner<sup>32</sup> have derived general equations in terms of excess charge density from which excess electrochemical free energy of mixing of the inner layer and the activity coefficients of the adsorbed species can be calculated. These equations have been derived on the basis of the theory of non-congruent electrosorption of organic compounds originally proposed by Mohilner et al in 1977.<sup>33</sup>

Recently, Sangaranarayan and Rangarajan have published a series of articles in five parts<sup>34-38</sup> dealing with adsorption isotherms for neutral organic compounds. The authors forwarded a non-congruent adsorption isotherm based upon statistical mechanical modelling of the solvent and adsorbate. They also reviewed other adsorption isotherms, and analysed the criteria for the charge congruence and the potential congruence of such in the light of their new isotherm.<sup>34</sup>

The work of Sangaranarayan and Rangarajan is likely to form a foundational basis from which the appropriateness of various assumptions made in determining adsorption data can be tested. It is not unlikely that the assumptions made in the commonly used procedures of the past will prove adequate for the description of various systems, while being unacceptable in the description of other systems.

The writer sees, therefore, that double layer capacitance measurements made in mixed solvent systems, such as  $H_2O + NMF$ , will be able to contribute toward a better understanding of the interaction of solvent and adsorbate at the metal/electrolyte solution interface.

## REFERENCES

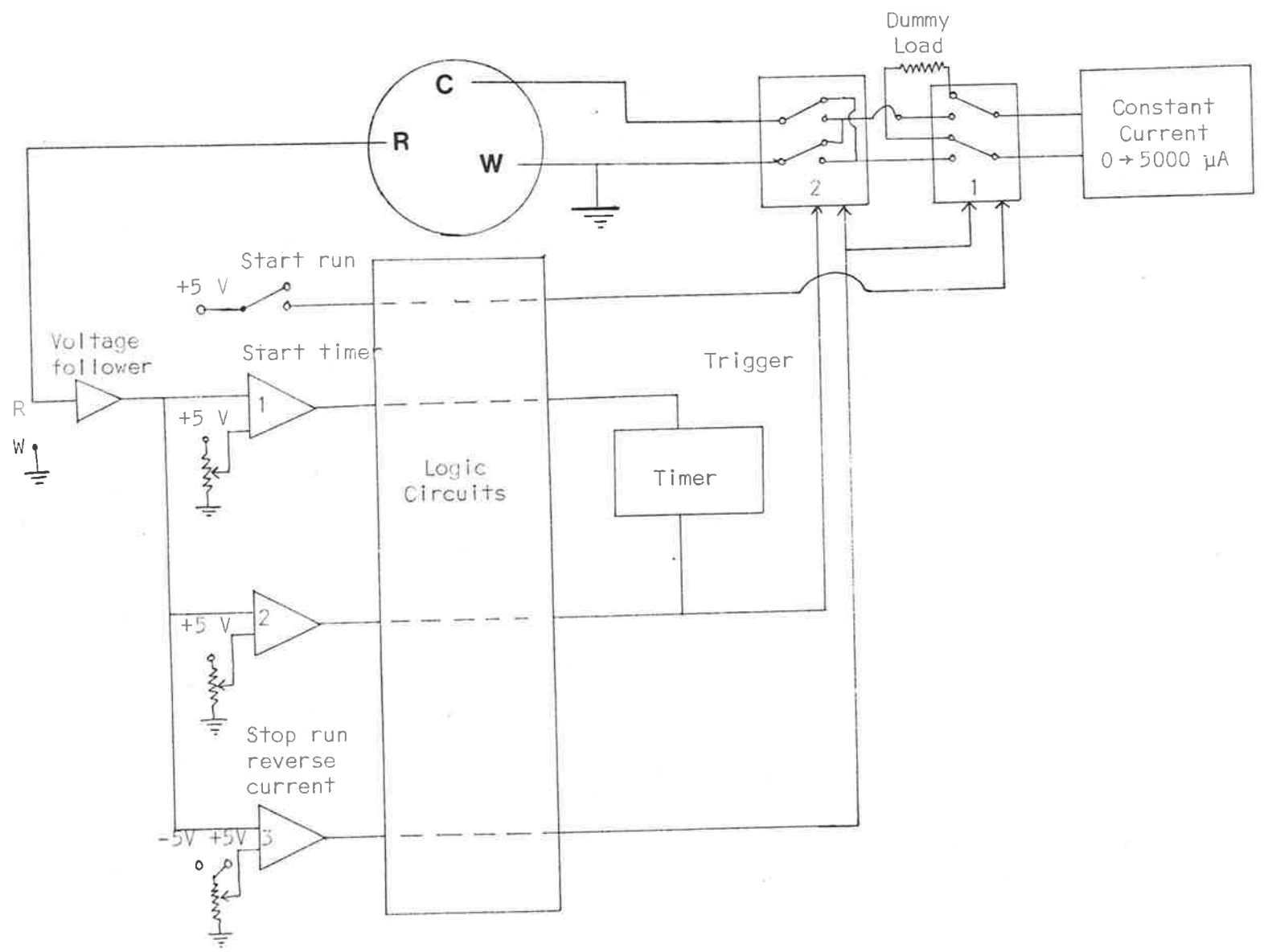
- 1 DAMASKIN, B. B. and POVAROV, Yu. M., *Dokl. Akad. Nauk. SSR*, 140(1961) 394.
- 2 DAMASKIN, B. B. and IVANOVA, R. V., *Zh. Fiz. Khim.*, 38(1964) 176; *Russ. J. Phys. Chem.*, 38(1964) 92.
- 3 KOZMINSKA, D., BORKOWSKA, Z. and BEHR, B., *Can. J. Chem.*, 59(1981) 2043.
- 4 BORKOWSKA, Z., DENOBRIGA, R. M. and FAWCETT, W. R., *J. Electroanal. Chem.*, 124(1981) 263.
- 5 PAYNE, R., *J. Phys. Chem.*, 73(1969) 3598.
- 6 PAYNE, R., *J. Electroanal. Chem.*, 47(1973) 265.
- 7 FAWCETT, W. R. and LOUTFY, R. O., *J. Electroanal. Chem.*, 39(1972) 185.
- 8 PAYNE, R., *Advan. Electrochem. Eng.*, 7(1970) 127.
- 9 PARSONS, R., *Electrochim. Acta*, 21(1976) 681.
- 10 MOHILNER, D. M. and NAKADOMARI, H., *J. Phys. Chem.*, 77(1973) 1549.
- 11 MOHILNER, D. M. and NAKADOMARI, H., *J. Electroanal. Chem.*, 65(1975) 843.
- 12 BORKOWSKA, Z., *J. Electroanal. Chem.*, 63(1975) 379.
- 13 TARASZEWSKA, J., *J. Electroanal. Chem.*, 121(1981) 215.
- 14 LEIKIS, D. I., RYBALKA, K. V., SEVASTYANOV, E. S. and FRUMKIN, A. N., *J. Electroanal. Chem.*, 46(1973) 161.
- 15 PANGAROV, N. and KOLAROV, G., *J. Electroanal. Chem.*, 91(1978) 281.
- 16 BOCKRIS, J. O'M., ARGADE, S. D. and GILEADI, E., *Electrochim. Acta*, 14(1969) 1259.
- 17 FRUMKIN, A. N., BALASHOVA, N. A. and KAZARINOV, V. E., *J. Electrochem. Soc.*, 113(1966) 1011.
- 18 PETRII, O. A., FRUMKIN, A. N. and KOTLOV, Yu. G., *Soviet Electrochem.*, 5(1969) 435.
- 19 BALASHOVA, N. A., GOROKHOVA, N. T. and KULEZNEVA, M. J., *Soviet Electrochem.*, 4(1968) 787.
- 20 SCHIFFRIN, D. J., *Electrochemistry*, 1(1970) 252.
- 21 PAYNE, R., *J. Electrochem. Soc.*, 113(1966) 999.



- 22 PETRII, O. A., KHOMCHENKO, I. G. and ZELINSKII, A. G., *Elektrokhimiya*, 15(1979) 400.
- 23 KHOMCHENKO, I. G. and PETRII, O.A., in *Double Layer and Adsorption on Solid Electrodes*, VI (in Russian). Izd. Tartusk Univ., 1981. p.368.
- 24 KHOMCHENKO, I. G. and PETRII, O. A., *Soviet Electrochem.*, 19(1983) 1010.
- 25 PETRII, O. A. and KHOMCHENKO, I. G., *Elektrokhimiya*, 14(1978) 1435.
- 26 KHOMCHENKO, I. G. and ZELINSKII, A. G., *Soviet Electrochem.*, 19(1983) 1381.
- 27 FRUMKIN, A. N., DAMASKIN, B. and SURVILA, A. A., *J. Electroanal. Chem.*, 16(1968) 493.
- 28 KATOH, K. and SCHMID, G. M., *Bull. Chem. Soc. Japan*, 44(1971) 2007.
- 29 KATOH, K. and KOSEKI, M., *J. Electrochem. Soc.*, 131(1984) 303.
- 30 MOHILNER, D. M. and KAROLCZAK, M., *J. Phys. Chem.*, 86(1982) 2838.
- 31 KAROLCZAK, M. and MOHILNER, D. M., *J. Phys. Chem.*, 86(1982) 2845.
- 32 KAROLCZAK, M. and MOHILNER, D. M., *J. Phys. Chem.*, 86(1982) 2840.
- 33 MOHILNER, D. M., NAKADOMARI, H. and MOHILNER, P. R., *J. Phys. Chem.*, 81(1977) 244.
- 34 SANGARANARAYANAN, M. V. and RANGARAJAN, S. K., *J. Electroanal. Chem.*, 176(1984) 1.
- 35 SANGARANARAYANAN, M. V. and RANGARAJAN, S. K., *J. Electroanal. Chem.*, 176(1984) 29.
- 36 SANGARANARAYANAN, M. V. and RANGARAJAN, S. K., *J. Electroanal. Chem.*, 176(1984) 45.
- 37 SANGARANARAYANAN, M. V. and RANGARAJAN, S. K., *J. Electroanal. Chem.*, 176(1984) 65.
- 38 SANGARANARAYANAN, M. V. and RANGARAJAN, S. K., *J. Electroanal. Chem.*, 176(1984) 99.

APPENDIX 1

Circuit of Galvanostat used in chronopotentiometry



## APPENDIX 2

Discussion concerning the scanning electron microscope (S.E.M.) micrographs presented in Figure 4 of Chapter 3.

Figures 4a, 4c and 4d represent the same platinum disc surface. This electrode was not the electrode used in Chapters 4, 6 and 7 for hydrogen atom adsorption and double layer capacitance measurements because mounting the disc in S.E.M. studies required the destruction of the electrode. The electrode is, however, likely to be representative of the disc electrode used if one does not take into account the larger defects. Figure 4d was included because the back scattered electron image, while insensitive to surface topography, shows dark spots of grease etc. collected from the atmosphere during the traverse of the samples from the laboratory to the Electron Optical Centre. The unusual deposits on the surface in Figures 4a and 4c are simply grease and other contaminants collected from the atmosphere.

Figure 4b is representative of the platinum surface finish of the electrodes used in the chronopotentiometry work of Chapter 2. Those electrodes were polished down with 1  $\mu\text{m}$  diamond paste. The surfaces used in the capacitance measurements were more finely polished, and showed fewer and smaller surface defects.